Inférence de la réfraction troposphérique par méthodes d'optimisation

Uygar Karabaş

Université Fédérale

Toulouse Midi-Pyrénées

THÈSE

En vue de l'obtention du

DOCTORAT DE L'UNIVERSITÉ DE TOULOUSE

Délivré par :

Institut Supérieur de l'Aéronautique et de l'Espace

Présentée et soutenue par :
Uygar KARABAŞ
le jeudi 4 novembre 2021

Titre :

Inferring tropospheric radio refractivity using optimization methods

Inférence de la réfraction troposphérique par méthodes d'optimisation

---

École doctorale et discipline ou spécialité :
ED AA : Électromagnétisme et Systèmes Haute Fréquence - Mathématiques et Applications

Unité de recherche :
ENAC - TELECOM - Electromagnétisme et Antennes ISAE - DISC - Mathématiques Appliquées

Directeur(s) de Thèse :

M. Michel SALAÜN (directeur de thèse)

Jury :
Mme Hélène BARUCQ Directrice de recherche INRIA Bordeaux - Présidente
M. Jacques CLAVERIE Maître de conférences Académie Militaire de Saint-Cyr Coëtquidan- Examinateur
M. Peter GERSTOFT Professeur Université de Californie San Diego - Rapporteur
M. Jérôme MONNIER Professeur INSA Toulouse - Examinateur
M. Michel SALAÜN Professeur ISAE-SUPAERO - Directeur de thèse
M. Jean VIRIEUX Professeur émérite Université Grenoble Alpes - Rapporteur

Inferring Tropospheric Radio Refractivity Using Optimization Methods

Acknowledgments

First of all, I would like to thank to Mr. Michel Salaün, professor of Institut Supérieur de l'Aéronautique et de l'Espace, for his great supervision, humanity and character. He is wonderful.

Secondly, I would like to thank to the reviewers Mr. Peter Gerstoft, professor of University of California San Diego and Mr. Jean Virieux, emeritus professor of Université Grenoble Alpes for reviewing the manuscript. I also thank to the jury members Mr. Jacques Claverie, maître des conferences of Academie Militaire de Saint-Cyr Coëtquidan and Mr. Jérôme Monnier, professor of Institut National des Sciences Appliquées (INSA) de Toulouse. Lastly, I thank to president of the jury Mrs. Hélène Barucq, research director of Institut National de Recherche en Informatique et en Automatique (INRIA) of Bordeaux Sud-Ouest. I thank to all jury members for their discussions, questions and suggestions on the thesis work.

I am grateful to the establishments of Ecole Nationale de l'Aviation Civile (ENAC), Institut Supérieur de l'Aéronautique et de l'Espace (ISAE-SUPAERO) and Ecole Doctorale Aéronautique Astronautique (EDAA) for providing this research opportunity.

I was introduced to this research subject by Mr. Rémi Douvenot and Mr. Youssef Diouane, associate professors of ENAC and ISAE-SUPAERO respectively, during my doctoral research in the beginning. The part of doctoral research work with them is published in [1]–[4]. A part of Chapter 2 of this thesis was published in the following work:

- U. Karabaş, Y. Diouane, and R. Douvenot, "On the use of adjoint methods for refractivity estimation in the troposphere," in *Proceedings of the 14th European Conference on Antennas and Propagation (EuCAP)*, Mar. 2020, pp. 1–5.
  DOI: 10.23919/EuCAP48036.2020.9135287
- U. Karabaş, Y. Diouane, and R. Douvenot,"A variational adjoint approach on wide-angle parabolic equation for refractivity inversion," *IEEE Transactions on Antennas and Propagation*, vol. 69, no. 8, pp. 4861– 4870, Aug. 2021.
  DOI: 10.1109/TAP.2021.3060073

and a preliminary attempt of multiscale strategies related to Chapter 3 was published in:

- U. Karabaş, Y. Diouane, and R. Douvenot, "A multiscale parametrization for refractivity estimation in the troposphere," in *Proceedings of the 15th European Conference on Antennas and Propagation (EuCAP)*, Mar. 2021, pp. 1–5.
  DOI: 10.23919/EuCAP51087.2021.9410989

Table of Contents

List of Figures

List of Tables

Abbreviations

2D	Two Dimensional
3D	Three Dimensional
AM	Adjoint Model
CPS	Complex Point Source
DSR	Data Space Reduction
EMWF	ElectroMagnetic Wave Field
FD	Finite Differences
FM	Forward Model
MAT	Multiscale Adjoint-based Tomography
MPT	Multiscale Parametrization Technique
NAPE	Narrow-Angle Parabolic Equation
PPI	Plan Position Indicator
PWE	Parabolic Wave Equation
RBT	Refractivity By Tomography
RFC	Refractivity From Clutter
SSR	Search Space Reduction
TLM	Tangent Linear Model
WAPE	Wide-Angle Parabolic Equation
WAPE-TC	Wide-Angle Parabolic Equation of Thomson and Chapman

Resume

Anomalous tropospheric refraction causes performance of naval radar systems to deviate from the normal. The main goal of this thesis is to develop a refractivity inversion technique to predict the anomalies in radar coverage accurately in real-time. In this study, the altitude-dependent refractivity is predicted from phaseless radio wave measurements taken in bistatic configuration.

We are interested in exploring the inversion techniques which are efficient in high-dimensional realistic scenarios during maritime operations and which can maintain accuracy with minimum possible need for case-specific *a priori* information. The long-term goal is to transfer the developed techniques and knowledge to advance to a 'Refractivity-From-Clutter' system, which is the ideal self-contained inversion technique to upgrade ship self-defense, but more complex to analyze and develop properly.

The inverse problem is formulated as a simulation-driven nonlinear optimization problem which is tackled using Quasi-Newton methods. The simulations are modeled with the 2D wide angle parabolic wave equation of Thomson and Chapman. The gradient of the optimization problem is obtained using variational adjoint approach and it is estimated cheaply at the cost of two forward model simulations regardless of parameter dimension. The derivations are validated numerically using synthetically-generated measurements.

The numerical tests confirmed the nonlinear and ill-posed character of the inverse problem which often led to inaccurate inversion results, even in ideal conditions when no modeling or measurement errors existed. Quality of the results was improved by using multiscale strategies which overcame non convexity and nonlinearity of the problem. Accurate inversion results are obtained using reduction in search and data spaces. The advantages and the limitations of the technique is discussed in realistic high-dimensional scenarios.

Résumé

Une réfraction troposphérique anormale peut entraîner une perte de performances des systèmes radar par rapport à la normale. L'objectif principal de cette thèse est de développer une technique d'inversion de la réfractivité pour prédire les anomalies de la couverture du radar avec précision et en temps réel. Dans cette étude, la réfractivité est supposée ne dépendre que de l'altitude et elle est estimée à partir de mesures faites en module des ondes radio en configuration bistatique.

Nous sommes intéressés par l'exploration de techniques d'inversion qui sont efficaces dans des scénarios réalistes pendant les opérations maritimes et qui peuvent maintenir la précision avec un minimum de besoin en connaissances *a priori* spécifiques au cas étudié. L'objectif à long terme est de transférer les techniques et les connaissances développées pour progresser vers un système de 'Refractivity-From-Clutter', qui est la technique d'inversion idéale pour améliorer l'autodéfense des navires, mais qui est plus complexe à analyser et à développer correctement.

Le problème inverse est formulé comme un problème d'optimisation non linéaire, qui est résolu à l'aide de méthodes de Quasi-Newton. Les simulations sont effectuées en utilisant l'équation d'onde parabolique dite grand angle de Thomson et Chapman. Le gradient du problème d'optimisation est obtenu à l'aide de l'approche variationnelle adjointe. Il est calculé grâce à deux simulations du modèle direct, quelle que soit la dimension de l'espace des paramètres. Les développements sont validés numériquement en utilisant des mesures générées synthétiquement.

Les tests numériques ont confirmé le caractère non linéaire et mal posé du problème inverse qui conduit souvent à des résultats d'inversion inexacts, même dans des conditions idéales, lorsqu'il n'existe aucune erreur de modélisation ou de mesure. Comme le problème est non linéaire et non convexe, des stratégies multi-échelles sont développées pour améliorer la qualité de la solution. Des résultats d'inversion plus précis sont obtenus en réduisant les espaces de paramètres et de mesures. Les avantages et les limites de cette méthode sont discutés à partir de scénarios réalistes en dimension élevée.

Chapter 1

Introduction

Contents

Synthèse – Les systèmes radar navals fonctionnent près du niveau de la mer en émettant des ondes radio à travers l'atmosphère. La propagation des ondes radio dépend de la distribution des indices de réfraction dans l'espace aérien autour du radar. Certaines distributions de l'indice de réfraction peuvent faire dévier la trajectoire de propagation du faisceau radar de manière significative par rapport à ce qui est normalement prévu et elles sont appelées conditions de réfraction anomales ou non standard. Ces conditions peuvent donner lieu à des anomalies dans les performances du système radar, comme l'apparition de zones aveugles dans l'espace aérien. Il est donc essentiel de connaître avec précision la réfractivité ambiante pour prédire les performances du radar.

La distribution de la réfractivité dans l'atmosphère est n'est pas prévisible *a priori*. Il n'est pas non plus possible de mesurer la distribution de la réfractivité atmosphérique tout autour d'une plate-forme radar de manière suffisamment détaillée et en temps réel pendant toute la durée d'une opération. Une technique appelée Refractivity-From-Clutter (RFC) est proposée pour inverser la réfractivité à partir des données mesurées par le radar. L'idée est d'exploiter l'écho de l'émission radar qui revient vers le navire à partir de la surface ondulée de la mer. Comme cet écho est dû aux ondes radio qui se sont propagées dans l'espace aérien, il doit contenir les traces de la distribution de la réfractivité ambiante et nous devrions être en mesure de les récupérer.

Il existe des modèles décrivant la relation entre la réfractivité m (paramètre distribué du système) et la puissance du signal reçu P_R (données observables) grâce aux Equations (1.2), (1.4), (1.7) et (1.5). Selon ces relations, le RFC est un problème inverse mal posé dans lequel les données et le paramètre sont liés de manière non linéaire. Une première question concerne la résolution du problème direct qui doit être énoncé clairement et précisément avant de résoudre le problème inverse car celui-ci est déjà très difficile à résoudre même lorsque les modèles physiques sont parfaitement connus. Une autre difficulté d'un tel problème est qu'il existe peut-être

plusieurs distributions de réfractivité qui peuvent expliquer les données de manière comparable. Les méthodes qui ont traité ces questions dans la littérature s'accompagnent de certaines hypothèses et limitations que nous voulons lever dans cette thése.

Afin d'explorer en détail la possibilité d'inverser la variation de réfractivité, nous avons construit un scénario idéal. Notre stratégie est de commencer nos investigations à partir du problème le plus simple que nous puissions avoir dans le contexte de l'inversion de la réfractivité en milieu maritime et d'augmenter progressivement la difficulté au fur et à mesure que nous le résolvons. L'objectif est de comprendre les questions liées à l'inversion de la réfractivité en général et de construire des méthodes qui sont également applicables au problème RFC original que nous avons considéré au début.

À cette fin, nous avons construit un scénario numérique idéal dans une configuration bistatique où nous prenons une tomographie de l'atmosphère en utilisant un réseau d'antennes réceptrices positionnées verticalement à une certaine distance du navire. Cette configuration est illustrée Figure 1.9 sous le nom de Refractivity-By-Tomography (RBT) en comparaison avec le RFC. Dans ce scénario, nous supposons également que les modèles physiques sont connus parfaitement. Nous réduisons notre problème à un problème d'identification de paramètres de réfractivité distribués dans une équation d'état aux dérivées partielles où la fonction d'état est connue dans une partie du domaine de calcul. De plus, nous supposons que nous pouvons mesurer le champ réduit u, qui est une grandeur associée au champ électrique, en chaque point de l'altitude avec ce réseau de récepteurs et que le paramètre de réfractivité m varie uniquement avec l'altitude.

Afin d'effectuer cette inversion de manière efficace, le problème inverse est formulé comme un problème d'optimisation des moindres carrés non linéaires piloté par la simulation où la différence entre les données mesurées et simulées sur u est minimisée sur le paramètre de réfractivité m. Nous utilisons des méthodes d'optimisation de Quasi-Newton pour minimiser la fonction d'erreur dont le gradient est calculé en utilisant l'approche variationnelle adjointe. Enfin, nous utilisons des stratégies multi-échelles comme dans les problèmes inverses géophysiques, afin d'atténuer la difficulté de l'inversion.

Naval radar systems operate near sea level by emitting radio waves through the atmosphere. The propagation of the radio waves depends on radio refractive index distribution around the radar, which depends on ambient atmospheric conditions. Some refractive conditions can cause the propagation path of radar beam to deviate significantly from what is normally expected. Those conditions can give rise to anomalies in radar system performance. For example, some part of the airspace can become a blind zone where targets cannot be detected. For that reason, it is important to have situational awareness about the refractive conditions in the surrounding of the radar.

In theory, we can predict the radar coverage and provide it as a diagram by simulating the propagation in the ambient conditions. However, the ambient refractive index information is not known well and detailed enough *a priori*, to feed the simulations as input. There exist numerous refractivity estimation techniques which respond to the needs of mission planners to certain extent during the maritime operations, some of which are still being improved. If we want our modern detection systems to be more precise, our systems need to exploit more detailed real-time accurate information about the ambient refractivity.

In this dissertation, the goal is to develop techniques which can predict the detailed vertical

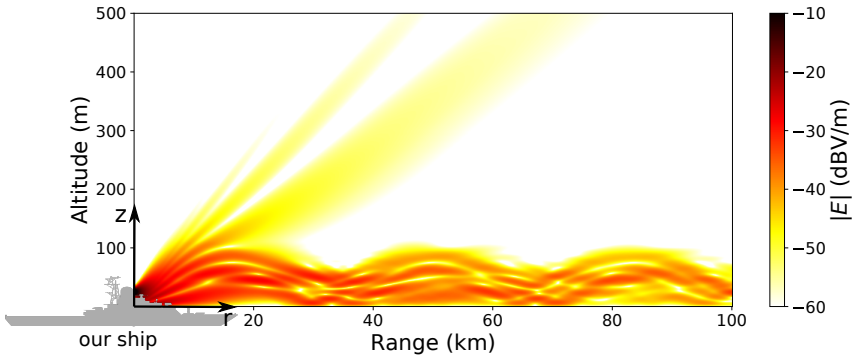

Figure 1.1: A 2D illustration of the radar coverage in non-standard maritime environment. White zones are weakly-illuminated zones in the airspace. See Section 1.1.2 for a detailed description of this diagram.

profile of the ambient radio refractive index in the first few hundred meters above sea surface. The prediction is made by analyzing the wave field of the radar emission measured at a distance from the ship, that is, at bistatic configuration.

In the following sections, we explain atmospheric refraction phenomenon in maritime environment in our context. Later we outline the methods that are used for predicting the refractivity in the literature and justify our choice of refractivity estimation technique.

1.1 The Phenomenological Background

1.1.1 Refraction of propagating waves

Everyone should be familiar with the effects of refraction of light from the visual daily life experiences. The three examples can be, (1) our perception of a spoon bent in a glass filled with water or (2) the blurry sight we have when looking at the trees through heat haze of the barbecue during picnic or (3) the spherical sun appearing shorter than normal during sunset. Although many may not be able to relate those experiences to the refraction of light waves readily, (4) being unable to catch a fish using our hands when swimming in the sea reminds many of us the refraction experiment that we had in the elementary school: (5) the bending of light beam when passing through a prism denser than air. Light beam change direction at the sea-air interface, so our brain miscalculates the direction to the fish and the depth.

We observe the phenomena (1) to (5) due to bending of propagation path of light before reaching our eyes. The bending of the propagation path is due to change of refractive index in the environment, along the propagation path of the light beam. Snell's law of refraction explains the phenomena (4)-(5) in a very basic framework by only considering the refractive index and geometry of the problem; bending of light wave depends on change of refractive index and the launch angle of the light.

Refraction is a phenomenon which is not specific to light (electromagnetic wave). Refraction is indeed, more broadly, related to the propagation of waves in an environment where the wave propagation speed changes in space and time, which does not necessarily require a contact discontinuity like a prism or sea interface with air, so depends on the medium state rather than the type to be more exact. Hence the refraction can occur even in the same type of medium. For

example, the distortion of sun during sunset in (3) is due to change of atmospheric state (pressure) with altitude. The bending of sunlight during sunset makes sun visible when the sun is beyond the geometric horizon. Radio waves, which is also an electromagnetic wave like light, launched from a ground station horizontally into atmosphere can be refracted significantly, upward toward outer space or downward to earth surface depending on variant refractive conditions. Consequently, it is sometimes possible to receive radio signals at locations beyond the geometric horizon of the broadcasting station. Also, the sound (acoustic wave) propagation path can be bent depending on sound speed distribution in the atmosphere. Four Day Battle[1] is an historical example where the acoustic refraction in the atmosphere did not allow some to hear the shocks from naval guns of the battle although explosions were heard by some others further away.

In sum, electromagnetic wave refraction depends on the spatio-temporal changes in propagation speed v in the medium through which the waves propagate. Conventionally, the electromagnetic propagation speed is measured relative to the propagation speed of the electromagnetic waves in vacuum c by defining refractive index n:

$$n(\boldsymbol{x}, t) = c/v(\boldsymbol{x}, t) \tag{1.1}$$

where t is time and $\boldsymbol{x}$ is the position vector in space.

1.1.2 Refraction of radio waves

Target detection After this general introduction to the refraction phenomenon, let us now restrict our focus on the refraction of radio waves emitted by radar systems of a naval ship. Maritime surveillance radars operate near sea level through the atmosphere, by sending out electromagnetic waves at radio frequencies at a direction into the surrounding airspace. When the waves hit an object, some part of the wave reflects from the object and returns back to radar. The radar system can identify the existence of a target from the emergence of a new echo that normally should not exist in the environment. The radar system can also predict the position of a target by analyzing the time difference between the emission and reception of the radio wave in some prescribed propagation channel (i.e., radar beam propagation pattern) [5, Chapter 1, p. 1].

Target detection and positioning performance of radar system depends on the ambient refractivity. Analogous to the examples given in Section 1.1.1, the propagation path of radar energy can be bent such that the radio waves do not illuminate the airspace at the direction that the radar is geometrically pointing at but illuminate somewhere else, like in the example (5) of light propagation through a prism. The ambient refractive conditions can enable the radar to detect target beyond geometric horizon, like in the example of visibility of the sun below geometric horizon during sunset. Similar to not being able to locate the fish in the sea as in the example (4), the refractive conditions may allow radar system to detect the target but cause to misestimate its position. In addition, the refracted radio waves may hit the sea surface more than normal and return back to radar, contaminating the target echo display with sea echo (called clutter). Moreover, radar holes may appear in the airspace near the radar where the wave field fades rendering the detection impossible although targets can be detected at longer ranges, very much like the acoustic signal void in the shadow zones that occurred at the British coastline during Four Day Battle.

[1] The naval battle that occurred in June 1666 between Kingdom of England and Dutch Republic.

Summing up by speaking technically, some abnormal refractive conditions create blind zones, increase clutter level, alter detection range and cause range-altitude errors [6]. It is crucial for the ship commanders to be aware such situations and take them into account in the mission planning, because these conditions can create problems in terms of ship self-defense [7].

Let us first present the mathematical model that can estimate which parts of airspace is covered at what refractive conditions. Using this mathematical model, we are going to elaborate on what the normal condition is and what those aforementioned abnormal refractive conditions are quantitatively more in detail.

Radar equation The radar system is effective up to a certain spatial extent, beyond which radio emission fades in the airspace and targets remain undetected. The radar equation explains how the target echo is related to the incident wave field on the target and its position. It is equation (1.2) that models the received signal power P_{R} (target echo) measured at the radar, as function of properties of radar ($P_{\mathrm{T}},\ G,\ \lambda$), target ($\sigma$), propagation channel ($\boldsymbol{F},\ \zeta_0,\ L_{\mathrm{misc}}$) and the distance between the radar and target (d):

$$P_{\mathrm{R}} = P_{\mathrm{T}}\ G\ \left(\frac{1}{4\pi d^2}\right)^2\ \sigma\ S_{\mathrm{eff}}\ ||\boldsymbol{F}||^4\ L_{\mathrm{misc}} \tag{1.2}$$

where P_{T} is the antenna power, G is the gain, d distance between the target and the antenna, σ is radar cross section of the target, $\boldsymbol{F}$ is the propagation factor in the channel, ζ_0 is the medium impedance and lastly L_{misc} is there to account for losses. The term S_{eff} is the effective area of the antenna and it is given by

$$S_{\mathrm{eff}} = \frac{G\lambda^2}{4\pi} \tag{1.3}$$

where λ is EMWF (ElectroMagnetic Wave Field) wavelength. The propagation factor $\boldsymbol{F}$ is related to the electric field $\boldsymbol{E}$, which is a complex vector field as function of position in space, according to (1.4)

$$\boldsymbol{F}(\boldsymbol{x}) = \frac{\sqrt{2\pi}d}{\sqrt{P_T\ G\ \zeta_0}}\ \boldsymbol{E}(\boldsymbol{x}). \tag{1.4}$$

For more details about the radar equation, see [6]. Also for discussions about the equation in the context of this thesis, see [8, Section 2.2] and [9, Section 3.2].

The dependency of the radar coverage on refraction of radio wave propagation appears in $\boldsymbol{F}$ in the maritime airspace. In what follows, we explain how we model the refractive effects to determine $\boldsymbol{F}$.

Propagation model Naval ship commanders want to know how far and well their radar can detect during the operations. In order to find out the spatial extent of the radar platform, we need to simulate the physics that can model the propagation of electromagnetic waves (i.e., electric field $\boldsymbol{E}$ appearing in (1.4)) from the radar source considering the atmosphere as propagation medium. This physics is ruled by the Maxwell's equations, for which we cannot propose a closed-form analytical solution. Therefore, the question has to be solved numerically on a computer, which is not only burdensome in terms of computing resources and time but also too accurate in theory for predicting the radar coverage in naval applications.

In this regard, several different approximations of Maxwell's equations are proposed, with their own assumptions and limitations, to reduce the computational load of modeling radio

wave propagation in the atmosphere. Those approximate models are transformed into computer software and are provided to the ship commanders as tactical decision aid by estimating the radar coverage in real-time [10]–[15]. Nowadays, a reasonable trade-off is found between the accuracy and the speed of radar coverage predictions in open-sea environment thanks to the numerical solution of (1.5a) [16] using split-step wavelet technique [17]:

$$\frac{\partial u}{\partial r} + j\left[k_0(m-1) + \left(\sqrt{k_0^2 + \frac{\partial^2}{\partial z^2}} - k_0\right)\right]u = 0, \tag{1.5a}$$

$$u(0,z) = \phi(z), \tag{1.5b}$$

$$u(r,0) = 0. \tag{1.5c}$$

where $k_0 \in \mathbb{R}_+$ is the wave number in vacuum and $m \in \mathbb{R}_+$ is the modified refractive index that accounts for earth roundness. The function $u(r,z) \in \mathbb{C}$ is related to the power at the receiver antenna by taking into account the distance, antenna gain and medium impedance [18] by modeling the propagating wave field at radar operation frequency $f = k_0 c/2\pi$ in cylindrical coordinate system in range, azimiuth and altitude (r,θ,z). This model considers the boundary condition of a flat perfectly-electric-conducting surface at $z = 0$ with source term $\phi(z)$ modeling the initial field of emitted radio waves at horizontal polarization.

The equation (1.5a) is known as the Wide-Angle Parabolic Equation (WAPE) in the radar community due to its theoretical accuracy. With this choice of the propagation model (1.5), we restrict our focus on 2D representation of the propagation at open-sea environment with azimuthal symmetry with respect to θ. The parameter m is the refractive index that accounts for the curvature of earth such that the earth can be considered as flat in rectangular computational domain. It is related to the physical refractive index n via [19], [20]:

$$m = n + \frac{z}{R_e} \tag{1.6}$$

with R_e being the radius of earth. The function $u(r,z) \in \mathbb{C}$ is related to the electric field $\boldsymbol{E}$ which is normally a vector quantity in 3D but replaced with a scalar E because it is only in the direction of θ in our 2D application, i.e., $\boldsymbol{E} = E\,\hat{\boldsymbol{\theta}}$, and the relation becomes (see Section 4.5 and 4.6 in [18]):

$$E(r,z) = u(r,z)\frac{1}{\sqrt{k_0 r}}e^{-jk_0 r}. \tag{1.7}$$

Here, the time dependency of the wave field is given by:

$$\mathcal{E}(r,z,t) = \Re\left\{E(r,z)\; e^{j\omega t}\right\} \tag{1.8}$$

where $\omega = k_0 c$ is angular velocity and $\Re\{y\}$ is the real part of $y \in \mathbb{C}$. The temporal phenomenon is considered in frequency domain at frequency $f = k_0 c/2\pi = \omega/2\pi$ assuming time-harmonic dependency. Lastly, in our context, the radar coverage is presented with the contour diagram of the amplitude of the complex wave field quantity E, in the unit of Volt per meter. It is customary to display the wave field amplitude in logarithmic scale in decibels as shown in Figure 1.1:

$$|E(r,z)|_{\mathrm{dB}} = 20\,\log_{10}(|E(r,z)|), \tag{1.9}$$

so $|E(r,z)|_{\mathrm{dB}}$ is in the unit of decibel Volt per meter (dBV/m).

In order to predict the radar coverage, we need to first solve (1.5) for unknown $u(r,z)$ for known $\phi(z)$, k_0, $m(r,z)$ and then use the relations (1.7) and (1.9) to display $|E(r,z)|_{\mathrm{dB}}$. The

problem is that m in (1.5a) is not known well and detailed enough in the atmosphere *a priori*, to be provided as input for solving (1.5a) with sufficient accuracy.

1.1.3 Estimation of Refractive Index

A priori knowledge about refractivity The refractive index n is typically around 1.00033 at sea level and it varies in the interval $[1.000250, 1.000400]$ in the first few hundred meters altitude in the atmosphere where we want to estimate the radar coverage [6]. However, this variation is not a fixed distribution like in solid media, also it is not smooth or monotonic. In fact, refractivity is controlled by atmospheric conditions which vary from one location to another in airspace and evolve dynamically with time. Hence n, and so m, are unpredictable *a priori*. Radio wave propagation is sensitive to the spatial details at around a-millionth of m and certain abrupt spatial variations can diverge the radar coverage from what is normally expected even if those variations are local compared to considered airspace. Therefore, we need to measure m according to some prescribed level of accuracy and detail within the spatial extent of the radar, and the measurements must be updated to keep pace with the changes in the atmospheric conditions. By the virtue of the fact that the variation of m is limited to a narrow interval above unity, the medium is characterized with a modified refractive index M which reads:

$$M = (m - 1) \times 10^6. \tag{1.10}$$

where m is defined in (1.6). Consequently, the atmospheric refractivity will be presented now with M belonging to the interval $[250, 400]$.

How to estimate the refractivity There are a number of factors that determine how precise and accurate refractivity should be measured in the airspace and with what measurement technique. The requirements depend on the maritime application. To begin with, aircrafts can be equipped with refractometer to measure n directly along the flight paths but the measurements cannot be taken cost-effectively everywhere in the airspace. Range-dependency of refractivity could be omitted during open-seas operations [21], [22], so baloonsondes and rocketsondes could be flown or fluttered down vertically with rather disposable pressure (P), temperature (T) and humidity (e) sensors to estimate n using empirical relation (1.11) [23]:

$$n = 1 + \left[\frac{77.6}{T}\left(P + 4810\frac{e}{T}\right) \times 10^{-6}\right] \tag{1.11}$$

but the use of sondes brings limitations in terms of desired resolution, extent and refresh rate of the measurements [24], [25]. An alternative is to model the thermodynamic state of air (P, T, e) numerically but it is a challenge when it comes to resolve the state accurately at a desired vertical resolution [26, pp. 41-42] and refresh rate [27, p. 13] in the lower troposphere because of the complex chaotic system that governs (P, T, e). Other approach is to infer the refractivity using some remote sensing method, such as the use of Doppler spread radars [28]–[31], lidar [32], [33], and GPS signals [34]–[38] which potentially solve the resolution and refresh rate related issues but still have certain drawbacks needing to be solved before operational use (for discussion, see [39] or Section 1.2.3 in [40]).

Another choice is to use the influence of the refractive conditions on radio wave field distribution over the sea surface, for estimating the ambient refractivity. This technique is called Refractivity-From-Clutter (RFC) [41] because refractivity is predicted from the clutter, which

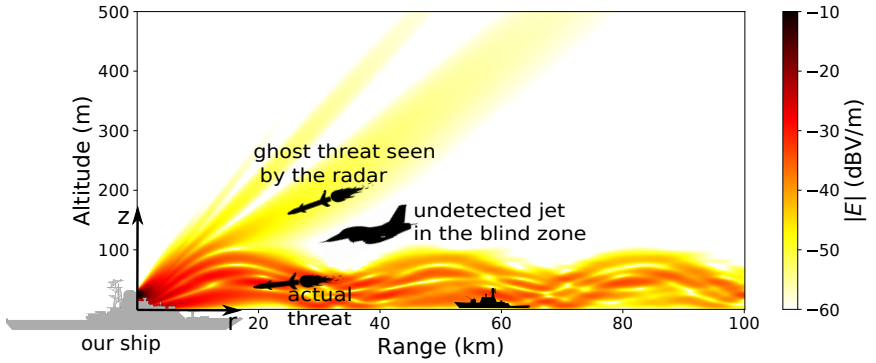

(a)

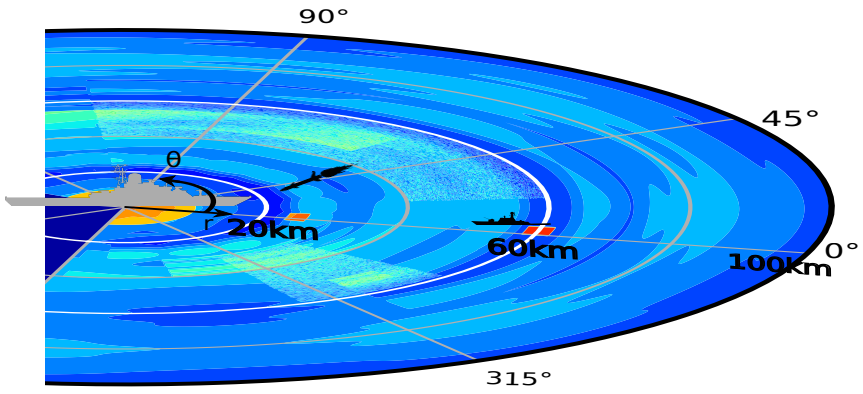

(b)

Figure 1.2: A realistic scenario. (a) The 2D view EMWF with respect to range and altitude, $\theta = 0$, (b) the clutter with respect to range and azimuth (radar PPI display in our ship).

is the back-reflected part of the radar emission returning from wavy sea surface back to radar, that is normally measured but filtered out from the Plan Position Indicator (PPI) display of the ship radar to keep only echo of the targets (see Figure 1.2b). Since the echo power P_{R} depends on propagation via (1.2) and (1.4), and the propagation depends on refractivity via (1.7) and (1.5), then there must be a way to deduce what the refractivity is by analyzing the clutter[2] [28], [41]–[43].

If RFC technique works in practice, it has the potential to outperform other refractivity estimation techniques. RFC constitutes a self-contained system that only uses the radar of the ship as measurement device which is already available in the ship and already capable of measuring the clutter. The measurements can be taken remotely at the spatial extent of the radar for entire operation duration in real-time dynamically in cost-efficient fashion. The independence of RFC system from other measurement assets provides various advantages, provided that the RFC system performs successfully without external aid.

Inversion of refractivity Let us now look more closely to the cause-and-effect relation between refractivity and clutter shown in Figure 1.3 to understand how we can develop an RFC system. Estimation of refractivity from clutter constitutes an inverse problem where the direct (or forward) problem is to go rightward in the workflow in Figure 1.3 so as to predict the clut-

[2]We cannot model the clutter from the electric field at the sea level if we use (1.5c) as the boundary condition at the sea level. For this reason, we have to select u of (1.7) not exactly at $z = 0$ but slightly above the sea level, depending on the application.

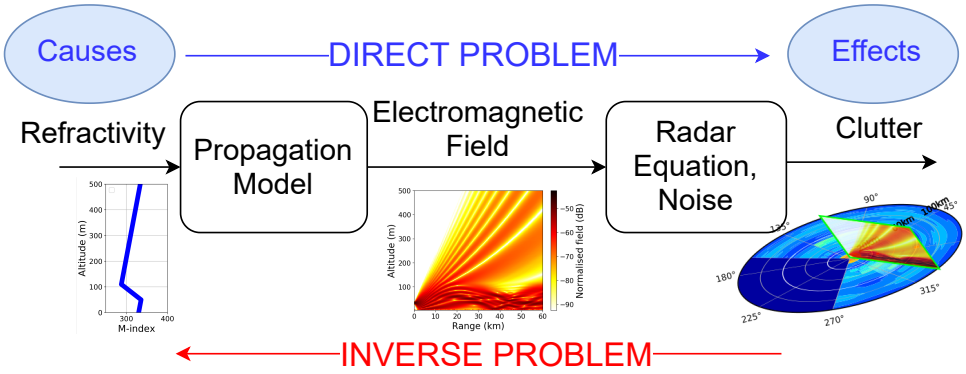

Figure 1.3: Direct and inverse problem workflow.

ter phenomenon by solving the physical model (forward model) for known model parameters including refractivity. The forward model is composed of problems (1.5), (1.7), (1.4) and (1.2) which are numerically well-posed (meaning their solution exist and are unique and the solutions continuously depend on the parameters) and it is assumed that the solution can explain the clutter phenomenon with an acceptable error. Whereas in the case of the inverse problem, we are dealing with an ill-posed problem because the clutter data is not enough to determine the refractivity in the whole airspace properly and uniquely.

The sources of the ill-posedness in the inverse problem are related to its formulation (metric), parametrization, data and physical model. To begin with clutter data, the measurements are taken at some part of the domain of interest, they are sparse and contain noise. On the other hand, the formulation of the inverse problem and the parametrization can lead to that many different refractivity solutions can explain the sparse and noisy clutter data comparably.

Avoiding modeling issues on nonlinear inverse problem The clutter model (1.2) that relates the propagation to measured clutter contains open questions in regard to modeling of σ and F which are scenario-dependent and still under research [40], [44], [45]. For example, one basic question is about how to relate u to P_R (clutter) the best if (1.5c) is used as the boundary condition, depending on the application. There are some aspects that should be considered when making an uninformed choice in the clutter model for the sake of developing an RFC system because the inverse problem might become more complex to solve. In fact, a small change on data can cause a big change on the estimated parameter, and noise can be such a cause in particular, and this already prevents us from approaching the solution satisfactorily. Furthermore, the clutter model relates the clutter data to the function u in (1.5) (see Figure 1.3) where the relation between the refractivity m and the function u is implicitly defined and nonlinear. It is already really hard to solve nonlinear inverse problems and there is not a general solution technique that can tackle them. Solving it (RFC) requires expertise in the forward problem and tedious step-by-step analysis of the inverse problem to arrive at a specially-tailored innovative solution for the particular problem in a specific setup. Ideally, there should not be question about the suitability of a physical model in the forward modeling part, or at least, the most accurate affordable model should be chosen, before starting to work on the inverse problem. As a non-specialist of clutter modeling, it is tough to choose one model from the literature without being able to work with real data, and tailor the algorithm accordingly and then claim that it will perform well in real world. We think that clutter model needs special attention and for some reasons given in the following, we put the attention on other aspect of the inverse problem and avoided working with a clutter model.

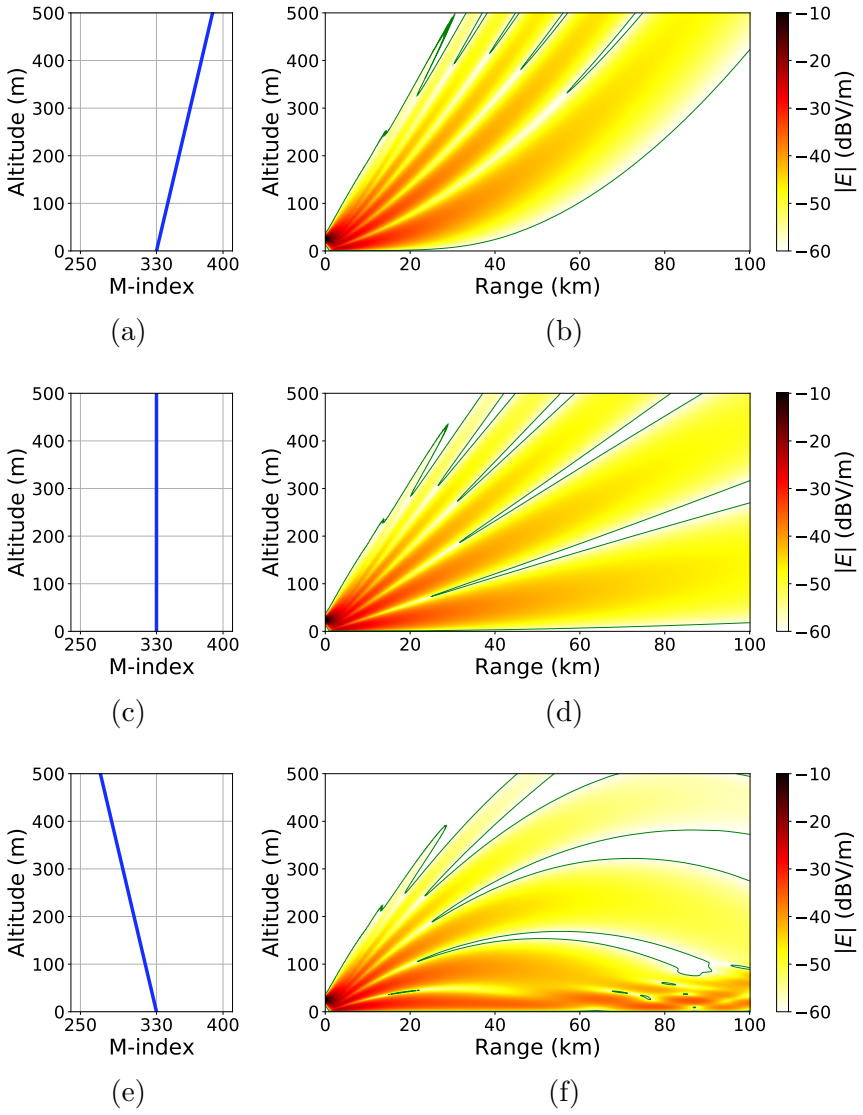

Figure 1.4: Standard, super-refraction and trapping (ducting) conditions at $f = 2$ GHz. (a) M-index for the standard atmosphere, (b) Propagation for (a), (c) M-index for the super-refracting atmosphere, (d) Propagation for (c), (e) M-index for the ducting atmosphere, (f) Propagation for (e).

Need for a priori knowledge Let us now be more specific about our goals when elaborating on the other aspects that should be taken into account when developing our RFC system. We are interested in retrieving the details of the atmosphere by representing the refractivity parameter with a very high-dimensional vector. Broadly speaking, the refractivity in the airspace of half a km in altitude, several hundred km in range and few degrees in azimuth can be represented by millions of refractivity parameter ideally. However, finite amount of data can be expressed by infinite number of continuous parameter functions when the problem has infinite degree of freedom. In the case of finite degree of freedom, the high-dimensionality in the problem may still lead to unphysical oscillating solutions. Identifying the proper solutions from the unphysical ones and stabilizing the problem (the solution) require some *a priori* knowledge to be employed in the solution process. How to use this *a priori* knowledge is a delicate question to be answered because if the knowledge is wrong, the solutions can be ruined. On the other side, we do not want a technique that relies on case-specific *a priori* information, that depends on geophysical location

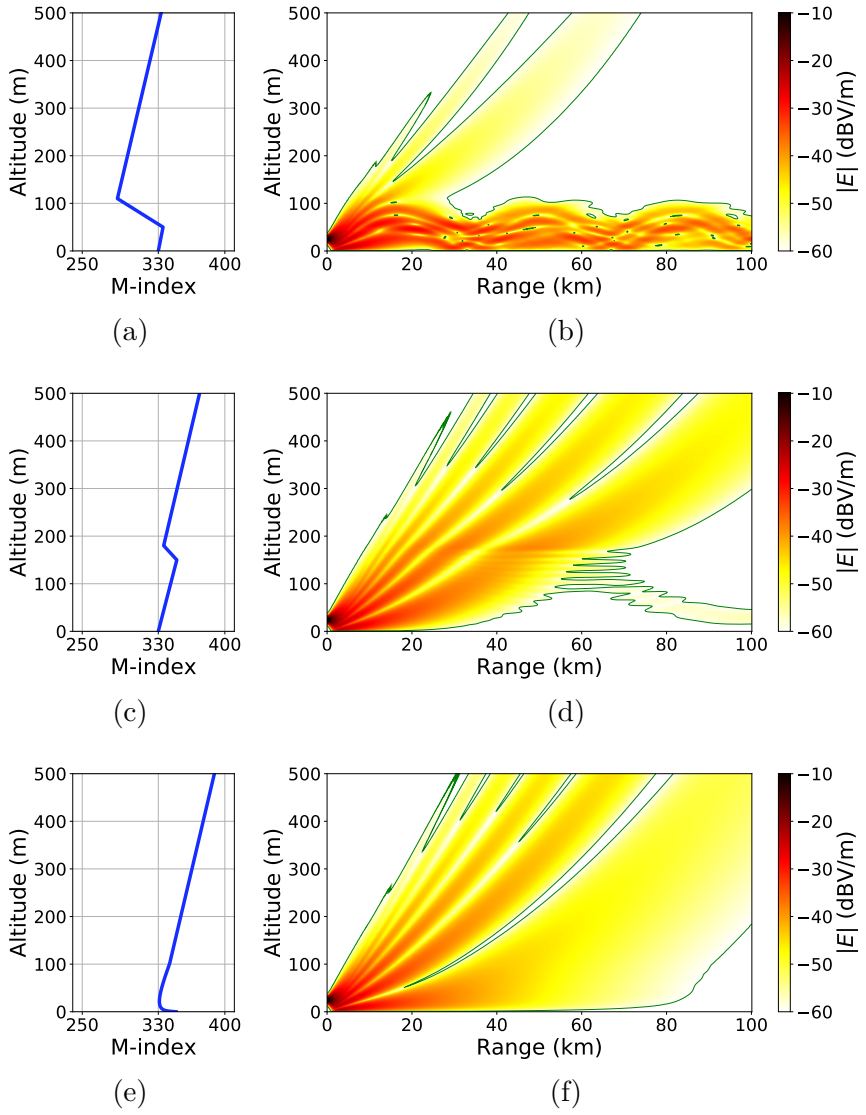

Figure 1.5: Examples for three general class of nonstandard conditions in maritime environment at $f = 2$ GHz. (a) M-index for a surface-based duct, (b) Propagation through the surface-based duct in (a), (c) M-index for an elevated duct, (d) Propagation through the elevated duct in (c), (e) M-index for an evaporation duct, (f) Propagation through the evaporation duct in (e).

of the ship and time of operation for example, because we are looking for a worldwide-applicable inversion method and such quality knowledge may not always be available.

Standard refractivity distribution The vertical refractivity distribution that obeys $dM/dz = 0.118$ M-unit/m is called as the standard refractivity distribution (see Figure 1.4a). The propagation condition under this parameter distribution is called as the standard propagation condition (see Figure 1.4b). The radio waves leave the earth surface with range under this propagation conditions as shown in Figure 1.4b.

Ducting refractivity distribution The gradient of the refractivity distribution governs how the radio energy is bent during propagation as shown in Figure 1.4. Typically, the refractivity variation is not straight like shown in Figure 1.4 but the refractivity profile contains some small

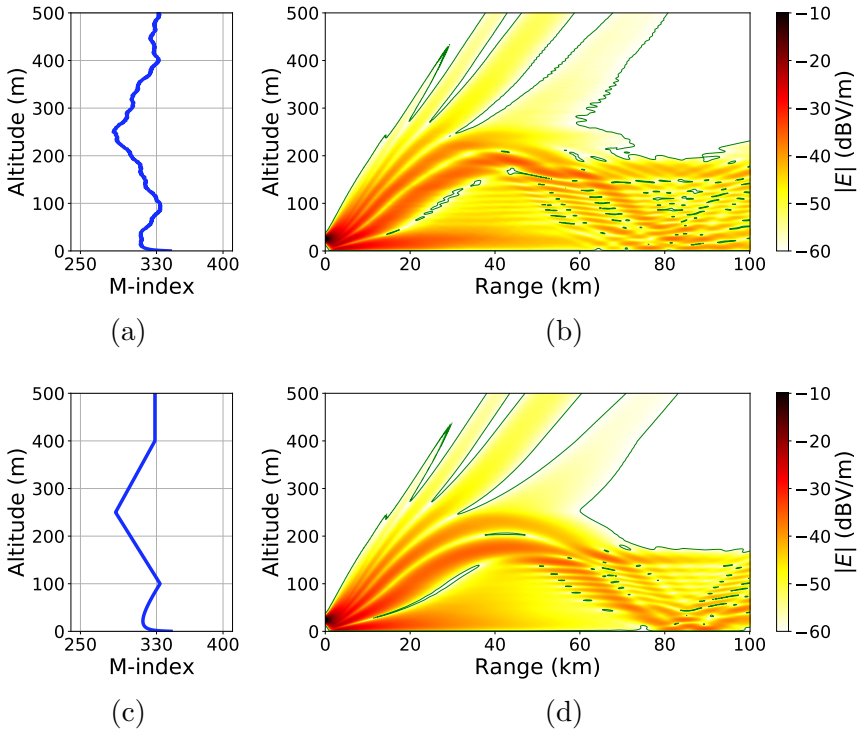

Figure 1.6: Impact of small spatial details on the propagation at $f = 2$ GHz. (a) M-index, (b) Propagation in the refractive conditions described in (a), (c) M-index obtained by removing the perturbations from (a), (d) Propagation in the refractive conditions described in (c).

scale departures from the global structure like shown in Figure 1.5. When those small scale structures contain parts with $dM/dz < 0$, the energy is bent downwards when propagating through those small scale structures like in Figure 1.4f. Such refractivity conditions are called ducting propagation conditions or anomalous propagation conditions. Three important ducting conditions in the context of maritime applications are illustrated in Figure 1.5.

Past parametrizations Another worth-mentioning aspect of such high-dimensional problem is how to parametrize the medium and how to retrieve it efficiently. The solution techniques which are proposed starting from the early introduction of the RFC [41] in 1997 till the end of 2000s [8], [22], [39], [46]–[53], require a lot of forward model simulations, and their computational cost increases with the number of parameter to invert. The techniques were made affordable by low dimensional parametrization of refractivity. Their assumptions were sometimes to neglect the range-dependency of m in the airspace, but more commonly to search for the gradient information in vertical m profile (see $dm/dz \rightarrow E$ relation in Figure 1.4) by idealizing the buried small-scale deviations from the major structure [5], [40], [54] with piecewise linear and logarithmic functions [55, p.4] (see Figure 1.5). A combination of the piecewise linear and logarithmic functions could be used for approximating a realistic refractivity profile, e.g., as in Figure 1.6a, more smoothly by using only a few control parameters to describe the profile with the aforementioned functions, e.g., as in Figure 1.6c [49], and this would not mean much change in the texture of the wave field (see Figure 1.6b and Figure 1.6d).

Need for high-dimensional parametrization Although these assumptions reduce the computational load of the inversion by reducing the number of degrees of freedom in the problem,

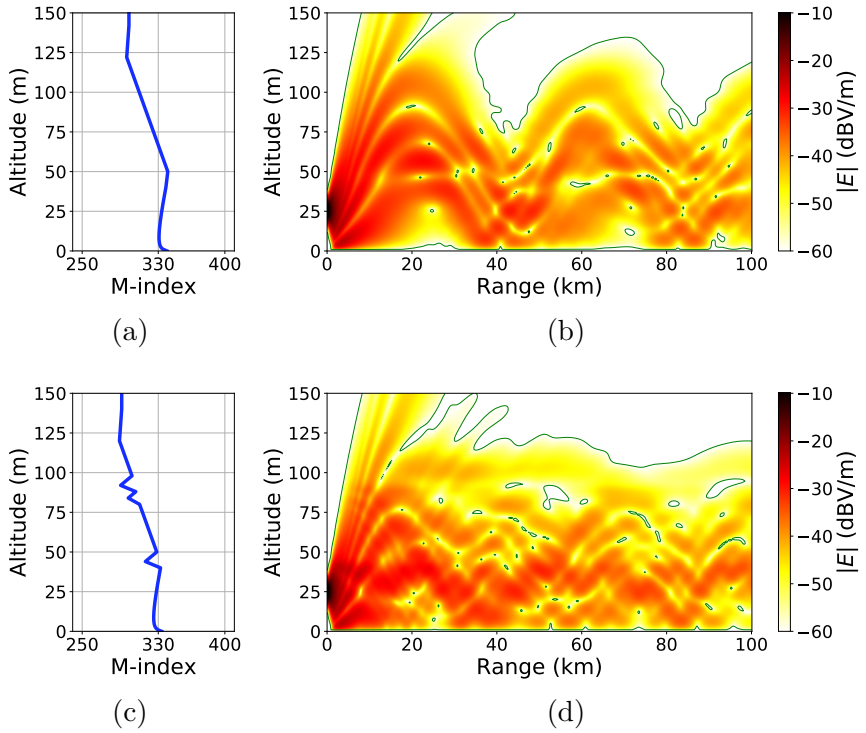

Figure 1.7: Impact of refractivity perturbation on the propagation at $f = 2$ GHz. (a) M-index, (b) Propagation in the refractive conditions described in (a), (c) M-index obtained by adding perturbations on (a), (d) Propagation in the refractive conditions described in (c).

the validity of the approximations are questionable in some cases. It is firstly unsure if the ill-posedness permits that such coarse approximation of the realistic continuous parametrization by using e.g., piecewise linear or logarithmic functions omitting small details always leads to correct radar coverage predictions with acceptable error[3] (cf. Figure A3 in [56]). Also, we can find instances where local departures from the mean profile should be taken into account without being filtered out as shown in Figure 1.7, contrary to the arguments given for Figure 1.6. In addition, the local departures gain more and more significance when the frequency f of the radar increases (see Figure 3 in [55]). When f increases from 2 GHz in Figure 1.7 to 10 GHz in Figure 1.8, we see that the propagation becomes more sensitive to the spatial details of the refractivity profile. More spatial details of the refractivity should be provided to the detection systems working at higher frequencies if higher detection precision is desired. This means refined parametrizations should be used during inversion to feed modern detection systems. That is why later works have investigated the inversion of refractivity efficiently using high-dimensional parametrization.

Large-scale inversions In 2010, an efficient solution of the high-dimensional refractivity inversion problem was developed in [57] using the variational adjoint approach and gradient-based optimization techniques. The studies using the adjoint technique have shown that the high-dimensional problem is severely ill-posed and the use of regularization techniques does not guarantee improvement of the solution [58]–[60]. Unfortunately, today adjoint-based RFC techniques still require unrealistically good initial guess with additional *a priori* information or need to incorporate dimensionality reduction techniques [61], [62]. The main drawback of the most recent

[3]An exception is when the ambient condition is dominated by the evaporation from the sea surface, then duct formations like in Figure 1.5e emerge. Such conditions are studied successfully in terms of parametrization and inversion using statistical and deterministic approaches.

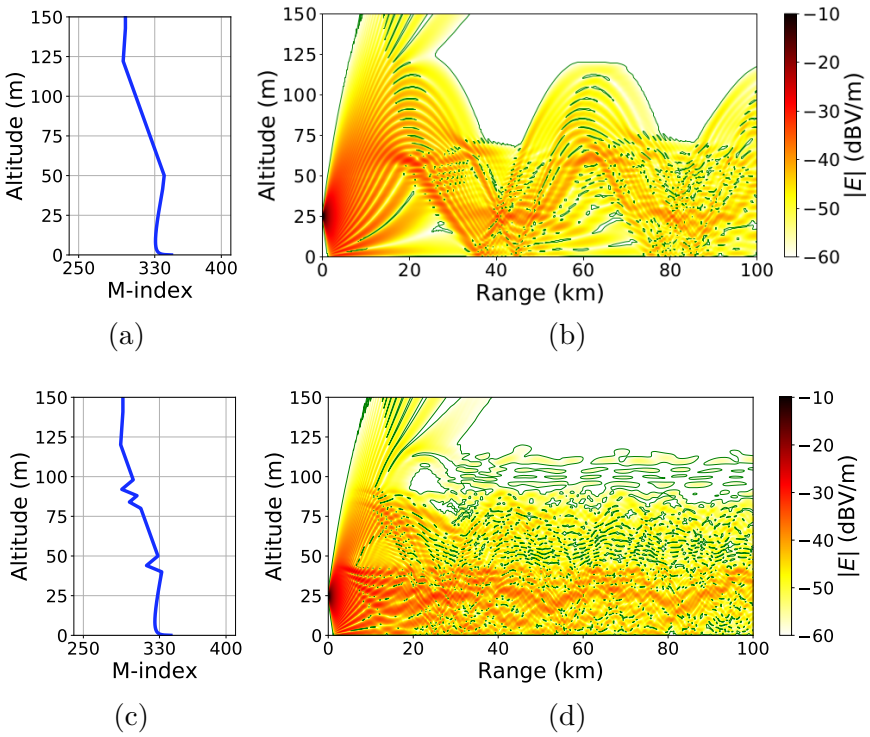

Figure 1.8: Impact of refractivity perturbation on the propagation at f=10 GHz. (a) M-index, (b) Propagation in the refractive conditions described in (a), (c) M-index obtained by adding perturbations on (a), (d) Propagation in the refractive conditions described in (c).

solution is that the inversion results depend on how the principal components of the reduction are estimated; the training of the algorithm should be done in similar conditions to that of ambient in order to have good results, so we are limited by *a priori* information. Also some other techniques have been proposed in 2010s, but their performance is not demonstrated in high-dimensional scenarios [63]–[67]. Thus, reliable inversions which are purely driven by real-time data have not been realized yet in high-dimensional realistic configurations in 2-D.

Successful examples Adjoint-based methods are widely used in many science and engineering disciplines because the method is very capable of handling problems efficiently. The literature is rich with examples. The method is used in the following problems, for example:

- fluid flow state control [68], [69],
- aircraft jet noise suppression [70],
- petroleum extraction from subsurface reservoirs [71],
- suppressing structural vibrations and attenuating contact forces [72], [73],
- structural optimization problems [74],
- sensitivity of materials to thermal stresses [75],
- controling object deformation in fluid-structure interaction [76],
- heat transfer [77],

- electromagnetism [78],
- geophysics [79].

Adjoint-based methods are particularly relevant to the partial differential equation-constrained nonlinear large-scale parameter estimation problems from limited data. In that context, the last subject in the list (geophysics) contains successful examples where acoustic wave propagation speed is inverted with greatly higher degree of freedom in parametrization than that we currently try to achieve in RFC community. If we examine the successful implementations [80]–[82], we notice that their success relies on (1) the forward model accuracy, (2) the richness of their excitation and so the data [83] in terms of frequency content (dynamite explosion) and (3) how smartly they benefit from what is called multiscale strategies [84] when using the adjoint-based methods [85]. In addition, successful examples in fluid mechanics present consistently first some validation graphs when a new adjoint code is developed, and then discuss the test results.

Refractivity inversion in 2021 Some notable present-day efforts try to enrich the RFC problem. Firstly, the work [86] considers enhancing the frequency content of the measurement data by taking the measurements at different radar operation frequencies like discussed in [87]. The work in [88] considers collecting the measurements above sea level using a receiver array antenna mounted on a ship like discussed in [89], [90]. The work [91] considers using vertically positioned receiver array antenna at a fixed distance from the source to take the measurements (called bistatic configuration) so that angle of arrival of the propagating radio beams can be estimated alongside the signal power P_{R}. We should also mention the possibility of using radar phase measurements [92] in conjunction with the aforementioned enrichment efforts, as also discussed in [93]–[95].

1.2 The Scope of the Thesis

The goal of this dissertation is to develop an efficient refractivity inversion algorithm that does not rely on case-specific *a priori* information for as wide applicability as possible. What is meant by case-specific *a priori* information is an empirical background knowledge that constraints the problem correctly only in limited scenarios in practice. Two examples are, (1) a background knowledge on refractivity distribution at a specific geophysical location based on climatic conditions, time of the day, meteorological conditions etc. (2) a background knowledge on the parametrization that evaporation ducts with logarithmic variation in altitude should be sought. Although the use of *a priori* information might seem inevitable in some cases, constraining the inverse problem with such type of knowledge will work well depending on how the actual ambient conditions deviate from the background knowledge.

We ensure the efficiency using gradient-based optimization techniques by formulating the problem as a least square optimization problem and then estimating the gradient using variational adjoint approach. Penalization of the least square problem is avoided as much as possible during the development of the algorithm at this stage because it would mean adding case-specific *a priori* information mostly, which could be added later if it is really necessary. Instead, we use multiscale strategies to cure the ill-posedness of the problem by adopting a generic approach.

The inverse problem is simplified by avoiding clutter models in the forward model. Namely, we cut the workflow in the middle in Figure 1.3 at the EMWF propagation model; we assume that

we can retrieve the function u in (1.5) perfectly from the measurement data. This assumption is made so as to focus on the development of an efficient adjoint code for WAPE, similar to what is done in [57], [58] for NAPE during initial stages of adjoint code development. In order to be able to test the inversion algorithm in real world, we find an application in bistatic configuration, where the propagating wave field is measured by a vertically positioned receiver array antenna at a certain distance from the radar. Additionally, we want to explore if it is interesting to use this configuration. We can test a wider range of refractivity profiles in this configuration than we could do in RFC because we do not have to worry about whether the ambient refractivity profile is retrievable[4] or not in the sense it is described in [96]. By measuring almost the entire propagating wave field with large receiver arrays in bistatic configuration, we can focus more on fixing the issues related to the nonlinearity of the inverse problem that leads to failure of inversion in a more ideal setup.

Therefore, the algorithm is developed and the numerical tests are performed in bistatic configuration. We call this method as Refractivity-By-Tomography (RBT) or the tomographic approach throughout the dissertation. Then effectively, our final goal is to complete the radar coverage diagram given in Figure 1.9 from the measurements collected at the end of the domain in radial direction. The measurements are limited by the receiver array height and spatial density of the receivers on the array. The measurement data are generated synthetically on the grid nodes with the same forward model that is used during inversions with the exact same numerical settings. We restrict our scope of analysis with such a setup because, firstly this is the most ideal condition where modeling error does not appear during the inversions, secondly RBT is also very ill-posed even in these ideal conditions, thirdly we hypothesize that the algorithm will not work in real world if it cannot deal with the synthetic problem in such ideal conditions. Thanks to the analysis, we are able to claim that the code is ready for being tested with real world data at the end, with some minor modifications on the algorithm because in reality we probably will not have a receiver at the position of every grid node.

The tests of the algorithm is done in ideal conditions. What we mean by the ideal conditions is that we guarantee that the data came from the forward model, which is not the case in reality. We perform the inversion tests by using the synthetically generated measurement data. We start the inversion with simple scenarios where the receiver array is positioned not so far from the source, the source is quasi plane wave, the phase information is measurable in addition to the amplitude of the wave field and the true ambient refractivity varies linearly. We increase the level of difficulty of the problem and at the end we work on the realistic scenarios where the receiver array is far from the source, the excitation source is a point source similar to radar, only the amplitude of the wave field is measurable, and the true ambient refractivity is a complex mixed type duct made of logarithmic and piecewise linear variations in altitude but also contains perturbations, which make the point-by-point inversion a harder problem.

Another worth-mentioning aspect of this study is that the developed techniques and knowledge in the aforementioned scope are transferable to the RFC problem. The derivation of the adjoint of WAPE operator in (1.5) is achieved by an analysis on the square-root propagation operator which does not change with the measurement configuration (RBT or RFC) and the 3D extension of the analysis is easy for the square-root propagation operator appearing in wide-angle formulation in Cartesian coordinates (see [97, Equation C.31]). The derived adjoint model constitutes the backbone on which our inversion strategy will be built. For this reason, we paid

[4]Retrievable duct in RFC refers to the type of refractivity distribution that bends the radio energy to the degree that part of the radar beam hits the sea surface and reflects back to the radar. In contrast, an anomalous propagation condition like in Figure 1.5d also ducts the radar energy in the airspace but without interacting with the sea. For details, see [96].

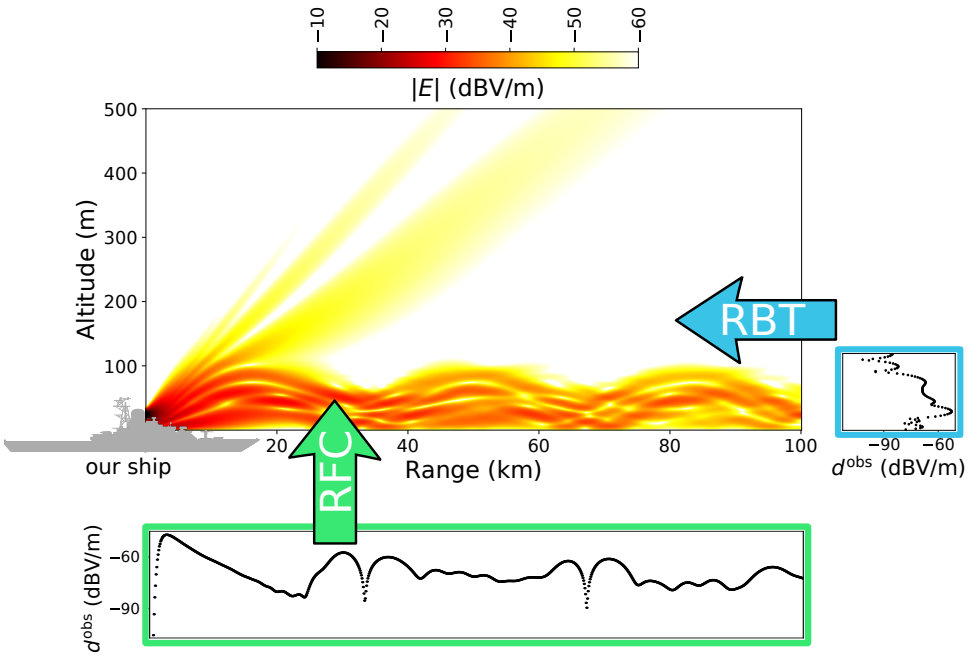

Figure 1.9: A 2D schematic of the two popular techniques to construct the radar coverage diagram in an airspace. For RFC, the plotted measurement data in the colorful frame is $d^{\text{obs}}(r) = |E(r, z)|$ for $r \in [0, 100]$ km, $z = 1$ m. For RBT, it is $d^{\text{obs}}(z) = |E(r, z)|$ for $r = 100$ km, $z = [0, 100]$ m.

attention to its validation more than normal, and we try to present as much validation result as possible in this dissertation. Lastly, the developed modules for the application of multiscale strategies are independent of the details of the problem so the derivations and the algorithm related to that part are reusable in future RFC applications in the project.

1.2.1 Assumptions and constraints in the thesis

Part of the assumptions made in this dissertation originates from the choice of the forward model. We are only listing them without elaborating on those aspects, the reader may refer to [18] for the details.

- The forward model (1.5) is derived from the Maxwell's equations assuming the medium through which the waves propagate is linear, homogenous and isotropic.
- The approximation (1.5) is valid in the far field from the source, as long as the medium has azimuthal symmetry in terms of refractivity distribution and the wave field propagates forward.
- Although the medium is assumed uniform and later range independent once more, those conditions are relaxed in the context of radio wave propagation in the troposphere where the atmospheric refractivity varies slowly in range and altitude.
- The earth-flattening transform applied in the refractivity parameter of (1.5) is valid within the first few hundred meters away from the source in altitude.
- There are errors related to the splitting of the refractive effects from the square-root propagation operator in one-way equation, which are reasonable in our context.

- In addition, we use split-step wavelet technique to accelerate the simulations and this technique introduces negligible errors due to wavelet compression, which are controllable.

- We approximate the sea surface as flat although it is wavy in reality, and the boundary condition (1.5c) can be replaced with Leontovich impedance boundary conditions to be more accurate [98].

The errors associated with those assumptions are accepted so as to obtain a reasonable trade-off between the accuracy and the speed of the propagation simulations not to get lost among the vast number of options.

From the inverse problem side, the main assumptions are as follows.

- The validity of the derived adjoint model is restricted to the propagating waves and does not include the evanescent waves which is also modeled with (1.5).

We have to give a little explanation on that at this point. Since the evanescent part of the wave field decay exponentially with range in the theory of the forward model (1.5), we assume that the evanescent part contributes to the measurements negligibly, so it is not a problem if the evanescent part is not modeled numerically. In the forward and the adjoint model this is ensured by choosing the mesh size as function of the wavelength λ, such that the grid spacing in the axial direction is greater than $\lambda/2$, according to Section 4 in [17]. In addition, the mesh size is already chosen greater than this condition in order to speed up the inversion, so this condition does not appear as a constraint from practical point.

- Another limitation is that the refractivity is considered invariant with range and only varies in altitude.

In reality, refractivity also varies in range although this variation is small compared to the variations in altitude. Also, propagation depends mostly on the variation of refractivity in altitude than in range [99] in the scenarios that we consider because the launch angle of the radio waves is zero in our analyze, that is to say, the radar points at a direction parallel to the radial axis geometrically. The extension of the derivations is straightforward when the refractivity varies in range as well, as discussed in the conclusion.

- Also, atmospheric attenuation is not considered.

Nevertheless, the scenarios can be extended to the presence of atmospheric attenuation, where the refractive index becomes a complex quantity with the imaginary part which accounts for the attenuation during the propagation, by modification in the derivations, as discussed in the conclusion.

1.2.2 Objectives of the thesis

The objectives are listed as follows:

- derive the adjoint model for the inversion of refractivity from wave field data measured in bistatic configuration where the forward model is the wide-angle parabolic equation of Thomson and Chapman
- construct a wavelet-based adjoint solver from an existing split step wavelet code that models the solution of WAPE so as to solve the adjoint model
- validate the derivations and the implementations by comparing the gradient computed with the adjoint model to that obtained by a Finite Difference approximation
- develop an inversion algorithm by feeding Quasi-Newton optimization methods with the gradient computed using the adjoint model
- perform inversion tests on synthetically generated measurement data by inverting the refractivity at every meter point in altitude
- increase the inversion difficulty step by step, analyze the results to identify the difficulties so that new ideas can be proposed in order to solve the issues
- employ basic multiscale strategies in the parameter and data to remedy the inversion difficulties
- invert a realistic refractivity profile which contains perturbations which cannot be approximated with only few parameters with the choice of multiscale basis in the parametrization
- show the limitations of the technique

These objectives are fulfilled throughout the thesis work and presented in this dissertation according to the plan described in the next section.

1.2.3 Outline of the thesis

In this dissertation, the inverse problem is formulated as a simulation driven nonlinear least squares optimization problem where the difference between the measured and simulated data is minimized over refractivity parameter. A main contribution of this dissertation is the derivation of the adjoint model that express the gradient of the error functional analytically when the problem is constrained with (1.5). The second contribution is the application of the multiscale strategies on inversion parameter and the measurement data. The work related to the derivation of the adjoint model and the application of multiscale strategies are presented in Chapter 2 and Chapter 3 respectively.

Chapter 2 is dedicated to the derivation of the adjoint model mainly but contains some preliminary tests. The derivation of the adjoint model is done for RBT. The derivations is validated numerically considering the quasi plane wave as the source. Two problems are considered when the phase is measurable alongside the amplitude of the wave field, and when only the amplitude is measurable. We analyze why the RBT is difficult to achieve when the measurements are taken at long ranges. RBT is shown to have local minima problem in most practical cases. The analysis shows that more knowledge about the wave field does not necessarily mean that the radar coverage will be predicted better, the way we use the information matters as much as the extent of the information. To be more precise, the inversions are successful when the receiver antenna is positioned within the first few km from the source if the difference between the simulated and the measured complex wave field u is minimized. When difference between the amplitudes are

considered only, the error functional contains fewer local minima and we can retrieve at least the synoptic structure of the true refractive index profile at longer receiver antenna positions. We have performed some inversion tests which revealed interesting features of RBT problem such as multimodality (in the problem) and robustness of the algorithm alongside how to pick the initial guess smartly and so on.

In Chapter 3, we consider more realistic scenarios where the source resembles more to a point source, only the amplitude of the wave field is measurable (as in the case of RFC) and true refractivity parameter contains perturbations. We have found out that point source makes the problem less stable, and the advantages that were gained with the removal of the phase from the measurement data are lost. We apply multiscale strategies to mitigate the nonlinearity of the problem. The multiscaling hierarchy is built using multiple subspace approaches firstly in the parametrization. We pick the simplest basis function that we could think of being capable to capture the variations, to construct the reduction basis and at the same time do not rely on any case-specific *a priori* knowledge or analysis: piecewise linear functions. We approach the inversion of any refractivity profile somewhat successfully at more distances from the source thanks to the use of a very basic multiscale parametrization. Later this subspace approach is extended to the data reduction in a multiscale hierarchy. Further improvement is achieved by search space reduction in synchronization with data space reduction. We show successful applications and limitations of the technique in realistic scenarios.

Lastly in Chapter 4, we make a synthesis of the findings and suggest some subjects to cover in future work.

Chapter 2

Adjoint-based Refractivity Inversion Technique

Contents

Synthèse – Dans ce chapitre, nous étudions deux problèmes différents d'inversion de la réfractivité à partir de la quantité mesurée u dans le montage tomographique illustré dans la Figure 2.1. Premièrement, nous résolvons ce problème en supposant que la phase et l'amplitude de u sont accessibles à partir des mesures (Equation (2.10)). Deuxièmement, nous le résolvons pour étudier comment les résultats de l'inversion seraient affectés lorsque seule l'amplitude de u est connue à partir des mesures (Equation (2.11)). Les gradients des deux fonctions d'erreur associées sont exprimés analytiquement en utilisant deux modèles adjoints différents dérivés dans la Section 2.5.3. Notre principal objectif dans ce chapitre est de valider le calcul des gradients.

Pour ce faire, nous comparons le gradient calculé avec la méthode basée sur les adjoints que nous construisons au gradient calculé à l'aide d'un schéma aux différences finies. Le résultat de cette validation est illustré par la Figure 2.6 et la Figure 2.8.

Nous effectuons ensuite des tests d'inversion pour les deux scénarios où la phase est mesurable et non mesurable. Dans ces tests, nous essayons d'inverser le profil objectif M_{OBJ} à partir de l'estimation initiale M_{IG} présentée dans la Figure 2.4a. À cette fin, nous générons les données de mesure qui correspondent au profil de réfractivité objectif recherché, calculée à l'aide du modèle numérique de propagation. La source est une onde quasi plane se propageant à la fréquence de $f = 2$ GHz. Les résultats de l'inversion sont calculés pour les mesures avec phase et sans phase pour cinq positions différentes de l'antenne dans la Figure 2.9 et la Figure 2.11 respectivement. Les résultats des tests nous montrent que les résultats d'inversion les plus précis sont obtenus lorsque la phase et l'amplitude de la fonction d'état sont toutes deux utilisées dans l'inversion lorsque les mesures sont prises à courte distance de la source (voir Figure 2.9a). La topographie de la fonction d'erreur devient beaucoup plus complexe lorsque nous plaçons le réseau de récepteurs plus loin de la source. Pour le problème que nous étudions, nous avons observé que l'inversion est réussie lorsque les données sont collectées dans les premiers kilomètres de distance.

L'inversion utilisant les données de mesure sans phase présente quelques caractéristiques intéressantes. Bien que la suppression de la phase dans les données rende de nombreuses solutions de réfractivité candidates moins distinguables les unes des autres, elle semble "convexifier" la topographie de la fonctionnelle de l'erreur. Pour le problème que nous étudions, nous observons qu'il est possible de retrouver la structure synoptique du profil objectif dans une plage de 14 km. De plus, ce problème possède des solutions multimodales qui sont récupérables dans la première plage de quelques km (voir Figure 2.20). Enfin, nous montrons que la précision de l'inversion pourrait potentiellement être améliorée dans une stratégie où l'inversion sans information de phase pourrait être améliorée en incorporant l'information de phase comme deuxième étape de l'inversion.

2.1 Introduction

Radar systems performance under anomalous propagation conditions can be predicted if the atmosphere is properly known. The accuracy of the simulated 2-D radar coverage diagrams depends on how accurate the atmospheric refractivity is known. The radar coverage diagrams can be estimated by solving parabolic wave equation in which the refractivity is an input. The refractivity can be inferred by solving a simulation-driven optimization problem where the error between measured and simulated wave field data is minimized.

We consider the bistatic configuration given in Figure 2.1. This section formulates two different nonlinear least-square problems for refractivity inversion depending on the two different wave field data type: with and without the phase information. The problems are solved iteratively using gradient-based methods where the gradient function is derived and computed efficiently using adjoint state method.

This gradient derivation is novel. Adjoint state method is applied to the 2-D wide-angle parabolic equation of Thomson and Chapman (WAPE-TC) [16] using variational adjoint approach.

The specificity of Thomson and Chapman's equation [16] is that it is the most accurate

propagation model on which numerically efficient split-step technique is applicable unlike other wide-angle propagation models. The use of this equation is supposed to reduce the ill-posedness of the inverse problem while keeping the simulation cost the same, as compared to standard narrow-angle parabolic equation since the modeling error is reduced theoretically. However, this preferable equation comes with a square-root propagation operator which makes the derivation of the adjoint model less straightforward than the other propagation models which are made of linear operators.

This section concerns the inversion of refractivity from data measured with an array of radio receivers in open-sea environment. It is shown how to derive the adjoint model for WAPE-TC in this scenario, explains how to construct the adjoint code, and validates the adjoint model by using a finite-difference approach. The parametric study indicates the potential use of this method as a refractivity gradient retrieval system under certain circumstances. Some overcomplicated scenarios are analyzed to show the limits of this adjoint-based tomographic approach.

2.2 Background

Non-standard refractive index variations cause performance anomalies for maritime communication and surveillance platforms [7]. Prediction of tropospheric refractivity in abnormal propagation conditions is crucial for survey radars because these conditions create blind zones, increase clutter level, alter detection range and cause range-altitude errors [6]. Although accurate radar coverage estimation methods exist taking refractivity as input [10]–[14], abnormal conditions are poorly quantified in practical sense [56]. It is necessary to quantify the refractivity over spatial extent of the platform for the entire operation time dynamically with robust, cost-effective methods [99]. Refractivity-from-clutter (RFC) is proposed to address these requirements in near-real time [41]–[43]. It is a self-contained remote sensing method for refractivity inversion which potentially outperforms other refractivity estimation techniques [40], [55].

The current objective of RFC is to invert refractivity from sea-surface reflected radar clutter typically under 10 minutes with high reliability in realistic numerically-high-dimensional[1] scenarios [100], [101]. Commonly, the inversion problem is formulated as a simulation-driven nonlinear optimization problem [55]. Computationally-efficient simulation methods exist solving parabolic equations with split-step techniques [17], [98]. The inversion technique [55] and the clutter model [45] are scenario-dependent open questions, however. Inversion of refractivity from sea-reflected radar clutter or array antenna measurements, as illustrated in Figure 2.1, is a complex nonlinear, ill-posed problem [102]. Historically, the inversion complexity has been reduced thanks to coarse parametrization with functional representations in altitude [46], [47]. In parallel, range-independent medium is assumed [22]. Until the end of 2000s, several RFC techniques have been proposed with varying degrees of simplification on the spatial variability of refractive index (e.g., [8], [39], [48]–[53]). However, these techniques are not applicable for numerically-high-dimensional problems since the computational cost of inversion increases with the number of parameters to invert. Therefore, they are not efficient for problems at high frequencies when the propagation becomes increasingly sensitive to the spatial details of the medium inhomogeneities [55].

The first refractivity inversion technique whose computational cost does not depend on the number of parameter to invert has been developed in [57] in the framework of variational adjoint

[1]High-dimensionality refers to the dimension of the parameter vector obtained after the discretization of the model, it is not about the geometric dimension of the inverse problem.

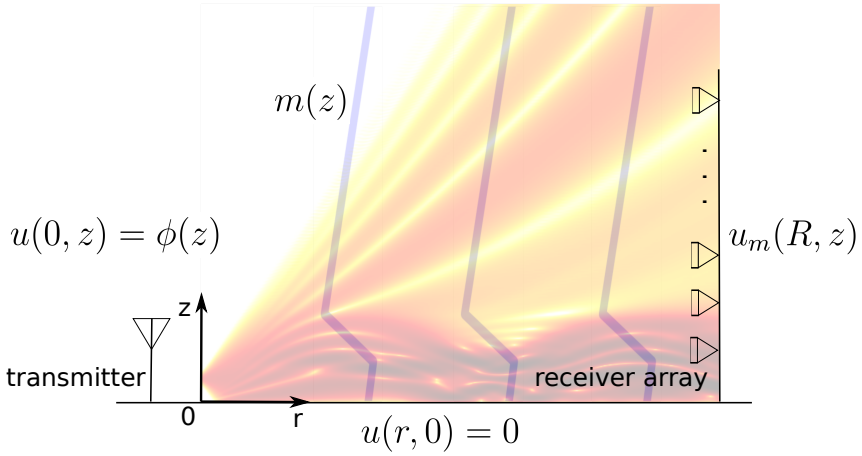

Figure 2.1: An illustration of the bistatic configuration. Initial field $\phi(z)$ propagates rightward in horizontally stratified atmosphere, which is characterized with refractivity $m(z)$. Our goal is to retrieve $m(z)$ from wave field measurements obtained with receiver array at distance R from the known source.

approach in 2010. The authors have derived the adjoint model (AM) for two-dimensional narrow-angle parabolic equation (2-D NAPE) which is solved using split-step Fourier (SSF) technique. Following studies have confirmed the severity of ill-posedness in high-dimensional scenarios despite regularization [58]–[60]. Unfortunately, adjoint-based RFC techniques of today still require unrealistically good initial guess with additional *a priori* information or need to incorporate dimensionality reduction techniques [61], [62]. Thus, reliable inversions which are purely driven by real-time data have not been realized yet in high-dimensional realistic configurations in 2-D. Other recent efforts concentrate on improving RFC in low-dimensional scenarios [63]–[67].

Despite the prominence of forward model (FM) accuracy in inverse problems, no previous study has attempted to fuse the adjoint-based approach with a wide-angle propagation model in RFC community. In this work, we extend the adjoint approach for 2-D wide angle parabolic equation (WAPE) by identifying the adjoint of square-root propagation operator. The proposed solution is validated numerically. Our main motivation is to enrich the pool of available adjoint models in radio and acoustic wave propagation communities with the most accurate WAPE on which split-step technique is applicable. We simulate the adjoint model with split-step wavelet (SSW) technique [17], which is faster than SSF, to tend towards a real-time accurate system. We aim at capturing any refractive condition at the spatial resolution of FM simulations by adopting point-by-point inversion approach in altitude [57].

Unlike previous work, the obtained gradient of the cost function is computed and validated successfully using a finite differences approximation. We also include the optimization landscapes in our analysis in order to visualize the inversion complexity and to explain how much the inversion is sensitive to initial guess for a given setup [103]. The method is presented for tomographic approach as an intermediate step towards a full effective RFC system. Although regularization techniques are kept out of scope of this work at this stage, our parametric study still shows the potential of our proposed approach.

The outline of the chapter is as follows. After general remarks in Section 2.3, the formulations of our problem are presented in Section 2.4. The adjoint problem is derived in Section 2.5 and the numerical methods are described in Section 2.6. The computational setup and the validation

of the derivations are presented in Section 2.7. Numerical test results are detailed in Section 2.8.

2.3 Adjoint Formalism

In this section, we first give an overview of adjoint method in generic sense. After defining the forward problem and the inverse problem, the adjoint model is derived in the next sections. The derivation is done in continuous adjoint form, so the parametrization and data are kept in functional forms. The recipe for the discrete adjoint formulation and finite dimensional setting of data and parametrization are explained in further sections. A basic introduction is given below.

Here, the inverse problem framework is presented following [104], [105] to put forward the motivation. The inverse problem is seen as the minimization of a square error functional over control parameter m in the bounded admissible set $\mathcal{M}_{\text{ad}}$ given by:

$$\min_{m\in\mathcal{M}_{\text{ad}}} J(m) = \min_{m\in\mathcal{M}_{\text{ad}}} \frac{1}{2}\left\|d_m^{\text{sim}} - d^{\text{obs}}\right\|_D^2. \tag{2.1}$$

The cost function $J(m)$ depends on the parameter m through the simulated measurement d_m^{sim}. The observation state d^{obs} is an experimental measurement function. We seek for a solution using an efficient gradient-based optimization method. For that reason, we choose to work with the square error functional (2.1) as this norm is differentiable. We present the standard formalism to obtain the gradient of the cost function below.

Consider the inverse problem (2.1) where $D = L^2(\Gamma_R)$ and Γ_R is a part of the physical domain Ω where the measurements are taken. The map of misfit quantification is given by:

$$\begin{aligned} K &: D \to \mathbb{R}, \\ d &\mapsto K(d) = \frac{1}{2}\left\|d - d^{\text{obs}}\right\|_D^2. \end{aligned} \tag{2.2}$$

The simulated measurements d_m^{sim} are taken via an observation operator P that applies to the the state $u_m \in U$, i.e.,

$$\begin{aligned} P &: U \to D, \\ u_m &\mapsto d_m^{\text{sim}} = P(u_m). \end{aligned} \tag{2.3}$$

The state u is uniquely defined for a given parameter m with the state equation $F(u, m) = 0$ at $u = u_m$. This latter is calculated from m using the forward map S:

$$\begin{aligned} S &: \mathcal{M}_{\text{ad}} \to U, \\ m &\mapsto u_m = S(m) \text{ such that } F(u_m, m) = 0. \end{aligned} \tag{2.4}$$

Note that the cost function J is a composite function given by $J(m) = K \circ P \circ S(m)$. The gradient of J with respect to m is given by [104]:

$$\nabla_m J = \psi'(m)^*(\psi(m) - d^{\text{obs}}), \tag{2.5}$$

where $\psi(m) = P \circ S(m)$ and $\psi'(m)$ is the differential of the mapping $\psi(m)$. The asterisk * denotes its adjoint. Since ψ is implicitly defined with the solution of the state equation, the implementation of (2.5) is not straightforward in our case. Therefore, we cast (2.5) using the variational form in order to obtain an explicit adjoint equation which allows the gradient to be identified and to be calculated more simply. In the following sections, the elements given in this

section are specified for our particular problem.

2.4 Problem Definition

The forward and inverse problems are presented here. In order to define the inverse problem more clearly, the forward problem is defined first.

The forward problem is to solve the physical model to estimate the ElectroMagnetic Wave Field (EMWF) in the environment for known source, geometric features and atmospheric parameters in the physical domain. In the inverse problem, we estimate the atmospheric parameter for known EMWF (which is measured in some part of the physical domain typically) and for known source and geometric features.

Throughout this dissertation, we estimate the vertical profile of atmospheric refractivity from wave field measurements by obtaining the measurement data in the bistatic configuration illustrated in Figure 2.1 using a receiver array antenna. This problem is called the tomography problem. From a known source, initial field propagates towards a vertically-positioned receiver array in horizontally stratified atmosphere, which is characterized by refractivity m as function of altitude z. The refracted propagating field is measured with this receiver array at several altitude points at a certain distance from the source. The goal is to deduce the refractivity of the atmosphere from the wave field measurements obtained with receiver array, for given source and ground conditions.

In this section, we present the formulations defining this inverse problem and describe our solution strategy.

2.4.1 The forward problem

This section discusses the physical modeling part in the adjoint formalism given by (2.4). In the context of propagation at open-sea environment with azimuthal symmetry, modeling of electromagnetic wave propagation considers solely forward propagating part of the Helmholtz equation in cylindrical coordinates:

$$\partial_r u - jk_0 \left(1 - Q\right) u = 0, \tag{2.6}$$

which is also called the one-way equation. The square-root operator Q is given by

$$Q = \sqrt{m^2(z) + k_0^{-2}\partial_z^2} \tag{2.7}$$

with k_0 the wave number in vacuum and $m(z) \in \mathbb{R}_+$ the modified refractive index that accounts for earth roundness. Equation (2.6) is exact for range-independent medium as long as the far field approximation holds, and takes into consideration the entire forward propagating wave field propagating at frequency $f = k_0 c/2\pi$. The reduced field $u(r, z) \in \mathbb{C}$ is related to the power at the receiver antenna by taking into account the distance, antenna gain and medium impedance [18]. In this work, (r, z) belongs to the domain Ω which is given by $[0, R] \times [0, Z]$ where R and Z are range of interest and altitude of interest respectively.

There are numerous choices to model the propagation in the lower troposphere depending on how accurate Q is approximated in (2.6) [18], [106]. The standard parabolic approximation (NAPE) is the first order approximation of Q [107]. It has limited accuracy [108] and it is the only

model used in adjoint-based RFC systems so far [57]–[62]. In this paper, we use the wider angle approximation (WAPE) as forward model, which is introduced by Thomson and Chapman [16] for underwater acoustics according to the splitting of Q as proposed by Feit and Fleck [109]:

$$\partial_r u + j\left[k_0(m(z)-1) + \left(\sqrt{k_0^2+\partial_z^2} - k_0\right)\right]u = 0, \tag{2.8a}$$

$$u(0,z) = \phi(z), \tag{2.8b}$$

$$u(r,0) = 0. \tag{2.8c}$$

This model considers the boundary condition of a flat perfectly-electric-conducting surface at $z = 0$ with source term $\phi(z)$ modeling the initial field of emitted radio waves at horizontal polarization. Note that the state equation (2.8a) could also consider a dielectric ground using a variable change proposed by [98].

To sum up, the forward problem is to determine the state u_m for a given parameter model m by solving (2.8).

2.4.2 The inverse problem

This section discusses the misfit quantification (2.2) in the adjoint formalism. In our inverse problem, we target to determine the parameter model m that minimizes the following cost function:

$$\min_{m\in\mathcal{M}_{\text{ad}}} J(m) = \min_{m\in\mathcal{M}_{\text{ad}}} \frac{1}{2}\left\|d_m^{\text{sim}} - d^{\text{obs}}\right\|^2_{L^2(\Gamma_R)} = \min_{m\in\mathcal{M}_{\text{ad}}} \frac{1}{2}\int_0^Z \left|d_m^{\text{sim}} - d^{\text{obs}}\right|^2 dz. \tag{2.9}$$

where $\mathcal{M}_{\text{ad}}$ is the admissible set of parameters which prescribes m to belong to a particular physical interval $[m_{\min}, m_{\max}]$, see Section 1.1.3. Depending on the type of measurement data d^{obs}, different cost functions can be constructed. For example, when both the amplitude and the phase of the field is available, we can choose $d^{\text{obs}} = u^{\text{obs}}(R,z)$ and we can formulate the cost function as:

$$J(m) = \frac{1}{2}\int_0^Z |u_m(R,z) - u^{\text{obs}}(R,z)|^2 dz. \tag{2.10}$$

and when the phase is not measurable, we can choose $d^{\text{obs}} = |u^{\text{obs}}(R,z)|^2$ and we can formulate the problem as:

$$J(m) = \frac{1}{2}\int_0^Z ||u_m(R,z)|^2 - |u^{\text{obs}}(R,z)|^2|^2 dz. \tag{2.11}$$

Also some other formulations are possible but not discussed here. In this section, we seek the most basic misfit forms which are also easily differentiable and are straightforward for substitution in the driver section of the adjoint model.

The problem (2.10) and (2.11) are designed with some idealizations which help the validation of the inversion process. Namely, for an objective refractivity model m_{OBJ}, the experimental measurements will be synthetically generated using the forward model (2.8). Referring to the tomographic approach described in Figure 2.1, the synthetic measurements are taken at the range $r = R$ such that

$$P : u(r,z) \mapsto u^{\text{obs}}(R,z) \text{ such that } F(u^{\text{obs}}, m_{\text{OBJ}}) = 0 \tag{2.12}$$

when phase is measurable and

$$P : u(r,z) \mapsto |u^{\text{obs}}(R,z)|^2 \text{ such that } F(u^{\text{obs}}, m_{\text{OBJ}}) = 0 \tag{2.13}$$

when phase is not measurable. Data space D is such that $\Gamma_R = \{R\} \times [0, Z]$. In our study, the parameter model m is function of altitude z only. Note that $d^{\text{obs}} \in \text{Im}(P \circ S)$ so the existence of global minimum is guaranteed for (2.9). But some other solutions become indistinguishable from m_{OBJ} especially when the phase is not measurable.

In a realistic scenario, simulated measurement with (2.8) would not perfectly produce the experimental measurement. The ground is modeled better as dielectric ground. The refractivity varies with range. In addition, measurements are time-averaged, contain noise and cannot be pointwise in practice. Modelling and measurement errors will add to the complexity of the idealized inverse problem. Therefore, it is of interest to avoid real-world data during validation of the inversion routine.

We note also that noise needs to be added to synthetic measurements in order to assess the robustness of the inversion algorithm against instabilities. Here, the noise modeling does not aim to be realistic and the inversion results from noisy data are neither an indicator of performance in real operation nor conclusive. Instead, the aim is to deduce the sensitivity of solver of (2.9) to perturbations. In order to be able to draw conclusion from inversion of noise-free synthetic data, it is necessary to show a certain level of robustness to noise. In that context, additive Gaussian noise can be added to the simulated measurements, i.e.,

$$d^{\text{obs}}_{\text{noisy}} = d^{\text{obs}} + \zeta \tag{2.14}$$

where ζ follows a centered normal Gaussian distribution with a standard deviation of $\tau \times \text{rms}\left(\sqrt{d^{\text{obs}}}\right)$. The function $\text{rms}(x)$ is root-mean-square of function $x \in \mathbb{R}$ and τ is termed as the level of noise in this work.

2.5 The Adjoint Problem

The adjoint problem is defined and solved in order to compute the gradient of the cost functions with respect to control parameters of refractivity efficiently. In this section, the derivation of the adjoint model is presented. Further theoretical and practical information can be found in [104], [110]–[113].

2.5.1 The tangent linear model

Let us denote $F(u_m, m) = F_m$ for brevity. Assume a linear perturbation on the parameter model $m(z) \in \mathcal{M}_{\text{ad}}$ in the direction $\hat{m}(z)$ as

$$\tilde{m}(z) = m(z) + \alpha\hat{m}(z). \tag{2.15}$$

The function $\tilde{u}$ is the state function evaluated at the parameter model $\tilde{m}$:

$$F(\tilde{u}, \tilde{m}) = F_{m+\alpha\hat{m}} = 0 \tag{2.16}$$

where $\tilde{u} = u_{\tilde{m}} = u_{m+\alpha\hat{m}}$. We seek for the operator F' which fulfills the following relation:

$$\lim_{\alpha\to 0} \frac{\|F_{m+\alpha\hat{m}} - F_m - F'(\hat{u}_m, m; \hat{m})\alpha\hat{m}\|}{\|\alpha\hat{m}\|} = 0. \tag{2.17}$$

Here, the operator F' is referred to as the Fréchet derivative of operator F. The function $\hat{u}_m$ satisfies the tangent linear model (TLM) $F'(\hat{u}_m, m; \hat{m}) = 0$ and it is referred to as the Gâteaux differential of u_m with respect to m in the direction of $\hat{m}$:

$$\lim_{\alpha \to 0} \frac{u_{m+\alpha\hat{m}} - u_m}{\alpha} = \hat{u}_m. \tag{2.18}$$

We are trying to estimate the impact of small linear perturbations of m on u in the physical system $F(u_m, m) = 0$, so that we can figure out how to reduce the misfit driven by u by controlling m. Now let us perturb linearly the physical system:

$$\partial_r \tilde{u} + j\left[k_0(\tilde{m}(z) - 1) + \left(\sqrt{k_0^2 + \partial_z^2} - k_0\right)\right]\tilde{u} = 0, \tag{2.19a}$$

$$\tilde{u}(0, z) = \phi(z), \tag{2.19b}$$

$$\tilde{u}(r, 0) = 0. \tag{2.19c}$$

We now subtract the two state equations to see the linear change in the physical model. In the limit of the vanishing perturbation amplitude $\alpha \to 0$, we have

$$\begin{aligned}
\lim_{\alpha \to 0}\Big\{ \frac{\partial_r(\tilde{u} - u_m)}{\alpha} + \frac{jk_0(m(z) + \alpha\hat{m} - 1)\,\tilde{u} - jk_0(m(z) - 1)\,u_m}{\alpha} + \frac{j\left(\sqrt{k_0^2 + \partial_z^2} - k_0\right)(\tilde{u} - u)}{\alpha} \Big\} &= 0 \\
\lim_{\alpha \to 0}\Big\{ \frac{\partial_r(\tilde{u} - u_m)}{\alpha} + \frac{j\left[k_0(m - 1) + \left(\sqrt{k_0^2 + \partial_z^2} - k_0\right)\right](\tilde{u} - u_m)}{\alpha} + \frac{jk_0\alpha\hat{m}\tilde{u}}{\alpha} \Big\} &= 0 \\
\partial_r \hat{u}_m + j\left[k_0(m - 1) + \left(\sqrt{k_0^2 + \partial_z^2} - k_0\right)\right]\hat{u}_m + jk_0\hat{m}u_m &= 0
\end{aligned} \tag{2.20}$$

Homogeneous initial and boundary conditions are obtained the same way using (2.18). For example, at $r = 0$ we obtain:

$$\begin{aligned}
\lim_{\alpha \to 0} \frac{u_{m+\alpha\hat{m}}(0, z) - u_m(0, z)}{\alpha} &= \hat{u}_m(0, z) \\
\lim_{\alpha \to 0} \frac{\phi(z) - \phi(z)}{\alpha} &= \hat{u}_m(0, z) = 0.
\end{aligned} \tag{2.21}$$

Boundary condition can be obtained at $z = 0$ in similar way. We obtain that $\hat{u}_m$ satisfies the Tangent Linear Model (TLM) given in the following:

$$\partial_r \hat{u}_m + j\left[k_0(m - 1) + \left(\sqrt{k_0^2 + \partial_z^2} - k_0\right)\right]\hat{u}_m + jk_0\hat{m}u_m = 0 \quad \text{on } \Omega, \tag{2.22a}$$

$$\hat{u}_m(0, z) = 0, \tag{2.22b}$$

$$\hat{u}_m(r, 0) = 0. \tag{2.22c}$$

In what comes next, for two given functions f and h, we will make use of the following inner products:

$$\begin{aligned}
\langle\langle f, h \rangle\rangle &= \int_0^Z \int_0^R f(r, z) \cdot \overline{h(r, z)}\, dr dz, \\
\langle f, h \rangle_{\mathcal{Z}} &= \int_0^Z f(R, z) \cdot \overline{h(R, z)}\, dz,
\end{aligned} \tag{2.23}$$

where $\bar{h}$ is the complex conjugate of h.

2.5.2 Gradient of the cost function

The gradient $\nabla_m J$ of the cost function J, at the parameter model m, can be obtained using the fact that

$$J'(m;\hat{m}) = J'(m) \cdot \hat{m} = \langle \nabla_m J, \hat{m} \rangle_{\mathcal{Z}}, \tag{2.24}$$

where $J'(m;\hat{m})$ is the Gâteaux differential of $J(m)$ with respect to m in the direction of $\hat{m}$

$$J'(m;\hat{m}) = \lim_{\alpha \to 0} \frac{J(m+\alpha\hat{m}) - J(m)}{\alpha} = \frac{\partial}{\partial \alpha} J(m+\alpha\hat{m})|_{\alpha=0}, \tag{2.25}$$

and $J'(m)$ is derivative of $J(m)$ with respect to m. In what comes next, we apply the chain rule of differentiation to obtain the gradient simpler than by using the limit (2.25). Referring to the formalism in Section 2.3, we find it beneficial to remind the reader about the formal application of the chain rule on the Gâteaux differential of the composite function $J(m) = K \circ \psi(m)$ with respect to m in the direction of $\hat{m}$. Our goal is to help the reader when following the terms appearing in the derivation because norm remains expressed with two dot products formally for some time.

$$\begin{aligned}
J(m) &= K \circ P \circ S(m) = K \circ \psi(m) = (K \circ \psi)(m) \\
J'(m;\hat{m}) &= (K \circ \psi)'(m;\hat{m}) = K'(\psi(m); \psi'(m;\hat{m})) \\
&= K'(\psi(m); \psi'(m) \cdot \hat{m}) = K'(\psi(m); \hat{\psi}) \\
&= K'(\psi(m)) \cdot \hat{\psi} \\
&= \Re\{(\psi(m) - d^{\text{obs}}) \cdot \hat{\psi}\} = \Re\{(\psi(m) - d^{\text{obs}}) \cdot \psi'(m) \cdot \hat{m}\}.
\end{aligned} \tag{2.26}$$

Here, $\Re\{x\}$ denotes the real part of $x \in \mathbb{C}$ and we recall that ψ is defined as $\psi(m) = d_m^{\text{sim}}$ according to the descriptions in Section 2.3. One can verify that taking the limit in (2.25) leads to the same results which are presented in the following of Section 2.5.2.

2.5.2.1 Gradient for the generic least square error functional

A generic expression for the gradient of the cost function (2.9) with respect to m is obtained observing the dependency of the simulated data d_m^{sim} on m during the differentiation.

$$\begin{aligned}
J(m) &= \frac{1}{2} \int_0^Z (d_m^{\text{sim}} - d^{\text{obs}}) \cdot \overline{(d_m^{\text{sim}} - d^{\text{obs}})} dz \\
J'(m) &= \frac{1}{2} \int_0^Z \left[(d_m^{\text{sim}} - d^{\text{obs}})' \cdot \overline{(d_m^{\text{sim}} - d^{\text{obs}})} + (d_m^{\text{sim}} - d^{\text{obs}}) \cdot \overline{(d_m^{\text{sim}} - d^{\text{obs}})}' \right] dz \\
&= \frac{1}{2} \int_0^Z \left[(d_m^{\text{sim}})' \cdot \overline{(d_m^{\text{sim}} - d^{\text{obs}})} + (d_m^{\text{sim}} - d^{\text{obs}}) \cdot (\overline{d_m^{\text{sim}}})' \right] dz \\
J'(m) \cdot \hat{m} &= \frac{1}{2} \int_0^Z \left[(d_m^{\text{sim}})' \cdot \overline{(d_m^{\text{sim}} - d^{\text{obs}})} + (d_m^{\text{sim}} - d^{\text{obs}}) \cdot (\overline{d_m^{\text{sim}}})' \right] \cdot \hat{m} \, dz \\
&= \int_0^Z \Re \left\{ (d_m^{\text{sim}} - d^{\text{obs}}) \cdot (\overline{d_m^{\text{sim}}})' \cdot \hat{m} \right\} dz
\end{aligned} \tag{2.27}$$

so from (2.24) we deduce that:

$$\langle \nabla_m J, \hat{m} \rangle_{\mathcal{Z}} = \int_0^Z \Re \left\{ (d_m^{\text{sim}} - d^{\text{obs}}) \cdot (\overline{d_m^{\text{sim}}})' \cdot \hat{m} \right\} dz. \tag{2.28}$$

2.5.2.2 Gradient when phase of wave field is measurable

For the cost function (2.10) with the phase information on the wave field, we substitute $d^{\text{obs}} = u^{\text{obs}}(R,z)$ and $d_m^{\text{sim}} = u_m(R,z)$ and use the definition of the Gateaux derivative of u at m in the direction $\hat{m}$ and use the definition of inner product $\langle\, .\ ,\ .\,\rangle_{\mathcal{Z}}$ to obtain the relation below:

$$\begin{aligned}\langle \nabla_m J, \hat{m} \rangle_{\mathcal{Z}} &= \int_0^Z \Re\left\{ (u_m(R,z) - u^{\text{obs}}(R,z)) \cdot \overline{u'_m(R,z)} \cdot \hat{m} \right\} dz \\ &= \int_0^Z \Re\left\{ (u_m(R,z) - u^{\text{obs}}(R,z)) \cdot \overline{\hat{u}_m(R,z)} \right\} dz \\ &= \Re\left\{ \left\langle (u_m(R,z) - u^{\text{obs}}(R,z)), \hat{u}_m(R,z) \right\rangle_{\mathcal{Z}} \right\}.\end{aligned} \tag{2.29}$$

2.5.2.3 Gradient when phase of wave field is not measurable

For the cost function (2.11) without the phase information on the wave field, we substitute $d^{\text{obs}} = |u^{\text{obs}}(R,z)|^2$ and $d_m^{\text{sim}} = |u_m(R,z)|^2$, and we obtain:

$$\begin{aligned}\langle \nabla_m J, \hat{m} \rangle_{\mathcal{Z}} &= \int_0^Z \Re\left\{ (|u_m(R,z)|^2 - |u^{\text{obs}}(R,z)|^2) \cdot \overline{|u_m(R,z)|^2}' \cdot \hat{m} \right\} dz \\ &= \int_0^Z \Re\Big\{ (|u_m(R,z)|^2 - |u^{\text{obs}}(R,z)|^2) \\ &\quad \cdot \left[\overline{u'_m(R,z) \cdot \overline{u_m(R,z)} + u_m(R,z) \cdot \overline{u'_m(R,z)}} \right] \cdot \hat{m} \Big\} dz \\ &= 2\int_0^Z \Re\left\{ (|u_m(R,z)|^2 - |u^{\text{obs}}(R,z)|^2) \cdot u_m(R,z) \cdot \overline{\hat{u}_m(R,z)} \right\} dz \\ &= 2\Re\left\{ \left\langle \left(|u_m(R,z)|^2 - |u^{\text{obs}}(R,z)|^2 \right) u_m(R,z), \hat{u}_m(R,z) \right\rangle_{\mathcal{Z}} \right\}.\end{aligned} \tag{2.30}$$

2.5.3 The formal derivation of the adjoint model

The variational problem The gradient $\nabla_m J$ is defined by deriving the adjoint state equation F'^* from the variational form of F'. Assume an adjoint state $w_m(r,z) \in \mathbb{C}$ exists such that[2]

$$\langle\langle w_m, F'(\hat{u}_m, m; \hat{m}) \rangle\rangle = 0. \tag{2.31}$$

Let us drop index m from the function w_m, u_m and $\hat{u}_m$ for brevity. The variational form of the TLM (2.22) reads

$$\langle\langle w, \partial_r \hat{u} \rangle\rangle + \langle\langle w, jk_0(m-1)\hat{u} \rangle\rangle + \langle\langle w, j(\sqrt{k_0^2 + \partial_z^2} - k_0)\hat{u} \rangle\rangle + \langle\langle w, jk_0 \hat{m} u \rangle\rangle = 0. \tag{2.32}$$

Applying rule of partial integration and the adjoint identity using the initial condition (2.22b) and the boundary condition (2.22c) of the TLM, we obtain, for the first term:

[2] See [111, Theorem 3.21] for further information.

$$
\begin{aligned}
\langle\!\langle w, \partial_r \hat{u} \rangle\!\rangle &= \int_0^Z \int_0^R w \cdot \overline{\partial_r \hat{u}} \; dr dz \\
&= \int_0^Z \Big(w \cdot \overline{\hat{u}} \Big) \Big|_{r=0}^{r=R} dz - \int_0^Z \int_0^R \partial_r w \cdot \overline{\hat{u}} \; dr dz \\
&= \langle w, \hat{u} \rangle_{\mathcal{Z}} |_{r=R} - \langle w, \hat{u} \rangle_{\mathcal{Z}} |_{r=0} - \langle\!\langle \partial_r w, \hat{u} \rangle\!\rangle \\
&= \langle w, \hat{u} \rangle_{\mathcal{Z}} |_{r=R} - \langle\!\langle \partial_r w, \hat{u} \rangle\!\rangle
\end{aligned}
\tag{2.33}
$$

because $\hat{u}(0, z) = 0$ in (2.22b). For the second term, we obtain:

$$
\begin{aligned}
\langle\!\langle w, jk_0(m-1)\hat{u} \rangle\!\rangle &= \int_0^Z \int_0^R w \cdot \overline{jk_0(m-1)\hat{u}} \; dr dz \\
&= \int_0^Z \int_0^R -jk_0(m-1) w \cdot \overline{\hat{u}} \; dr dz \\
&= \langle\!\langle -jk_0(m-1) w, \hat{u} \rangle\!\rangle \, .
\end{aligned}
\tag{2.34}
$$

The analysis of the third term is not as straightforward as the first and the second because it contains the square-root operator. The considerations are given below. We begin with using the adjoint identity $\langle\!\langle w, A\hat{u} \rangle\!\rangle = \langle\!\langle A^* w, \hat{u} \rangle\!\rangle$ and keep the asterisk above the square-root term for which we do not know readily what the adjoint is:

$$
\left\langle\!\left\langle w, j \left[\sqrt{k_0^2 + \partial_z^2} - k_0 \right] \hat{u} \right\rangle\!\right\rangle = \left\langle\!\left\langle -j \left[\left(\sqrt{k_0^2 + \partial_z^2} \right)^* - k_0 \right] w, \hat{u} \right\rangle\!\right\rangle
\tag{2.35}
$$

Let the operator A be equal to $k_0^2 + \partial_z^2$. In fact, using an already existing theorem in functional analysis [114, Theorem 1] and combining it with the knowledge on what this square-root operator models in free-space propagation, we can find out what $\sqrt{A}^*$ is in our context. Firstly, observe that A is a self-adjoint operator in our context. The term $k_0 \in \mathbb{R}_+$ is a coefficient that is fixed with the frequency of the radar, so $\langle\!\langle w, k_0^2 \hat{u} \rangle\!\rangle = \langle\!\langle k_0^2 w, \hat{u} \rangle\!\rangle$. The operator ∂_z^2 is found to be self-adjoint when homogeneous Dirichlet type boundary conditions are applied on the function $\hat{u}$ and w:

$$
\begin{aligned}
\left\langle\!\left\langle w, \partial_z^2 \hat{u} \right\rangle\!\right\rangle &= \int_0^Z \int_0^R w \cdot \partial_z^2 \overline{\hat{u}} \; dr dz \\
&= \int_0^R \Big[w \cdot \partial_z \overline{\hat{u}} \Big]_{z=0}^{z=Z} dr - \int_0^Z \int_0^R \partial_z w \cdot \partial_z \overline{\hat{u}} \; dr dz \\
&= \int_0^R \Big[w \cdot \partial_z \overline{\hat{u}} \Big]_{z=0}^{z=Z} dr - \left(\int_0^R \Big[\partial_z w \cdot \overline{\hat{u}} \Big]_{z=0}^{z=Z} dr - \int_0^Z \int_0^R \partial_z^2 w \cdot \overline{\hat{u}} \; dr dz \right) \\
&= \left\langle\!\left\langle \partial_z^2 w, \hat{u} \right\rangle\!\right\rangle + \int_0^R \Big[w \cdot \partial_z \overline{\hat{u}} \Big]_{z=0}^{z=Z} dr - \int_0^R \Big[\partial_z w \cdot \overline{\hat{u}} \Big]_{z=0}^{z=Z} dr \\
&= \left\langle\!\left\langle \partial_z^2 w, \hat{u} \right\rangle\!\right\rangle .
\end{aligned}
\tag{2.36}
$$

Then, A is a self-adjoint operator when $w(r, 0) = w(r, Z) = 0$ and $\hat{u}(r, 0) = \hat{u}(r, Z) = 0$. The homogenous Dirichlet boundary conditions of the TLM and AM at the upper boundary, i.e.,

$\hat{u}(r, Z) = w(r, Z) = 0$, are assumptions that are reasonable in our context from numerical point of view and they are going to be validated [115, p. 795], [116, p. 386]. In a way, zero boundary condition is assumed at an artificial upper boundary above the physical boundary at $z = Z$ in order to make our numerical technique work. Also note that this assumption is valid when u is zero at $z = Z$ and so w is at the top of the domain.

Secondly, observe that the sign of A depends on the considered eigenvalue spectrum of ∂_z^2 at fixed $k_0^2 \in \mathbb{R}_+$ because ∂_z^2 is a negative operator for $f(z = 0) = f(z = Z) = 0$ in its domain:

$$\begin{aligned}
\left\langle\!\left\langle f, \partial_z^2 f \right\rangle\!\right\rangle &= \int_0^Z \int_0^R f \cdot \partial_z^2 \overline{f} \; dr dz \\
&= \int_0^R \left[f \cdot \partial_z \overline{f} \right]_{z=0}^{z=Z} dr - \int_0^Z \int_0^R \partial_z f \cdot \partial_z \overline{f} \; dr dz \\
&= - \int_0^Z \int_0^R \partial_z f \cdot \partial_z \overline{f} \; dr dz \\
&= - \langle\!\langle \partial_z f, \partial_z f \rangle\!\rangle = - \left\| \partial_z f \right\|^2 \leq 0. \qquad (2.37a)
\end{aligned}$$

We can observe that,

$$\langle\!\langle Af, f \rangle\!\rangle \geq 0 \text{ when } \langle\!\langle -\partial_z^2 f, f \rangle\!\rangle \leq \langle\!\langle k_0^2 f, f \rangle\!\rangle, \qquad (2.38a)$$

$$\langle\!\langle Af, f \rangle\!\rangle < 0 \text{ when } \langle\!\langle -\partial_z^2 f, f \rangle\!\rangle > \langle\!\langle k_0^2 f, f \rangle\!\rangle. \qquad (2.38b)$$

Let us now elaborate on (2.38) briefly. As ∂_z^2 is a negative operator, we cannot expect to have (2.38a) for all f. However, when a numerical scheme is used, the eigenvalues of the discretized ∂_z^2 are lower bounded and (2.38a) becomes possible when k_0 matches with discretized ∂_z^2. This matching is linked to a condition on the mesh size described in Section A. To sum up, we can describe the sign of A after laying out the spectrum of the operator numerically (see Section A).

In addition, from a physical point of view, observe that (2.38a) is effectively the case when propagating part of the wave field is accounted in the numerical solution of (2.8). The case when $\langle\!\langle Af, f \rangle\!\rangle < 0$ in (2.38b) numerically corresponds to the evanescent waves in the numerical solution which decay exponentially with range during propagation [18], [106][3].

Lastly, there exists a self-adjoint square-root operator $\sqrt{A} = \sqrt{A}^*$ when A is a positive self-adjoint operator, according to [114, Theorem 1], as in the case of propagating (non-evanescent) part of numerical solution coming from (2.8a) in our context [18]. Thus, $\sqrt{A}^* = \sqrt{A}$ is valid as far as the scope of resolution is restricted on the propagating part of the field. If we assume that propagating part of the wave field corresponds to the essential part of the physical measurements because the evanescent part vanishes exponentially as stated, self-adjointness of the square-root operator can be asserted in the context of our study.

Numerically this corresponds to restricting the eigenvalues that would otherwise extent to $-\infty$ by choosing a mesh such that step size in the axial direction is greater than λ times a multiplicative constant C. This means ensuring $\Delta z \geq C\lambda$ where Δz is the step size in the axial direction of the domain Ω and λ is the wavelength. The value of the constant C should be obtained by analyzing the numerical method that is used for solving the WAPE and also should be verified empirically by experimenting with the FM and AM. We discuss about this in

[3]The reader may refer to the discussion in Section 2.4.1, Section 2.4.3 and Section 3.4 of reference [18].

Section A. In our case for example, we should satisfy $\Delta z \geq \lambda/\pi$ (see Section A)[4]. Under this condition, the third term reads:

$$\left\langle\!\left\langle w, j\left[\sqrt{k_0^2+\partial_z^2}-k_0\right]\hat{u}\right\rangle\!\right\rangle = \left\langle\!\left\langle -j\left[\sqrt{k_0^2+\partial_z^2}-k_0\right]w, \hat{u}\right\rangle\!\right\rangle \tag{2.39}$$

with homogeneous Dirichlet boundary conditions applied on w in z. Finally, for the fourth term, we have:

$$\begin{aligned}\langle\!\langle w, jk_0\hat{m}u\rangle\!\rangle &= \int_0^Z\int_0^R w \cdot \overline{jk_0\hat{m}u}\, drdz = \int_0^Z\int_0^R -jk_0 w\overline{u}\cdot\hat{m}\, drdz \\ &= \langle\!\langle -jk_0 w\overline{u}, \hat{m}\rangle\!\rangle .\end{aligned} \tag{2.40}$$

In sum, we arrive at the following variational problem:

$$\begin{aligned}&-\langle\!\langle \partial_r w, \hat{u}\rangle\!\rangle + \langle w, \hat{u}\rangle_{\mathcal{Z}}|_{r=R} - \langle\!\langle jk_0(m-1)w, \hat{u}\rangle\!\rangle \\ &-\langle\!\langle j((k_0^2+\partial_z^2)^{1/2}-k_0)w, \hat{u}\rangle\!\rangle - \langle\!\langle jk_0 w\overline{u}, \hat{m}\rangle\!\rangle = 0.\end{aligned} \tag{2.41}$$

Let operator $B(m) = \partial_r + jk_0(m-1) + j(A-k_0)$, then the variational problem becomes

$$-\langle\!\langle B(m)w, \hat{u}\rangle\!\rangle + \langle w, \hat{u}\rangle_{\mathcal{Z}}|_{r=R} - \langle\!\langle jk_0 w\overline{u}, \hat{m}\rangle\!\rangle = 0. \tag{2.42}$$

Measurement with phase The gradient $\nabla_m J$ can be identified from the following equations:

$$\begin{aligned}\langle \nabla_m J, \hat{m}\rangle_{\mathcal{Z}} &= \Re\left\{\left\langle (u_m(R,z) - u^{\text{obs}}(R,z)), \hat{u}_m(R,z)\right\rangle_{\mathcal{Z}}\right\} \\ \langle\!\langle jk_0 w_m\overline{u}_m, \hat{m}\rangle\!\rangle &= -\langle\!\langle B(m)w_m, \hat{u}_m\rangle\!\rangle + \langle w_m(R,z), \hat{u}_m(R,z)\rangle_{\mathcal{Z}}\end{aligned} \tag{2.43}$$

Measurement without phase The gradient $\nabla_m J$ can be identified from the following equations:

$$\begin{aligned}\langle \nabla_m J, \hat{m}\rangle_{\mathcal{Z}} &= 2\Re\left\{\left\langle \left(|u_m(R,z)|^2 - |u^{\text{obs}}(R,z)|^2\right) u_m(R,z), \hat{u}_m(R,z)\right\rangle_{\mathcal{Z}}\right\} \\ \langle\!\langle jk_0 w_m\overline{u}_m, \hat{m}\rangle\!\rangle &= -\langle\!\langle B(m)w_m, \hat{u}_m\rangle\!\rangle + \langle w_m(R,z), \hat{u}_m(R,z)\rangle_{\mathcal{Z}}\end{aligned} \tag{2.44}$$

Observing the symmetry of the operators in the variational form, we can think of obtaining an adjoint state equation which is the same as (2.8a) so that the forward model (FM) solver can be inherited for the adjoint model (AM) with minimal modification.

Measurement with phase Now let us identify the gradient and the adjoint model explicitly. When the phase is measurable, let w_m be given by:

$$\partial_r w_m + j\left[k_0(m-1) + \left(\sqrt{k_0^2+\partial_z^2}-k_0\right)\right]w_m = 0, \tag{2.45a}$$

$$w_m(R,z) = u_m(R,z) - u^{\text{obs}}(R,z), \tag{2.45b}$$

$$w_m(r,0) = 0, \tag{2.45c}$$

[4]Please also see [17] and [117] for the comments about how to choose Δz as function of λ.

Measurement without phase When only the amplitude is measurable, let w_m be given by:

$$\partial_r w_m + j\left[k_0(m-1) + \left(\sqrt{k_0^2 + \partial_z^2} - k_0\right)\right] w_m = 0, \tag{2.46a}$$

$$w_m(R,z) = 2\left(|u_m(R,z)|^2 - |u^{\text{obs}}(R,z)|^2\right) u_m(R,z), \tag{2.46b}$$

$$w_m(r,0) = 0, \tag{2.46c}$$

such that (2.47) holds for both measurement data types:

$$\nabla_m J = \Re\left\{ jk_0 \int_0^R w_m(r,z)\overline{u_m(r,z)}\, dr \right\}. \tag{2.47}$$

The estimation of such gradient will now enable us to use gradient-based optimization methods (e.g., Quasi-Newton methods) which are suitable for large-scale inversion problems. In the next section, we give the implementation details for the adjoint models and present an approach to validate both the derivation and the implementation.

2.6 Algorithm

In this section, we explain how we build our inversion algorithm following the descriptions of the workflows in [57] and Chapter 6 of [104].

2.6.1 Adjoint-based Inversion Algorithm

The inversion process starts from an initial guess m_{IG} which gives a simulated measurement data d_m^{sim} using propagation model (2.8). Next, the adjoint equation is solved in order to estimate the gradient using (2.47). The iteration parameters are estimated with a gradient-based minimization algorithm, which includes inner cost function estimations using the propagation model. The same process continues until a convergence criteria is met.

In our study, we do not have access to measurements. Therefore, we generate the measurements d^{obs} synthetically using the forward model given by (2.8) for a known objective refractivity profile m_{OBJ}. The workflow given in Figure 2.2 summarizes the inversion strategy and the used notations. Next section presents the numerical methods which we use.

2.6.2 Numerical Methods

Simulation technique The functions u_m and w_m are estimated numerically from the forward and adjoint models using split-step wavelet (SSW) technique [17]. The function u_m is computed numerically using a forward model (FM) that is developed at ENAC during the thesis work of Hang Zhou [118] and Thomas Bonnafont [97]. I use the forward model as a black-box. My task is to derive the adjoint code for the given forward model code and I do not have contribution on the SSW technique.

Discretized Model The variables presented until this section are in functional form for simplicity. However in the following, u, w, d and m are treated as finite dimensional vectors in a

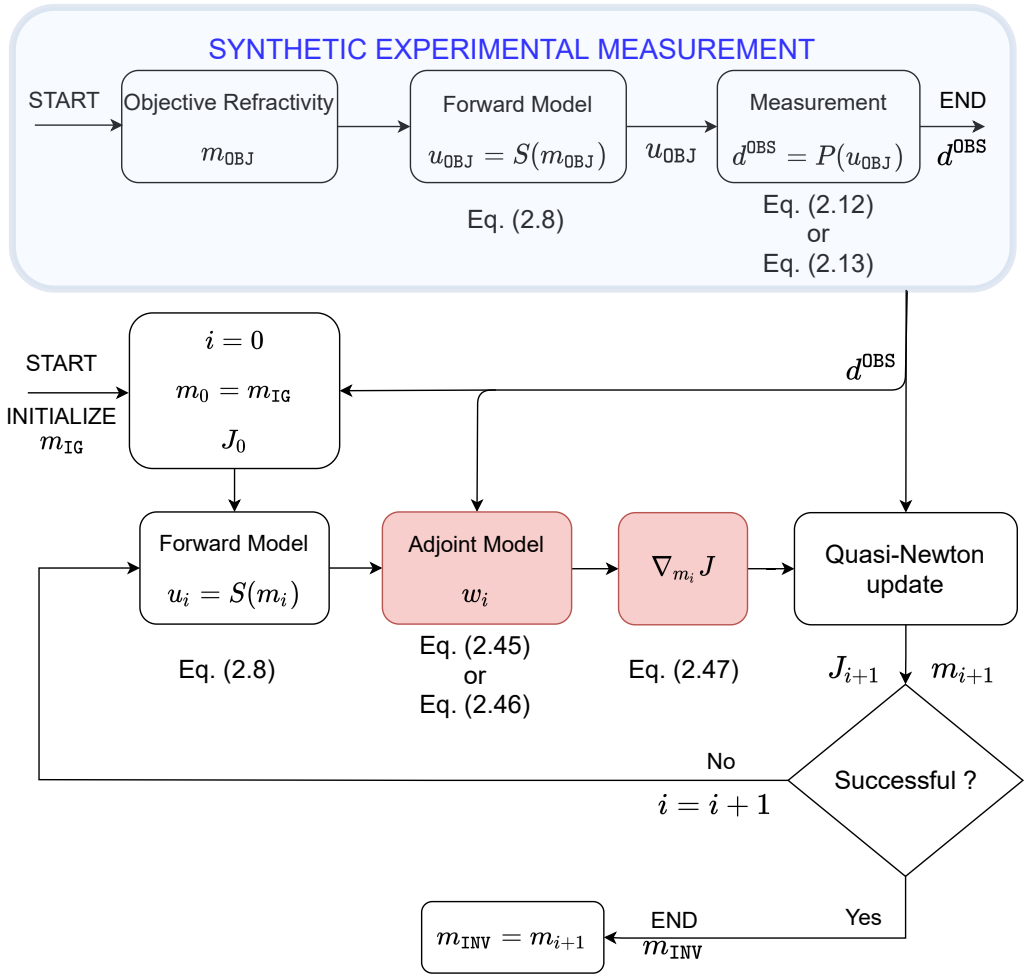

Figure 2.2: Scheme of inversion workflow. The algorithm corresponding to the red boxes will be validated.

numerical method that tackles the partial differential equations and the integrals. We are going to introduce their finite representations so as to explain our techniques.

Our numerical domain is illustrated in Figure 2.3. It extends from 0 to R and Z in the radial and the axial directions, respectively. The domain is discretized using a structured mesh. The position (r, z) becomes (r_{n_r}, z_{n_z}) in this domain, which are controlled by uniform mesh size and station number on the grid. The position vector is expressed by the following relations.

$$r_{n_r} = n_r \, \Delta r, \quad n_r \in [0, N_r], \tag{2.48a}$$
$$z_{n_z} = n_z \, \Delta z, \quad n_z \in [0, N_z]. \tag{2.48b}$$

Here, N_r and N_z are the number of grid nodes (computation stations) on the discretized domain. Accordingly, $u(r, z) \in \mathbb{C}$, $w(r, z) \in \mathbb{C}$, $m(z) \in \mathbb{R}$ and $\nabla_m J(m) \in \mathbb{R}$ becomes of dimension $u(r_{n_r}, z_{n_z}) \in \mathbb{C}^{N_r \times N_z}$, $w(r_{n_r}, z_{n_z}) \in \mathbb{C}^{N_r \times N_z}$, $m(z_{n_z}) \in \mathbb{R}^{N_z}$ and $\nabla_m J(m) \in \mathbb{R}^{N_z}$, respectively. The finite dimensional representations are built on the punctual values computed at grid nodes. One example is given for u in Figure 2.3.

Adjoint code derivation The adjoint model solver is derived from the forward model solver. The forward model can be treated as a black box with minor modifications when deriving the adjoint code because we can derive an adjoint-PWE thanks to the symmetry of the operators

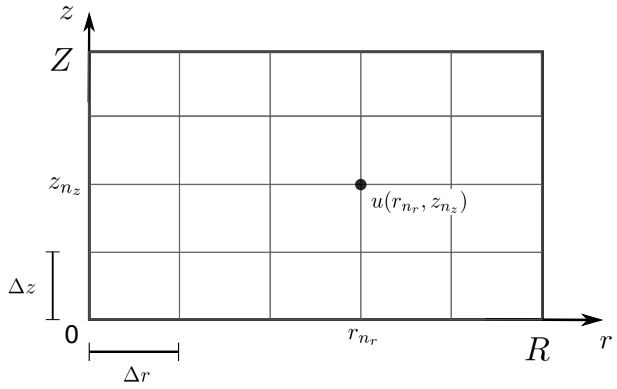

Figure 2.3: Discretized computational domain.

appearing in the numerical application in our particular context. The adjoint initial condition is achieved by replacing (2.8b) with (2.45b) or (2.46b) in the FM solver depending on the choice of the cost function. Adjoint backpropagation is achieved by changing sign of range step from Δr to $-\Delta r$ and 180° rotation of computational domain around axial direction in the FM solver. This change of sign occurs in the free-space propagator, boundary condition and phase screen operators in [17].

In the forward and adjoint solver, the field is apodised with the Hanning absorbing window for $z > Z$. The ground boundary is modeled using local image method. So as to improve the accuracy of the numerical method, we have used the splitting scheme given below [17], [106]:

$$u|_{r+\Delta r,z} = e^{B/2}\mathcal{T}^{-1}\left\{\mathcal{P}\mathcal{T}\left\{e^{B/2}u|_{r,z}\right\}\right\}, \tag{2.49}$$

where $B = \{-jk_0(m-1)\Delta r\}$ is the term accounting for the atmosphere, $\mathcal{T}$ is the wavelet transform operator with compression, $\mathcal{T}^{-1}$ is the inverse wavelet transform, and $\mathcal{P}$ is the operator modelling the free-space propagation in the wavelet domain.

Computing the norm and its gradient The cost function (2.9) and its gradient (2.47) are computed using Simpson's rule of integration.

Optimization The optimization algorithm is the well-known BFGS algorithm [119]. The optimization process stops when the cost function can no longer be decreased sufficiently respecting Wölfe conditions [120], [121] in the descent direction as described in [119, Section 3.1].

2.7 Validation of the Gradient

The algorithm presented in Figure 2.2 is suited for inverting the air refractivity above sea surface which corresponds to the measured wave field data. In order to be sure that the algorithm works properly, a validation experiment can be organized. We choose an ambient refractivity distribution and generate the corresponding measurement data synthetically with a physical modeling technique.

During synthetic data generation, the modeling technique is chosen as the same as the forward model of the inversion algorithm with the same code and mesh which is used during inversion.

This inversion experiment falls in the category of an *inverse crime* [104], [122], [123]. Such a setup eliminates measurement errors, modeling errors and noise which exists in real-world operations in practice. With this experimental setting, we check if our algorithm is capable to find the ambient refractivity distribution in ideal conditions.

As discussed later, even in ideal conditions, the inversions often fail because the problem is ill-posed. In this case, we want to check, at least, if the analytical derivation of the gradient and the numerical implementation is correct or not. After the contribution is validated, we can analyze the test cases to figure out the mechanism behind the failure.

In order to make the validation and analysis easier, we choose the parameters and the source condition of the validation experiment as given in Figure 2.4. The details are given in the next section. The baseline computational setup of the validation process is given in Section 2.7.1 which also contains some notes on the validation methodology. Numerical validation is given in Section 2.7.3.

Remember that the variation of the refractivity is discussed in terms of M which is related to the parameter m of the FM through (2.50).

$$M = (m - 1) \times 10^6. \tag{2.50}$$

The refractivity m varies at the order of part per million in the troposphere. The refractivity is discussed with the modified parameter $M(z)$ in the following sections.

2.7.1 Computational Setup

In the baseline computational setup, the geometry of the computational domain Ω is a two dimensional plane constructed on axial and radial directions as given in Figure 2.1. The geometry is truncated such that $\Omega = [0, R] \times [0, Z]$. Altitude of interest Z is limited to 150 m. Range of propagation R is considered mainly at 5 different values, and it is equal to 1, 5, 10, 30, 60 km respectively.

The mesh of discretized domain Ω_{N_r,N_z} is a uniform grid. The parameter N_r and N_z are the number of grid points along the directions $\hat{r}$ and $\hat{z}$, respectively. The cell size in altitude is set to $\Delta z = 1$ m for all cases. The cell size in range Δr is determined such that $r \in [0, R]$ is discretized into 100 equal intervals with $\Delta r < 100$ m, otherwise the cell size is fixed at $\Delta r = 100$ m for the control of numerical error.

The initial condition $\phi(z)$ is obtained from a Complex Point Source (CPS) positioned at $(r_s, z_s) = (-100 \text{ km}, 25 \text{ m})$ and its amplitude and phase is shown in Figure 2.4b and Figure 2.4c respectively. The CPS has width of 5 m and emission frequency $f_s = 2$ GHz at horizontal polarization. The source is placed far from the computational domain in order to obtain a $|\phi(z)|$ profile which is close to a plane wave. This quasi plane wave profile is necessary for illuminating the entire domain in short ranges, which is useful for validation.

The synthetically generated data d^{obs} is obtained by solving the forward model for parameter model $M = M_{\text{OBJ}}$. Therefore the global minimum of the nonlinear least squares problem is M_{OBJ} and the success of the inversion is evaluated by checking how far inverted parameter M_{INV} is from M_{OBJ}. The iterations start from an initial guess refractivity M_{IG}.

The objective and the initial modified refractivity parameters of the baseline computational

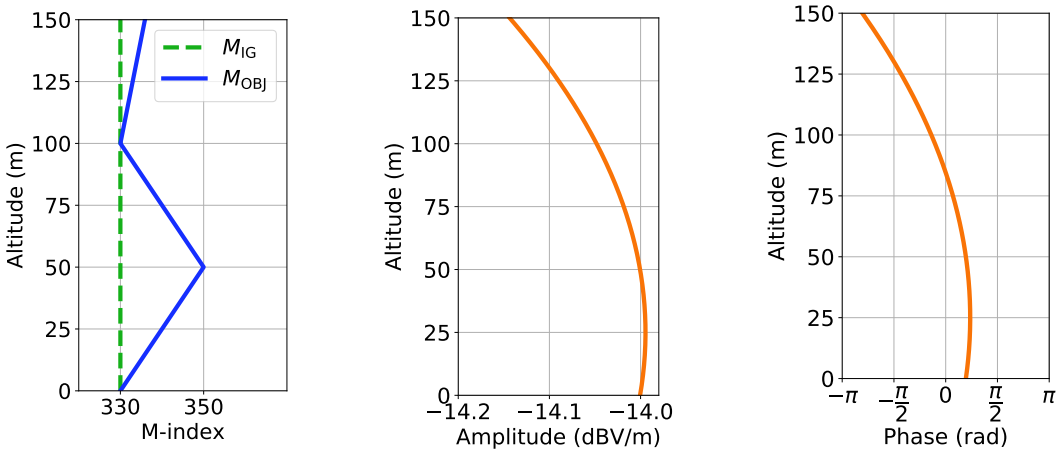

(a) (b) (c)

Figure 2.4: The selected source profile and refractivity profiles suited to the validation purposes. (a) M_{IG} and M_{OBJ}, (b) $|\phi(z)|$, (c) $arg(\phi(z))$.

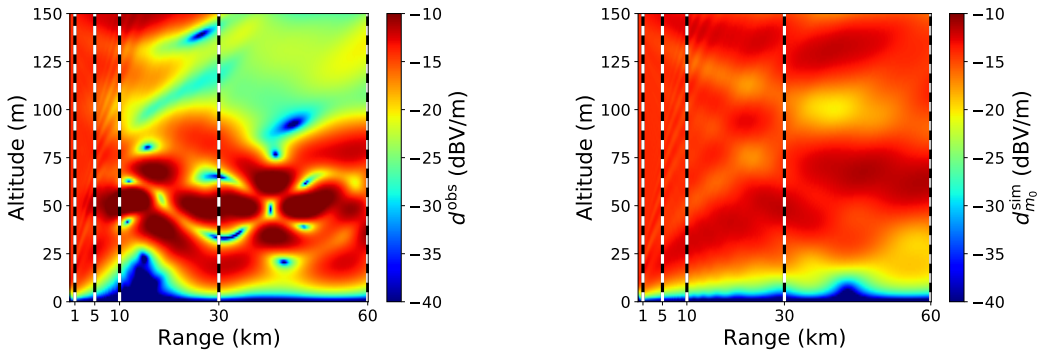

(a) (b)

Figure 2.5: Propagating fields at different measurement array position R for the computational setup given in Section 2.7.1. (a) Synthetically-generated measured field, (b) simulated field for initial guess.

setup are given in Figure 2.4a. The initial guess profile $M_{\text{IG}}(z)$ assumes uniform guess at $M_{\text{IG}}(z) = 330$ M-unit. The objective refractivity $M_{\text{OBJ}}(z)$ has a trilinear structure of surface based ducts [47]. The duct is described by the following altitude-refractivity pair: $(z, M_{\text{OBJ}}(z)) = \{(0, 330.0), (50, 350.0), (100, 330.0), (150, 335.90)\}$. Refractivity does not depend on range.

The parameters $M_{\text{OBJ}}, M_{\text{IG}}$ and M_{INV} all belong to $\mathbb{R}^{N_z}$. The measurement data and the simulated data also belongs to N_z-dimensional space. Accordingly, the aim is to invert $N_z = 151$ refractivity parameters from 151 experimental data sample, all of which are estimated at each one of grid node in altitude. To be clear, there are 151 receivers on the receiver array extending from ground level to the altitude of interest $Z = 150$ m, with the receiver spacing of Δz in the scenarios that we consider in this chapter.

In the next section, we give the inversion results of the workflow given in Figure 2.2 at different ranges for the baseline computational setup. The objective and initial guess fields are given in Figure 2.5 with their difference.

2.7.2 Validation Method

For solving this least squares inverse problem, we use gradient-based optimization method for the inversion. Therefore, the validation of the gradient is crucial. The contribution from the variational adjoint approach is its accuracy and efficient calculation of the gradient of the objective function to a large number of medium parameters. This gradient is derived analytically and expressed by (2.47). Assuming our physical system is approximated with our state function properly, the accuracy of the gradient depends on the quality of the measurement function and the adjoint state function. The validation is a classical and compulsory process which is described in [104], [111]. After validating the gradient of the optimization, the next question is going to be if there is local minima for this least squares inverse problem.

In the last decade of adjoint-based RFC systems, inversion of synthetically generated data have been used for demonstrating the proper derivation and implementation. However, the problem (2.9) is difficult to solve accurately even in the absence of modeling errors, measurement errors and noise. In fact, the inversion results are not accurate enough for validating the quality of the implementation except for oversimplified cases which are not interesting in terms of practical applications (e.g., [2]). Therefore, we cannot rely on inversion results for validation and it is necessary to perform the validation process starting from checking the gradient computation for interesting overcomplicated inversion scenarios. Clearing the validation step of the gradient (which includes the adjoint model validation) provides a solid basis for holding ill-posedness responsible for inaccurate inversion results. In that context, the part of the inversion algorithm lacking validation is shown in the workflow in Figure 2.2 in red.

If the adjoint state w_m is formulated and simulated properly, $\nabla_m J_{\mathrm{AM}}$ would match the gradient computed with a reference method. A costly approximation of the gradient from a finite differences (FD) scheme can be treated as a secure reference method respecting some conditions as described in [104]. The reference estimation of the gradient can be obtained using a first order forward differences scheme. Typically, for a number N_z of inversion parameters, the i^{th} component of the FD approximation of the gradient is given by

$$[\nabla_m J_{\mathrm{FD}}]_i = \frac{J(m + \epsilon \boldsymbol{e}_i) - J(m)}{\epsilon}, \tag{2.51}$$

where $\boldsymbol{e}_i$ is the n-sized column vector whose ith component is one while all the others are zeros, and ϵ is chosen as 10^{-6}. Note that the estimation of the gradient with a finite differences scheme requires $n + 1$ evaluations of the cost function, while $\nabla_m J_{\mathrm{AM}}$ is computed at the cost of 2 FM runs [104].

To sum up, the gradients $\nabla_m J_{\mathrm{FD}}$ and $\nabla_m J_{\mathrm{AM}}$ should follow each other if the adjoint field is formulated and simulated properly and the numerical integration of (2.47) is done properly.

2.7.3 Validation

In this section, the adjoint model and the gradient presented in Section 2.5.3 are validated numerically at the computational setup described in Section 2.7.1, by comparing the gradients obtained from finite differences and adjoint model $\nabla_m J_{\mathrm{FD}}$ and $\nabla_m J_{\mathrm{AM}}$. The gradients are computed for the first descent iteration (i.e., $M_0 = M_{\mathrm{IG}}$). This validation is performed for both data types.

The validation is performed qualitatively by presenting the gradients as line graphs with respect to altitude. In fact, J is function of m, so $\nabla_m J$ is a function of parameter m as well. Therefore, the gradient which is computed numerically in discrete manner should be presented pointwise with respect to parameter index in the vectorial representation. However, m is function of altitude. Thanks to that relation, we can display the gradient with respect to altitude like in Figure 2.6. Here, the gradient value at an altitude point is actually the value at the parameter index that belongs to that altitude.

2.7.3.1 Adjoint model: measurement with phase

In this section, we present the results related to the validation of the gradient for the problem (2.10). The gradient of (2.10) is computed using (2.47) in which w is the solution of (2.45).

The gradient from the adjoint model ($\nabla_m J_{AM}$) is compared to that of finite differences ($\nabla_m J_{FD}$) in Figure 2.6. The gradients $\nabla_m J_{AM}$ and $\nabla_m J_{FD}$ follow each other at different measurement antenna position R, so the validation is successful. This validation automatically validates the derivation of the adjoint model formulation (2.45) according to the workflow of the algorithm given in Figure 2.2.

In short ranges, the nonlinearity between m and J is weak (we will confirm that later). The normalized gradient profile in the first few hundred meters range (not shown here) looks almost like the function $-(M_{OBJ} - M_{IG})/\left\|M_{OBJ} - M_{IG}\right\|$ (see Figure 2.4a and Figure 2.6a). The gradient is validated also for $R > 1$ km in Figure 2.6 at several different R to be sure that we can compute it correctly. In Figure 2.6, we observe that the gradient changes with R. This evolution is displayed also in Figure 2.7 and might reveal some features of the nonlinearity and local minima problems reported in [57].

2.7.3.2 Adjoint model: measurement without phase

In this section, we present the results related to the validation of the gradient for the problem (2.11). The gradient of (2.11) is computed using (2.46) where the adjoint function w is the solution of (2.47). The adjoint model (2.46) is validated by comparing the gradient which is obtained thanks to this equation, to the gradient obtained by finite differences.

In Figure 2.8, the gradient calculated with the AM and with FD are plotted with respect to altitude for the different values of R. Both gradients perfectly match, except that at $R = 1$ km there exists some differences due to the very low value of the gradient. Thus the gradient estimation is more robust for long range applications.

Numerical issues become prominent in the computation of the gradient when the gradient is low as in the case of Figure 2.8a. For AM, this occurs when the driver of the adjoint model $w(R, z)$ approaches to zero and the gradient is small like when it is estimated near a stationary point, according to (2.46b) and (2.47). This causes numerical problems which gives even worse validation curves at $R = 100$ m (not plotted here). From FM point of view, this corresponds to the case where the difference between the field bending effect of different m is not significant on $|u|$ at short ranges. For this reason, impact of the perturbations of m on J are insignificant, according to (2.51). This observation leads us to the conclusion that a stationarity check is recommended for RFC applications at the end of inversion. Furthermore, one must be aware that the gradient might be miscomputed near stationary point and one must take some precautions to compensate

for this, which is discussed in other sections.

To sum up, the adjoint model is validated with the comparison of the gradient with FD.

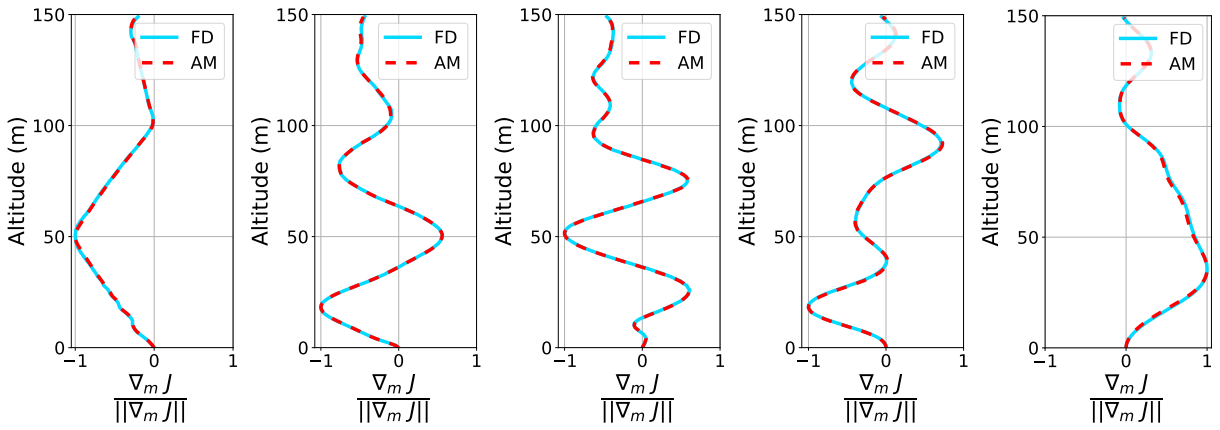

Figure 2.6: Validation of the gradient for the first descent iteration for complex measurement data type. Comparison of the gradient $\nabla_m J_{\mathrm{FD}}$ computed with finite differences (FD) method vs. $\nabla_m J_{\mathrm{AM}}$ computed with adjoint model (AM). (a) $R = 1$ km, (b) $R = 5$ km, (c) $R = 10$ km, (d) $R = 30$ km, (e) $R = 60$ km.

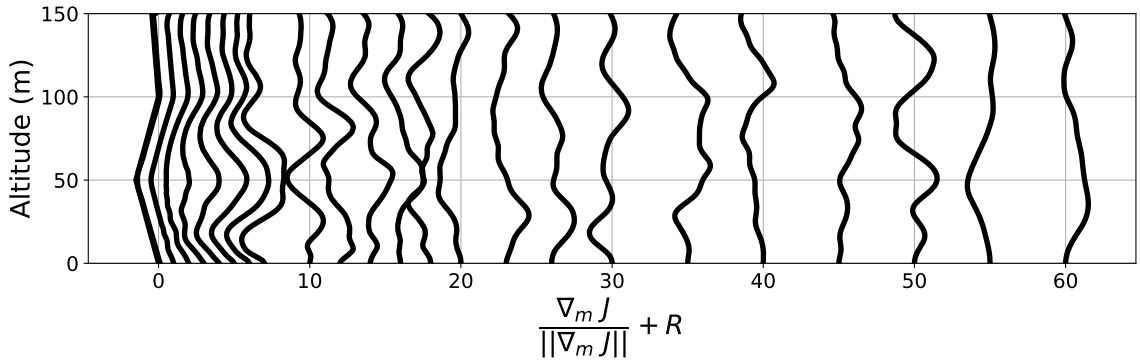

Figure 2.7: Evolution of the the gradient of the first descend iteration as function of R.

2.8 Inverse Problem Resolution

In this section, the inversion routine given in Figure 2.2 is tested for its capability to retrieve M_{OBJ} from the corresponding measurement.

At this stage, a user-defined convergence criterion is not implemented. The iterations continue until the optimization algorithm cannot improve the cost function anymore. This is also a sort of convergence criteria effectively. Therefore, a convergence criteria or maximum number of iterations is not imposed in this test. The iterations continue until arriving at a stationary point of the error functional. Furthermore, the parameters of the optimization are not bounded. The results of this section are preliminary. These questions are left for the realistic scenarios in the next Chapter.

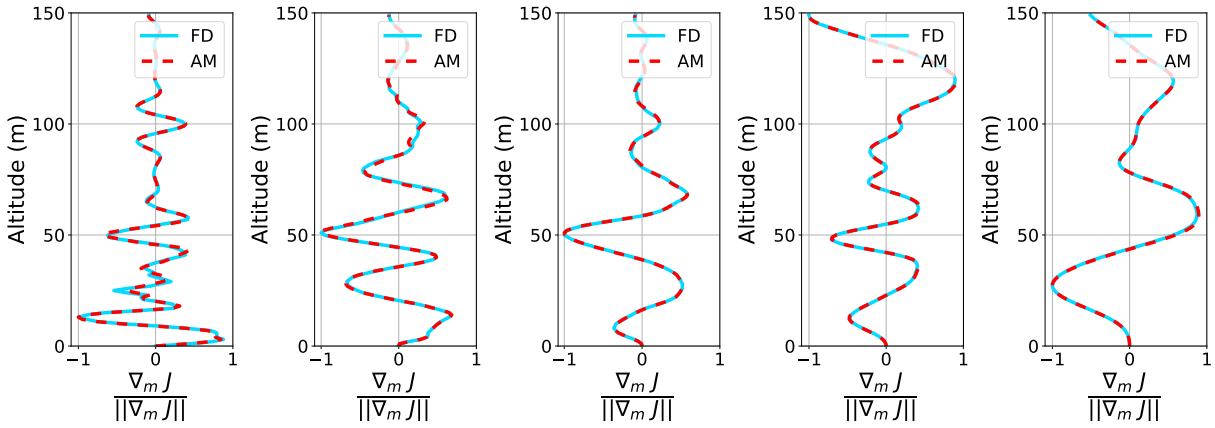

Figure 2.8: Validation of the gradient for the first descent iteration for phaseless measurement data type. Comparison of the gradient $\nabla_m J_{\mathrm{FD}}$ computed with finite differences (FD) method vs. $\nabla_m J_{\mathrm{AM}}$ computed with adjoint model (AM). (a) $R = 1$ km, (b) $R = 5$ km, (c) $R = 10$ km, (d) $R = 30$ km, (e) $R = 60$ km.

2.8.1 Results: inversion with phase information

In this section, we assume that the phase information of the complex wave field is measurable. Since no wave field information is lost and error sources are absent, the initial expectation is that the inversion routine given in Figure 2.2 should invert the objective refractivity M_{OBJ} successfully if the implementation is correct.

The distribution of the inverted parameters at each altitude point is given in Figure 2.9. The success of the inversion varies with the measurement array antenna position R. For this reason, the results are shown at different $R \in \{1, 5, 10, 30, 60\}$ km in order to observe the range-dependency progressively.

The inversion is successful in short ranges at R =1 km as shown in Figure 2.9a. We obtained good results for R <1 km and at longer ranges up to a certain critical range R_{crit} similar to that obtained at R =1 km. Beyond $R > R_{\mathrm{crit}}$ we do not have good results as shown in Figure 2.9 in the case of R=5, 10, 30 and 60 km. Not only the deterioration of the results are quite sudden when changing R from 1 to 5 km, but also M_{INV} looks further from M_{OBJ} at 5 km than at longer ranges in Figure 2.9. The dependency of the dispersion of M_{INV} looked strange and not in accord from our background knowledge from the relation between propagation range and ill-posedness of the problem, which should increase with R regularly [57]. For that reason, we wanted to analyze this transition towards worse results from 1 to 5 km in range and check if we do something wrong during the optimization. We have found out that this transition starts in the range interval between 4 km and 4.1 km in our case, as shown in Figure 2.10. The dispersion is measured with the percent relative error computed with the Euclidian norm according to (2.52):

$$\epsilon_1 = \frac{\|M_{\mathrm{OBJ}} - M_{\mathrm{INV}}\|}{\|M_{\mathrm{OBJ}}\|} \times 100. \tag{2.52}$$

The dispersions are quantified using ϵ_1 and presented in the caption of the Figure 2.10. The dispersions are found to be related to the evolution of the error functional topography rather than numerical techniques. Our analysis has shown that the dispersion in the results given in

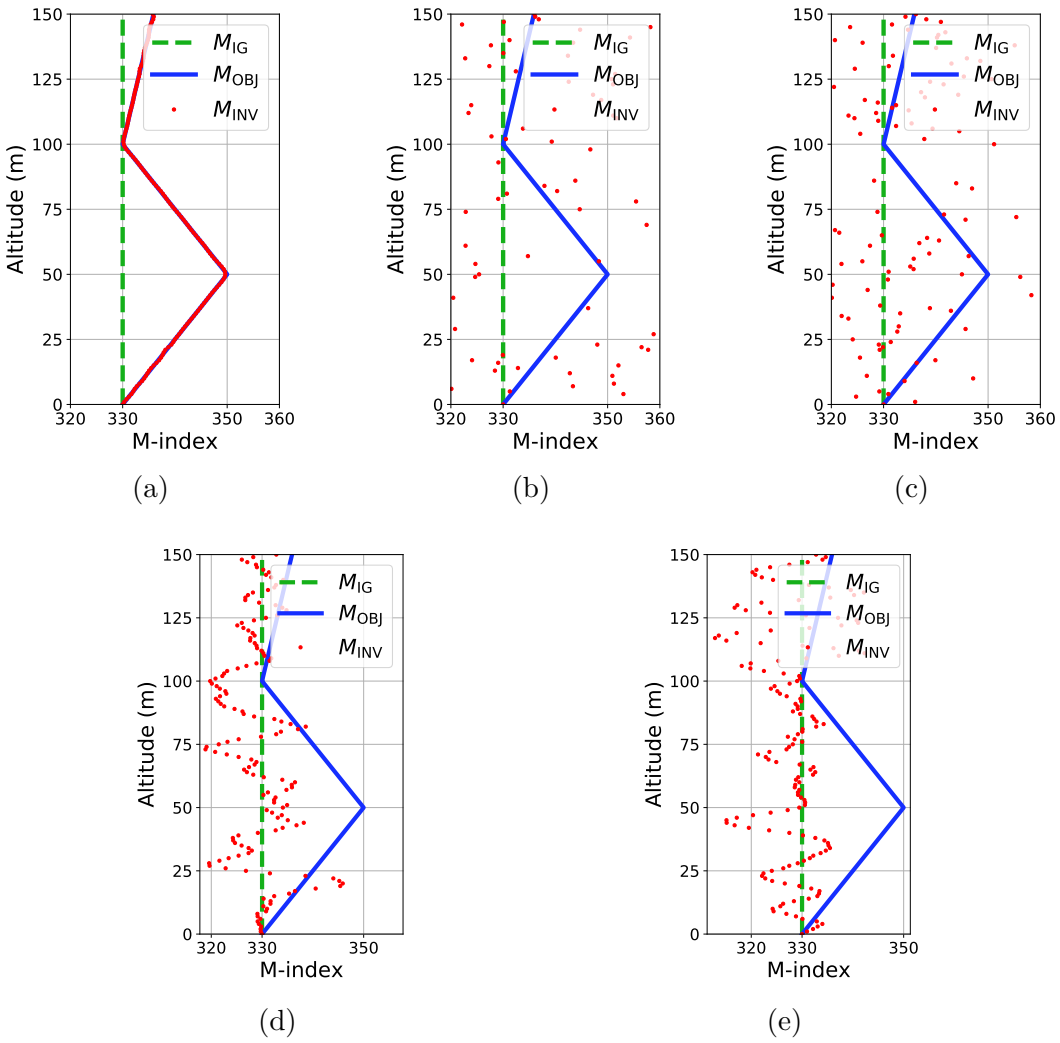

Figure 2.9: Inverted parameters from data with phase measured at different range R. (a) $R =$ 1 km, (b) $R = 5$ km, (c) $R = 10$ km, (d) $R = 30$ km, (e) $R = 60$ km.

Figure 2.10 is related to the emergence of new local minimum along the path of iterations in the parameter space. Although not shown here, we have found out that $\nabla_m J$ of the first iteration gives us an indication about the fate of inversion; we needed to be able to guess the sign of perturbation on m correctly in the direction of the function $-(M_{OBJ} - M_{IG})$. If the sign is predicted different than $-(M_{OBJ} - M_{IG})$ even if only in some part of the $\nabla_m J$ in altitude, the dispersions start. The dispersion ϵ_1 is measured as 9.9% at $R = 4.1$ km, 16.7% at $R = 5$ km, and 6.2% at $R = 10$ km. As for the reason why the dispersed M_{INV} is stacked around M_{IG} at longer ranges such as at 30 and 60 km is found to be related to the emergence of more local minima in the error functional topography which cuts the iterations path of the dispersed parameter model shorter, so the inverted parameters stay near the initial guess nicer compared to the results obtained at $R = 5$ km.

The conclusion of this study is that successful application of this approach is limited to the very short ranges in our test case, even when there is no modeling and measurement errors and the measured data do not contain noise. Also, the objective parameter is a very basic trilinear profile and the initial guess is close to the objective parameter so it is a good initial guess. In real world applications, we are going to encounter with scenarios where the true ambient profile is far more complex than that studied in our tests. Given the difficulty of the problem even in ideal

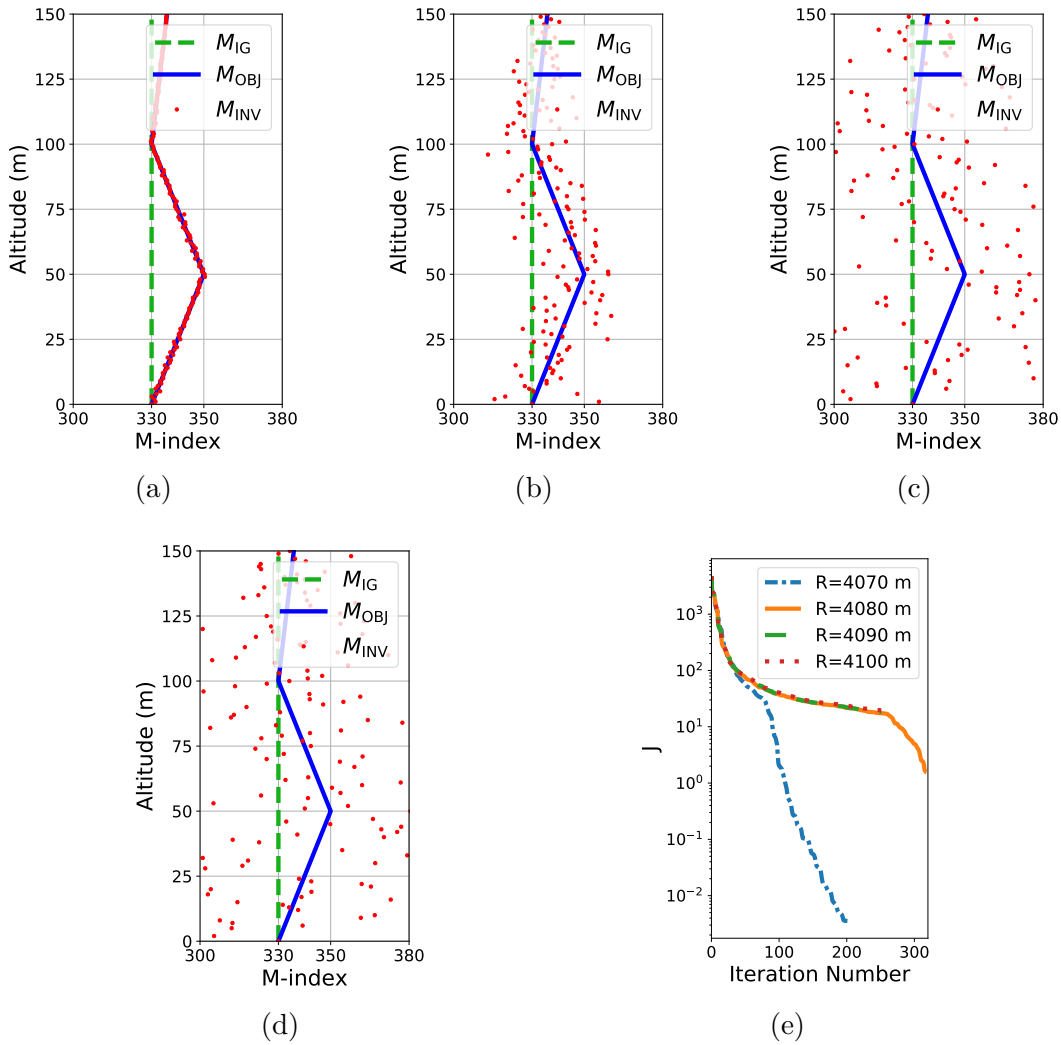

Figure 2.10: Inverted parameters from data with phase measured in the vicinity of $R = 4$ km at different range R. (a) $R = 4070$ m, (b) $R = 4080$ m, (c) $R = 4090$ m, (d) $R = 4100$ m, (e) Convergence graphs. The dispersions are characterized with $\epsilon_1 =$ (a) 0.15% , (b) 2.3% , (c) 9.6% , (d) 9.9% in parameter M.

conditions, we do not see much interest in analyzing this problem more deeply with different initial guesses and in upgrading it with techniques to stabilize the problem because we are also unsure if we could measure the phase alongside the amplitude of the wave field in reality. Also, the receiver array contains one receiver at each meter point, which may not be the case in reality.

At this point, several potential remedies can be identified right away: change of the error functional to reduce nonconvexity and local minima (change of data space, change of norm, regularization techniques), reduction of number of control parameters to invert (subspace approaches like principal component analysis or inversion in Fourier/Wavelet basis), a better initial guess (global search, historical data, numerical weather prediction, multistart techniques). The suggestions can be expanded to include windowing of the measured data or filtering of the parameter model or perturbations etc., if applicable.

In the next section, we take only the amplitude of the data into account because firstly we want to change the error functional topography which seems very difficult to work on according to the indications from the inversion results. Secondly, removal of some information in data

improved error functional topography in geophysics applications and led to improvement of the results in [124].

2.8.2 Results: inversion without phase information

The inversion routine given in Figure 2.2 is tested for its capability to retrieve M_{OBJ} from the corresponding amplitude measurement. The distribution of the inverted parameters at each altitude point is given in Figure 2.11 for different $R \in \{1, 5, 10, 30, 60\}$ km.

Similar to the results given in Section 2.8.1, success of inversion depends on R in the range interval of $1 - 60$ km. Different from the results given in the same Section 2.8.1, the inversion success at $R = 1$ km is lost with the removal of the phase from data in Figure 2.11a when compared to its counterpart with phase information in Figure 2.9a. Inversion result M_{INV} appears with limited dispersion which allows identification of the similarities between M_{INV} and M_{OBJ}. A major trilinear structure is retrieved, with slopes in the same direction as M_{OBJ} globally. The appearance of M_{INV} with leftward shift from M_{OBJ} is linked to the fact that the topography allows multimodal solutions. It is mainly the wave speed differential in the atmosphere that governs $|u|$ in the error functional (2.11). Therefore, many other refractivity profiles with a shape similar to M_{OBJ} appearing with some random shift as explained, gives $J \sim 0$ and the true solution becomes indistinguishable from other solutions. One of the multimodal solutions is retrieved in Figure 2.11a in the vicinity of M_{IG}.

At $R = 5$ and 10 km, M_{INV} can represent the true solution M_{OBJ} around M_{IG} by capturing the slope of M_{OBJ} with limited dispersion. The major trilinear synoptic structure of M_{OBJ} cannot be recognized in M_{INV} when $R > 14$ km (not plotted). For $R = 30$ and 60 km, M_{INV} stays closer to the M_{IG} for increasing R like it was in Section 2.8.1. The synoptic structure (gradient) of the objective refractivity is not retrieved in those two cases. As failure of the inversion and stocking of M_{INV} around M_{IG} are progressive with the increase of R, we conclude that (2.9) contains more local minima with R, and the local minima prevent the iterations to arrive at one of the multimodal solutions.

The conclusions are as follows. Failure to invert is not due to the proposed adjoint model. It is probably due to that the error functional topography is rough. In other words, problem (2.9) is ill-posed even without measurement, modeling and theoretical errors. Potentially, the ill-posedness could be combined with convergence issues which could be included in a future work. In the next section, we are interested in visualizing the error functional topography of the two error functionals (2.10) and (2.11), which give different results, so that the iterations can skip some local minima and can be guided towards global minimum further.

2.8.3 Results: landscapes of the cost function

There is no general technique to tackle a nonlinear inverse problem [104], [125]. Solving it requires the development of a special technique considering the characteristics of the problem.

We are asked to find the true parameters at the global minimum of an error functional. In the context of adjoint-based refractivity inversion, some of the difficulties in finding the true parameters are reported as: sensitivity to initial guess [60], loss of signal at long ranges [57], failure of some regularization techniques [58], insufficiency of measurement data [57], high-dimensionality [61]. These difficulties are commonly seen as the consequence of nonlinearity

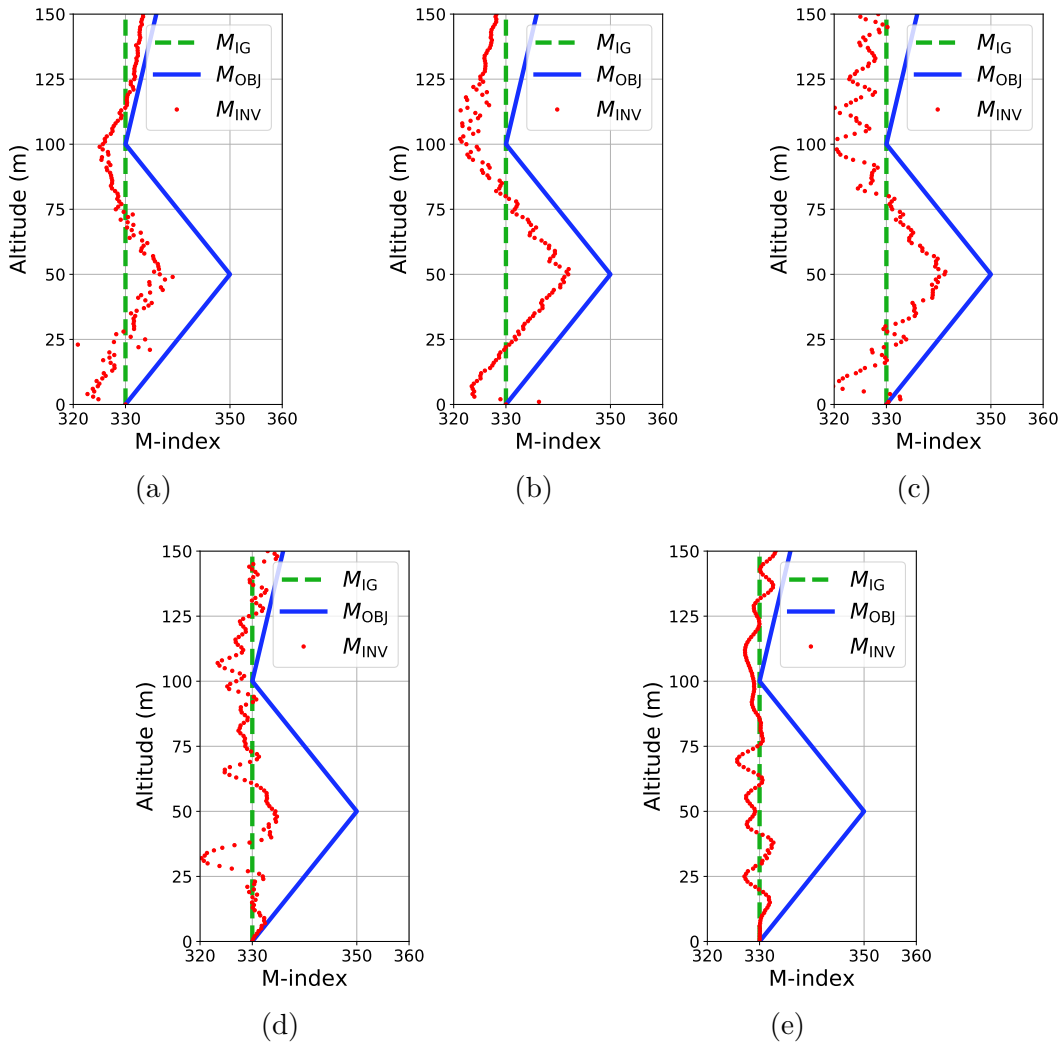

Figure 2.11: Inverted parameters from phaseless data measured at different range R. (a) $R = 1$ km, (b) $R = 5$ km, (c) $R = 10$ km, (d) $R = 30$ km, (e) $R = 60$ km.

and ill-posedness characteristics of the problem. In practice, those two characteristics reflect on the problem (2.9) as nonconvexity of the optimization landscape. Thus, the desired special technique is the one that can mitigate the nonconvexity on the landscape. For that reason, visualization of the cost function landscape can be used as a tool to analyze the difficulty and to develop the right technique for an improved refractivity inversion [103]. The optimization landscape analysis of RBT problem can be seen as an intermediate step for understanding why also RFC is still an open problem, which is more complex to analyze.

For the landscape analysis, the baseline setup described in Section 2.7.1 is considered. In this setup, the parameter model M is controlled by 151 control parameters, so visualizing the entire error functional topography is not possible. Nevertheless, visualizing several directional topographies (i.e., in certain directions in M) gives us an idea about the entire topography. While this does not necessarily reveal local minima, it demonstrates the degree of nonconvexity of the error functional around the true parameter. At this preliminary stage, such analysis gives an idea about the width of the attraction basin of the global minimum and its sensitivity to the sources of nonlinearity and ill-posedness (i.e., those listed in the previous paragraph). The analysis can reveal some strategies to guide the iterations into the attraction basin of the true

objective parameter, which is the capability of the ideal inversion technique.

In this work, we limit our analysis to three different one-dimensional optimization landscapes of the high-dimensional problem. They allow to visualize the cost function around some given solutions (the true global minimum) and some initial guess with a one-dimensional variation. Firstly, we define:

$$\begin{aligned} &\alpha \mapsto J(M_1(\alpha)),\ \alpha \in [-2, 2], \\ &\text{with } M_1(\alpha) = M_{\text{OBJ}} + \alpha(M_{\text{IG}} - M_{\text{OBJ}}). \end{aligned} \tag{2.53}$$

By varying the parameter model using M_1, we construct the cost function landscape around the objective refractivity profile. Note that $M_1 = M_{\text{OBJ}}$ at $\alpha = 0$ and $M_1 = M_{\text{IG}}$ at $\alpha = 1$. Secondly, we define:

$$\begin{aligned} &\alpha \mapsto J(M_2(\alpha)),\ \alpha \in [-2, 2], \\ &\text{with } M_2(\alpha) = M_{\text{OBJ}} + \alpha(M_{\text{STD}} - M_{\text{OBJ}}). \end{aligned} \tag{2.54}$$

where M_{STD} is the modified standard refractivity profile in the troposphere. It is the linear refractivity profile with $M(z = 0) = 330.0$ M-unit which varies with the slope of 0.118 M-unit/m in altitude. Similar to $\alpha \mapsto J(M_1(\alpha))$, by varying the parameter model using M_2, we construct the cost function landscape around the objective refractivity profile but in another direction. The interest in using M_1 and M_2 is to see the landscape between a starting parameter and the true objective parameter. Note that $M_2 = M_{\text{OBJ}}$ at $\alpha = 0$ and $M_2 = M_{\text{STD}}$ at $\alpha = 1$. Finally, we define:

$$\begin{aligned} &\alpha \mapsto J(M_3(\alpha)),\ \alpha \in [-1, 1], \\ &\text{with } M_3(\alpha) = M_{\text{IG}} + \alpha \left\| M_{\text{MAX}} - M_{\text{IG}} \right\|_\infty \frac{\nabla_m J}{\left\| \nabla_{m_0} J \right\|_\infty}, \end{aligned} \tag{2.55}$$

where $M_{\text{MAX}} = 400$ M-unit. The interval in which α varies is chosen such that the variation scans $\mathcal{M}_{\text{ad}}$ thoroughly. The landscape using the parameter model M_3 is constructed around the initial guess in the direction of the gradient. The three landscapes are plotted and commented below.

In Section 2.8.1 and 2.8.2, we have seen inaccurate inversion results although it is shown that the gradient is computed accurately in the beginning of the iterations as shown in Section 2.7.3.1 and 2.7.3.2. The invertibility clearly depends on range and the type of cost function (e.g., whether the phase is considered or not). Therefore we draw the directional cost function landscapes with respect to range $R \in \{1, 5, 10, 30, 60\}$ km for both cost functions (2.10) and (2.11).

Firstly, the landscape is computed for model M_1 using (2.53) at different ranges for measurements with and without phase and the landscapes are shown in Figure 2.12 and 2.13 respectively. Comparison of the landscapes in Figure 2.12 and 2.13 indicates less nonconvexity for a given range when the phase is removed from the data. For both cost functions, $J(M_1)$ resembles landscape of a convex nearly quadratic function at $R = 1$ km. Increase of R decreases convexity and increases number of local minima at different rates. The cost function with phase information appears to be more sensitive to increase in R while the landscape without phase looks more easily convexifiable with regularization methods in the interval $\alpha \in [0, 1]$, with wider attraction basin around $\alpha = 0$. Lastly, we note that the landscape is rather flat at $R = 1$ km without phase (Figure 2.13a) but the quasiconvexity is maintained until $R = 10$ km in the interval $\alpha \in [0, 1]$ (Figure 2.13c) unlike when the phase is included (Figure 2.12c). Let us now check if the comments made with these landscapes are valid for other directions as well.

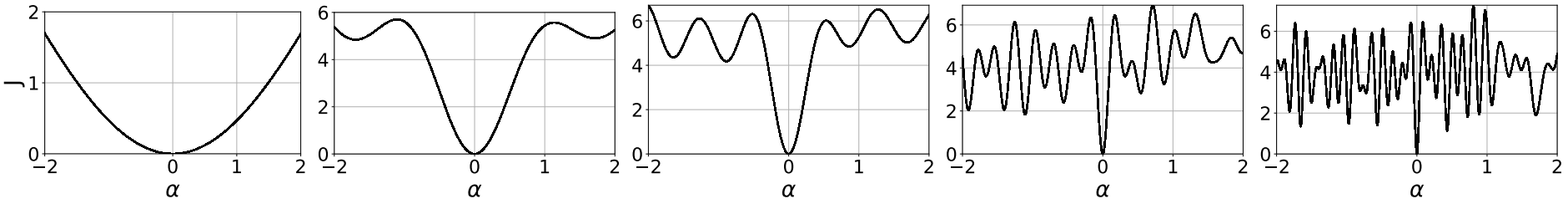

Figure 2.12: Obtained landscape for the function $\alpha \to J(M_1(\alpha))$ at different range R, see (2.53). The phase is measurable. (a) $R = 1$ km, (b) $R = 5$ km, (c) $R = 10$ km, (d) $R = 30$ km, (e) $R = 60$ km.

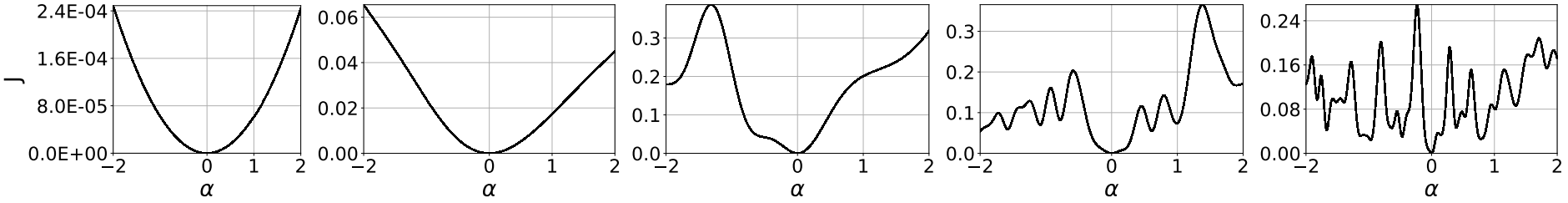

Figure 2.13: Obtained landscape for the function $\alpha \to J(M_1(\alpha))$ at different range R, see (2.53). The phase is not measurable. (a) $R = 1$ km, (b) $R = 5$ km, (c) $R = 10$ km, (d) $R = 30$ km, (e) $R = 60$ km.

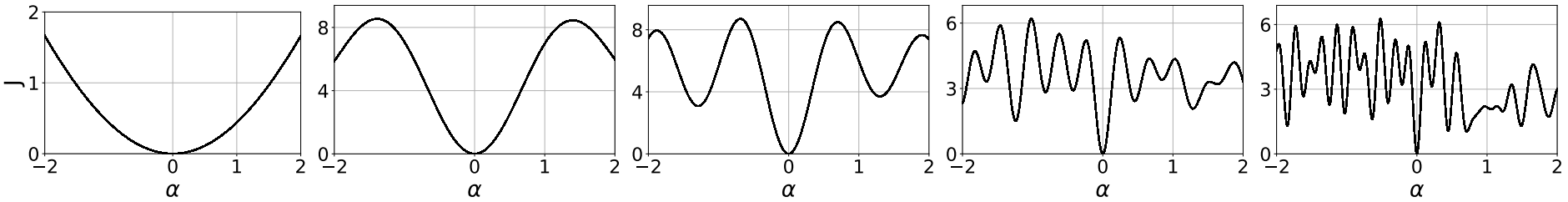

Figure 2.14: Obtained landscape for the function $\alpha \to J(M_2(\alpha))$ at different range R, see (2.54). The phase is measurable. (a) $R = 1$ km, (b) $R = 5$ km, (c) $R = 10$ km, (d) $R = 30$ km, (e) $R = 60$ km.

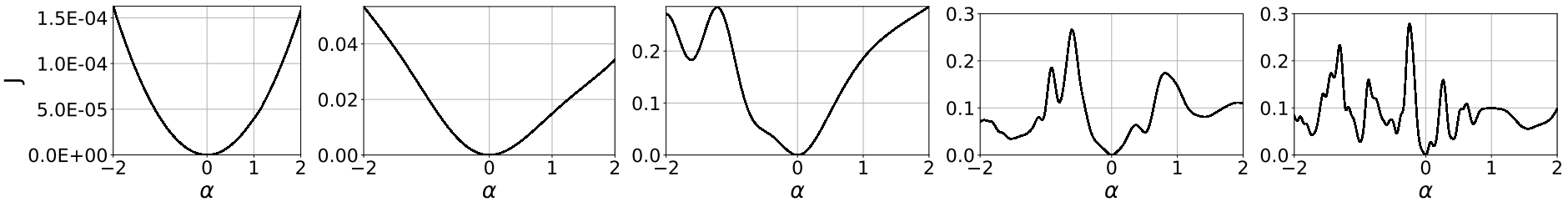

Figure 2.15: Obtained landscape for the function $\alpha \to J(M_2(\alpha))$ at different range R, see (2.54). The phase is not measurable. (a) $R = 1$ km, (b) $R = 5$ km, (c) $R = 10$ km, (d) $R = 30$ km, (e) $R = 60$ km.

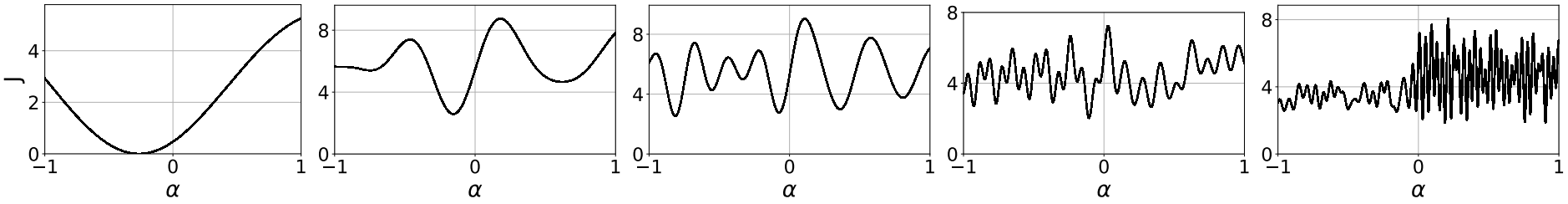

(a) (b) (c) (d) (e)

Figure 2.16: Obtained landscape for the function $\alpha \to J(M_3(\alpha))$ at different range R, see (2.55). The phase is measurable. (a) $R = 1$ km, (b) $R = 5$ km, (c) $R = 10$ km, (d) $R = 30$ km, (e) $R = 60$ km.

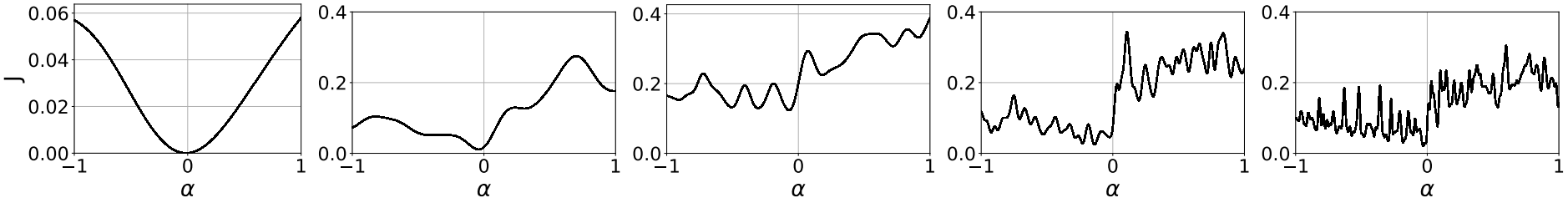

(a) (b) (c) (d) (e)

Figure 2.17: Obtained landscape for the function $\alpha \to J(M_3(\alpha))$ at different range R, see (2.55). The phase is not measurable. (a) $R = 1$ km, (b) $R = 5$ km, (c) $R = 10$ km, (d) $R = 30$ km, (e) $R = 60$ km.

Secondly, the landscape is computed for model M_2 using (2.54) and presented in Figure 2.14 and 2.15. All the comments made for M_1 are also valid for M_2. However, the landscapes cannot explain few questions such as why the inversion at $R = 5$ km fail with complex data, which multimodal solutions appear with the removal of phase from data, why M_{INV} is further from M_{IG} at long ranges with complex data although the attraction basins appear narrower than that of phaseless data. When questioning the coherence between the landscapes and the inversion results, attention must be paid to the dimension of the parameter model. There are infinitely many 1-D line cuts in 151-D hypercube and indications of nonlinearity and ill-posedness can be hidden at some other line cuts.

The analysis is enriched with the landscape drawn at the direction of the gradient according to (2.55) as given in Figure 2.16 and 2.17. Note that M_{IG} is located at $\alpha = 0$ on this landscape. The functional (2.9) has more local minima on this 1-D view with the inclusion of the phase in data. Again, it is more difficult to invert at long ranges because the optimization landscape becomes more nonconvex. In the next section, we expand our analysis with inversion tests by using different initial guesses.

2.8.4 Results: impact of initial guess

When a nonlinear least squares problem is solved using gradient based methods, the standard question is about whether there is local minima in the error functional topography of the admissible parameter set. Until this section, the analysis has assumed that the optimization is reasonably well done and the failure to find the global minimum is because of the local minima in the error function topography. If this statement is true, one expects that increasingly-better initial guesses improve the inversions progressively by diminishing the undesirable effects of nonlinearity and ill-posedness. In that context, the aim of this section is to investigate if we can observe the predicted improvement with different initial guesses and if the conclusions made in the previous section are reasonable for other initial guesses as well. This preliminary investigation is limited to the use of phaseless data at $R = 10$ km.

In Figure 2.18, we present the inverted parameters in altitude for increasingly better initial guesses. The inversion improves progressively when M_{IG} is set closer to M_{OBJ} progressively. In Figure 2.18b, we observe essentially similar inversion result to that in Figure 2.11c but with a shift towards M_{OBJ}. This shift of M_{INV} is towards M_{OBJ} consistently with the shift of M_{IG} towards M_{OBJ}, M_{INV} exhibits further self-regularization and the refractivity gradient information is retrieved more smoothly. This numerical evidence not only give confidence about the stability of the inversion but also supports the idea about the existence of multimodal solutions.

Next, we are motivated to investigate the existence of multimodal solutions because if so, we can explore the search space more efficiently and we can exploit this knowledge when developing the inversion technique. Among many possibilities, two ways of collecting the numerical evidence about multimodality are considered. Firstly, if there is multimodality as far as the gradient of the parameters is concerned, shifting the initial guess while preserving its synoptic structure would change the synoptic structure of the inversion results negligibly. In Figure 2.19, we show that such multimodality exists; synoptic structure (gradient information) of M_{INV} mainly depends on the synoptic structure of M_{IG} and M_{OBJ} pair. The difference of the inversion results is measured using (2.56):

$$\epsilon_2 = \frac{\|(M_{\text{INV}} - \text{mean}\{M_{\text{INV}}\}) - (M_{\text{INV,REF}} - \text{mean}\{M_{\text{INV,REF}}\})\|}{\|M_{\text{INV,REF}} - \text{mean}\{M_{\text{INV,REF}}\}\|} \times 100, \tag{2.56}$$

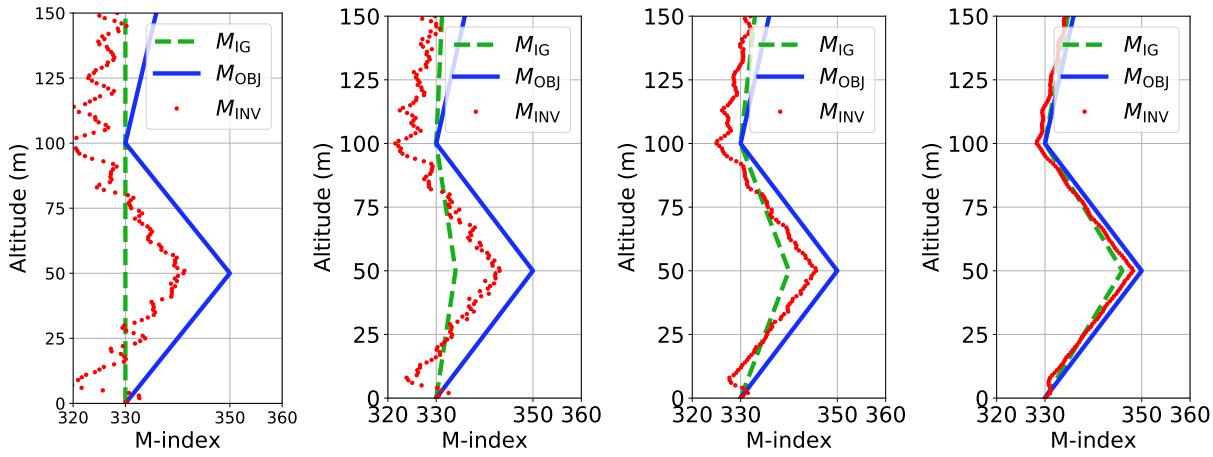

Figure 2.18: Inversion at $R = 10$ km for three improved initial guesses.

where the difference is taken between the inversion result of an initial guess and the reference inversion result $M_{\text{INV,REF}}$ obtained for the initial guess $M_{\text{IG}} = 330$ M-unit using Euclidean norm. According to the measure (2.56), the results obtained for $M_{\text{IG}} = 290$ M-unit and $M_{\text{IG}} = 370$ M-unit differs from the result obtained for $M_{\text{IG}} = 330$ M-unit by 1.6% and 3.7%, respectively.

In another example in Figure 2.20, we show once more that the synoptic structure (gradient) of the inversion result mostly depends on the synoptic structure of the objective parameter and the initial guess. These observations might lead to important conclusions to help us to explore the search space efficiently. Firstly, we know that local minima exist in the error functional topography and solutions depend on the initial guess. Secondly, the radar coverage depends on the vertical gradient information of the ambient refractivity (the synoptic structure) more than what value the ambient refractivity has at each altitude point[5]. Then we can explore the search space efficiently by considering only one initial guess from the family of the admissible initial guesses with the same synoptic structure. Increasing or decreasing the values of refractivity on the same initial guess profile by the same amount at all altitude points does not change the synoptic structure of the inversion results and the predicted radar coverage. Based on that, we explore the dependency of the objective parameter to a linear initial guess profile by only changing the slope of the linear profile in Figure 2.21. Ducting conditions as an initial guess can be a good initial guess to resolve parameter of a ducting condition but the guess should not be far from the objective parameter (Figure 2.21b vs. Figure 2.21a). Upward refracting initial guesses in Figure 2.21c and Figure 2.21d are not good initial guesses to invert the synoptic structure of this objective ducting condition.

2.8.5 Results: noise impact and robustness test

It is necessary to show that the inversions are robust to noise (see 2.4.2 for details). The motivation is to see if the conclusions made without noise are reasonable in the presence of perturbations on data. If our system is robust, it should be insensitive to small perturbations or precision errors on data; this increases confidence in the inversion results. Robustness test is performed at $R = 10$ km with different levels of noise τ on measurements according to (2.14).

[5]We will elaborate more on that aspect in Chapter 3.

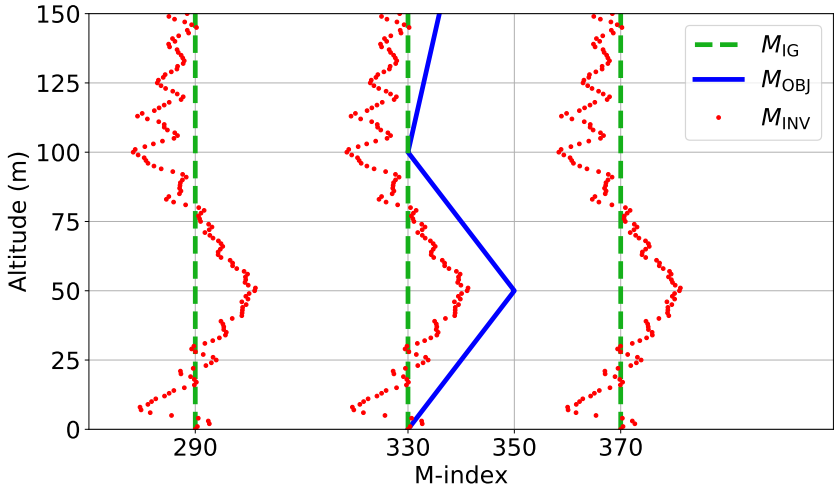

Figure 2.19: Inversion at $R = 10$ km for different constant initial guesses $M_{IG} = \{290, 330, 370\}$ M-unit. Difference between the inversions are $\epsilon_{2_{290}} = 1.6\%$, $\epsilon_{2_{370}} = 3.7\%$ with respect to reference inversion result for $M_{IG} = 330$ M-unit.

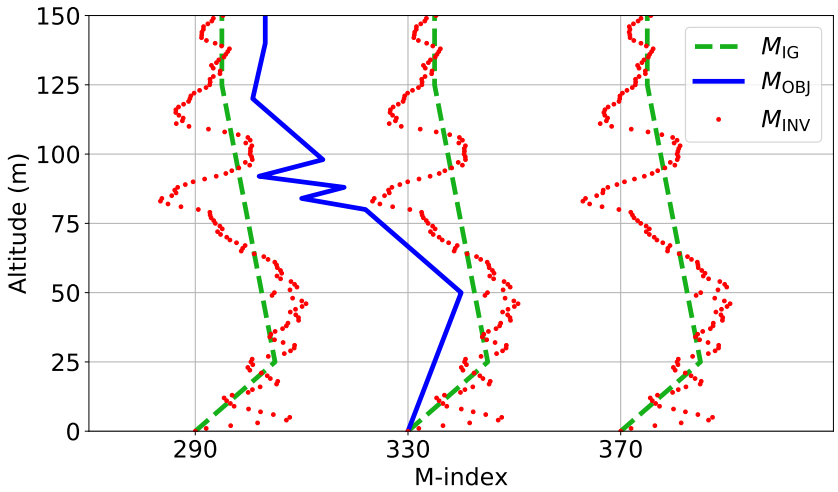

Figure 2.20: Inversion at $R = 10$ km for different initial guesses with the same rate of increase with altitude. Difference between the inversions are $\epsilon_{M_{IG}(0)=290} = 6\%$, $\epsilon_{M_{IG}(0)=370} = 4.7\%$ with respect to reference inversion result for $M_{IG}(0) = 330$ M-unit.

In Figure 2.22, we present the inverted parameters in altitude for different noise level τ at $R = 10$ km. The inversions naturally become more dispersed with the addition of noise on measurement data. The mean of the inversions seems to follow $M_{INV}|_{\tau=0}$ which is in Figure 2.18c but dispersion of the parameters grows with τ.

We change the initial guess and perform the same test in Figure 2.23. The inversion result become more sensitive to noise as because the initial guess is placed further from the objective parameter as compared to Figure 2.22.

The conclusion is that the inversion is resilient to higher level of perturbation on data if the initial guess is better, in the sense that the gradient of M_{OBJ} can be captured. The inversion deviates progressively from the attraction basin of $M_{INV}|_{\tau=0}$ as τ increases.

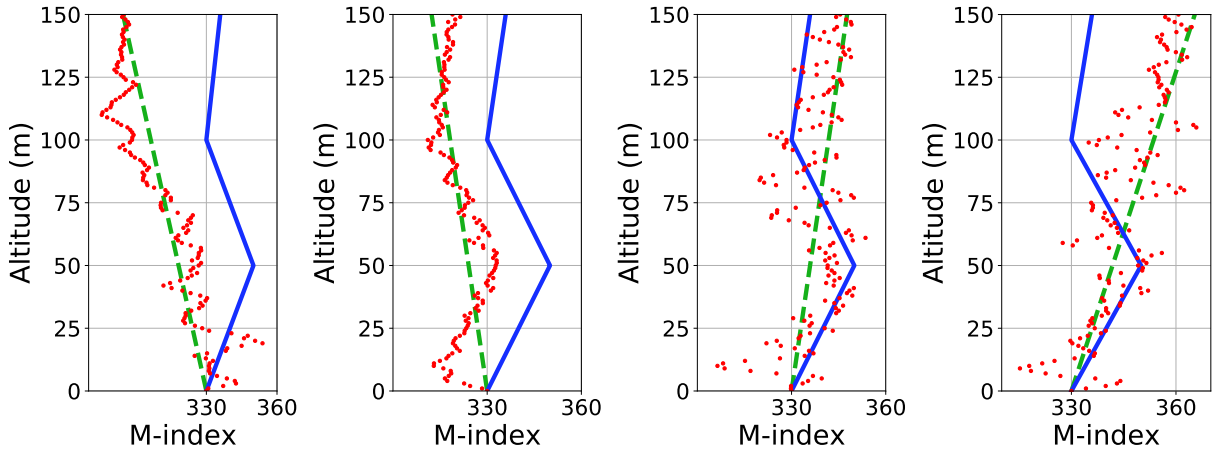

(a) (b) (c) (d)

Figure 2.21: Inversion at $R = 10$ km for four different initial guesses. Blue curve: M_{OBJ}, red dots: M_{INV}, green dashed curve: M_{IG}.

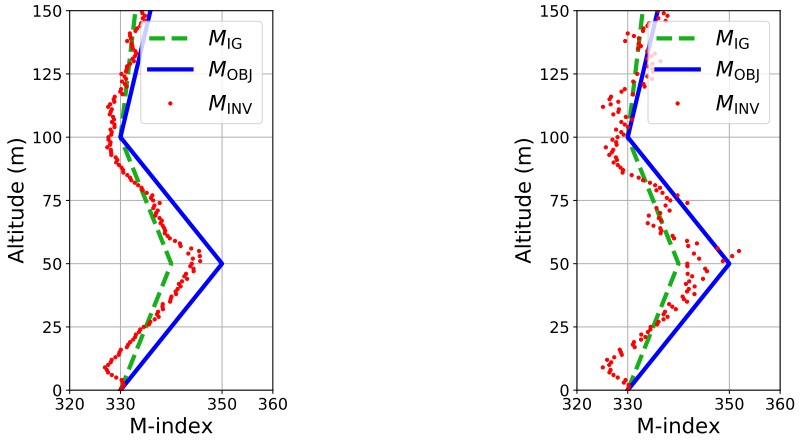

(a) $\tau = 10\%$ (b) $\tau = 50\%$

Figure 2.22: Robustness at different noise level τ at $R = 10$ km for the trilinear initial guess.

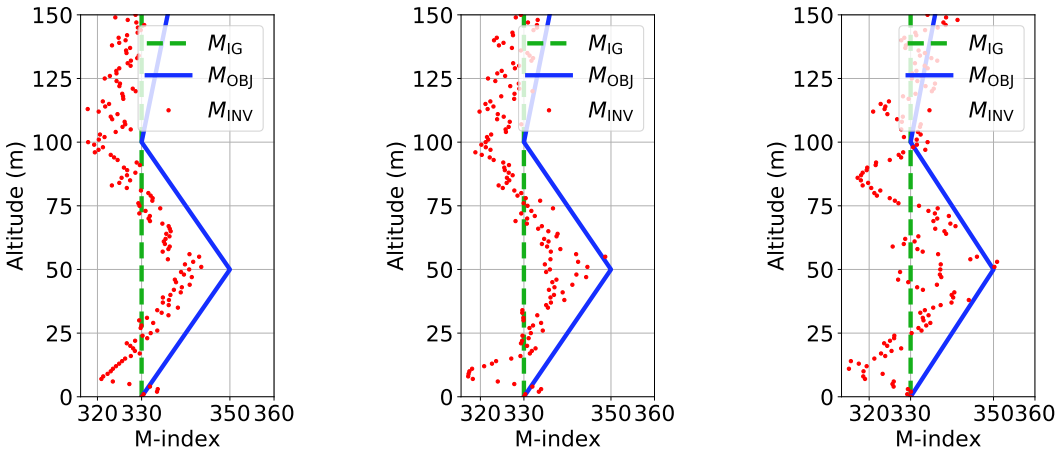

(a) $\tau = 1\%$ (b) $\tau = 10\%$ (c) $\tau = 50\%$

Figure 2.23: Robustness at different noise level τ at $R = 10$ km for the uniform initial guess.

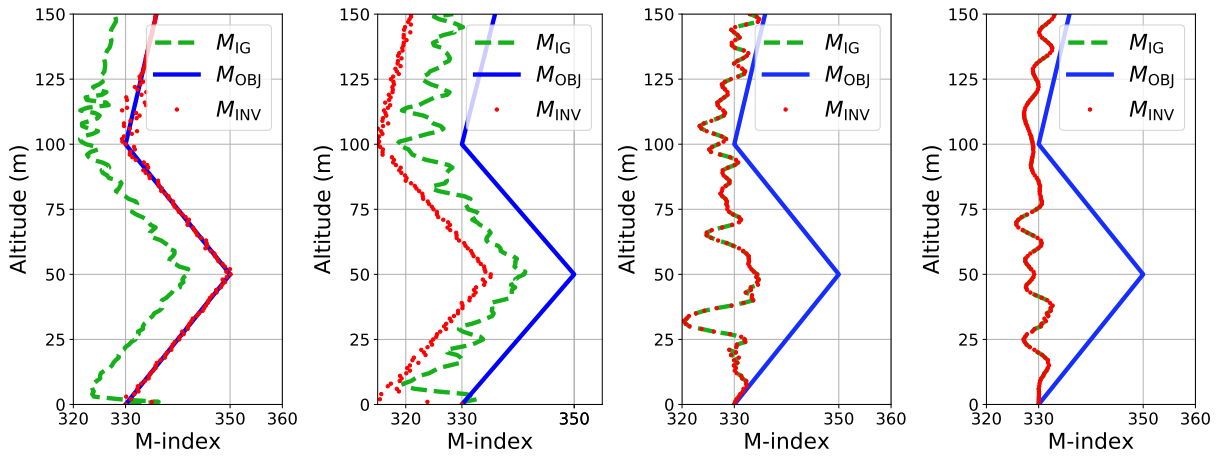

Figure 2.24: Inverted parameters from data with phase measured at different range R. Initial guesses M_{IG} comes from M_{INV} obtained from phaseless data measured at the corresponding R, which are displayed in Figure 2.11. (a) $R = 5$ km, (b) $R = 10$ km, (c) $R = 30$ km, (d) $R = 60$ km.

2.8.6 Results: a preliminary inversion strategy

In this section, we try to improve our inversion results coming from the inversion of phaseless data by adding the phase content to the inversion and use phaseless data inversion results as the initial guess. We will again work on the baseline inversion test setup described with the objective and the initial guess parameters in Figure 2.4a.

We know that the solution of (2.10), which includes phase information in the cost function, does not give good results for the range beyond 5 km as shown in Figure 2.9 and the results are good only at 1 km in that same Figure. However, we can retrieve the synoptic structure (the gradient information) of the objective parameter when we remove the phase information from the data (i.e., by solving (2.11)) at 5 and 10 km as shown in Figure 2.11. However, the synoptic structures are not retrieved without dispersion and shift from the objective parameter. We also know about the existence of multimodal solutions on the error functional topography. Then, can we improve the inversion results obtained from the inversion of phaseless data by using them as initial guess of the problem (2.10)?

In other words, we incorporate the phase information at the second step of inversion and expect some improvement on the results. The prediction with the phase removal can be used as an initial guess of the full inverse problem with complex data type. In this section, we check if the inversion results improve with such strategy and if yes, to what extent this strategy is favorable.

The inversion results of this strategy is given in Figure 2.24. The results improve considerably with the inclusion of the phase information to refine the results, at 5 and 10 km in Figure 2.24a and 2.24b as compared to the direct inversion with full wave field data in Figure 2.9b and 2.9c. We do not observe improvement at longer ranges in Figure 2.24c and Figure 2.24d. The reason is probably that local minima of the two different error functional topographies of (2.10) and (2.11) coincide at those ranges. Still, if the phase can be measured, this information has the potential to be exploited for amelioration of the inversion results. In our example scenario, the results got better than the case of phaseless data at 5 and 10 km ranges.

2.9 Conclusion

In this section we made theoretical analysis, validation and numerical experiments with plane wave as the source. Those results should be considered as part of a preliminary analysis for validation and demonstration of the features of the problem. We will focus more on the problem and increase the range of success beyond 10 km in Chapter 3 in more realistic setup with point source and more complex objective parameter profiles. Nevertheless, the analyze and concepts which are mentioned in this chapter will be recalled when developing the proper solution technique in the next chapter.

This chapter presents our preliminary attempts to predict the ambient refractive index in the troposphere. The goal is to provide real-time situational awareness for modern seaborne and airborne electromagnetic emitters under anomalous propagation conditions. The adjoint method properly addresses the high-dimensionality of the refractivity inversion for such modern detection systems and it is the backbone method on which our inversion strategy will be built. For this reason, we focused more on its validation in this Chapter, which is a classical compulsory step during the development of the inversion algorithm. We still tried to reveal the difficulties in this problem so as to cure them properly in the next study.

We attach importance to upgrade the forward model to tighten the control on inversion accuracy for this ill-posed inverse problem in real-world scenarios. Despite being hypothetical for the implications, we advocate the use of the wide-angle approximation of the parabolic equation for adjoint-based refractivity inversions because the method is available at no additional cost when compared to that of NAPE. In this paper, we show how to derive the adjoint WAPE, explain how to construct the adjoint code, and validate the adjoint model by using a finite-difference approach. Thanks to the validation of the gradient, we are sure that it is the ill-posedness of the regarded inverse problem that leads to failure of inversion. We explain this failure with nonconvexity of directional cost function landscapes and high-dimensionality of the problem. Since the gradient-based method which we use is prone to be attracted to local minimum during iterations, the increasing sensitivity to initial guess with range can be inferred from the cost function landscape. This latter is seen to lose convexity with distance, as the problem contains more local minima.

The parameter study shows the potential use of this method as a refractivity gradient retrieval system. In this study, we have obtained acceptable results until around 10 km range using phaseless data but it can be improved with the use of phase information in a suitable strategy. We have also verified the validity of our assessments using different initial guesses. The ducting initial conditions are found to work better as initial guesses for the regarded objective refractivity profile. The proposed method is shown to be robust for small Gaussian perturbations in the measurements.

More detailed analyses are necessary to assess the performance prediction quality of the emitters. Nevertheless, it is a good sign to be able to retrieve the synoptic structure of the objective parameter with our validated basic strategy. We have to note that the problem is expectedly more ill-posed in real world scenarios due to measurement and modeling errors. Our next step will be to investigate multiscaling strategies in Chapter 3 to deal with inversion at long-distance and more realistic high-dimensional scenarios.

2.10 Acknowledgments

A part of this chapter was published in the following work:

- U. Karabaş, Y. Diouane, and R. Douvenot, "On the use of adjoint methods for refractivity estimation in the troposphere," in *Proceedings of the 14th European Conference on Antennas and Propagation (EuCAP)*, Mar. 2020, pp. 1–5.
  DOI: 10.23919/EuCAP48036.2020.9135287
- U. Karabaş, Y. Diouane, and R. Douvenot,"A variational adjoint approach on wide-angle parabolic equation for refractivity inversion," *IEEE Transactions on Antennas and Propagation*, vol. 69, no. 8, pp. 4861– 4870, Aug. 2021.
  DOI: 10.1109/TAP.2021.3060073

This chapter is a revision and an extension of that work.

Chapter 3

Multiscale Strategies for Refractivity Inversion

Contents

Synthèse – Dans le Chapitre 2, les caractéristiques du problème ont été exposées et la validation a été effectuée en utilisant une source d'ondes quasi-planes pour éclairer l'atmosphère. L'utilisation d'une source ponctuelle réaliste rend l'inversion de la réfractivité plus difficile. En outre, les profils de réfractivité réalistes ne ressemblent pas au modèle trilinéaire simple utilisé au Chapitre 2. De plus, les données réalistes sont rares et contiennent du bruit, et on s'attend à ce qu'elles soient sans phase, sans compter les erreurs de modélisation théorique et numérique dans la réalité. Pour ces raisons au moins, nous ne nous attendons pas à pouvoir récupérer la structure synoptique du profil de réfractivité de donnés réelles aussi bien qu'à partir de données synthétiques. Avant de tester l'algorithme sur des données réelles, et afin de garantir sa précision, nous devons vérifier que nous pouvons obtenir des résultats d'inversion parfaits dans des scénarios en grande dimension en inversant des données synthétiques dans des conditions idéales.

Dans ce chapitre, nous explorons les avantages de la combinaison de la méthode adjointe avec la paramétrisation multi-échelle pour l'inversion de la réfractivité troposphérique. Notre priorité est d'atténuer la difficulté de l'inversion. Nous voulons également améliorer la précision de l'inversion dans le cas général c'est à dire sans prendre en compte, autant que possible, des informations spécifiques liées au cas étudié. Nous avons appliqué l'approche multi-échelle aux données ainsi qu'à la paramétrisation.

Nous proposons certaines modifications des formulations standard basées sur les adjoints obtenues au Chapitre 2 afin de réduire l'espace de recherche et l'espace de données dans notre stratégie multi-échelle. Dans cette étude, nous utilisons une stratégie de raffinement progressif dans la paramétrisation en synchronisation avec les données. À cette fin, la réduction de l'espace de recherche peut être obtenue en appliquant simplement un opérateur de restriction sur le gradient obtenu à l'aide du modèle adjoint standard, comme indiqué dans (3.9). La réduction de l'espace de données peut être obtenue en modifiant la fonction de coût et la condition initiale du problème adjoint comme décrit dans la Section 3.3.3.2. La validité de ces modifications est démontrée en vérifiant la précision du gradient dans la Section 3.5 comme cela est fait dans le Chapitre précédent.

Ensuite, nous essayons d'inverser des profils de réfractivité plus réalistes présentés dans la Figure 3.6. Plusieurs profils sont inversés à partir de données sans phase mesurées à une distance de 10 km de la source radar en utilisant la technique de paramétrisation multi-échelle décrite dans la Section 3.6.1. Nous améliorons l'efficacité du processus d'inversion en restreignant uniquement les perturbations sur le paramètre en appliquant (3.12). Pour certains profils que nous étudions, nous sommes capables de récupérer la structure synoptique du profil à une distance de 30 km. En incorporant la technique de réduction des données à la technique multi-échelle appliquée sur le paramètre, certains cas qui n'étaient pas inversibles deviennent inversibles à 30 et 40 km de distance.

3.1 Introduction

In Chapter 2, the features of the problem have been exposed and the validation has been performed using a quasi-plane wave source to illuminate the atmosphere. Use of realistic point source makes refractivity inversion more difficult. In addition, realistic refractivity profiles do not resemble the simple trilinear model used in Chapter 2. Furthermore, realistic data are sparse and contain noise and are expected to be phaseless. Finally, theoretical and numerical modeling errors are expected in reality. For at least these reasons, we do not expect to be able to recover the synoptic structure of the refractivity profile from real data as quality as from synthetic data. Before testing our algorithm on real data and guarantee its accuracy, we have to check we want to obtain perfect inversion results in high-dimensional scenarios with the *inverse crime*. In this chapter, we would like to approach towards realistic scenarios step by step to reveal the invertibility phenomenon and to justify the upgrades to the basic inversion technique described in Chapter 2.

This chapter mainly shows the benefits of blending the adjoint method with multiscale parametrization for tropospheric refractivity inversion. One motivation is to improve the accuracy of inversion in the general case, which means without penalizing the problem with case-specific *a priori* information as much as possible. Another motivation is to search the parameter space more efficiently in order to accelerate the inversions. At the same time, we want to mitigate

the nonlinearity of the inverse problem. In addition, we want to be able to invert any possible vertical refractivity profile without being limited with our choice of the parametrization. These points are clarified in appropriate sections with examples during the following analysis.

The main point of the multiscale parametrization technique (MPT) in our context is to make the gradient-based optimization method give result as if it is a global one on a nonconvex optimization topography [126]. Different from the mainstream global optimization methods, MPT benefits from the analytical gradient which can be imported from the previous chapter, thereby it is not only efficient but also free from tedious derivations. Secondly, MPT is independent of the forward model, the parameter model and the measurement function. Thus, the technique can be directly transferred to future clutter inversions. Additionally, this technique retrieves the details of the refractivity distribution progressively from large to smaller scales by dividing the original problem into subproblems solved in an order. Therefore, the computations can be terminated at a desired resolution level in order to use the computing resources efficiently. These aspects of the technique are highlighted in the case studies.

We have applied the multiscaling to data as well as in parametrization. We have called the studied problem as Multiscale Adjoint-based Tomography (MAT) problem in the sense that multiscale strategies are employed efficiently by manipulating the cost function and gradient using the adjoint method, and the refractivity estimation problem is solved in the tomography setup described in Chapter 2. The proposed formulation for multiscale adjoint tomography is validated and is confronted to numerical tests like in Chapter 2, that is, mainly when the phase is not measured.

We observe that the multiscale strategies mitigate the dependence on the initial guess (nonlinearity) and cures the curse of dimensionality (ill-posedness) and do that without requiring additional penalty functions. Therefore the solutions are not biased towards *a priori* information employed in the penalization of the cost function. But of course, we incorporate some *a priori* knowledge with the choice of multiscale basis in our strategy. However, our *a priori* knowledge is independent of the studied scenario. It is very general and it definitely does not come from background information historical data or numerical weather prediction. We rely on this assumption: the major refractivity structures in the propagation model govern the major wave field structures in the data, and so does the minor details in the parameter to the minor details in the data. Incorporation of this knowledge in MPT is much different from many mainstream methods of regularization used in RFC community. We do not penalize the results with a background *a priori* refractivity model or measurements, do not impose regularity on the variations in wave field etc. which depends on the quality of empirical knowledge about the ambient conditions which we already do not know well in detail.

3.2 Background

The inverse problem is driven by the simulations of Parabolic Wave Equation (PWE). Initial RFC techniques have required lots of PWE simulations, so their scope has been limited to the problems with small parameter dimension [55]. Since the work [57], high-dimensional RFC problems are solved efficiently using the adjoint state method. The adjoint-based RFC techniques have been studied in the last decade commonly relying on regularization with penalty functions [61].

Let us recall that the inversion of refractive index in PWE is a complex nonlinear ill-posed problem which contains many local minima in the error functional topography. Therefore, there

are many candidate solutions from which the true solution should be distinguished because the solution cannot be identified uniquely in most practical cases. In order to achieve this, it is necessary to constraint the problem by incorporating additional *a priori* information to the inversion process. Accordingly, regularization and space reduction techniques have been used in RFC systems. The advantage of these technique is that the idea works and many non-physical local minima can be avoided during gradient-based optimization iterations. On the other hand, the success of these technique depends on *a priori* information. For example, performing a principal component analysis and using the most dominant few eigenvectors to cure the curse of dimensionality in RFC or RBT would work well if the training realizations are done in the conditions comparable to the true ambient conditions that we try to invert. Otherwise, we might lose accuracy in results. Another drawback is that we may not always have quality *a priori* information to choose a regularization technique and construct a reduction basis so that we can obtain results near the global minimum. Nevertheless, such techniques are used successfully in RFC [62], [127]. But in this thesis, we do not have access to real world data and the experience with real world scenarios, so we seek for a technique that can be justified for the general case and that is applicable in all scenarios in our context.

Different from the previous work in our community, we are interested in exploring the advantages of using multiscale strategies in refractivity inversion problems. This choice is motivated by the contribution of multiscale strategies in recent progress in acoustic full-waveform inverse problem in geophysics (e.g., [80]–[82], [124], [128]). The objective of this chapter is to investigate the potential of multiscale strategies to mitigate the nonlinearity of the tomography problem, prior to application of regularization techniques through penalization of the cost function [84], [128]. The proposed techniques are validated numerically and the improvement is shown via the application of the technique in a hierarchical refinement strategy during the inversion tests.

The problem is formulated in Section 3.3. The computational setup is described in Section 3.4. The derivations of the techniques are validated in Section 3.5. The advantages and limitations of the techniques are presented with inversion results in Section 3.6.

3.3 Modeling

We study the problem of inferring the atmosphere from wave field measurements obtained in the bistatic configuration illustrated in Figure 3.1, which is called here the tomography problem. The recipe to construct the adjoint algorithm from a given PWE algorithm has been explained in Chapter 2. In this chapter, we focus on how to upgrade the standard adjoint-based algorithm using MPT and how to build the proper multiscale strategy.

The idea of search space reduction is presented and the need for multiscaling is justified with quantitative examples. The multiscale parametrization is introduced. We explain how to make use of the standard adjoint solver to estimate the gradient with respect to the multiscale parametrization. The presented MPT formulation appears independent of the problem and therefore the technique is completely transferable to other problems like RFC. This is what motivates continuing with the tomography problem since efforts are not wasted when passing to the RFC. Later we extended reduction technique and the multiscale strategy to data.

In this section, we first remind what the standard RBT problem has been. Later, we explain the search space reduction and data space reduction techniques, and show how we can make use of the standard problem to obtain the subproblems with reductions. Then we explain how

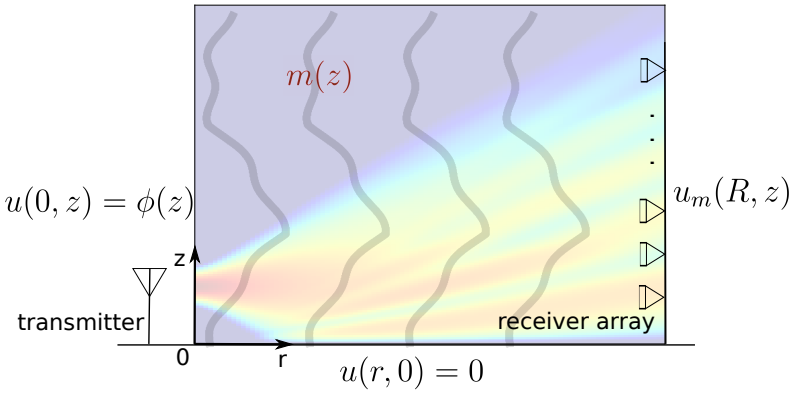

Figure 3.1: Scheme of the bistatic configuration. Initial field $\phi(z)$ propagates rightward in horizontally stratified atmosphere, which is characterized with refractivity $m(z)$. Our goal is to retrieve $m(z)$ from wave field measurements obtained with receiver array at distance R from the known source.

to use the subproblems to solve the original problem in a hierarchy thanks to using multiscale approaches.

3.3.1 Standard Adjoint-based Tomography

We are interested in the estimation of the refractivity coefficient $m(z)$ of the wide-angle parabolic wave equation given below [16], [106]:

$$\partial_r u + j\left[k_0(m(z)-1) + \left(\sqrt{k_0^2+\partial_z^2} - k_0\right)\right]u = 0, \tag{3.1a}$$

$$u(0,z) = \phi(z), \tag{3.1b}$$

$$u(r,0) = 0. \tag{3.1c}$$

Estimation from phaseless data When we do not have access to the phase of the complex function u during measurements, the inverse problem is formulated as:

$$\min_{m\in\mathcal{M}_{\text{ad}}} J(m) = \min_{m\in\mathcal{M}_{\text{ad}}} \frac{1}{2}\int_0^Z \left||u_m^{\text{sim}}(R,z)|^2 - d^{\text{obs}}\right|^2 dz. \tag{3.2}$$

where d^{obs} is the synthetically generated measurement function. The gradient of the cost function $J(m)$ with respect to control parameter m is given as:

$$\nabla_m J = \Re\left\{jk_0\int_0^R w_m(r,z)\overline{u_m(r,z)}\,dr\right\}. \tag{3.3}$$

Here, the function $w_m(r,z)\in\mathbb{C}$ is the solution of the following equation:

$$\partial_r w_m + j\left[k_0(m-1) + \left(\sqrt{k_0^2+\partial_z^2} - k_0\right)\right]w_m = 0, \tag{3.4a}$$

$$w_m(R,z) = 2\left(|u_m(R,z)|^2 - |u^{\text{obs}}(R,z)|^2\right)u_m(R,z), \tag{3.4b}$$

$$w_m(r,0) = 0. \tag{3.4c}$$

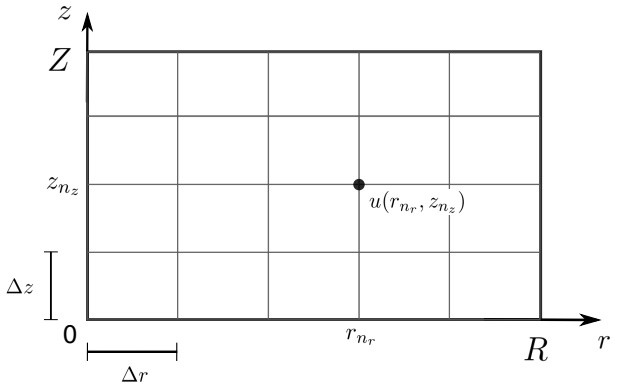

Figure 3.2: Discretized computational domain.

Estimation from complex data When we have access to the phase of the complex function u during measurements, the inverse problem is formulated as:

$$\min_{m\in\mathcal{M}_{\text{ad}}} J(m) = \min_{m\in\mathcal{M}_{\text{ad}}} \frac{1}{2}\int_0^Z |u_m(R,z) - u^{\text{obs}}(R,z)|^2 dz. \tag{3.5}$$

In that case, w_m in (3.3) becomes the solution of the following equation:

$$\partial_r w_m + j\left[k_0(m-1) + \left(\sqrt{k_0^2 + \partial_z^2} - k_0\right)\right] w_m = 0, \tag{3.6a}$$

$$w_m(R,z) = u_m(R,z) - u^{\text{obs}}(R,z), \tag{3.6b}$$

$$w_m(r,0) = 0. \tag{3.6c}$$

3.3.2 The Discretized Model

The variables presented in Section 3.3.1 are in functional form for simplicity. However in the following, u, w, d and m are treated as finite dimensional vectors in a numerical method that tackles the partial differential equations and the integrals. We are going to introduce their finite representations so as to explain our multiscale techniques easier later. Our numerical domain is illustrated in Figure 3.2. It extends from 0 to R and Z in the radial and the axial directions, respectively. The domain is discretized using a structured mesh. The position (r,z) becomes (r_{n_r}, z_{n_z}) in this domain, which are controlled by uniform mesh size and station number on the grid. The position vector is expressed by the following relations.

$$r_{n_r} = n_r\ \Delta r, \quad n_r \in [0, N_r], \tag{3.7a}$$

$$z_{n_z} = n_z\ \Delta z, \quad n_z \in [0, N_z]. \tag{3.7b}$$

Here, N_r and N_z are the number of grid nodes (computation stations) on the discretized domain like in Chapter 2. Accordingly, $u(r,z) \in \mathbb{C}$, $w(r,z) \in \mathbb{C}$, $m(z) \in \mathbb{R}$ and $\nabla_m J(m) \in \mathbb{R}$ becomes of dimension $u(r_{n_r}, z_{n_z}) \in \mathbb{C}^{N_r \times N_z}$, $w(r_{n_r}, z_{n_z}) \in \mathbb{C}^{N_r \times N_z}$, $m(z_{n_z}) \in \mathbb{R}^{N_z}$ and $\nabla_m J(m) \in \mathbb{R}^{N_z}$, respectively. The finite dimensional representations are built on the punctual values computed at grid nodes. One example is given for u in Figure 3.2.

Our goal is to solve (3.2) for m at the vertical resolution N_z of the mesh. This is a complex high-dimensional problem even in the absence of modeling or measurement errors and noise as we showed in Chapter 2. In the next section, we explain how to apply the space reduction

techniques to reduce the complexity of (3.2), referring the works in [84], [128].

3.3.3 The Subspace Approaches

3.3.3.1 Search Space Reduction

Background We now explain the Search Space Reduction (SSR) adapting the generalized descriptions in [128]–[131] to our context. Search space reduction means we allow the solutions to be given by only the m that belongs to a certain subset of the admissible parameter set. This is achieved by restricting the parameter model or restricting only the perturbations on the parameter model. The goal is to obtain a model m which has desired features. Namely, the restriction can be done so that the parameter models are regular, become restricted to contain evaporation ducts or octo-linear profiles, for example. There are basically two ways to achieve this: (1) reducing the parameter model dimension below N_z or (2) restricting the perturbations applied to the parameter model kept at the dimension of N_z.

Method 1 Restriction of the parameter model is described in the following. In our context, the model m_p at iteration p belong to $\mathbb{R}^{N_z}$. The model is restricted by making it lie in an N_L-dimensional subspace of $\mathbb{R}^{N_z}$, with $N_L < N_Z$. Here, the vectors $\{a_i\}_{i=1,...,N_L}$ span this new finite dimensional subspace. The parameter model reads:

$$m_p = \sum_{i=1}^{N_L} q_i a_i = A\ q_p. \tag{3.8}$$

In this case, the optimization is done on the new control parameter $q_p \in \mathbb{R}^{N_L}$ in this reduced subspace [128]. The reduction basis $A = [a_1, ..., a_{N_L}] \in \mathbb{R}^{N_z \times N_L}$ maps the new control parameters to the physical system parameter m of dimension N_z in forward and adjoint model simulations.

Now the question is how to do the gradient-based optimization efficiently on q in this case. Minimizing $J(m)$ (3.2), which is now expressed as $J(Aq) := \tilde{J}(q)$, with the new control parameter q requires the gradient information with respect to q, not m. The gradient of the cost function $\tilde{J}(q)$ with respect to q, for this reduced parameter space, can be inherited from the $\nabla_m J(m)$ in (3.3) using the chain rule:

$$\tilde{J}(q) := J(Aq) \quad \text{then} \quad \nabla_q \tilde{J}(q) = A^T\ \nabla_m J(m). \tag{3.9}$$

The term $\nabla_q \tilde{J}(q) \in \mathbb{R}^{N_L}$ is called the reduced gradient in this thesis.

In sum, the additional work that we need to do so as to apply this search space reduction technique is that we firstly construct the matrix that controls simulation parameter m via few parameters in vector q according to our wish. When it comes to perform gradient-based optimization, we feed the optimization method with q as the parameter vector and $A^T\ \nabla_m J(m)$ as the gradient vector.

Method 2 Restriction of the perturbation model is discussed in the following. In our context, this means we perform the inversion at the dimension of N_z instead of N_L and make the reduced gradient of dimension N_L belong to the image of A. To be more precise by mathematically

speaking, we are talking about the parameter model m_p at iteration p that is perturbed by $\tilde{m}_p$ iteratively:

$$m_{p+1} = m_p + \tilde{m}_p. \tag{3.10}$$

Here, the perturbation model reads:

$$\tilde{m}_p = \sum_{i=1}^{N_L} \tilde{q}_i a_i = A\ \tilde{q}_p. \tag{3.11}$$

Just in case, we emphasize that the control parameter of the optimization is m; parameter q does not appear here but it is going to be embedded in the perturbations. This is clarified in the following.

The parametrizations are kept at the dimension of N_z and the reduction effect coming from the basis A should be reflected on $\tilde{m}_p$. This is achieved by mapping the reduced gradient with the reduction basis.

$$\text{If}\ \ \tilde{m}_p = A\ \tilde{q}_p\ \ \text{and}\ \ \tilde{q}_p \propto A^T\ \nabla_m J(m)\ \ \text{then}\ \ \tilde{m}_p \propto AA^T\ \nabla_m J(m). \tag{3.12}$$

In sum, the additional work that we need to do so as to apply this search space reduction technique is to construct a reduction basis A and apply AA^T on the gradient that we already had obtained using the standard adjoint approach and feed the optimization method with this new product as the gradient vector.

At this point, we remark that these two techniques that we develop for the tomographic configuration is directly transferable to the RFC problem because the FM and AM remains untouched; we only interact with the output of the adjoint-based algorithm: the gradient.

Search space reduction in refractivity inversion Subspace approaches are not new to the refractivity inversion problem [47], [127], [132]. Typically, the studies in RFC community have looked for a good choice of reduction basis A that appears in (3.8) to construct a proper subspace so as to improve inversion performance. The aim has been to find a basis A such that the refractivity is resolved with an acceptable agreement to the truth. One possibility to construct such bases properly is to exploit accurate *a priori* knowledge about the atmospheric conditions that we do not actually know and try to invert. For example, this *a priori* information can be a global synoptic structure of the refractivity parameter variation in altitude at the geographic location where the inversion system is tested. Statistical knowledge and numerical weather prediction tools can be employed in the process of constructing such bases as well.

Empirical studies about the atmospheric conditions have assembled refractivity data around the globe since the last century [11], [20], [133]–[141]. The investigations have revealed that the downward refracting deviations (ducts) from the standard conditions are the ones which explain the refractivity-driven anomalies in radar performance in our context. Those deviations could be approximated with three primal vertical refractivity variation models: log-linear, bilinear and trilinear model [55, p. 4]. Five-parameter models could be used for representing mixed type ducts with more complex variations embedded in a vertical refractivity profile [47].

Thanks to empirical studies, one could analyze the pre-studied statistics of the region where the measurement is collected and incorporate this *a priori* information in the construction of the basis A when testing the inversion system in that region. For example, if evaporation duct is a common occurrence in the region, the basis A could correspond to log-linear variations to approx-

imate the data with acceptable agreement [61]. If the atmospheric conditions are significantly more complex than what the log-linear approximation could represent, more detailed information could be incorporated to achieve better reductions using empirical orthogonal function, principal component analysis or Karhunen-Loeve transform as explained in [47], [62], [127], [132]. Although these reduction techniques improve the performance of the algorithm, these methods either lack generality or include a lot of forward model simulations or there are assumptions involved in the process [47], [132].

Our goals with SSR Here, we are looking for the possibility of building an inversion technique which especially does not require case-specific local empirical *a priori* information. Instead, we are looking for a technique which is more globally applicable wherever the system operates. Namely, we want to justify the improved performance with the accuracy and robustness of the algorithm independent of the acquired additional information which depends on location and time. At the same time, the construction of the basis should be a fast and simple process.

In our context, a very general reduction basis which does not incorporate empirical knowledge often cannot be trusted to provide accurate inversion because the results are restricted according to this uninformed choice and probably inferior solutions are obtained due to not using the best option. Nevertheless, the inversion result obtained with such a general basis can be useful as an initial guess of another inversion problem where we invert for more detailed structure of the atmosphere. In that context, it would be enough if the inversion could capture the global structure of the atmosphere.

Choice of reduction basis We use piecewise linear function to construct the vectors that spans the aforementioned subspace $\mathbb{R}^{N_L}$ and the control points are equally distributed in altitude. There is not a specific reason that justifies this choice when compared to other options we had. We choose this basis to begin with because it is an elementary basis and it is easy to construct and manipulate. If necessary, the basis can be upgraded to a higher order or to Fourier's sinus basis or Haar's basis and so on later. In the case of piecewise linear functions, A becomes the matrix that performs linear interpolation in an interval, A^T becomes the matrix that takes weighted sum in an interval where the weight distribution is linear.

Reduction process The application of the reduction is illustrated on a numerical example. Let us suppose that we apply reduction on the parameter model and we are going to do four-parameter inversion to explain a given measurement data. Suppose that our initial guess is given by the four dimensional vector q which is shown in Figure 3.3a. We obtain the parameter model $m \in \mathbb{R}^{N_z}$ that is used in the forward and adjoint model simulations from $m = Aq$, as shown in Figure 3.3b. After the simulations, the gradient is obtained at the dimension of N_z as shown in Figure 3.3c. The restriction is achieved by using the relation (3.9) to obtain the gradient of the four control parameters, as shown in Figure 3.3d.

Our results depend on the reduction basis. In what follows, we introduce multiscale optimization strategy to mitigate the importance of finding the best reduction basis in order to represent the ambient refractive index in our context. The discussions follow the ideas presented in [84], [112] on multiscale parametrization.

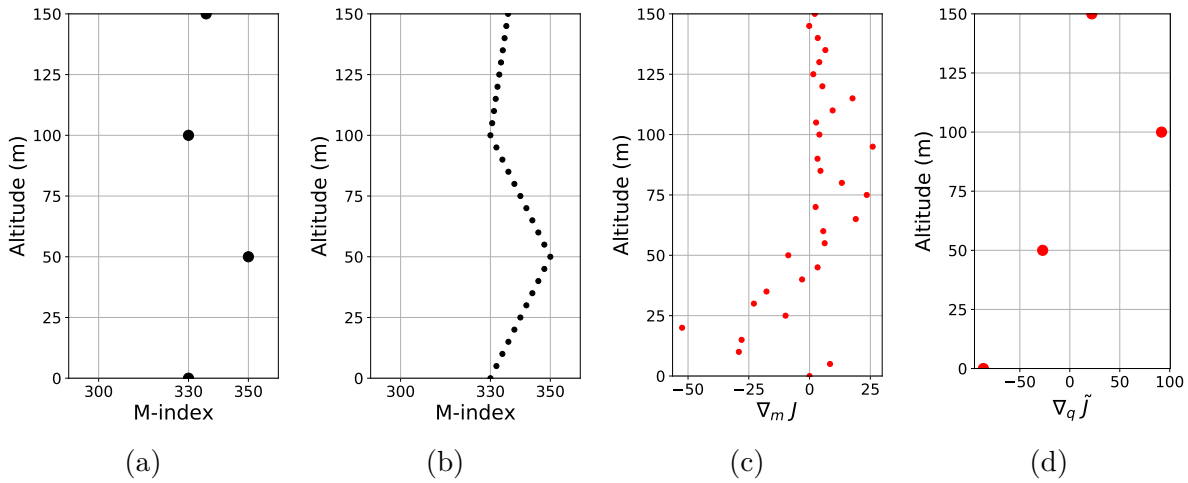

Figure 3.3: Example of reduced parametrization controlled by piecewise linear functions for M_{OBJ} in Figure 3.6a. (a) $q(z)$, (b) $m(z)$, (c) $\nabla_m J$, (d) $\nabla_q \tilde{J}$.

Multiscale Approach Proper parametrization can improve the performance of inversion algorithm drastically. The speed and accuracy of the inversion depends on the choice of reduction basis. In practice, it is not easy to check the inversion results for multiple bases and to conclude about which one gives the best possible result. The limitations on the inversion accuracy can be weakened using multiscale parametrization techniques that are described in [80], [84].

Multiscale parametrization approach can be used for weakening this dependency on the reduction basis, by approaching from the reduction basis towards the punctual values in the forward model simulations progressively. In this thesis, multiscaling with a hierarchical refinement strategy is employed in the parametrization. The multiscale basis is constructed from the local bases put together in a hierarchy, by organizing those subproblems in the order of increasing control parameter vector dimension.

In practice, all we need is to organize the inverse RBT problems that uses the aforementioned SSR technique with different parameter dimension N_L such that the parameter dimension increases as we move along the order. All N_Ls combined forms a sequence of numbers in increasing order:

$$N_L := \{N_{L,i},\ i \in [1, i_{\max}),\ i \in \mathbb{N},\ N_{L,i} < N_z\} \cup \{N_z\}. \tag{3.13}$$

Starting from an initial guess we perform the inversion at the lowest N_L at $i = 1$, and provide the inversion result as the initial guess at the next level $i = 2$ by projecting the result with a projection operator, which will be called H, from the the subspace at $i = 1$ to that at the next level $i = 2$. The next scales inherit the inverted parameters at one previous scale as their initial guesses the same way. In other words:

$$M_{\text{IG},i+1} = H(M_{\text{INV},i}) \tag{3.14}$$

where $M_{\text{INV},i}$ is the inversion result in M-unit at the multiscale level i and $M_{\text{IG},i+1}$ is the (inherited) initial guess at the next level.

With that strategy, we are effectively refining the parameter model. At the end we perform the inversion for N_z number of parameter (the original baseline problem) using the inversion result of the last reduction level as the initial guess. The algorithm is described in Workflow 1 and the multiscale inversion process is exemplified in Figure 3.4.

Workflow 1: Multiscale Parametrization

```
# INPUT data d^obs, initial guess parameter M_IG, sequence of parameter dimension N_L
# OUTPUT inverted parameter M_INV, cost function J
# INITIALIZE cost function J_best
FOR i = 1 to i = i_max
  CALL FunctionOptimize(d^obs, H(M_IG), N_{L,i}); RETURN M_INV, J
  IF we apply parameter restriction AND J < J_best
    set J_best = J and M_IG = M_INV
  ELSEIF parameter restriction AND J > J_best
    M_INV = M_IG
  ELSE
    # we apply perturbation restriction or data reduction
    set M_IG = M_INV
  END IF
END FOR
CALL FunctionOptimize(d^obs, H(M_IG), N_z); RETURN M_INV, J
```

Workflow 2: Optimization Algorithm FunctionOptimize

```
# INPUT data d^obs, inherited initial guess parameter H(M_IG), dimension of reduced
  parameter N_{L,i}
# OUTPUT inverted parameter M_INV, cost function J
IF we apply parameter restriction
  build A from N_{L,i}; set q_IG = H(M_IG)
  CALL FunctionBFGS(q, q_IG, A^T ∇_m J); RETURN q_INV, J
ELSEIF we apply perturbation restriction
  build A from N_{L,i}; set m_IG = AH(M_IG)
  CALL FunctionBFGS(m, m_IG, AA^T ∇_m J); RETURN m_INV, J
ELSE
  set m_IG = H(M_IG)
  CALL FunctionBFGS(m, m_IG, ∇_m J); RETURN m_INV, J
END IF
```

In Figure 3.4 we show how this refinement is accomplished in an example scenario that we will describe later in Section 3.4, where the initial guess parameter is shown by the green dashed curve and the objective parameter in blue curve in Figure 3.4a. If we had adopted a subspace approach that search for trilinear parameter model in this problem, the results look like what is shown with red curve in Figure 3.4a. But in a multsicale strategy, we can use this inversion result as the initial guess of the same problem where we increase the number of parameters to invert this time. By doing that refinement in the parametrization successively, we finally arrive at the problem where the parameter dimension is equal to N_z. So, the purpose of solving those subproblems is to produce a initial guess for the next subproblem in the hierarchy. We hope that the initial guess provided to the next scale is in the attraction basin of the global minimum of the next problem in the hierarchy. At the end, we expect to provide a good initial guess to the N_z-dimensional refractivity estimation problem without using any knowledge about what the true ambient refractive condition is.

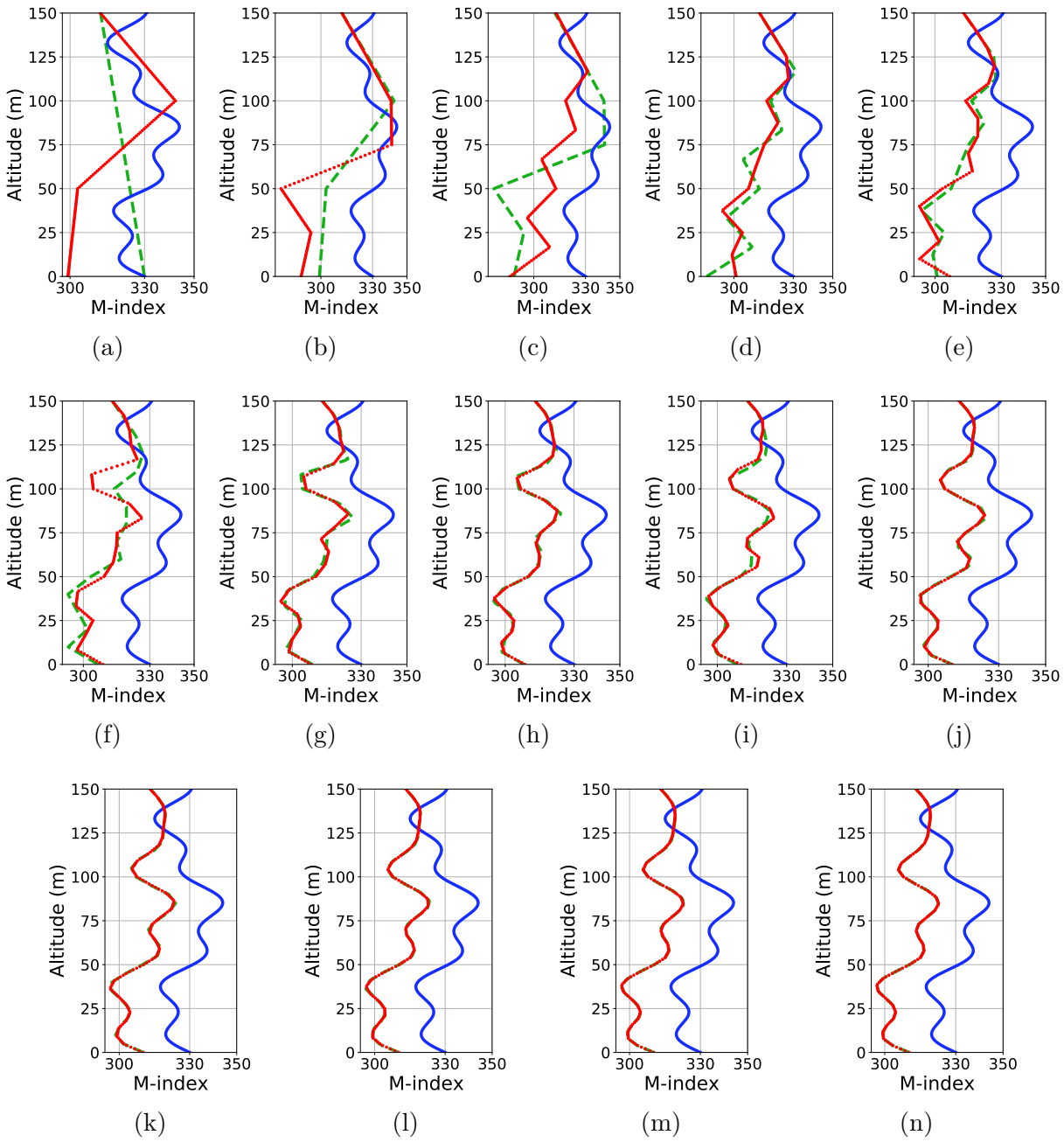

Figure 3.4: A level-by-level demonstration of multiscale resolution using local bases in a hierarchy. (Blue line: true (objective) parameter, red dotted-line: predicted (inverted) parameter, green dashed-line: the initial guess (inherited from the previous level in the multiscale hierarchy)).

3.3.3.2 Data Space Reduction

The reduction can be done on measurement data as well as it is done on parametrization. Let B be the operator that performs the reduction on data. Then the cost function reads:

$$\min_{m\in\mathcal{M}_{\text{ad}}} J(m) = \min_{m\in\mathcal{M}_{\text{ad}}} \frac{1}{2}\left\|Bd_m^{\text{sim}} - Bd^{\text{obs}}\right\|^2_{L^2(\Gamma_R)} = \min_{m\in\mathcal{M}_{\text{ad}}} \frac{1}{2}\int_0^Z \left|Bd_m^{\text{sim}} - Bd^{\text{obs}}\right|^2 dz. \quad (3.15)$$

Then, its gradient reads:

$$\langle \nabla_m J, \hat{m} \rangle_{\mathcal{Z}} = \int_0^Z \Re \left\{ B^* B (d_m^{\text{sim}} - d^{\text{obs}}) \cdot (\overline{d_m^{\text{sim}}})' \cdot \hat{m} \, dz \right\}. \tag{3.16}$$

Then, it is sufficient to modify the adjoint initial condition in the adjoint models to implement this technique. When phase is not measurable, the adjoint model (3.4) should be modified in the driver of the adjoint initial condition:

$$\partial_r w_m + j \left[k_0 (m-1) + \left(\sqrt{k_0^2 + \partial_z^2} - k_0 \right) \right] w_m = 0, \tag{3.17a}$$

$$w_m(R,z) = 2B^* B \left(|u_m(R,z)|^2 - |u^{\text{obs}}(R,z)|^2 \right) u_m(R,z), \tag{3.17b}$$

$$w_m(r,0) = 0. \tag{3.17c}$$

Similarly, when phase is measurable, the adjoint model (3.6) should be modified in the driver of the adjoint initial condition:

$$\partial_r w_m + j \left[k_0 (m-1) + \left(\sqrt{k_0^2 + \partial_z^2} - k_0 \right) \right] w_m = 0, \tag{3.18a}$$

$$w_m(R,z) = B^* B \left(u_m(R,z) - u^{\text{obs}}(R,z) \right), \tag{3.18b}$$

$$w_m(r,0) = 0. \tag{3.18c}$$

Choice of reduction basis Derivation is shown in a form where the functions are in their continuous form. They are discretized for numerical modeling as described in Section 3.3.2. Accordingly, B is a matrix in practice. We use linear interpolation basis as done in the parametrization, so the case when $B = A^T$ and $B^* = B^T = A$ is considered in this study. Matrix A is defined with the choice of reduction basis in Section 3.3.3.1.

Multiscale approach We apply multiscale approach in the exact same way as we do in parametrization. When data reduction is performed in a multiscale basis, it is used in synchronization with the multiscale parametrization. How this is going to be achieved is going to be discussed in the results section. In the baseline setup, one can suppose for the moment that the dimensions of parameter and data vectors are kept the same during the multiscaling.

Our goals with DSR Data space reduction (DSR) is applied in the multiscale strategy because we assume that global structure in parameter model explain mostly the global structure of the data. DSR is particularly relevant to the accurate inversions when low dimensional representations of parameter model with piecewise linear functions cannot explain the data in the least square sense in the admissible parameter set. In addition to that, DSR brings convexification to the error functional topography. Ideally, we expect to find the true ambient conditions (global minimum) as a result of the convexification.

This convexification feature is illustrated in Figure 3.5. Here, optimization landscape is obtained at $R = 30$ km for the objective and initial guess parameter given in Figure 3.6g using the approach described with (2.53) in Chapter 2. The optimization landscape is as shown in Figure 3.5c. Initial guess parameter is located at $\alpha = 1$. We try to find the objective parameter that is located at $\alpha = 0$. Obviously, the iteration parameters would be trapped at the local minima seen on the Figure if gradient-based optimization method is used (for one parameter inversion). When we use data reduction with $N_L = 4$, the optimization landscape gets convexified

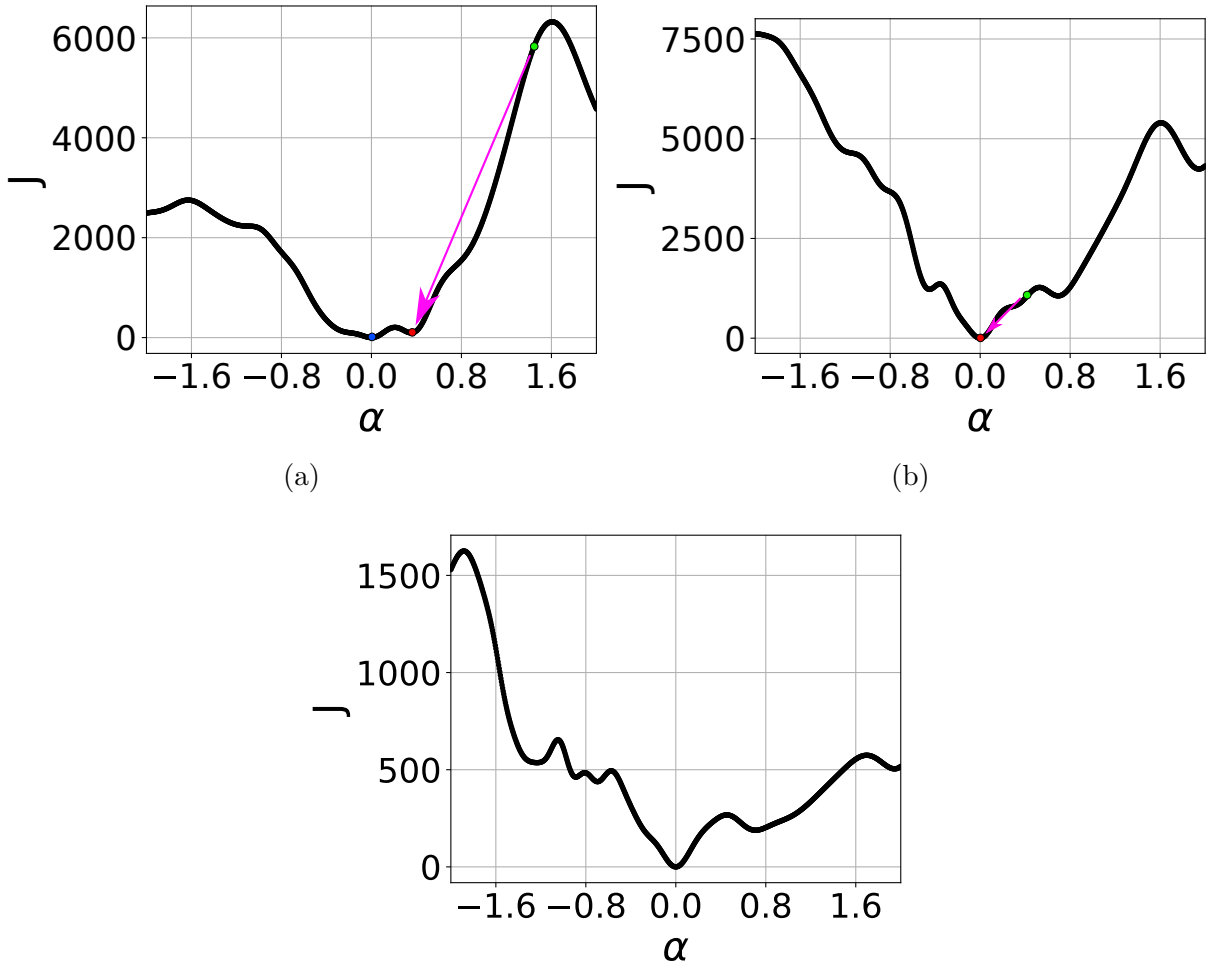

(a) (b)

(c)

Figure 3.5: Convexification of the error functional topography in the multiscale approach. Data dimensions: (a) 4, (b) 10, (c) 151.

as shown in Figure 3.5a. It can give more mobility to the optimization parameter to move inside a wider attraction basin that is closer to the true solution. The local minimum obtained at that level can be inherited as the initial guess of the next multiscale level in the following iterations, which is finally going to provide a good initial guess for the final run where we invert N_z number of parameters at each meter point in altitude. Like that, we can have more chance to retrieve a result close to the true parameter.

3.4 Computational Setup

The details of the baseline computational setup is already presented in Section 2.7.1. The same information is not repeated here. Instead, we present the differences from the baseline setup.

One difference from the baseline setup presented in Section 2.7.1 is that the initial condition $\phi(z)$ which is this time produced by the complex-point source positioned at $(r_s, z_s) = (-100 \text{ m}, 25 \text{ m})$. Therefore, the source profile resembles a more pointwise radar source as shown in Figure 3.6h. This is different than the initial field which is in Chapter 2 which resembles more to a quasi-plane wave. In order to be clear, we repeat that the source frequency is $f = 2$ GHz.

Data is generated synthetically like in Chapter 2. This is achieved by executing a forward model simulation for an objective refractivity distribution. The numerical settings of this simulation is the exact same as the simulations which are executed during the inversion process. Then, a trace operator is applied at the range of interest R to collect the vector $u(R, z_{n_z})$ for $n_z \in [0, N_z]$. This means, we sample the measurements at each grid node in altitude at a certain distance R from the radar. Then, we take the square of the vector elements to assign it to d^{obs} if we study the problem of phaseless data inversion, or keep it as it is if we study the problem of inversion from measurements with phase.

In this chapter, we try to invert the objective refractivity profiles that are used for generating the data of different ducting propagation conditions. Those conditions are characterized with the true ambient parameters that vary only in altitude. They are denoted by M_{OBJ} and are plotted like in Figure 3.6. Let us now elaborate about those profiles. The objective parameter in Figure 3.6a is inherited from the previous chapter to compare the inversion results with our new source condition. Additionally, this parameter is studied in order to investigate the invertibility when the wave field is guided through upward and downward refracting conditions of equal strength due to such symmetry in $z \in [0, 100]$ m. In Figure 3.6b periodic perturbations are added on M_{OBJ} of Figure 3.6a to obtain more realistic nonlinear parameter variation with altitude, which is supposed to make the inversion more difficult than with M_{OBJ} of Figure 3.6a by disturbing the regularity of the observed wave field in Ω. For this reason, it would be difficult to invert M_{OBJ} accurately with the standard technique and we want to see how Multiscale Parametrization Technique (MPT) performs in such a situation. In Figure 3.6c we are interested in how the inversion would be affected if the perturbed duct of Figure 3.6b appears with a mixed structure due to an evaporation ducting condition at sea level. In Figure 3.6d, an idealized (linear) surface duct profile is modeled, which is going to cause stronger downward refraction than with M_{OBJ} of Figure 3.6a, hence higher level of inversion difficulty is expected. In Figure 3.6e, a perturbation that resembles an evaporation duct is superposed on the surface based duct of Figure 3.6d. In Figure 3.6f, periodic perturbations are added on M_{OBJ} of Figure 3.6e, to compare the inversion difficulty. In Figure 3.6g, a non-smooth perturbation is added on M_{OBJ} of Figure 3.6f in $z \in [75, 100]$ m to see if our technique can preserve such local variations in the inversion results.

3.5 Validation of the Gradient

In this section, we repeat the validation process that was executed previously in Chapter 2. Our goal is to check the following two points. At the first step, we want to be sure that the derivations that were proposed previously in Chapter 2 for the standard adjoint-based approach are still valid for the scenario of Chapter 3 after the modifications in the setup. At the second step, we want to be sure that the reduction in parameter and data is done correctly. These two are going to be checked by comparing the gradients computed using finite differences ($\nabla_m J_{FD}$) and the adjoint model ($\nabla_m J_{AM}$).

The gradients of the first descent iteration $\nabla_m J_{FD}$ and $\nabla_m J_{AM}$ are computed numerically for the objective-initial guess parameters pair given in Figure 3.6g. The validation is performed by comparing $\nabla_m J_{AM}$ to $\nabla_m J_{FD}$. If those two gradients match, the method passes the validation test. The numerical setting is the baseline setup which is explained in Section 3.4. Here, $\nabla_m J_{FD}$ is obtained using forward difference scheme for perturbation tolerance $\epsilon = 10^{-6}$. Range is considered at four different values at $R = \{1, 10, 60, 100\}$ km.

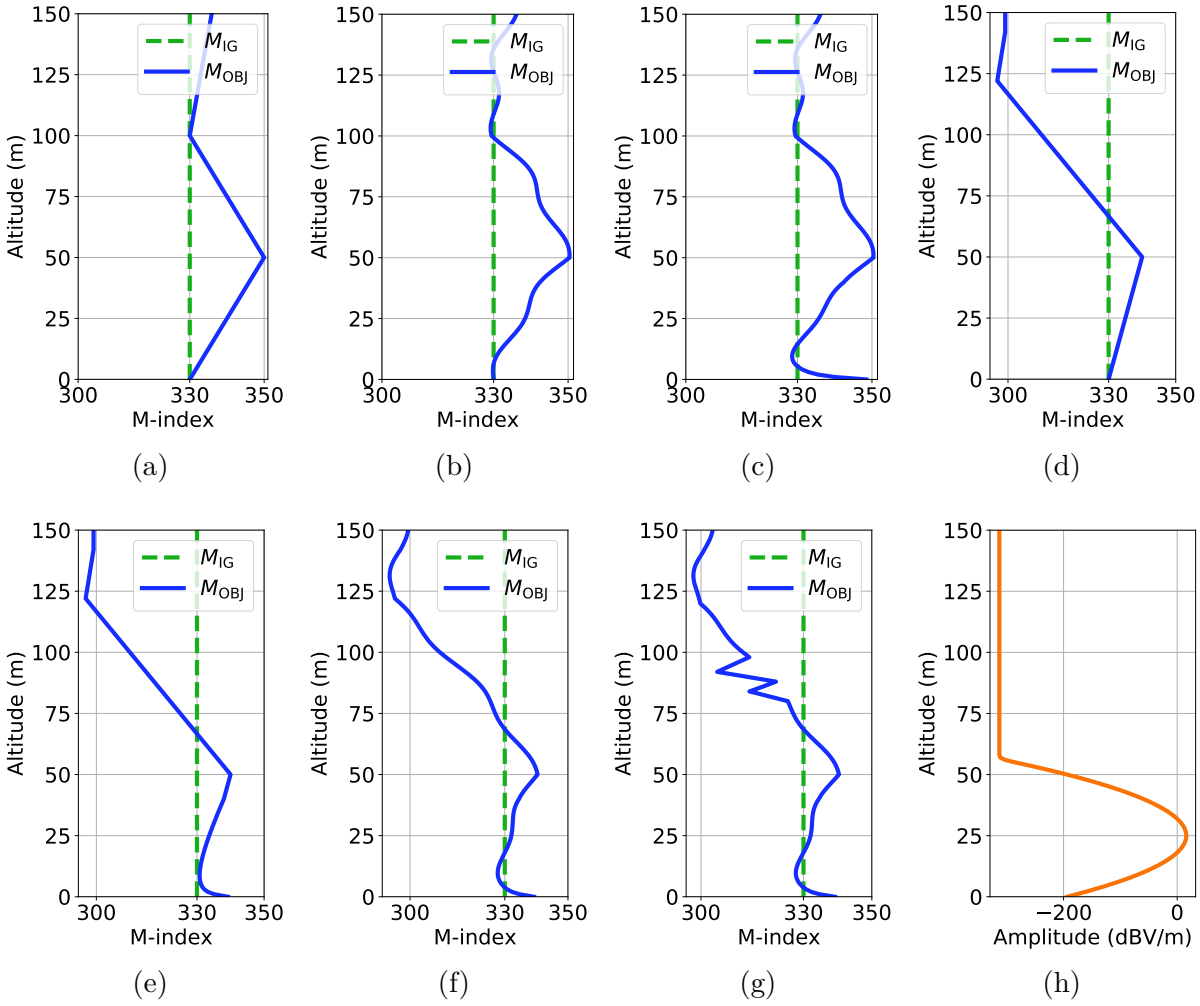

Figure 3.6: The selected source profile and refractivity profiles for inversion. (a)-(g) Starting parameter of optimization (initial guess parameter) M_{IG} and global minimum (objective parameter) M_{OBJ}. (h) initial source field amplitude $|\phi(z)|$.

	without SSR		with SSR	
	with phase	without phase	with phase	without phase
without DSR	Figure 3.7	Figure 3.8	Figure 3.9	Figure 3.10
with DSR	Figure 3.11	Figure 3.12	Figure 3.13	Figure 3.14

Table 3.1: Organization of the validation results.

The organization of the validation results are given in Table 3.1. Firstly, we study the case when standard adjoint-based formulations are used for computing the gradient. This means search space reduction (SSR) and data space reduction (DSR) are not applied. In Table 3.1, the rows and columns corresponding to the results of that standard application are shown as "without SSR" and "without DSR". Secondly, we study the case when the parameter reduction and data reduction are applied separately and corresponding results are shown as "with SSR" and "with DSR" in Table 3.1. Lastly, we study the case when the parameter reduction and data reduction are applied at the same time. All these tests are performed when the phase is measurable and not measurable. The results corresponding to these two measurement data type are shown as "with phase" and "without phase" respectively.

As stated also Chapter 2, the validations graph is plotted with respect to altitude. In fact, what is shown in the graph is the gradient and it is a vector in which i-th element is the derivative value with respect to the i-th element of the parameter vector. Therefore, normally, the gradient should be presented with respect to parameter vector index. However, we project the derivative value to the altitude at which i-th element is located and then present it in the plot, by connecting the punctual values in altitude.

3.5.1 Standard adjoint-based tomography

Measurement with phase We validate adjoint-based computation of the gradient of optimization problem (3.5), which is proposed for the case when the measurements contain phase. The validation is done for the gradient at the first descent iteration at different receiver array antenna positions in Figure 3.7. The gradient is computed using the formula (3.3) where the adjoint function in this formula is given with the solution of (3.6). The computed gradient is compared to the gradient estimated by using FD. The equations and implementations are validated because the gradients computed with the two approaches match in Figure 3.7.

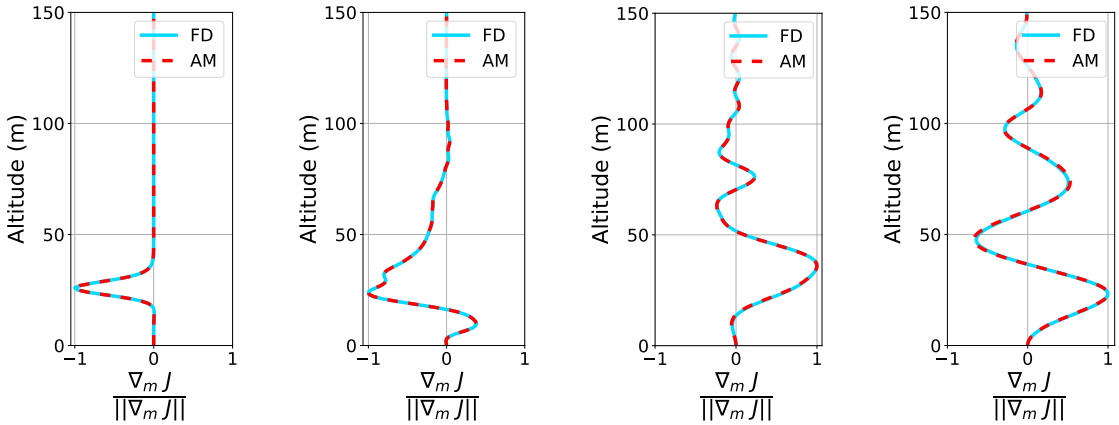

Figure 3.7: Validation of the gradient for measurements with phase. FD: Finite Differences vs. AM: Adjoint Model. (a) $R = 1$ km, (b) $R = 10$ km, (c) $R = 60$ km, (d) $R = 100$ km.

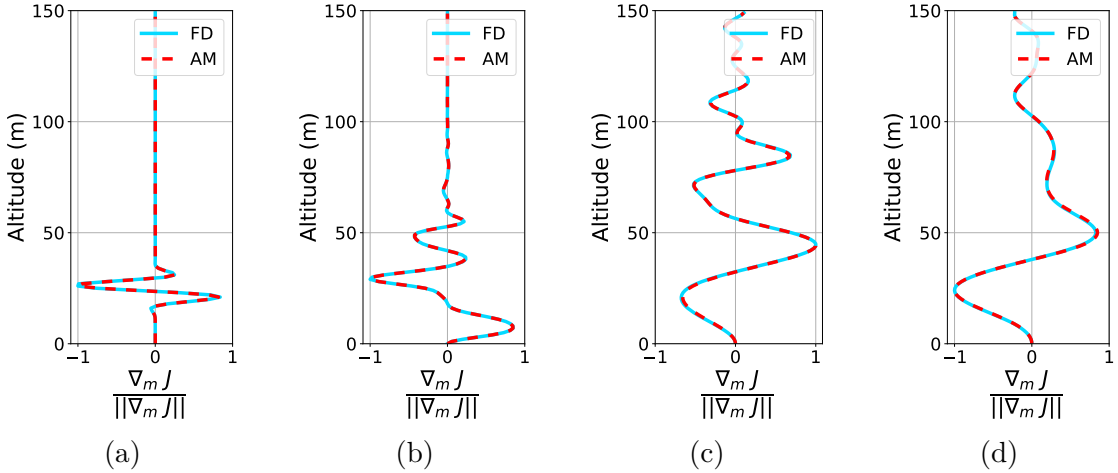

Figure 3.8: Validation of the gradient for measurements without phase. FD: Finite Differences vs. AM: Adjoint Model. (a) $R = 1$ km, (b) $R = 10$ km, (c) $R = 60$ km, (d) $R = 100$ km.

Measurement without phase We validate adjoint-based computation of the gradient of optimization problem (3.2). The validation result is presented in Figure 3.8. Note that, the gradient is computed using the formula (3.3) where the adjoint function is the solution of (3.4). The equations and implementations are validated because the gradients computed with the two approaches match in Figure 3.8.

3.5.2 Search space reduction

In this section, finite difference approximation of the gradient is obtained by perturbing q, not m.

Measurement with phase We validate adjoint-based computation of the gradient of optimization problem (3.5), which is proposed for the case when the measurements contain phase. The validation is done for the reduced gradient at the first descent iteration at different receiver array antenna positions in Figure 3.9. The reduced gradient is computed with (3.9) using the gradient of the N_z-dimensional optimization problem, where the latter is computed using the formula (3.3), where the adjoint function in (3.3) is given with the solution of (3.6). The computed gradient is compared to the gradient estimated by using FD. The equations and implementations are validated because the gradients computed with the two approaches match in Figure 3.9.

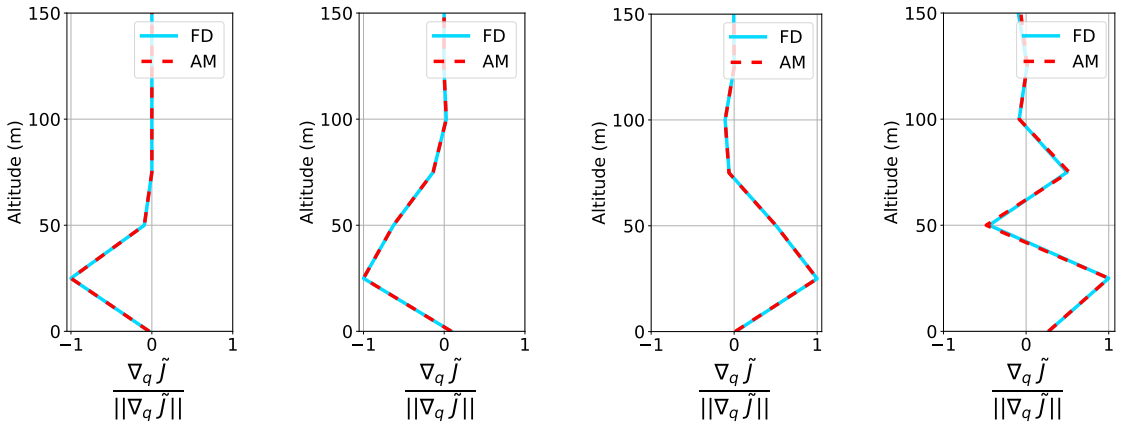

Figure 3.9: Validation of the gradient for measurements with phase and with application of search space reduction. FD: Finite Differences vs. AM: Adjoint Model. (a) $R = 1$ km, (b) $R = 10$ km, (c) $R = 60$ km, (d) $R = 100$ km.

Measurement without phase We validate adjoint-based computation of the gradient of optimization problem (3.2). The validation result is presented in Figure 3.10. Note that, the reduced gradient is computed with (3.9) in which the (unreduced) gradient is computed using the formula (3.3) with the adjoint function being the solution of (3.4). The equations and implementations are validated because the gradients computed with the two approaches match in Figure 3.10.

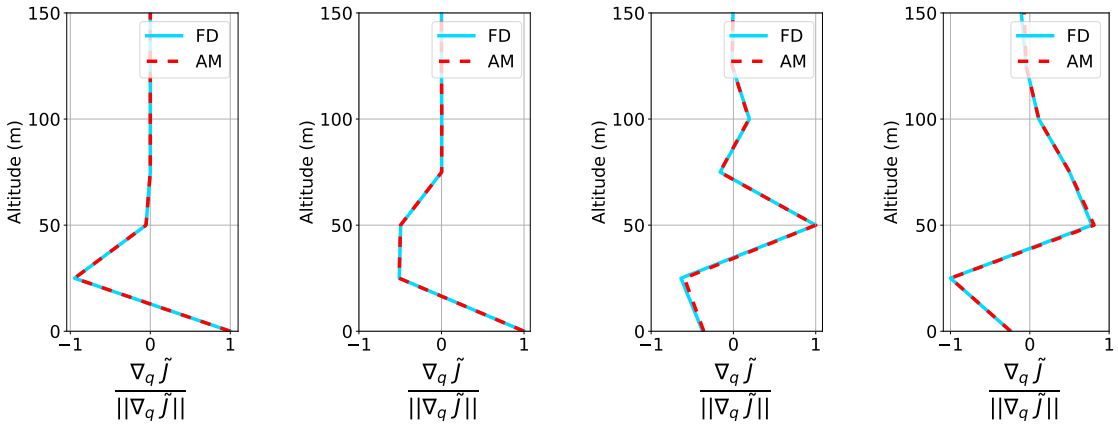

(a) (b) (c) (d)

Figure 3.10: Validation of the gradient for measurements without phase and with application of search space reduction. FD: Finite Differences vs. AM: Adjoint Model. (a) $R = 1$ km, (b) $R = 10$ km, (c) $R = 60$ km, (d) $R = 100$ km.

3.5.3 Data space reduction

Measurement with phase We validate adjoint-based computation of the gradient of optimization problem (3.5), which is proposed for the case when the measurements contain phase. In the case of data reduction, the cost function J in (3.5) is evaluated after applying a reduction operator B (a matrix) on data, so the new cost function is written in the form shown in (3.15) (see Section 3.3.3.2). The gradient is computed using the formula (3.3) where the adjoint function in this formula is given with the solution of (3.18). The computed gradient is compared to the gradient estimated by using FD and presented in Figure 3.11. The equations and implementations are validated because the gradients computed with the two approaches match.

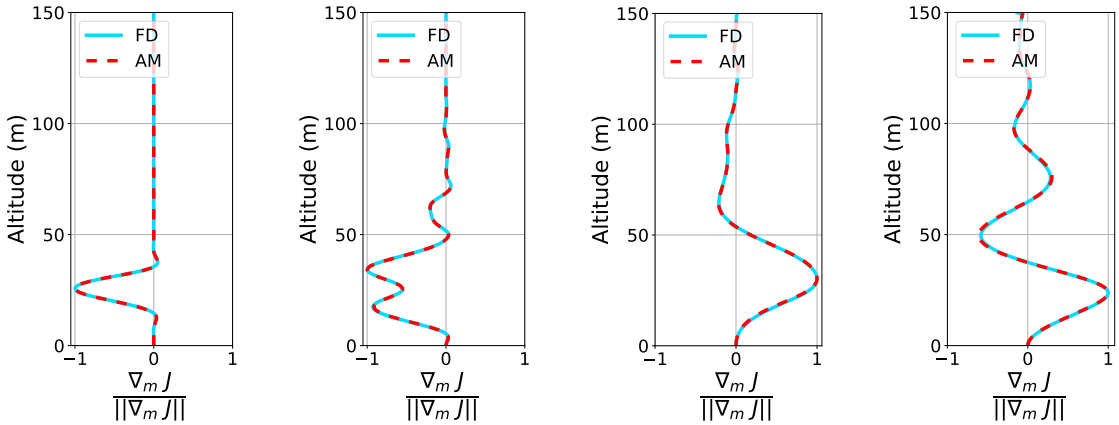

(a) (b) (c) (d)

Figure 3.11: Validation of the gradient for measurements with phase and with application of data space reduction. FD: Finite Differences vs. AM: Adjoint Model. (a) $R = 1$ km, (b) $R = 10$ km, (c) $R = 60$ km, (d) $R = 100$ km.

Measurement without phase We validate adjoint-based computation of the gradient of optimization problem (3.2), which is proposed for the case when the measurements do not contain phase information. Data reduction is achieved following the procedure described in Section 3.3.3.2 the same as in the case of measurement with phase. The gradient is computed using (3.3) and (3.17). The method is validated as shown in Figure 3.12.

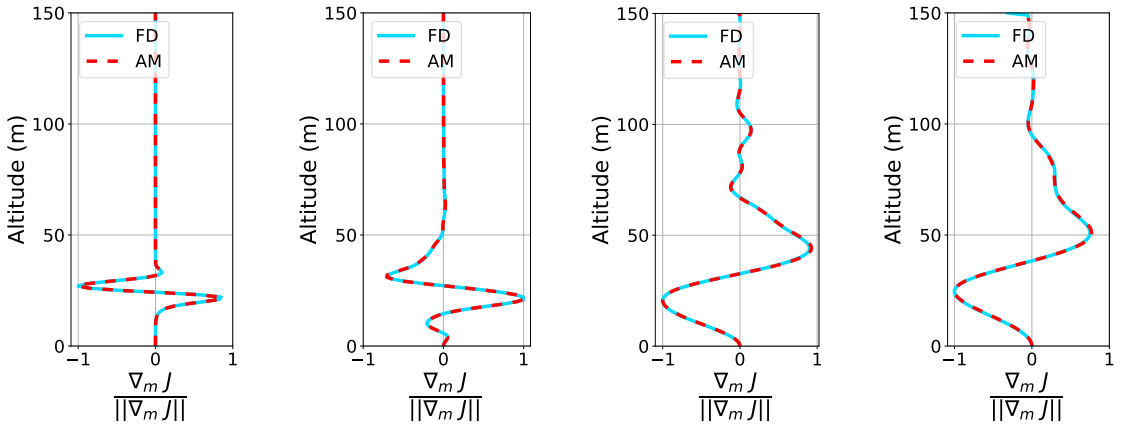

Figure 3.12: Validation of the gradient for measurements without phase and with application of data space reduction. FD: Finite Differences vs. AM: Adjoint Model. (a) $R = 1$ km, (b) $R = 10$ km, (c) $R = 60$ km, (d) $R = 100$ km.

3.5.4 Search and data space reduction

In this section, FD approximation of the gradient is obtained by perturbing q, not m.

Measurement with phase We validate adjoint-based computation of the gradient of optimization problem (3.5), which is proposed for the case when the measurements contain phase. The simultaneous application of the parameter and data reduction is validated in Figure 3.13.

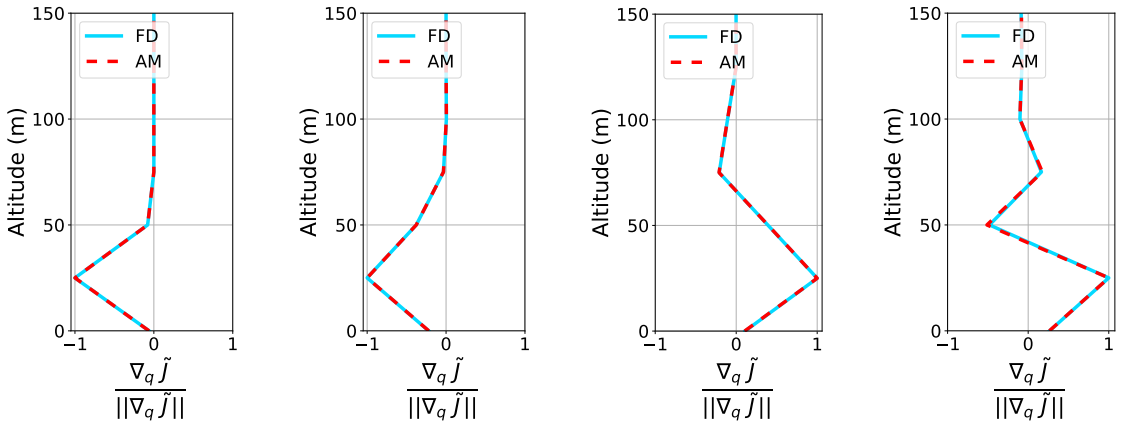

Figure 3.13: Validation of the gradient for measurements with phase and with application of search and data space reduction. FD: Finite Differences vs. AM: Adjoint Model. (a) $R = 1$ km, (b) $R = 10$ km, (c) $R = 60$ km, (d) $R = 100$ km.

Measurement without phase We validate adjoint-based computation of the gradient of optimization problem (3.2), which is proposed for the case when the measurements do not contain phase information. The simultaneous application of the parameter and data reduction is validated in Figure 3.14.

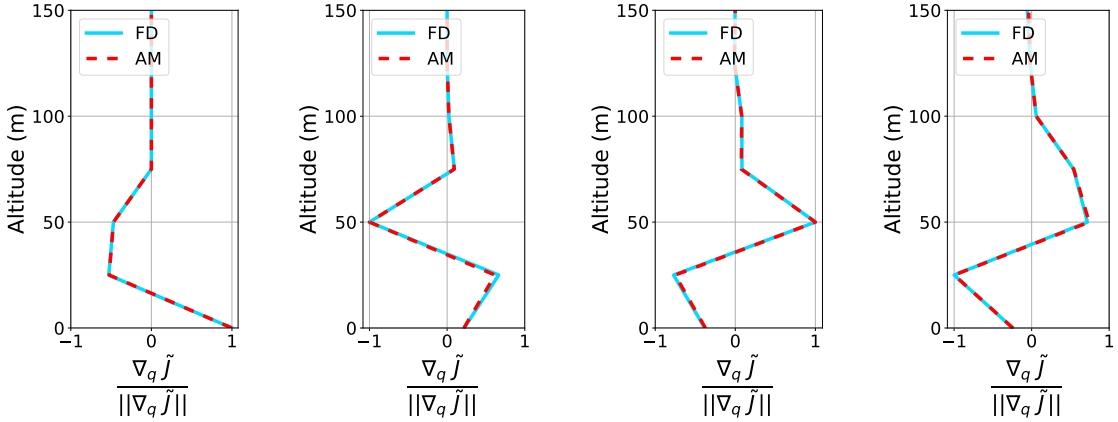

Figure 3.14: Validation of the gradient for measurements without phase and with application of search and data space reduction. FD: Finite Differences vs. AM: Adjoint Model. (a) $R = 1$ km, (b) $R = 10$ km, (c) $R = 60$ km, (d) $R = 100$ km.

3.6 Study of the Inversion of Phaseless Data

We limit our scope of analysis to the inversion of synthetically generated measurement data which does not include phase of the wave field. In this section, we first show that the use of point source does not make the baseline 151-parameter inverse problem easier, so the case remains worth analyzing and upgrading. Namely, we show the effect of reduction of parameter on stabilization of the oscillations in inversion results. Secondly, we make the problem more difficult by adding perturbations on the objective refractivity profile. This makes the profile more detailed and realistic. Thanks to that, we are testing the performance of the algorithm in more realistic scenarios which are more difficult to handle. We start our analysis at R=10 km and extent the range of application progressively as the algorithm passes the tests successfully. Beyond a certain level of profile complexity and range, plain use of subspace approach in parametrization does not permit capturing the global refractivity variation reliably. We show examples of how to approach accurately at those complex scenarios using multiscale strategies.

3.6.1 Search space reduction technique

3.6.1.1 Impact of parameter dimension at 10 km range

In this section, we investigate the impact of parameter vector dimension N_L on inversion using only a plain parameter reduction technique, without using multiscale strategies. For this purpose, we choose $R = 10$ km and $\Delta r = 100$ m with the objective parameter M_{OBJ} shown in Figure 3.6a. The reader is familiar with this scenario because the inversion of the synthetic data corresponding to this objective parameter has been studied in Chapter 2. We know that in the numerical setup

of Chapter 2 we were able to identify the synoptic structure (gradient) of the refractivity at many altitude points in the inversion results when phase was removed from the data and a quasi-plane wave was used as the source (see Figure 2.4b). In Chapter 3, we use a more realistic point source as shown in Figure 3.6h. Different from the study in Chapter 2, we choose a downward refracting initial guess with $dM/dz = -0.118$ M-unit/m. Now with these modifications, we verify if 151-parameter inversion is still problematic and worth analyzing. Note that are interested in finding the cases where 151-parameter inversion result does not look as good as that in Figure 2.9a so that there is a point on working on them to improve the results.

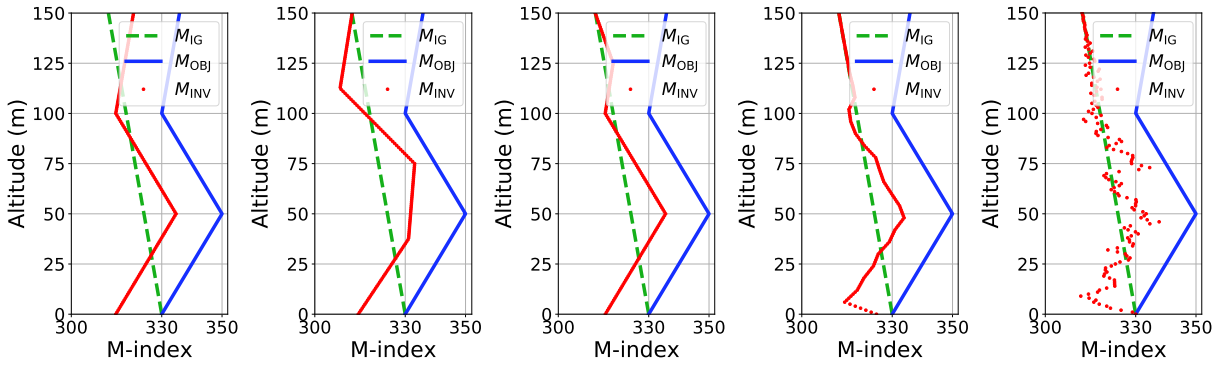

Figure 3.15: Inverted parameters for different N_L: (a) 4, (b) 5, (c) 7, (d) 26, (e) 151.

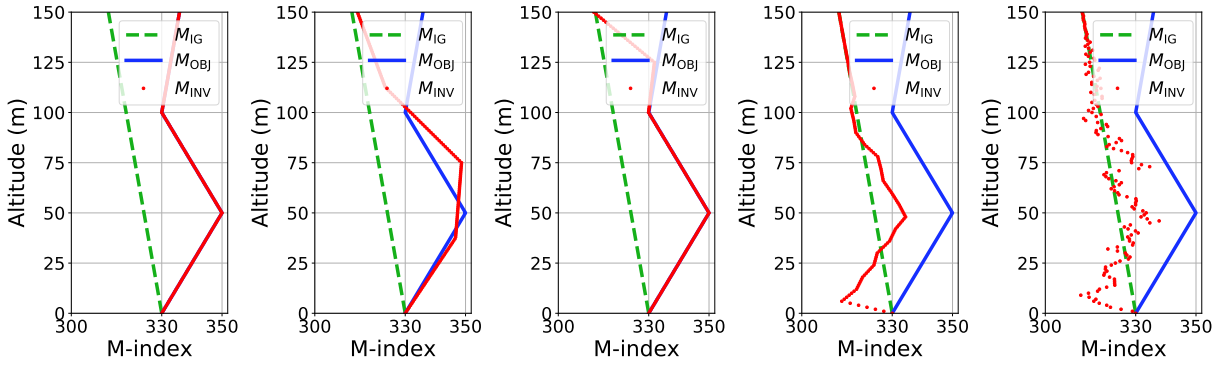

Figure 3.16: Inverted parameters for different N_L when $M(0)$ is known. N_L: (a) 4, (b) 5, (c) 7, (d) 26, (e) 151.

Firstly, we study the impact of dimensionality of the problem on inversion accuracy. Our goal is to show whether the solution contains more oscillations with increasing parameter dimension, if a good initial guess is not given (see Section 2.8.4). To show the effect of dimensionality, we increase the parameter dimension N_L in our subspace approach from 4 points to 151 in 5 steps. Note that 4 is the least possible number of points that is necessary to describe the objective parameter accurately. Also note that problem of 151 parameter inversion is the original problem that we wanted to solve from Chapter 2. The test results show the inverted parameter M_{INV} of those 5 steps in Figure 3.15. We notice that the synoptic structure of the objective parameter is retrieved at $N_L = 4$ with an offset (leftward shift) that was observed throughout Chapter 2. Qualitatively speaking, inferior solutions are obtained when $N_L = N_z$ and M_{INV} oscillates more

with N_L. When $N_L = 151$, that is, when parameter reduction is not effective, the solution does not permit the identification of the synoptic structure of the objective parameter, unlike it was before in Chapter 2 (cf. Figure 2.11c or Figure 2.21b). We conclude that using more realistic point source might have made the inversions more oscillatory[1].

Secondly, we want to see if the synoptic structure of M_{INV} would change the results in Figure 3.15 if we knew the refractivity only at the sea level. To study the improvement of the inversion results with this additional knowledge, we impose $M(0) = M_{\text{OBJ}}(0)$ during the optimization iterations. We are interested in studying this because we have observed that the leftward shift of M_{INV} from M_{OBJ} is driven by $\nabla_m J$ near sea level during iterations. The test results given in Figure 3.16 shows that the synoptic structure of the inversion results remained essentially the same as it was before in Figure 3.15.

The conclusion is that the inversion problem is still difficult with point source at $R = 10$ km. There are oscillations that needs to be stabilized in the 151-parameter inversion problem and parameter reduction can potentially cure this issue. However the subspace should be spanned with the good vectors that leads the iterations near the global minimum like in the case of Figure 3.16a. Otherwise, stable but inferior solutions can be obtained like in the case of Figure 3.16b. More refinement can retrieve more detailed structure of the refractivity profile stably but the advantage will be lost with further refinement as shown in Figure 3.16d.

3.6.1.2 Impact of objective profile at 10 km range

In this section, we study the inversion of objective parameters which are more complex than the previously studied simple trilinear profile. We achieve this by adding perturbations on the objective parameter profile which are built initially with piecewise logarithmic and linear functions in altitude such as in Figure 3.6a and Figure 3.6e. After adding the perturbations, we obtain more realistic refractivity variations such as given in Figure 3.6b and Figure 3.6g. We call it more realistic because the refractivity variation in altitude is often not as much regular as it is portrayed with M_{OBJ} in Figure 3.16 in reality even if a major trilinear structure could be identified; it oscillates in space around some mean value. The specificity of these perturbed profiles is that resolution of their propagation conditions require solving the baseline inversion problem at $N_z = N_L$ level because the true solution parameter is not included in the image of reduction basis $\text{Im}(A)$. In other words, we cannot find a subspace dimension $N_L :\neq N_z$ that can resolve the objective parameter with our choice of basis function, unlike in the case of Figure 3.16a for instance.

We first try to invert the objective profile M_{OBJ} given in Figure 3.6b which is obtained by adding sinusoidal perturbations on the trilinear objective profile that was studied in Figure 3.15 and Figure 3.16. In order to see the effect of the complexity, we repeat the study that was done to obtain the results given in Figure 3.15 for the aforementioned more complex objective profile and compare the both. The inversion results are given in Figure 3.17. Inversion of this objective profile gives regular but inaccurate results for low N_L. More detailed but oscillating inaccurate results are obtained for high N_L. There exists a sweet spot in the refinement (see Figure 3.17d) where a reasonable trade-off can be obtained between accuracy and precision (regularity).

[1] Additional tests were performed to reach this conclusion which are not presented here.

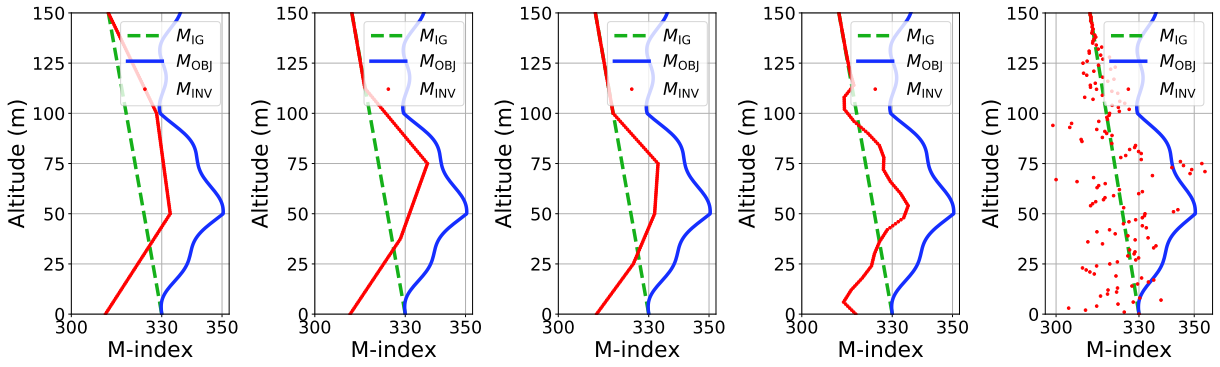

(a) (b) (c) (d) (e)

Figure 3.17: Inverted parameters in different parameter subspaces characterized by N_L. (a) $N_L = 4$, (b) $N_L = 5$, (c) $N_L = 7$, (d) $N_L = 26$, (e) $N_L = 151$.

We change the objective profile to verify if these conclusions are valid for the inversion of other ambient conditions. For that purpose, we mix evaporation and surface ducts in a number of ways to obtain six different objective profiles in each Figure from Figure 3.18 to Figure 3.23 and repeat the test that was done to obtain the results given in Figure 3.17. The good choice of N_L depends on the objective profile, so we find it difficult to propose a sweet spot in N_L that generally allows good inversion results in this setup. We observe that the quality of the approximation at low value of N_L worsens as the objective profile get more complex (see Figure 3.21a vs. Figure 3.22a and Figure 3.21c vs. Figure 3.22c). We also observe that the low dimensional approach failed to be representative of global structure of objective profile as the profile gets more complex (see Figure 3.19b vs. Figure 3.20b). Also the performance of the refined approach is questionable. The 26-parameter approximation which used to give sufficiently good results in the previous steps of analysis struggles to resolve the synoptic structure of the objective profile with increasing profile complexity (see Figure 3.22d and Figure 3.23d). Clearly, quality resolution of the objective profile at $R = 10$ km requires a bit knowledge of what kind of profile shape we are looking for in the general case, even when the initial guess is near the objective profile. Such *a priori* knowledge is what we try to avoid using in this work. Now we are going to look for other ways to remedy this issue.

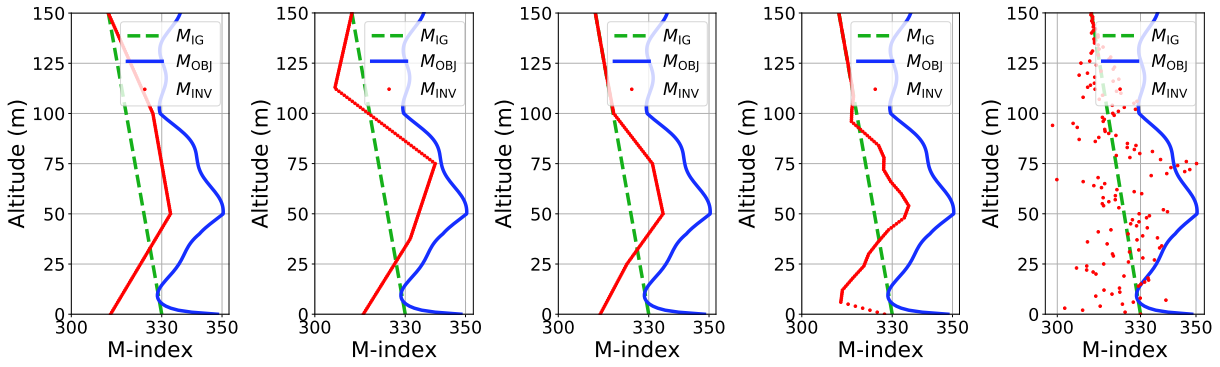

(a) (b) (c) (d) (e)

Figure 3.18: Inverted parameters in different parameter subspaces characterized by N_L. (a) $N_L = 4$, (b) $N_L = 5$, (c) $N_L = 7$, (d) $N_L = 26$, (e) $N_L = 151$.

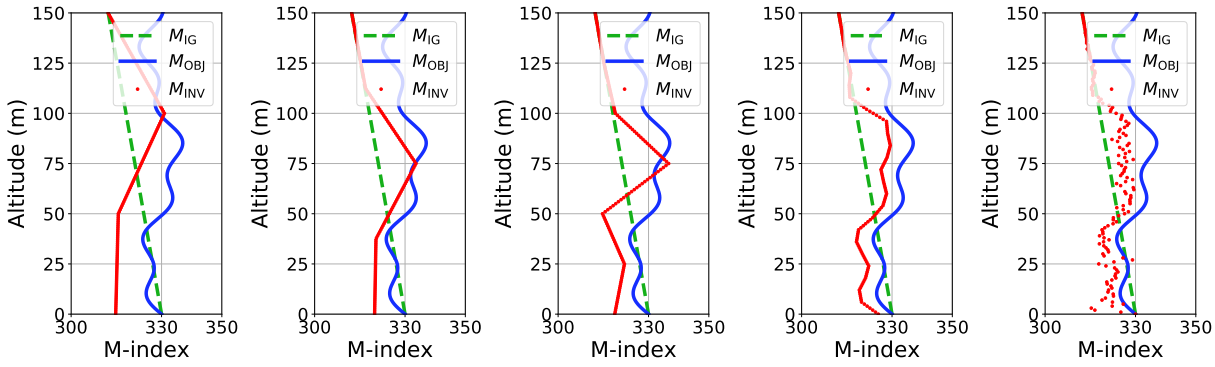

(a) (b) (c) (d) (e)

Figure 3.19: Inverted parameters in different parameter subspaces characterized by N_L. (a) $N_L = 4$, (b) $N_L = 5$, (c) $N_L = 7$, (d) $N_L = 26$, (e) $N_L = 151$.

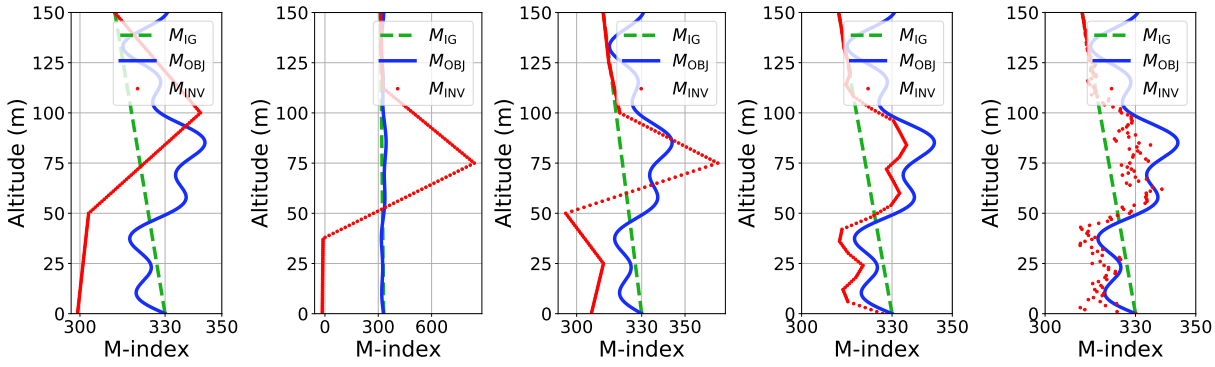

(a) (b) (c) (d) (e)

Figure 3.20: Inverted parameters in different parameter subspaces characterized by N_L. (a) $N_L = 4$, (b) $N_L = 5$, (c) $N_L = 7$, (d) $N_L = 26$, (e) $N_L = 151$.

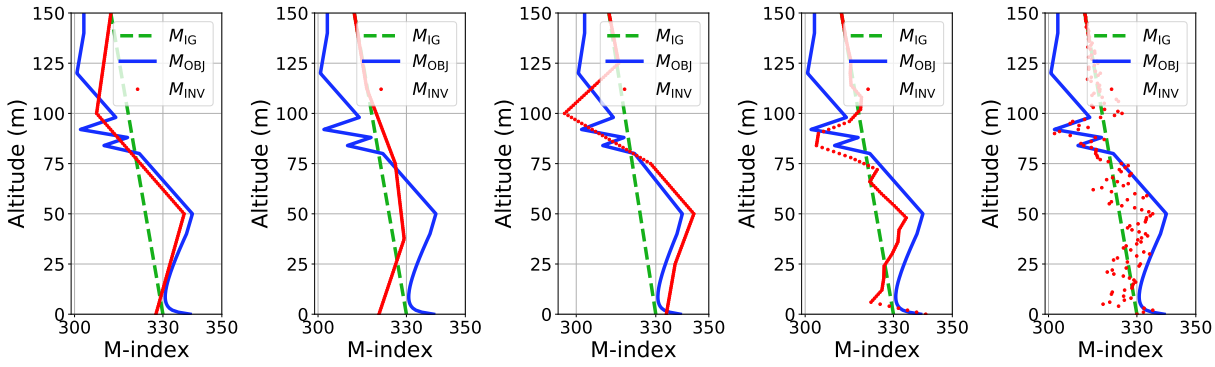

(a) (b) (c) (d) (e)

Figure 3.21: Inverted parameters in different parameter subspaces characterized by N_L. (a) $N_L = 4$, (b) $N_L = 5$, (c) $N_L = 7$, (d) $N_L = 26$, (e) $N_L = 151$.

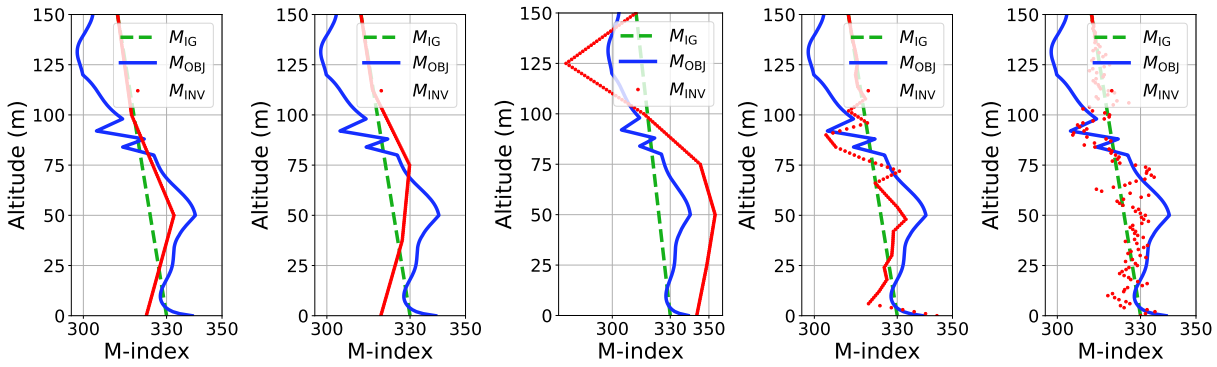

Figure 3.22: Inverted parameters in different parameter subspaces characterized by N_L. (a) $N_L = 4$, (b) $N_L = 5$, (c) $N_L = 7$, (d) $N_L = 26$, (e) $N_L = 151$.

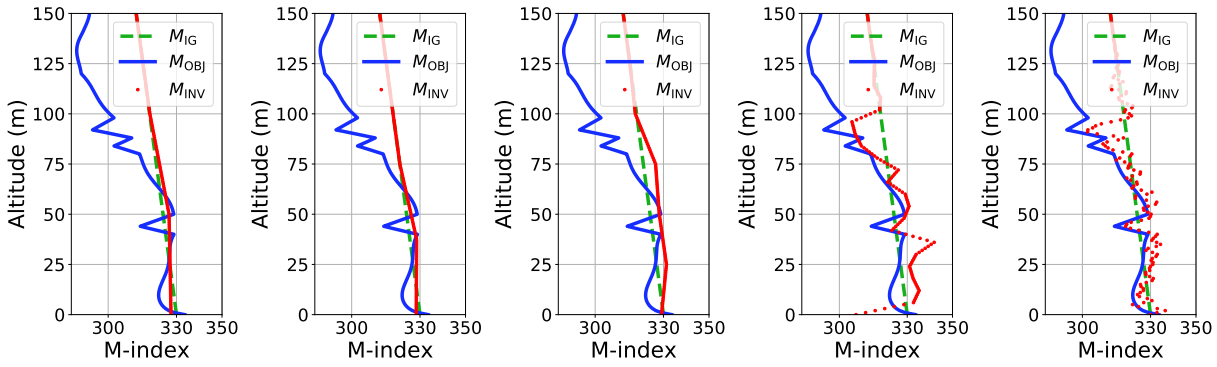

Figure 3.23: Inverted parameters in different parameter subspaces characterized by N_L. (a) $N_L = 4$, (b) $N_L = 5$, (c) $N_L = 7$, (d) $N_L = 26$, (e) $N_L = 151$.

3.6.2 Multiscale strategies

In the previous section, we see that parameter reduction does not remedy the inversion difficulty well. Neither the plain (standard) full-scale (i.e., 151-dimensional) adjoint-based inversion method nor the search space reduction technique work well in general. When they seem to work, it is either the initial guess is unrealistically close to the objective parameter, or it works only at some dimensions depending on the objective profile, or sometimes it is by chance that the objective parameter can be represented well at a particular dimension. Also note that there is not measurement noise. Overall, we cannot propose a generic strategy to get good results with a plain SSR as well.

The failure is partly due to the uninformed choice of reduction basis. Our goal in the beginning was to solve the problem without incorporating case-specific *a priori* information. Let us see if we can achieve that with Multiscale Parametrization Technique (MPT). If MPT works, we also need to discover what the limits of MPT are in our ideal conditions. We will check the range and objective profile complexity in particular, based on our experience from Section 3.6.1.2 and Chapter 2.

Our goal is to resolve the problem using the same uninformed choice of reduction basis. We expect to obtain a method that is applicable for a wider range of scenarios, without the need to invent a good reduction basis for each scenario.

3.6.2.1 Impact of multiscale parametrization at 10 km range

Here, our goal is to study the inversion of the objective profiles studied in Section 3.6.1.2 using Multiscale Parametrization Technique (MPT). We provide a quick summary of MPT to help the reader before describing what we present in order to show the results. The reader should visit Section 3.3.3.1 for details and a worked example presented in Figure 3.4.

We begin with choosing an increasing sequence of N_L up to N_z according to (3.13). Here, in short, N_L is given by $N_L = \{N_{L,i}\} \cup \{N_z\}$. The subscript i in $N_{L,i}$ denotes the resolution dimension (reduced parameter vector dimension) at the i-th level in the hierarchy. The inversion routine is initialized at M_{IG} at $i = 1$. Inversion result M_{INV} obtained at level i is projected to the $N_{L,i+1}$ dimensional subspace to be the initial guess of the inversion routine at level $i + 1$. The last element of the sequence is set equal to N_z so as to retrieve the inversion result at the full-scale resolution.

Firstly, we check whether there would be an improvement if MPT is used instead of plain Search Space Reduction (SSR). We verify this by repeating the analysis with MPT in a scenario which was previously studied with SSR to obtain the results given in Figure 3.17. The MPT strategy is built by combining the subspaces considered in Figure 3.17. This means we use the "parameter restriction" (the classical search space reduction technique) option in the Workflow 1 titled "Multiscale Parametrization". This MPT is just one of the techniques that we use so we distinguish it by labeling it as T-1 meaning Technique-One. The strategy is controlled by the sequence N_L. For this study it is given by:

$$\text{T-1-S-1}: \; N_L = \{4, 5, 7, 26, 151\} \tag{3.19}$$

where the strategy is labeled as T-1-S-1 meaning the Strategy-One of the Technique-One.

The results obtained with T-1-S-1 are given in Figure 3.24. In this Figure, the inversion results obtained at the five levels of (3.19) are given in order from Figure 3.24a to Figure 3.24e. The final result obtained with T-1-S-1 is that indicated with M_{INV} in Figure 3.24e. In this result, the synoptic structure of the objective parameter seems resolved at many altitude points. Qualitatively speaking, we notice a significant improvement in the inversion result in this Figure obtained with MPT as compared to that in Figure 3.17 obtained with a plain SSR.

We know that most of the information about the propagation condition is contained in the gradient information of the refractivity variation. Therefore, the quality of the result looks satisfactory. Therefore, we add more content in the presentation of the inversion results. In Figure 3.24f, we include the convergence history. In this Figure, we observe six order of magnitude of decrease in the cost function. The five intervals created by six vertical dashed lines in Figure 3.24f are used for indicating the convergence history that is obtained in the five levels in (3.19). We observe that cost function does not improve (decrease) at multiscale level $i = 2$ from iteration number 11 to 32. Therefore, the best inversion result obtained at the end of $i = 2$ is the result obtained at $i = 1$. For this reason, the initial guess at $i = 3$ (see M_{IG} in Figure 3.24c) is the inversion result obtained at $i = 1$ (see M_{INV} in Figure 3.24a), so the computational resources are wasted at $i = 2$. We remark on this waste because we will cure it by upgrading the technique

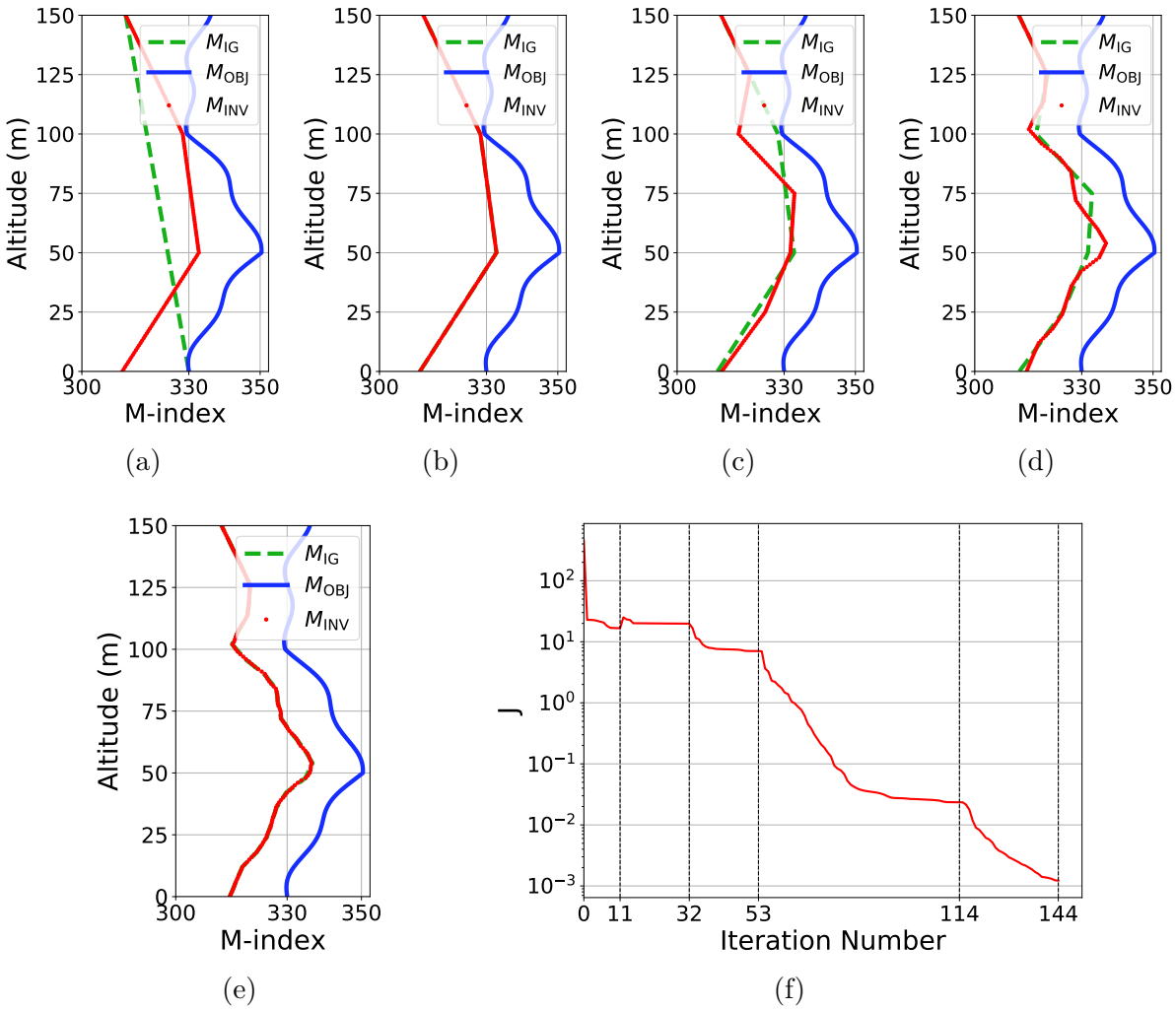

Figure 3.24: Inverted parameters at all multiscale levels in the hierarchy using T-1-S-1. (a) $N_L = 4$, (b) $N_L = 5$, (c) $N_L = 7$, (d) $N_L = 26$, (e) $N_L = 151$, (f) Convergence history.

and make the algorithm efficient.

We expand our analysis by presenting the contour plots of the wave field u. The goal is to understand how close the estimated radar coverage diagram would be to the truth. To make the comparison, we present the wave field u^{obs} and u_m^{sim}, which correspond to the objective and inverted parameter respectively, in dBV/m using:

$$|u(r,z)|_{\text{dB}} = 20\ \log_{10}(|u(r,z)|) \tag{3.20}$$

in Figure 3.25a and Figure 3.25b respectively. Their difference is presented using:

$$|\text{Error}(u^{\text{obs}}, u_m^{\text{sim}})|_{\text{dB}} = 10\ \log_{10}(||u^{\text{obs}}(r,z)|^2 - |u_m^{\text{sim}}(r,z)|^2|) \tag{3.21}$$

in Figure 3.25c. We observe that the true and predicted wave fields in Figure 3.25a and Figure 3.25b are very close. Although the texture of the wave field looks the same, we cannot perceive if there is any shift in the radar lobes due to the shift of the inverted parameter from the objective as shown in Figure 3.24e. For that reason, we check the difference of the wave fields in Figure Figure 3.25c. Their difference at the receiver antenna position $R = 10$ km is low around -25 dBV/m but the error exceeds that level in the airspace. In Figure 3.25c, we observe

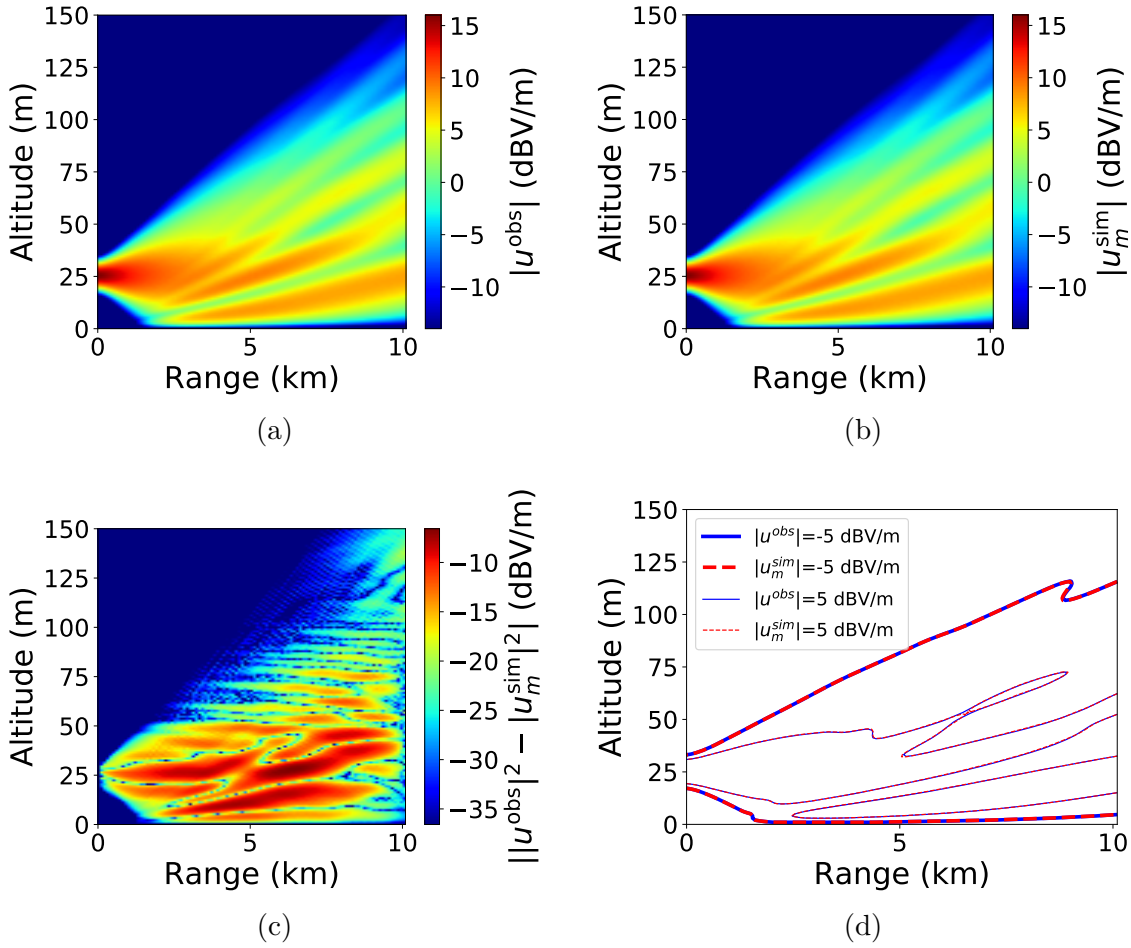

Figure 3.25: Comparison of true and predicted wave field. (a) True wave field, (b) Predicted wave field. (c) Difference between true and predicted wave field (d) Isolines of true and predicted wave field.

that the error increases with distance from the receiver antenna. The error seems to remain lower than -5 dBV/m in this example. This error does not come from the aforementioned leftward shift in M_{INV} from M_{OBJ} in the inversion results shown in Figure 3.24e. In order to check this, we have shifted M_{INV} manually on top of M_{OBJ} such that $||M_{\text{OBJ}}||_\infty - ||M_{\text{INV}}||_\infty$ becomes zero. We measured the norm of the error in the entire airspace with:

$$\epsilon_\Omega = \frac{\left\| |u^{\text{obs}}(r,z)|^2 - |u_m^{\text{sim}}(r,z)|^2 \right\|_2}{\left\| |u^{\text{obs}}(r,z)|^2 \right\|_2}. \tag{3.22}$$

The norm of the error in the entire airspace did not change, it remained identical until the 13-th significant digit. Therefore, we concluded that the shift in the inversion result does not have a prominent impact on the predicted radar coverage. What is important is to retrieve the synoptic structure of M_{OBJ}. However, it is not easy to say that two wave field textures are the same in Figure 3.25a and in Figure 3.25b. In order to show that they are very close, we draw the isolines of those contours at 5 dBV/m and -5dBV/m in Figure 3.25d.

3.6.2.2 Impact of the objective profile at 10 km range

Secondly, we change the objective parameter to verify if the comments made in the previous analysis are valid for other objective profiles as well. For that purpose, we try to invert some of the objective profiles studied with SSR in Section 3.6.1.2. The inversion results using T-1-S-1 are given in the same order as in Section 3.6.1.2 from Figure 3.26 to Figure 3.31. In these Figures, we observe that 151-parameter inversion results contain less oscillations. In Figure 3.26 and Figure 3.27, we observe that the synoptic structure of the objective parameter is resolved accurately without oscillations at many altitude points. In all the results from Figure 3.26 to Figure 3.31, we observe that the upper and lower ends of the objective profile is resolved inaccurately, except in Figure 3.27 at sea level. This means there is less difficulty in resolving the details in interior part of the objective profile. Resolving the lower end of the objective profile accurately is important in the real-world applications because that part can contain strong gradients in reality, so it can diminish the accuracy of radar coverage predictions. The results in Figure 3.28 shows that increasing complexity of the objective profile might make the inversion process divergent from the admissible parameter set. The results in Figure 3.29a, Figure 3.30a and Figure 3.31a shows that more complex profiles are inverted with more oscillations in parameter. This makes the coverage predictions less accurate: see the increase of error levels from Figure 3.29e to Figure 3.31e and difference between the isolines of the true and predicted wave fields from Figure 3.29f and Figure 3.31f.

Some important conclusions of the analysis are as follows: (1) computational resources might be wasted at some scales, (2) a good representation of data might not exist in a low dimensional subspace in the admissible bounds, (3) resolution of the parameter near sea level might be inaccurate. Although there are some other results that could be emphasized at the end of this section, we restrict our focus on these drawbacks of our approach to keep the discussion short. The three weaknesses which we labeled are going to lead us to improved techniques in the following sections.

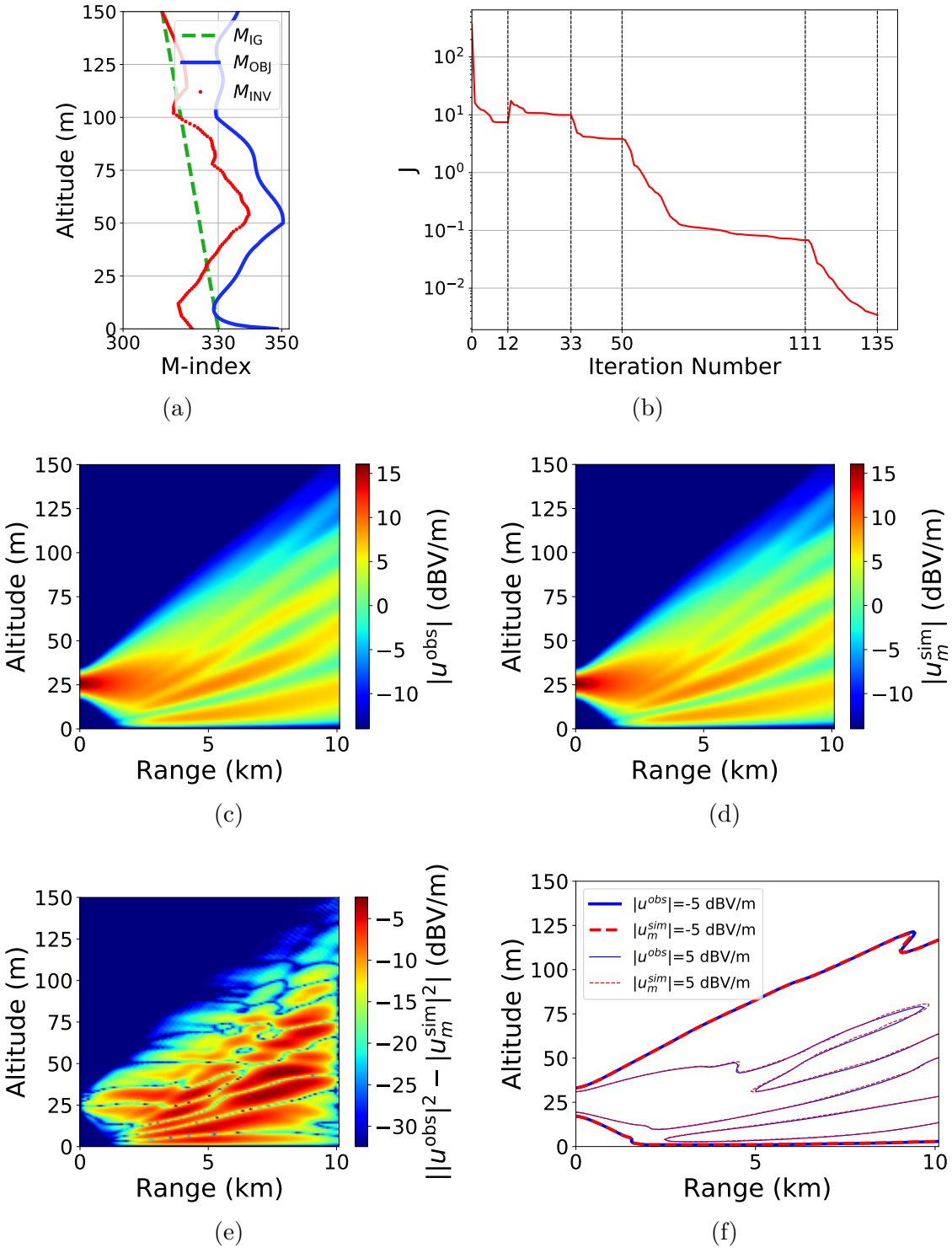

Figure 3.26: Inversion results. (a) Inverted parameter, (b) Convergence history, (c) True wave field, (d) Predicted wave field. (e) Difference between true and predicted wave field, (f) Isolines of true and predicted wave field.

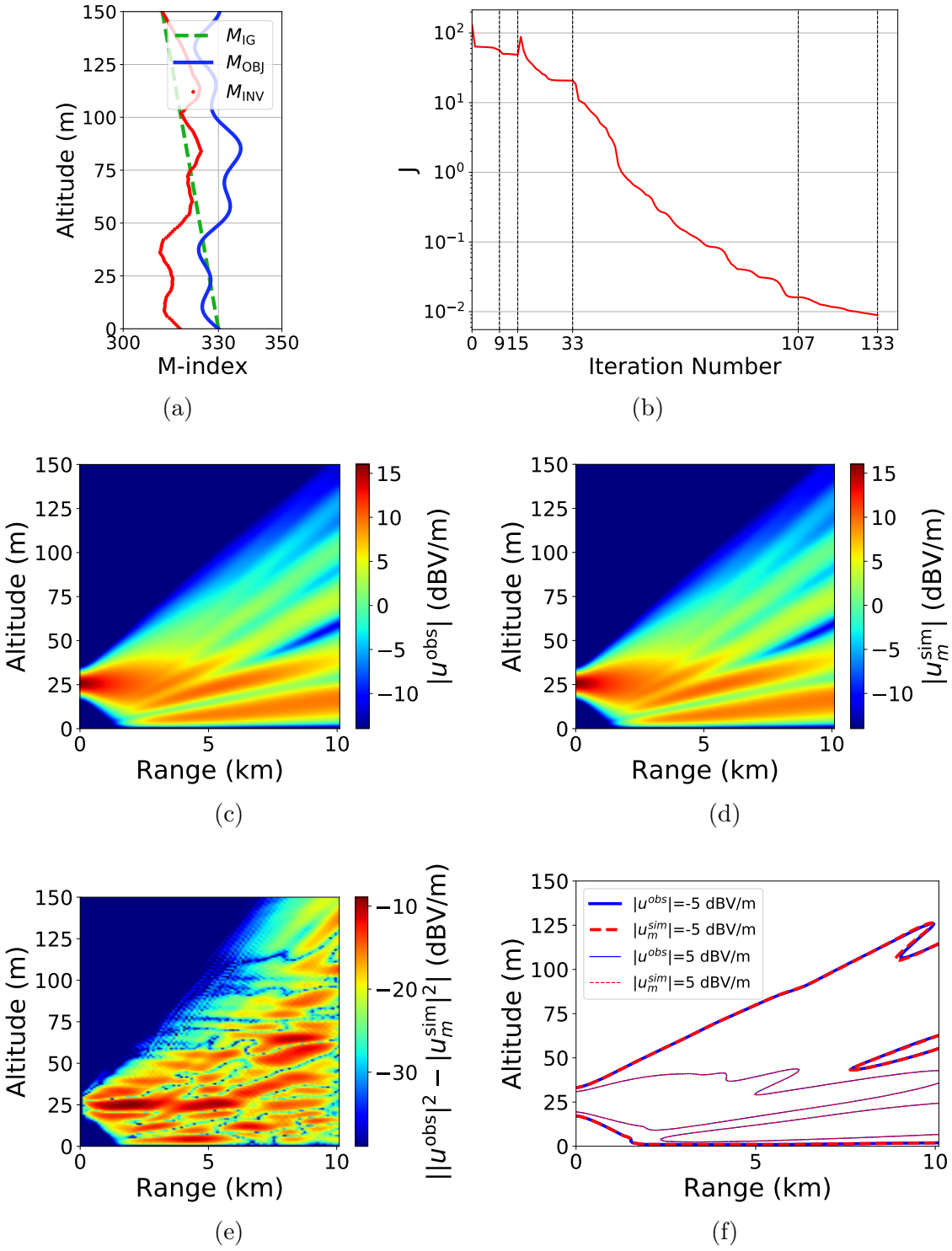

Figure 3.27: Inversion results. (a) Inverted parameter, (b) Convergence history, (c) True wave field, (d) Predicted wave field. (e) Difference between true and predicted wave field, (f) Isolines of true and predicted wave field.

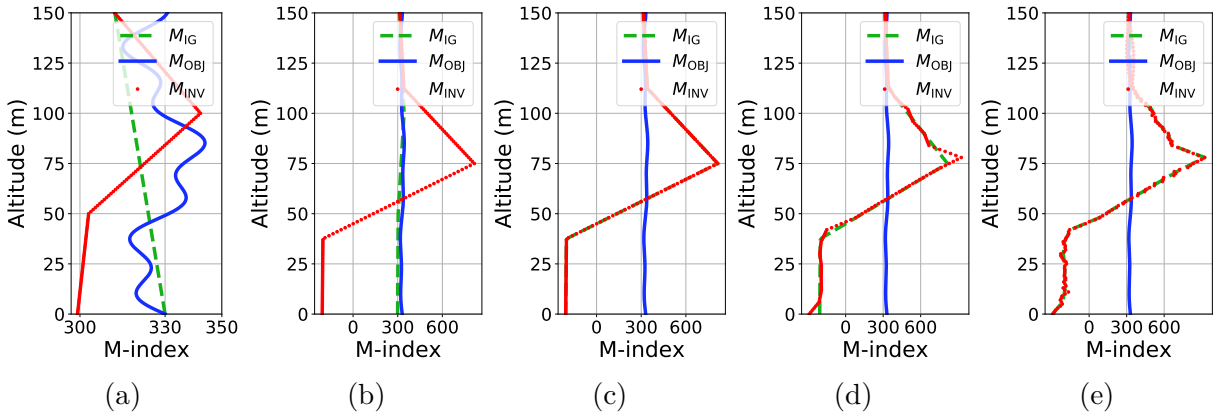

(a) (b) (c) (d) (e)

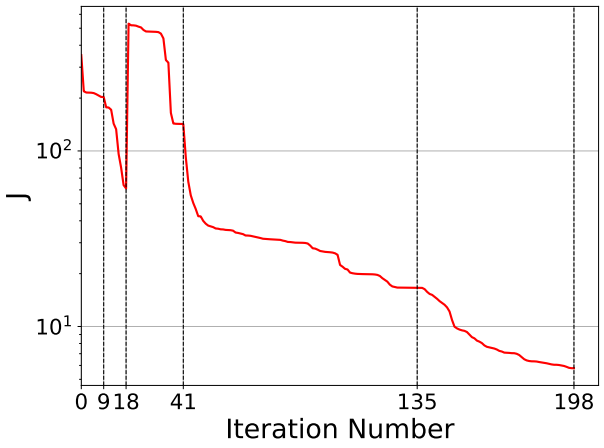

(f)

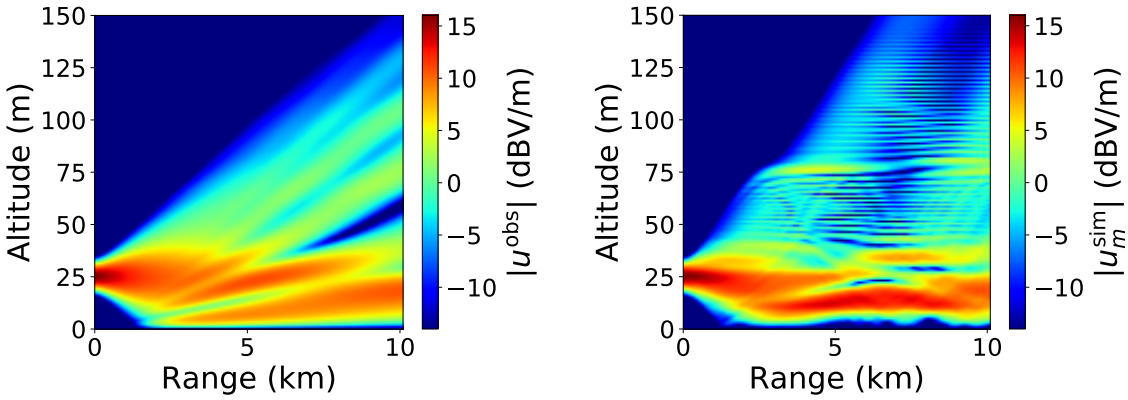

(g) (h)

Figure 3.28: Inverted parameters using multiscale hierarchy composed of different parameter subspaces characterized by N_L. (a) $N_L = 4$, (b) $N_L = 5$, (c) $N_L = 7$, (d) $N_L = 26$, (e) $N_L = 151$, (f) Convergence history, (g) True wavelfield, (h) Predicted wave field. (i) Difference between true and predicted wave field.

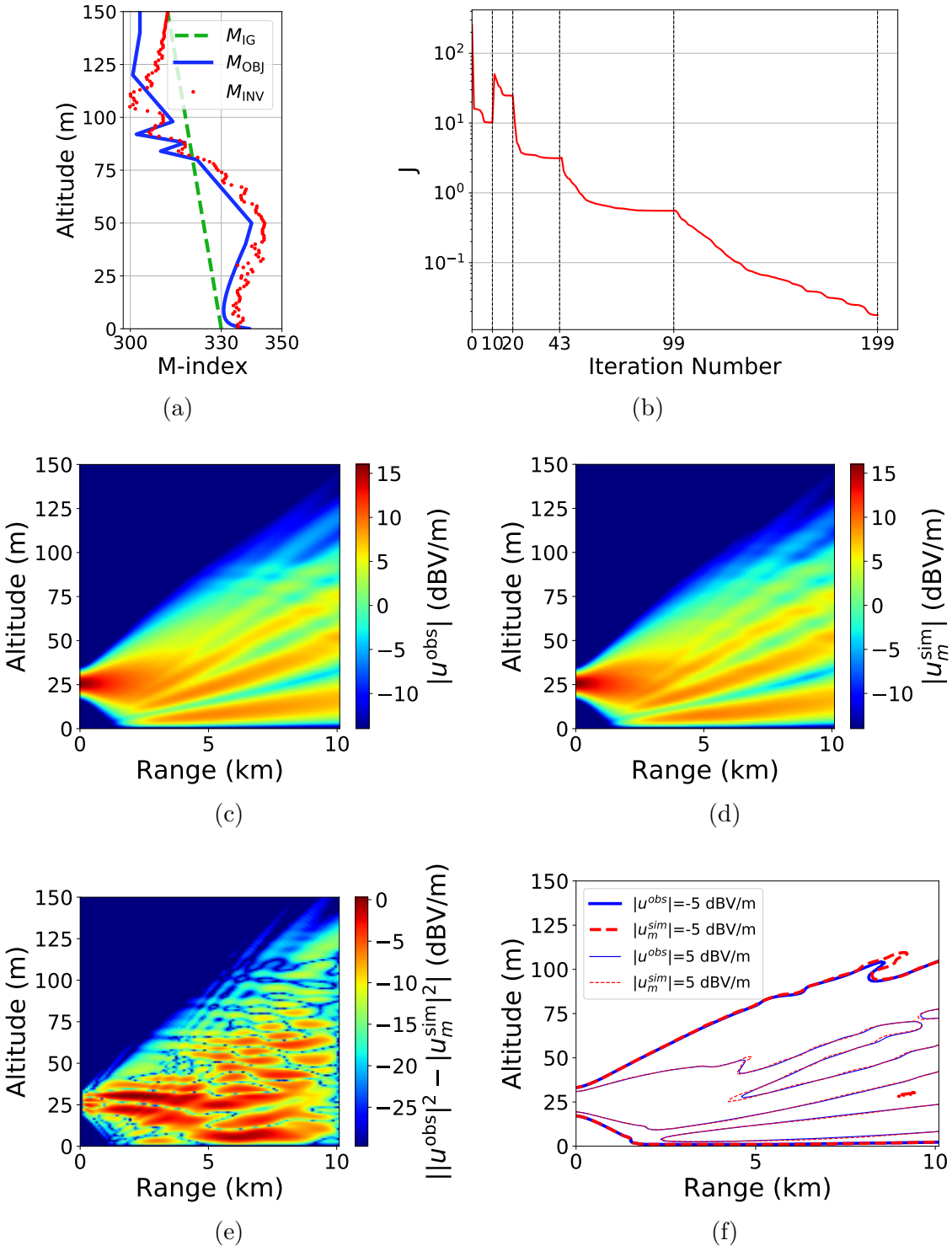

Figure 3.29: Inversion results. (a) Inverted parameter, (b) Convergence history, (c) True wave field, (d) Predicted wave field. (e) Difference between true and predicted wave field, (f) Isolines of true and predicted wave field.

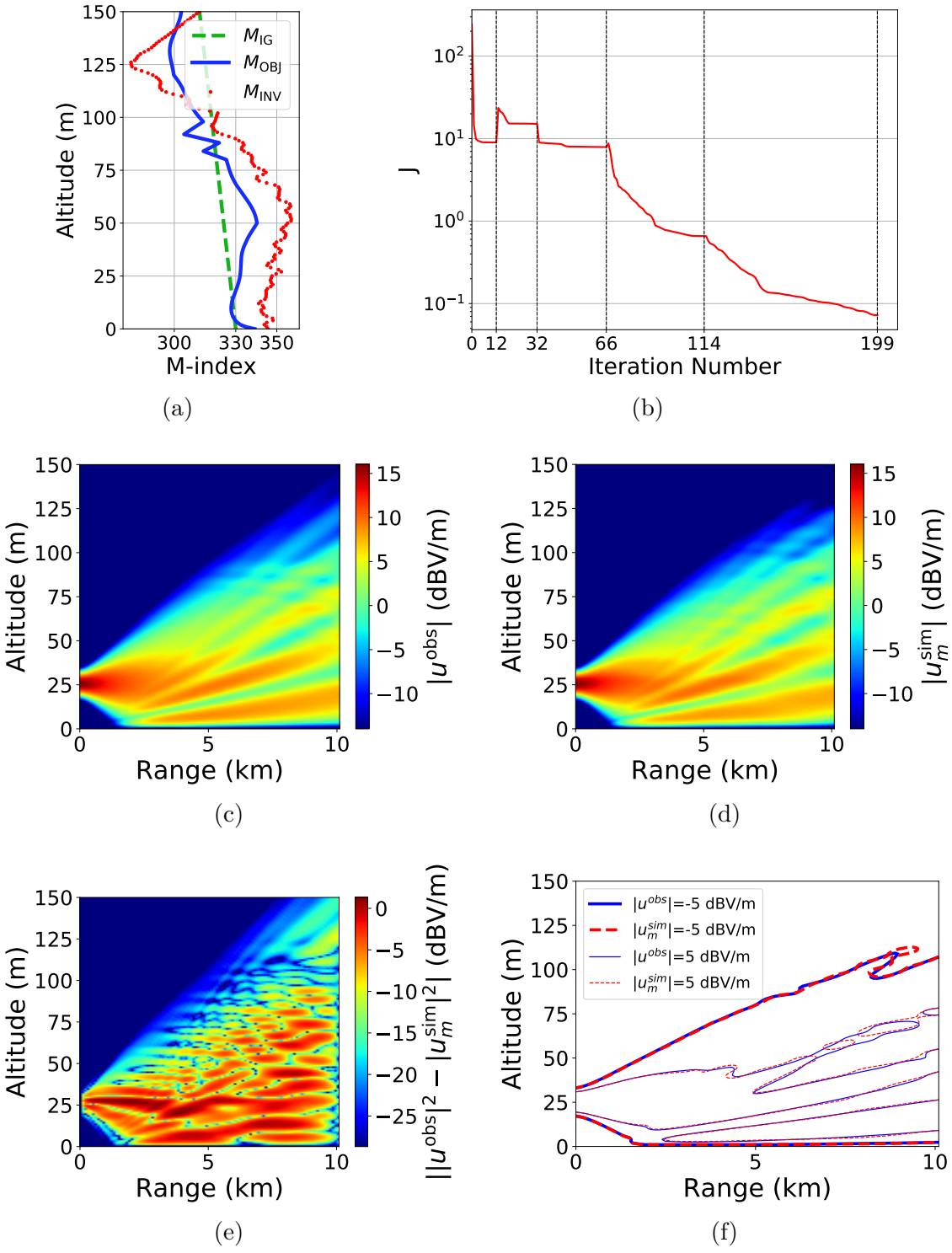

Figure 3.30: Inversion results. (a) Inverted parameter, (b) Convergence history, (c) True wave field, (d) Predicted wave field. (e) Difference between true and predicted wave field, (f) Isolines of true and predicted wave field.

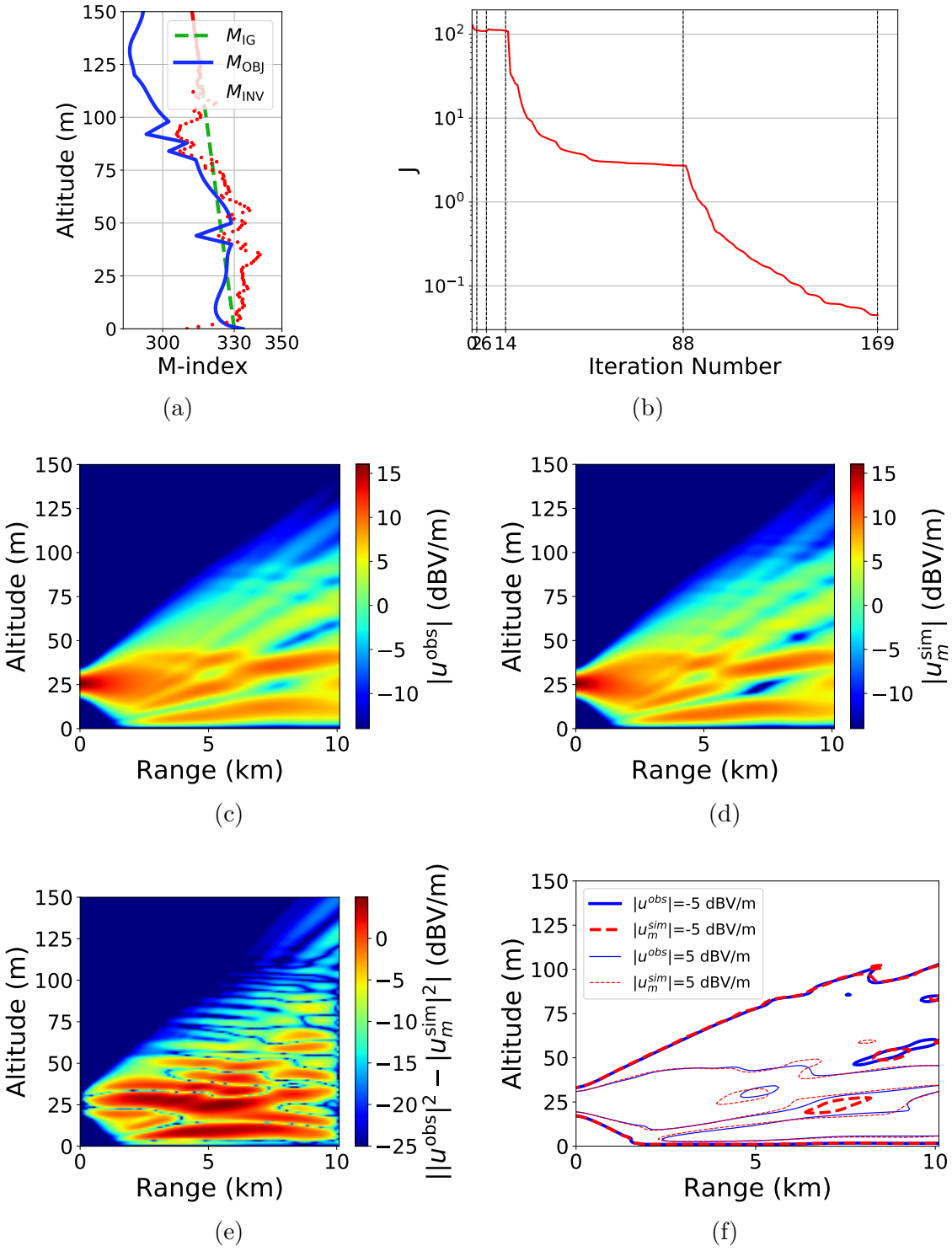

Figure 3.31: Inversion results. (a) Inverted parameter, (b) Convergence history, (c) True wave field, (d) Predicted wave field. (e) Difference between true and predicted wave field, (f) Isolines of true and predicted wave field.

3.6.2.3 Impact of refinement strategy at 10 km range

In this section, we try to improve the inversion results obtained using T-1-S-1 by analyzing the impact of the rate of increase in N_L. In order to increase the chance of success, we choose a proper rate of refinement in the strategy. For this purpose, we create the following refinement strategies with the same technique to compare the results:

$$\text{T-1-S-2}: \; N_L := \{N_{L,i} = 3 \times 4^{i-1} + 1, \; N_{L,i} < 151\} \cup \{151\} \; , \tag{3.23a}$$

$$\text{T-1-S-3}: \; N_L := \{N_{L,i} = 3 \times 3^{i-1} + 1, \; N_{L,i} < 151\} \cup \{151\} \; , \tag{3.23b}$$

$$\text{T-1-S-4}: \; N_L := \{N_{L,i} = 3 \times 2^{i-1} + 1, \; N_{L,i} < 151\} \cup \{151\} \; , \tag{3.23c}$$

$$\text{T-1-S-5}: \; N_L := \{N_{L,i} = 3i + 1, \; N_{L,i} \leq 40\} \cup \{151\}. \tag{3.23d}$$

For instance, T-1-S-2 is characterized by $N_L = \{4, 13, 49, 151\}$. Note that in the case of T-1-S-2, the refinement is done the least progressively whereas it is done the most gradually in T-1-S-5. However, we stop the refinement earlier in T-1-S-5 because there would be many levels making the inversion very costly otherwise. We see the inversion results in Figure 3.32 for the strategies described in (3.23). The coverage prediction error is given in Table 3.2. We observe that prediction quality increases with a more progressive approach in refinement with one exception: T-1-S-2 vs. T-1-S-3.

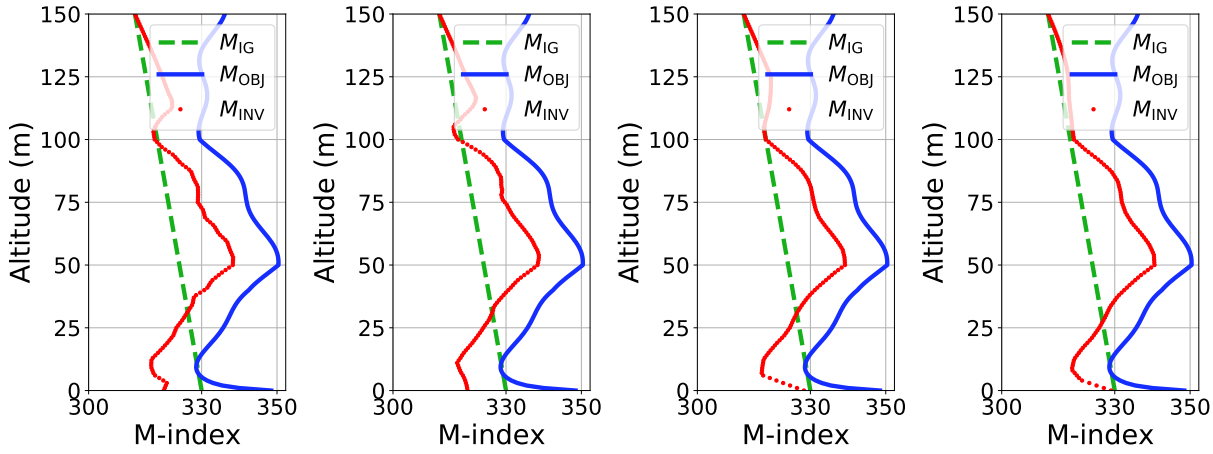

Figure 3.32: Inversion for four different refinement strategies. (a) T-1-S-2, (b) T-1-S-3, (c) T-1-S-4, (d) T-1-S-5.

	T-1-S-2	T-1-S-3	T-1-S-4	T-1-S-5
ϵ_Ω	1.78%	1.97%	0.59%	0.27%

Table 3.2: Prediction error for T-1 for different strategies.

We now check if the objective profiles whose synoptic structure are not resolved well in Section 3.6.2.1 could be retrieved using T-1-S-5. For this reason, we repeat the inversion test for the objective profiles studied previously using T-1-S-1 in Figure 3.26, Figure 3.29, Figure 3.30 and Figure 3.31. The results obtained using T-1-S-5 are given in Figure 3.33, Figure 3.34, Figure 3.35 and Figure 3.36 respectively. In these Figures, we observe an overall decrease of error in the accuracy of the coverage prediction. More progressive refinement seems to improve the results. There

is a potential that some difficult problems could be solved better if more progressive refinement can be afforded.

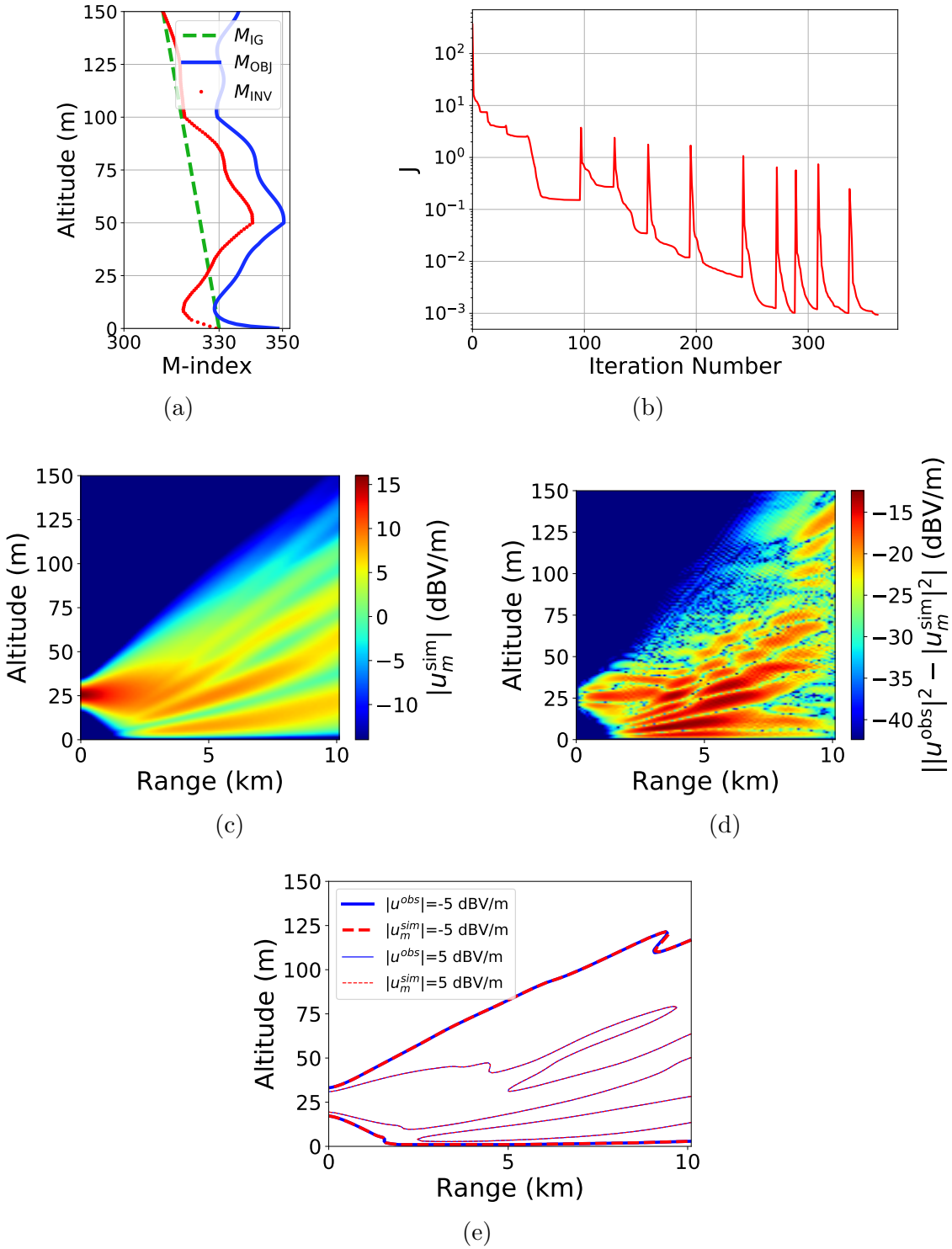

Figure 3.33: Inversion results using T-1-S-5. (a) Parameters, (b) Convergence history, (c) Predicted wave field. (d) Difference between true and predicted wave field, (e) Isolines of true and predicted wave field.

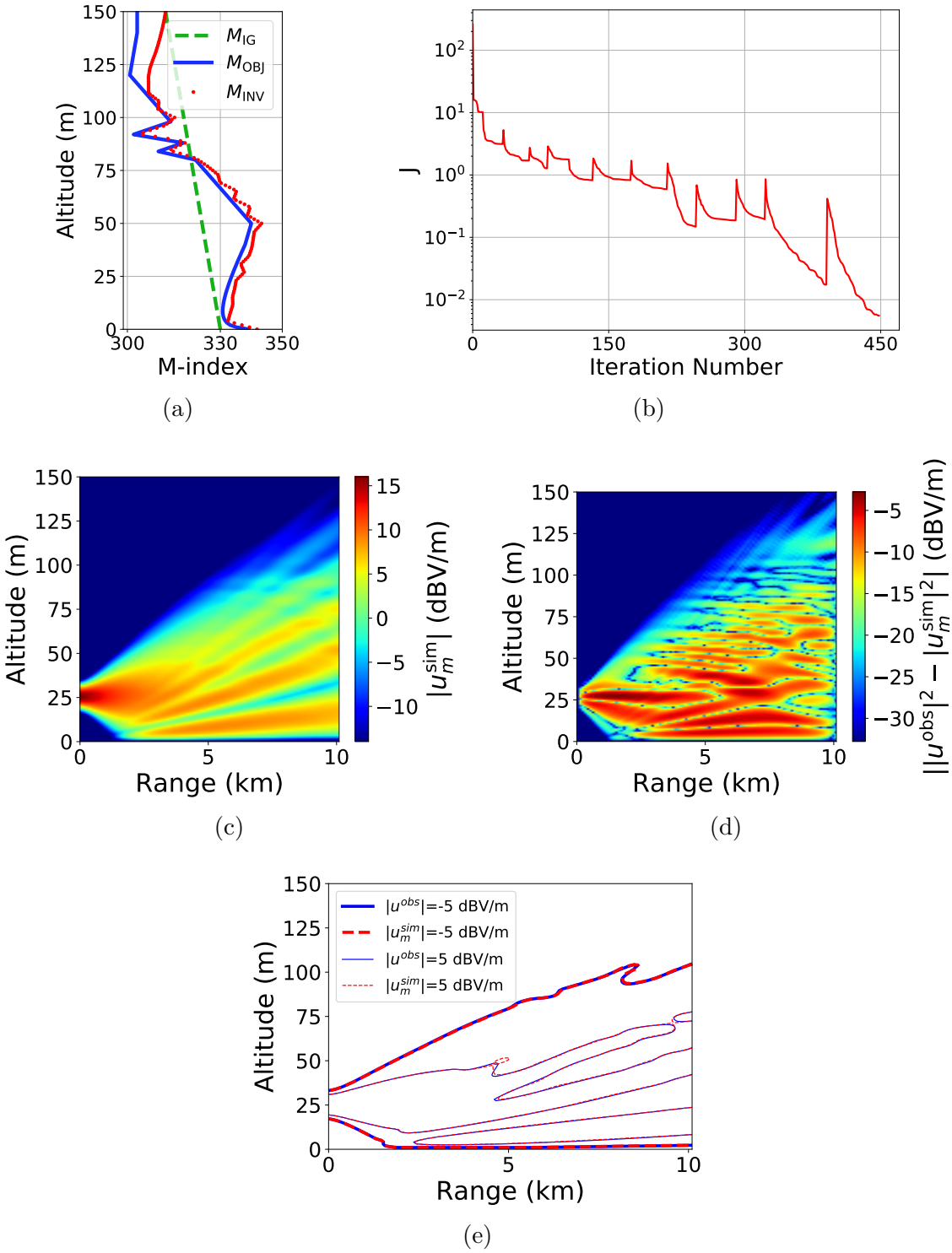

Figure 3.34: Inversion results using T-1-S-5. (a) Parameters, (b) Convergence history, (c) Predicted wave field. (d) Difference between true and predicted wave field, (e) Isolines of true and predicted wave field.

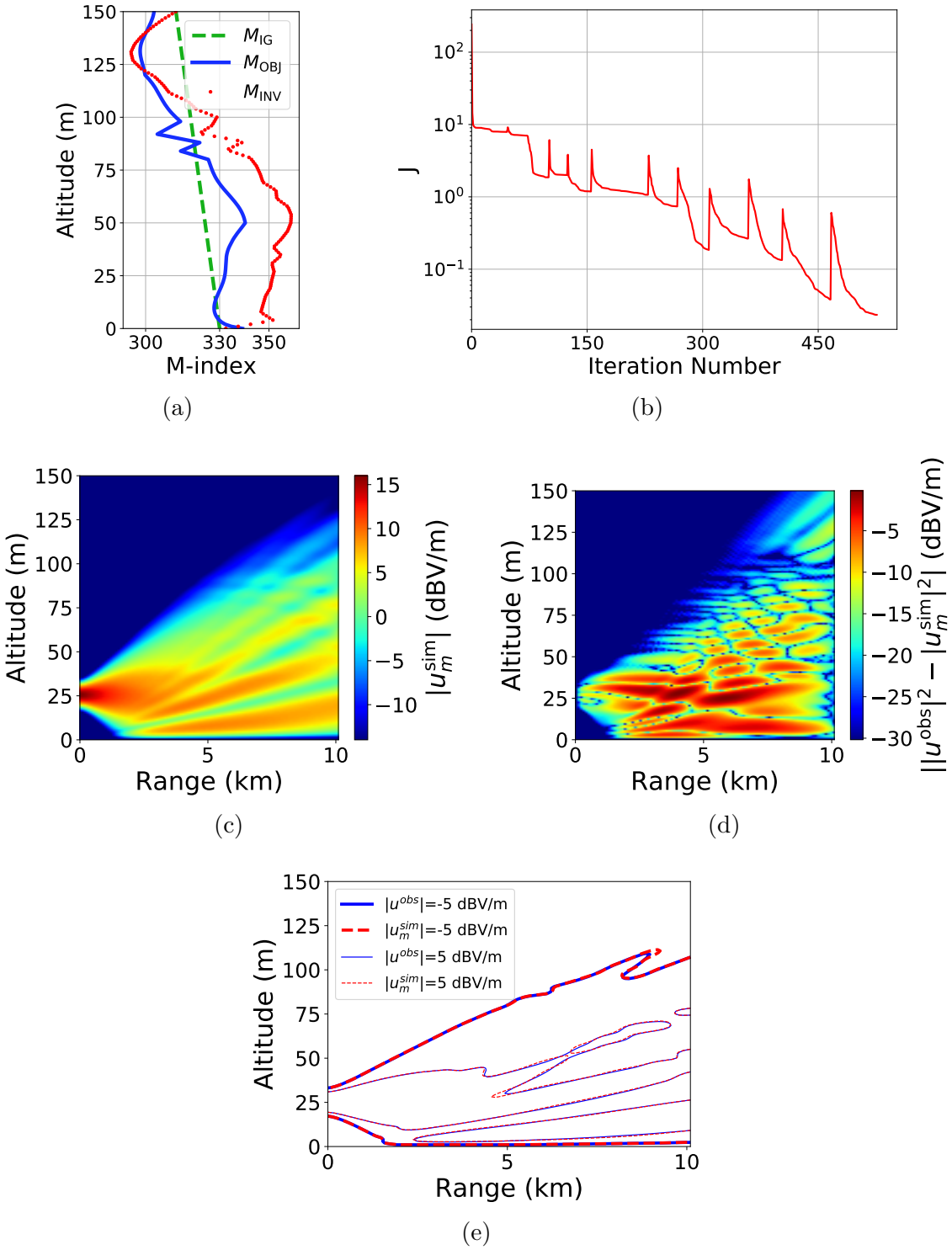

Figure 3.35: Inversion results using T-1-S-5. (a) Parameters, (b) Convergence history, (c) Predicted wave field. (d) Difference between true and predicted wave field, (e) Isolines of true and predicted wave field.

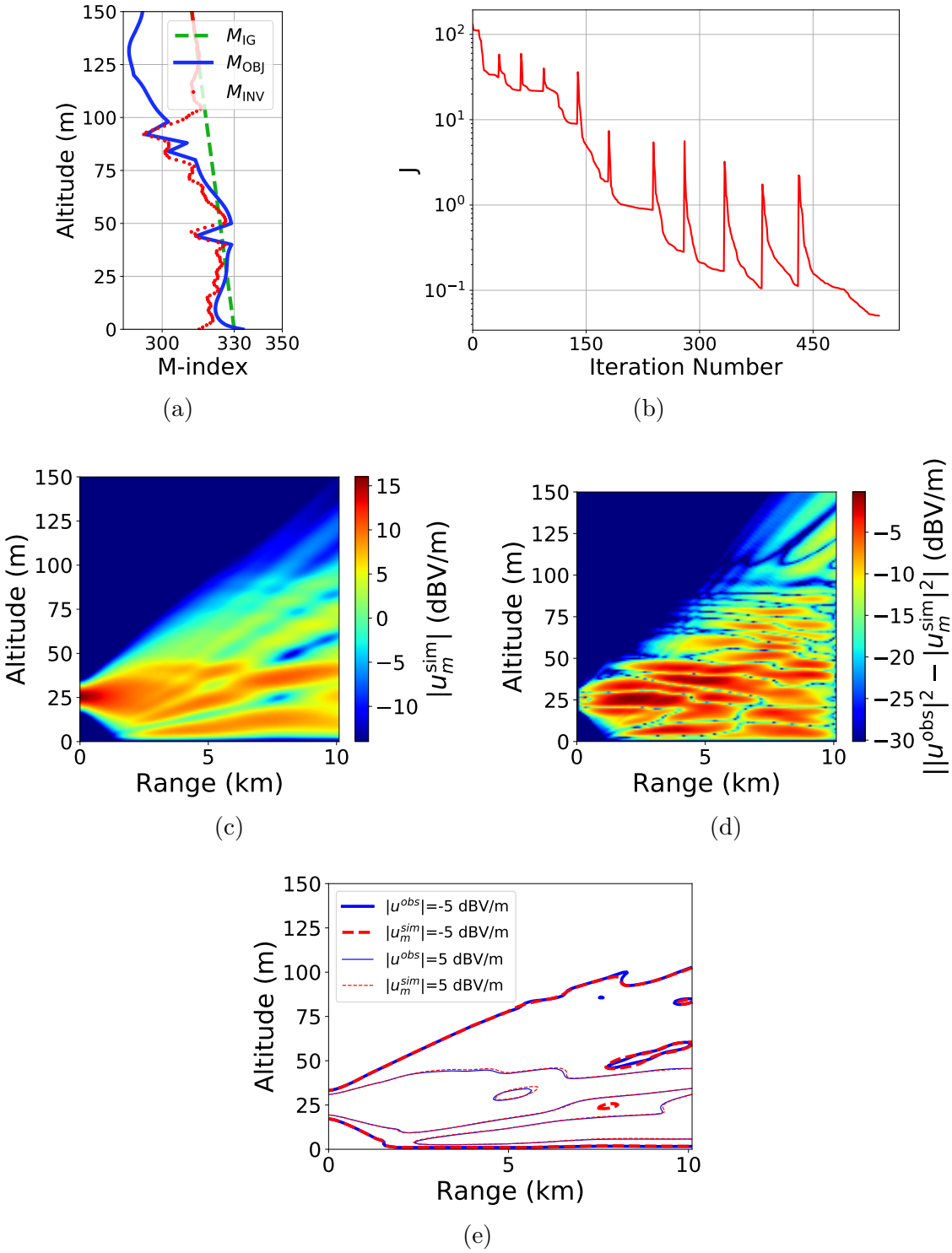

Figure 3.36: Inversion results using T-1-S-5. (a) Parameters, (b) Convergence history, (c) Predicted wave field. (d) Difference between true and predicted wave field, (e) Isolines of true and predicted wave field.

3.6.2.4 Impact of initial guess at 10 km range

In this section, we want to see if the conclusions made in Section 3.6.2.3 are valid for other objective and initial guess profiles. For that purpose, we apply T-1-S-5 to the objective profile which has been studied previously in Figure 3.28 and Figure 3.30 using T-1-S-1. We choose these two profiles because they were difficult to invert without progressive refinement, so their dependence to the initial guess could be noticeable.

The inversion results obtained for four different initial guesses are given in Figure 3.37 and Figure 3.38 respectively. Although we observe some dependence on the initial guess, the synoptic structure of the objective profile is retrieved in the interior. However, the synoptic structure depends more on the initial guess at the upper and lower boundaries. In addition, the isolines of the wave field for the four inversions of the two objective profiles are presented in Figure 3.39 and Figure 3.41 respectively. Similarly, the difference between the true and the predicted wave fields are given in Figure 3.40 and Figure 3.42 respectively. The prediction quality does not depend much on the initial guess for these test cases.

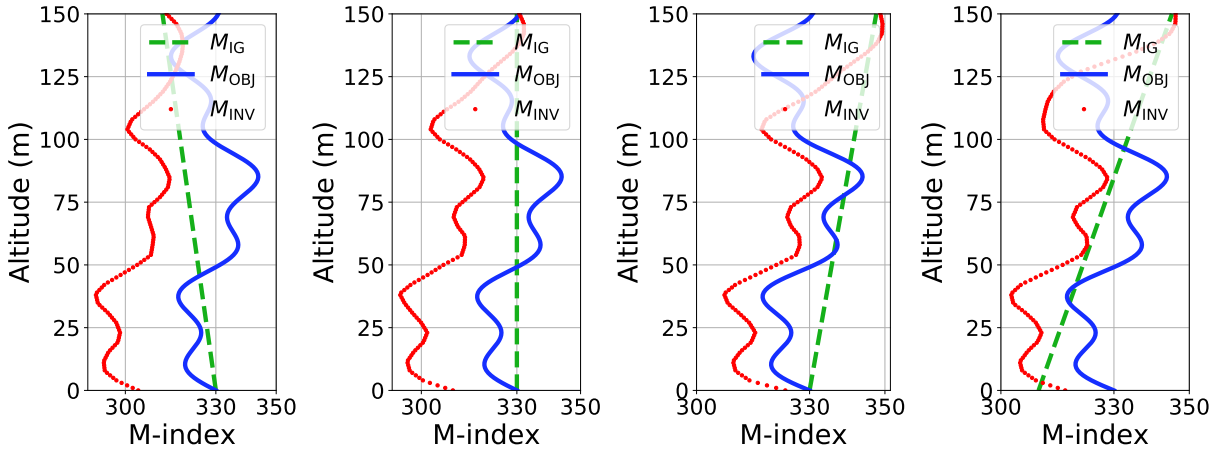

Figure 3.37: Inversion for four different initial guesses.

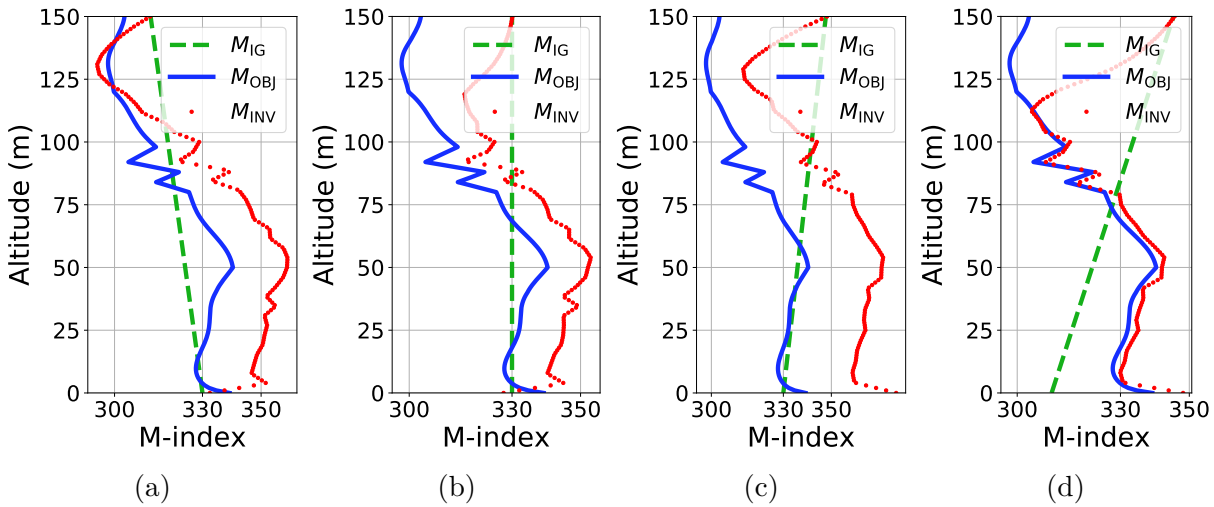

Figure 3.38: Inversion for four different initial guesses.

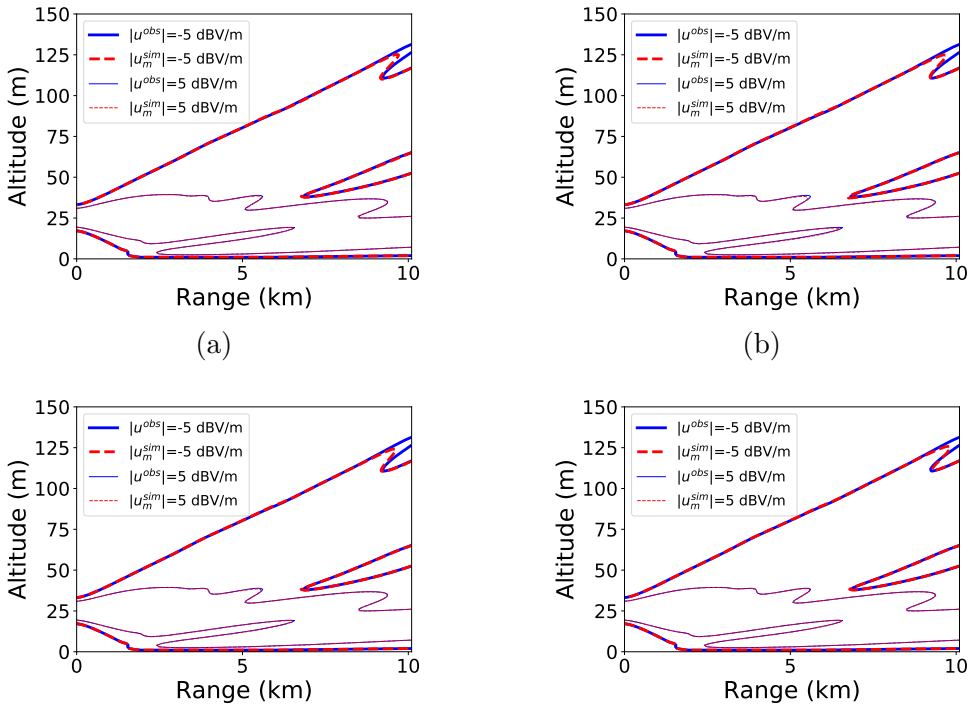

Figure 3.39: Isolines of the true and the predicted wave field for four different initial guesses presented in Figure 3.37 respectively.

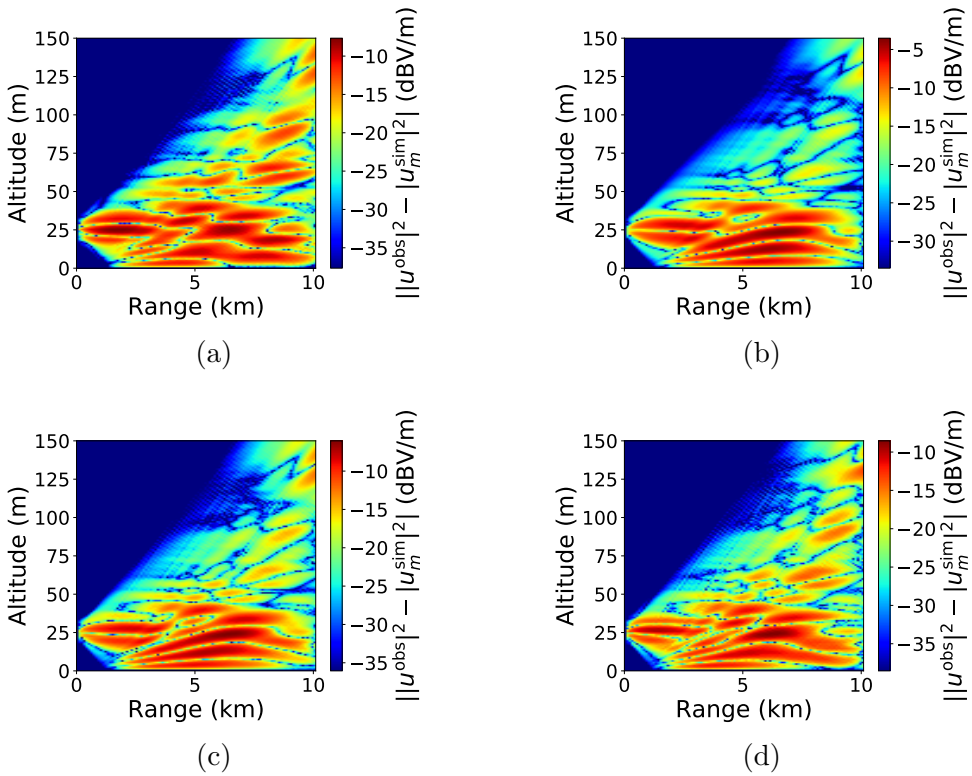

Figure 3.40: Difference between true and predicted wave field for four different initial guesses presented in Figure 3.37 respectively.

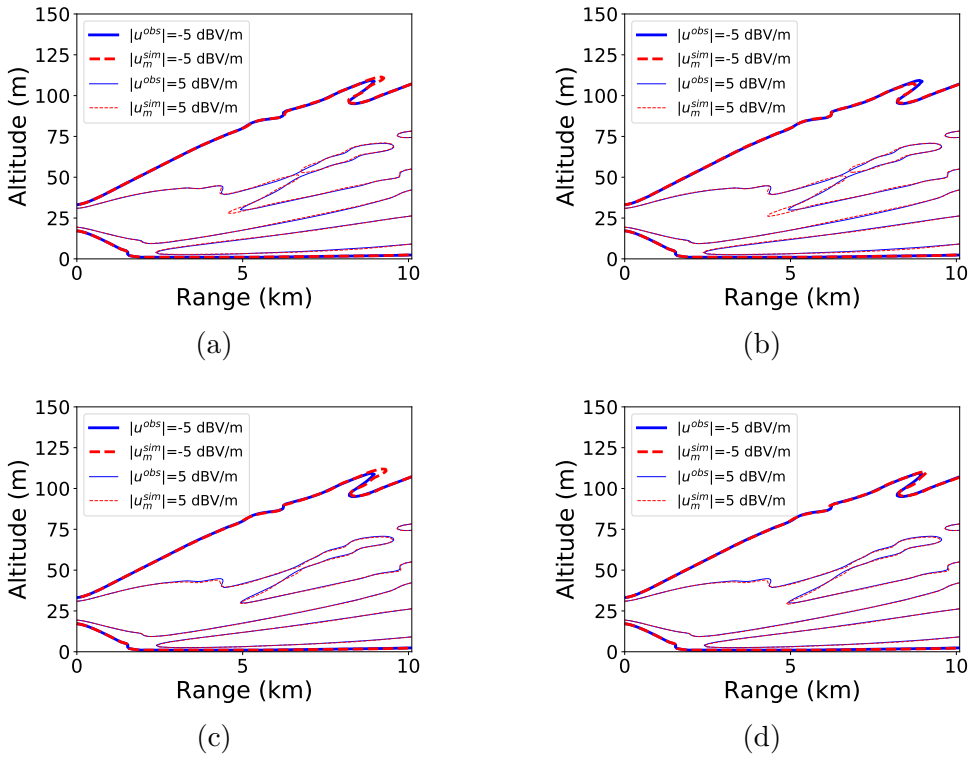

Figure 3.41: Isolines of the true and the predicted wave field for four different initial guesses presented in Figure 3.38 respectively.

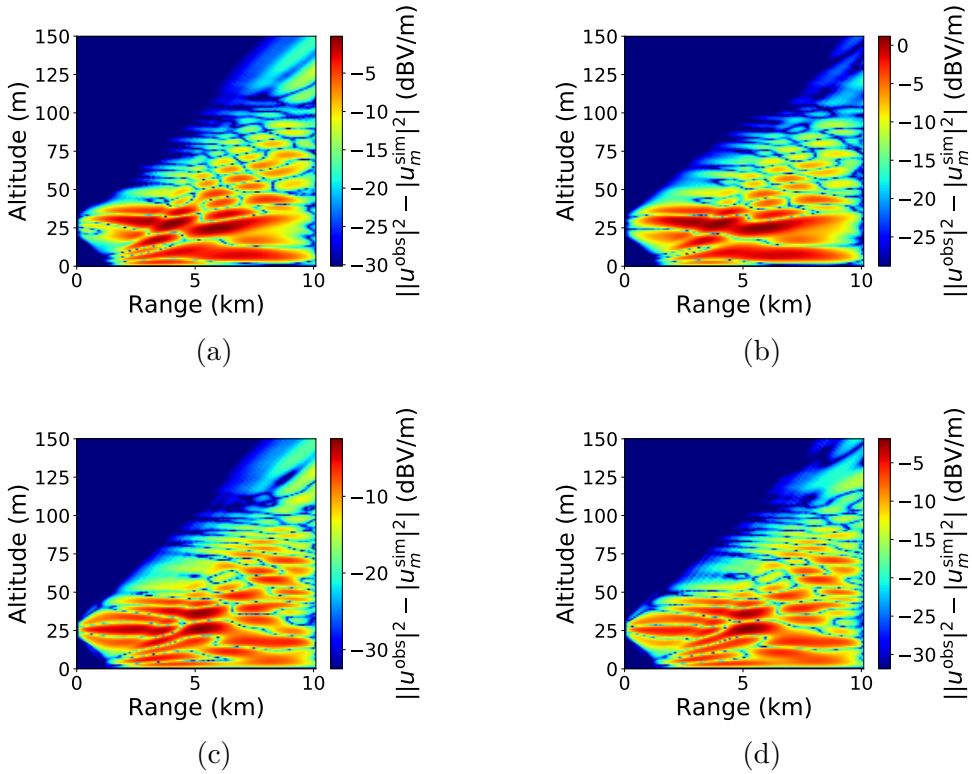

Figure 3.42: Difference between true and predicted wave field for four different initial guesses presented in Figure 3.38 respectively.

3.6.2.5 Preliminary results at 30 km range

In this section, we perform some inversion tests with the refinement strategies T-1-S-2, T-1-S-3, T-1-S-4 and T-1-S-5, so as to conduct preliminary exploration for applications at longer ranges. We study the objective profiles presented in Figure 3.6b and Figure 3.6c at $R = 30$ km. The inverted parameters are given in Figure 3.43 and Figure 3.44 respectively. The corresponding wave fields, difference from the true wave field and comparison of isolines are found in the following.

We observe that it is more difficult to invert at $R = 30$ km these two refractivity profiles which were relatively simple to study at $R = 10$ km. It is also difficult to reach general conclusions at this configuration. However, there is a certain level of success in predicting the radar holes with T-1 that can be inferred from Figure 3.49 and Figure 3.50. It is unclear why more progressive refinement (T-1-S-4) does not give the best result in Figure 3.50. Results with other previously studied objective profiles are not good (not shown here). It seems that we are around the limits of what we can achieve with MPT with this linear interpolation basis.

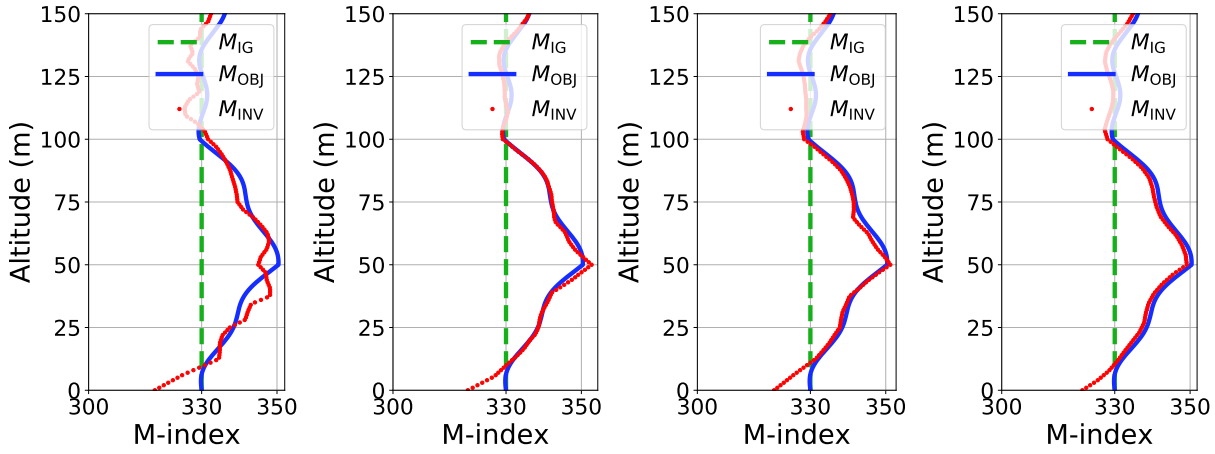

Figure 3.43: Inversion at $R = 30$ km. (a) T-1-S-2, (b) T-1-S-3, (c) T-1-S-4, (d) T-1-S-5.

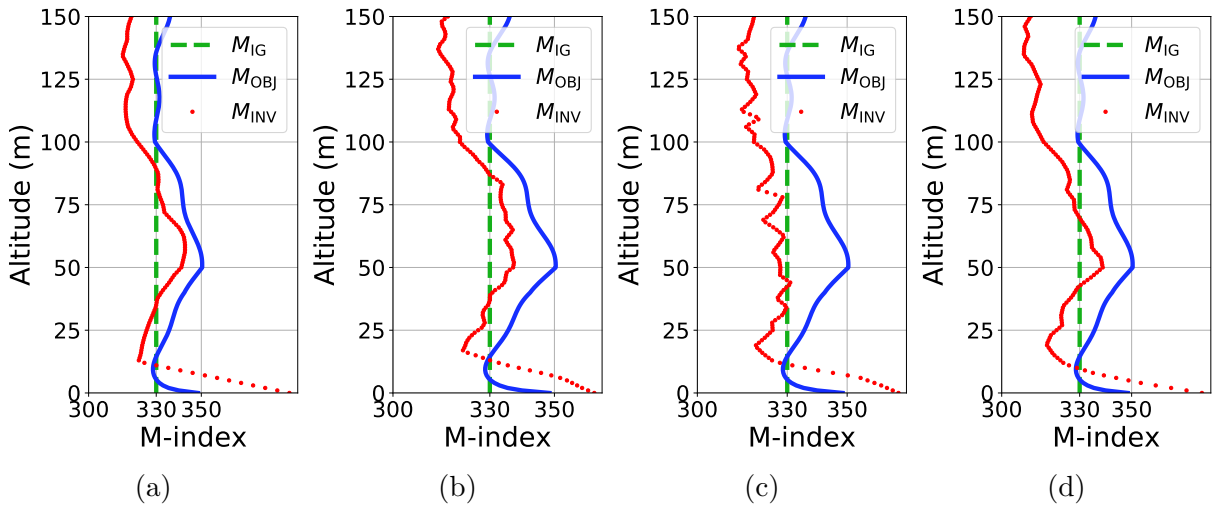

Figure 3.44: Inversion at $R = 30$ km. (a) T-1-S-2, (b) T-1-S-3, (c) T-1-S-4, (d) T-1-S-5.

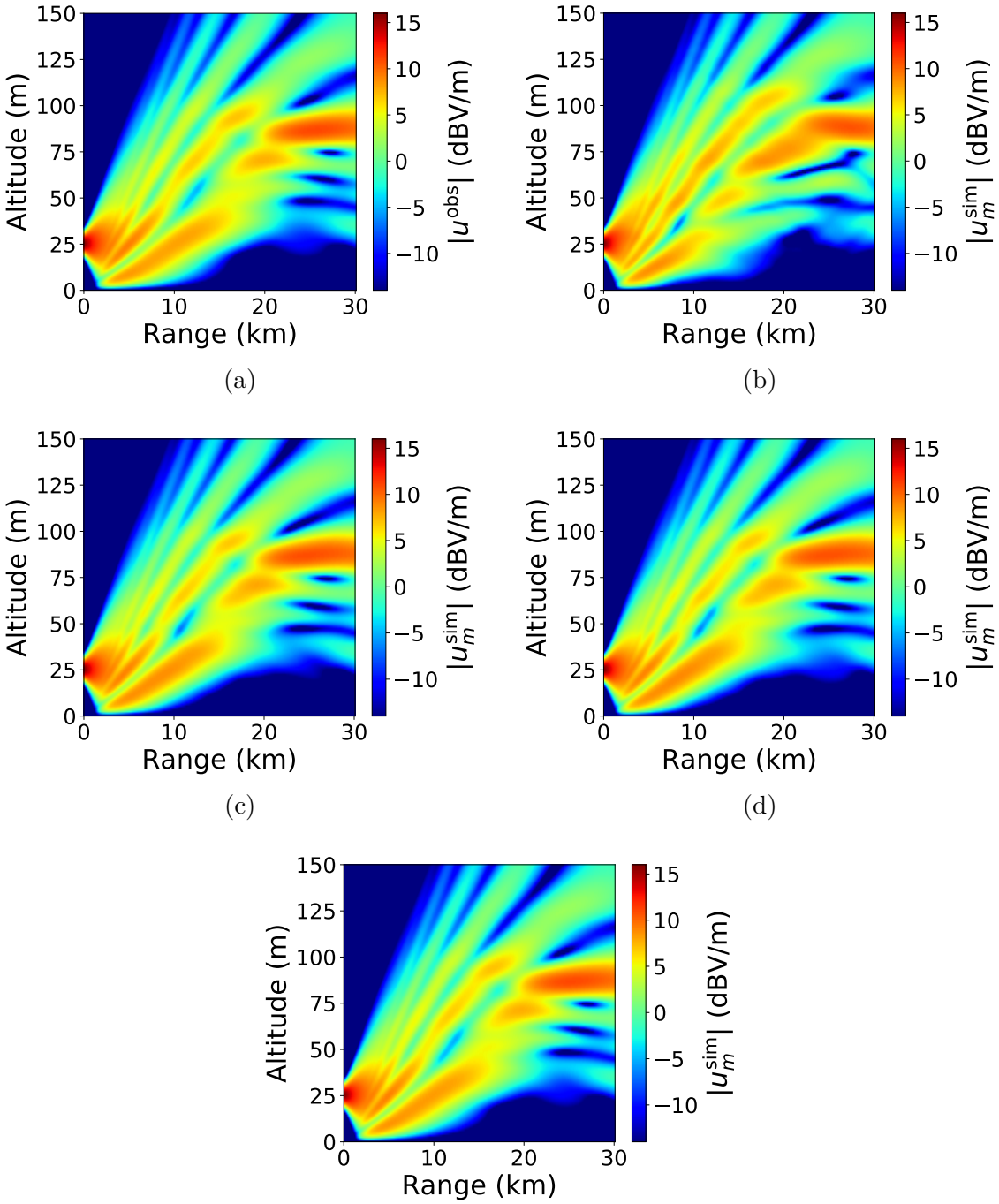

Figure 3.45: Wave field for the case studied in Figure 3.43 respectively, at $R = 30$ km (a) True (b) T-1-S-2, (c) T-1-S-3, (d) T-1-S-4, (e) T-1-S-5.

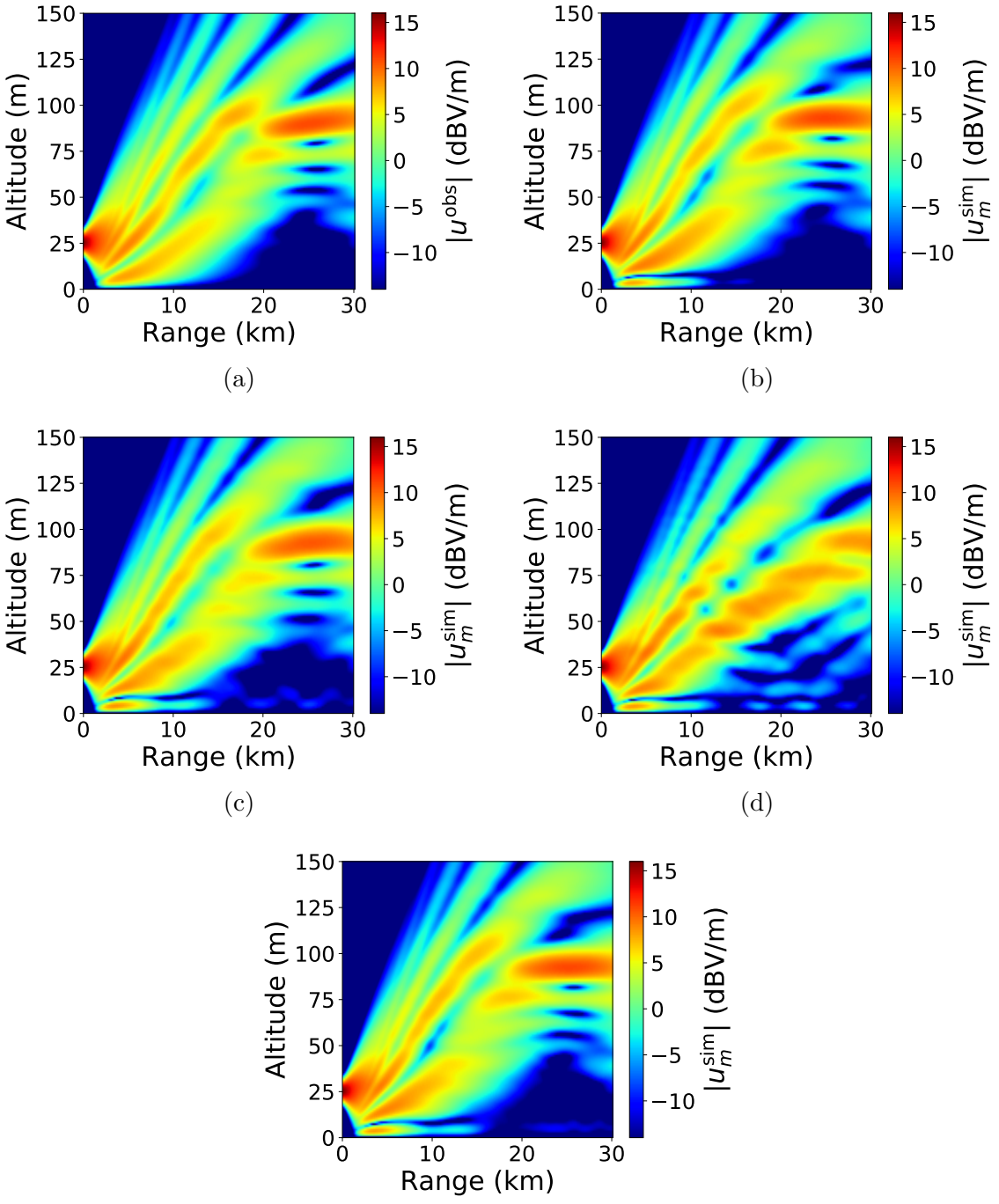

Figure 3.46: Wave field for the case studied in Figure 3.44 respectively, at $R = 30$ km (a) True (b) T-1-S-2, (c) T-1-S-3, (d) T-1-S-4, (e) T-1-S-5.

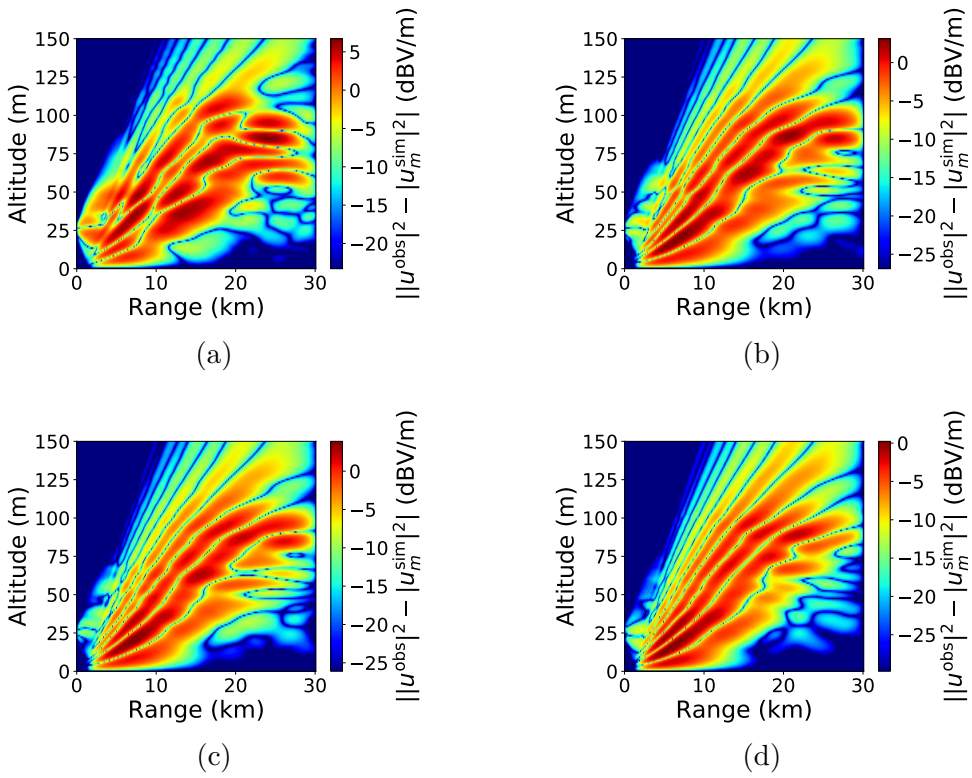

Figure 3.47: Difference between true and predicted wave field for the case studied in Figure 3.43 respectively, at $R = 30$ km (a) T-1-S-2, (b) T-1-S-3, (c) T-1-S-4, (d) T-1-S-5.

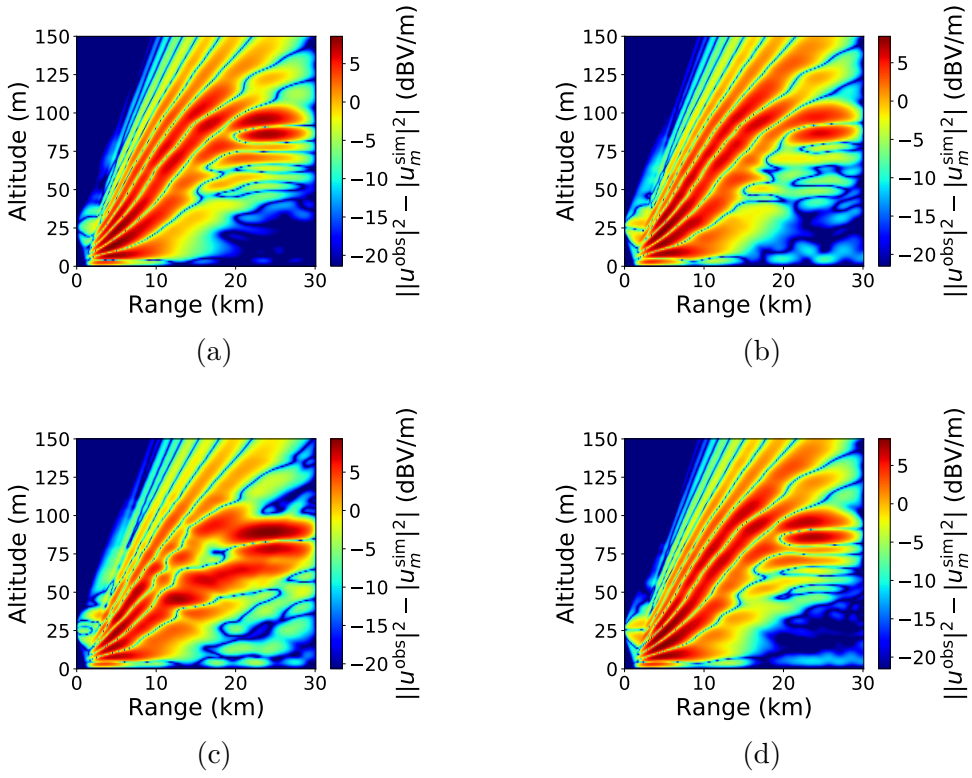

Figure 3.48: Difference between true and predicted wave field Wave field for the case studied in Figure 3.44 respectively, at $R = 30$ km (a) T-1-S-2, (b) T-1-S-3, (c) T-1-S-4, (d) T-1-S-5.

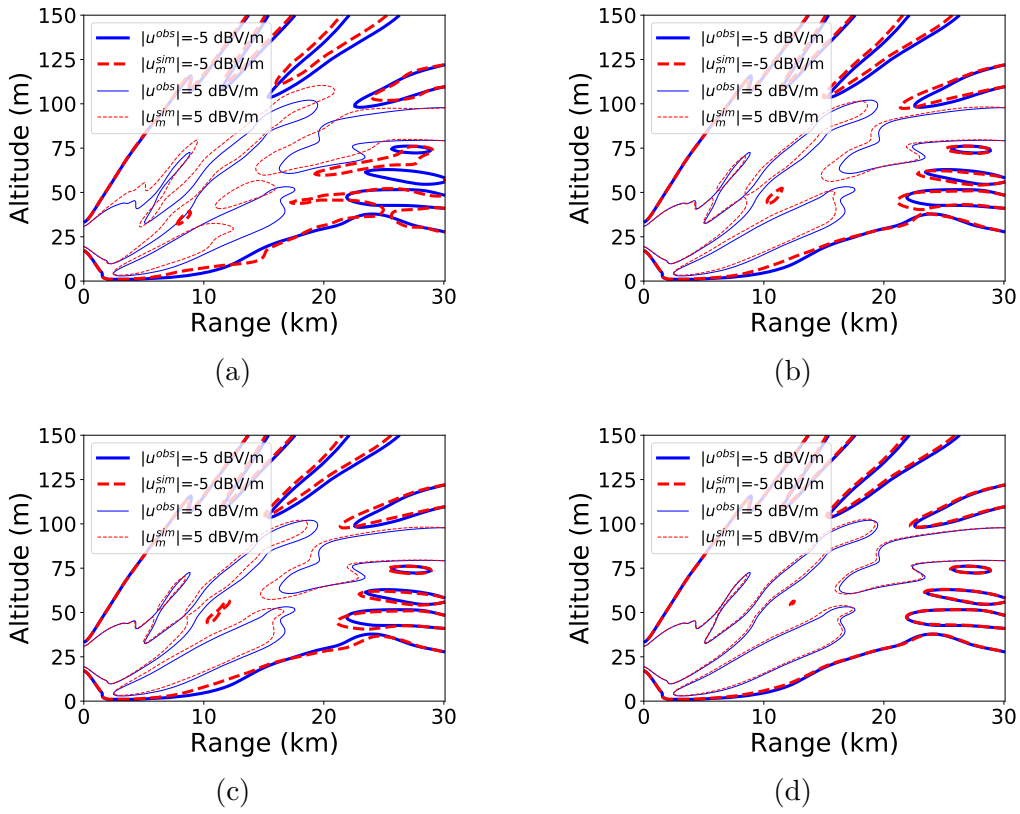

Figure 3.49: Isolines of the true and the predicted wave field for the case studied in Figure 3.43 respectively, at $R = 30$ km (a) T-1-S-2, (b) T-1-S-3, (c) T-1-S-4, (d) T-1-S-5.

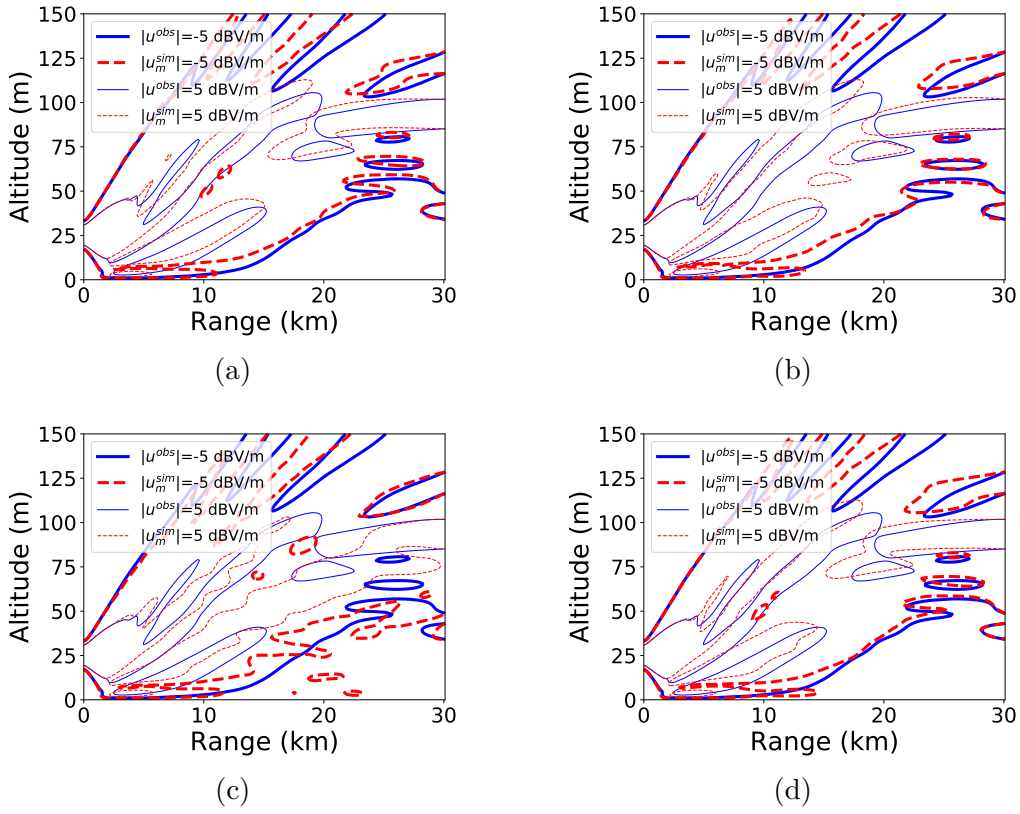

Figure 3.50: Isolines of the true and the predicted wave field for the case studied in Figure 3.44 respectively, at $R = 30$ km (a) T-1-S-2, (b) T-1-S-3, (c) T-1-S-4, (d) T-1-S-5.

3.6.2.6 Preliminary results with data reduction at 30 km range

Let us start this final results section with some remarks to explain how we got to this point of "data reduction". The success of the inversion algorithm with strategy T-1-S-5 comes with a high cost in terms of number of iterations. This is due to the projection of parameter from one subspace to another between multiscale levels. We have tried to avoid it by using the "Method 2" described in Section 3.3.3.1 because such a projection, denoted with H, disappears effectively. With the use of this method, the cost function was never increasing unlike, for example, in Figure 3.33b and the optimization became very efficient. However, this method brought stability issues to the inversion. To be more precise, the parameters started to contain more and more oscillation as we refined the model. Those bad results are not presented here.

We think that this problem could be solved by upgrading the multiscale basis (to wavelets) or the optimization strategy. In this thesis, we choose to keep the basis unchanged and upgrade the optimization technique. In this study, we improve the optimization technique by using SSR "Method 2" (perturbation restriction) and data space reduction (DSR) at the same time and synchronizing the dimensions of the reductions. We label the SSR technique that uses "Method 2" as T-2. When T-2 is used with DSR, we label this as a new technique as T-3, in which dimensions of the data subspaces are given with N_D. In this preliminary study, we choose:

$$\text{T-2-S-6}: \quad N_L := \{N_{L,i} = i + 1,\ i < 10\} \cup \{151\} \tag{3.24}$$

for T-2 and

$$\text{T-3-S-6}: \quad N_L := \{N_{L,i} = i + 1,\ i < 10\} \cup \{151\} \tag{3.25a}$$

$$N_D := \{N_{D,i} = i + 1, i < 10\} \cup \{151\} \tag{3.25b}$$

for T-3. The inversion results obtained with these techniques are given in Figure 3.51 with wave field contours and isoline graphs in Figure 3.52 and Figure 3.53 respectively. We observe that T-1-S-5, which is the most successful strategy until this point, cannot predict the ambient refractivity well anymore in this complex scenario. The new technique T-2 has stability issues but when used in synchronization with DSR, predictions improve significantly. In addition, we have also tried synchronizing T-1 with DSR but T-1 has some accuracy issues when used with DSR. These are preliminary results and T-3 technique is under development.

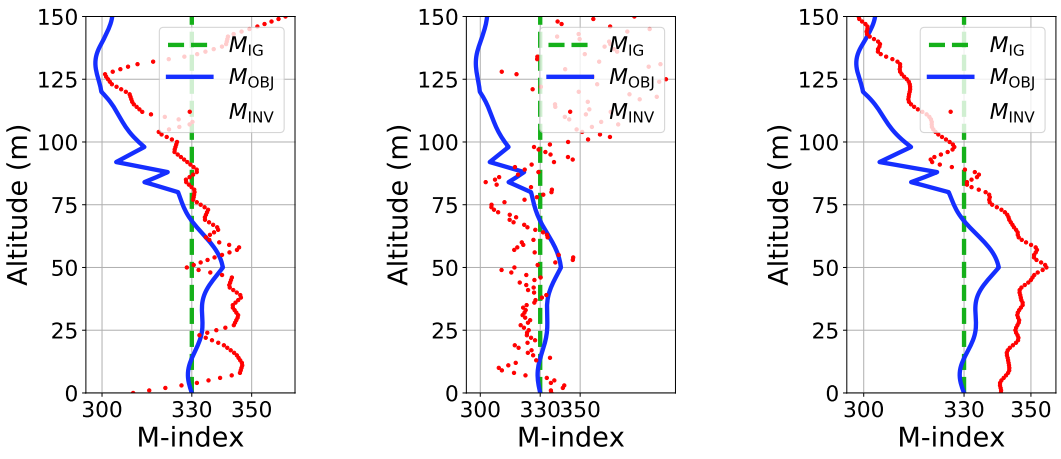

Figure 3.51: Inversion at $R = 30$ km. (a) T-1-S-5, (b) T-2-S-6, (c) T-3-S-6.

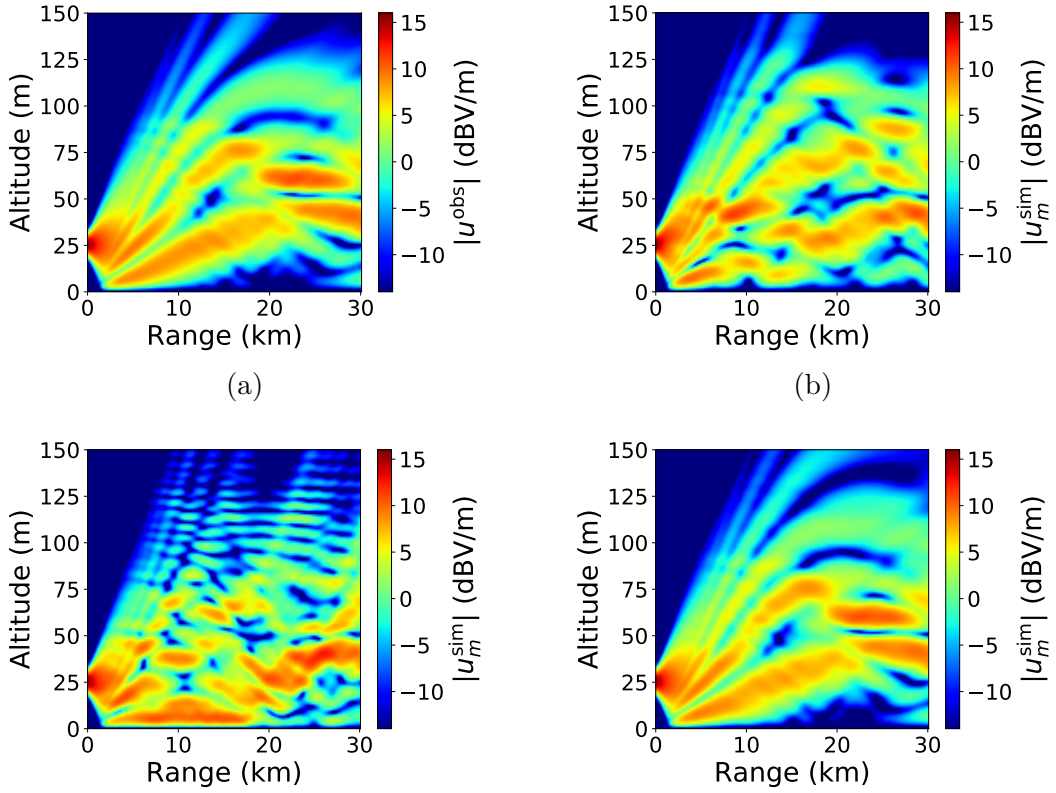

Figure 3.52: Wave field for the case studied in Figure 3.51 respectively, at $R = 30$ km (a) True, (b) T-1-S-5, (c) T-2-S-6, (d) T-3-S-6.

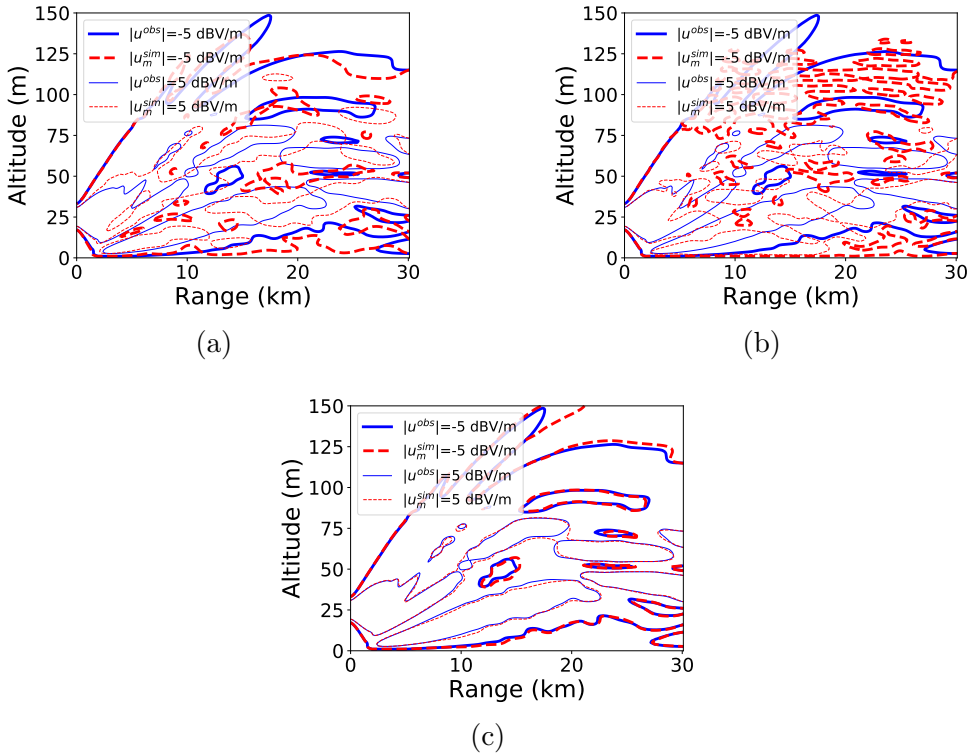

Figure 3.53: Isolines of the true and the predicted wave field for the case studied in Figure 3.51 respectively, at $R = 30$ km (a) T-1-S-5, (b) T-2-S-6, (c) T-3-S-6.

3.7 Conclusion

This chapter presents our attempts to solve the refractivity inversion problem in realistic source and ambient refractive conditions from phaseless data measured in bistatic configuration. We discover how the inversion results obtained using our plain adjoint-based inversion technique that we presented in Chapter 2 would be affected by the fact that ambient refractivity profiles contain perturbations in reality. Our goal is to discover the potential problems related to the inversion of realistic profiles in ideal conditions and propose upgrades for our plain adjoint-based inversion technique. In our perspective, if our technique cannot cope with resolving the perturbations in refractivity profile in ideal scenarios where the modeling, measurement errors and noise are eliminated, there is not a motivation to test it in real world. In addition, we would not be confident to claim that we have a method that can retrieve details of ambient refractivity profile point by point in altitude. Remember that in the beginning we chose the adjoint-based approach so as to to retrieve details of the refractivity efficiently. If details are going to be omitted, then there are already many techniques in the literature that accomplish this task.

We have observed that existence of perturbations in the refractivity destabilizes the regularity of the inversion results in high-dimensional scenarios (Figure 3.15e vs Figure 3.17e). This effect is potentially combined with higher level of dependency to the initial guess. Search space reduction techniques can be used to obtain inversion results without oscillation as it is done in the literature. However, we need to choose a good reduction basis based on the ambient conditions, which constitutes a case-specific *a priori* information that may not be available. If such an information is not exploited well, then inferior solutions can be obtained (see Figure 3.20c).

One way to handle these issues is to use a multiscale parametrization technique (MPT) that refines the control parameter vector progressively. We choose basic piecewise linear functions as our reduction basis to show the positive effect of MPT on inversions. For this purpose, we performed numerical tests at $R = 10$ km. We have the impression that MPT can be used for retrieving the details of the synoptic structure of the ambient refractivity profile in general. Nevertheless, attention must be paid to the suitability of the refinement strategy so as to get the best possible results. Namely, more progressive refinement increases the success of the inversion results in general. Still, some very complex profiles may not be handled well. Here, the problem is that stationary point may not be found in the admissible parameter set at low control parameter dimension in some cases. We think that the issue is related to the representability of the data in the least square sense. In the example of Figure 3.28, the data that belongs to complex refractivity profile given in the Figure cannot be explained with only few control parameters in the linear basis.

In the most general case, we have to assume that there is going to be the aforementioned representability issues when applying MPT in real world applications as well. For this reason, we incorporate Data Space Reduction (DSR) technique into the multiscale strategy. The idea is that the global structure of the parameter profile must explain the global structure of the data, not necessarily (including) its details, in the least square sense. Incorporating DSR with the Search Space Reduction (SSR) in the multiscale strategy increased the quality of inversion results noticeably only in some selected cases that we studied. DSR-related modules are currently under development in this project. More testing is necessary to discover the benefits of extending the multiscale approach from parameter reduction to data reduction and to have confidence in the validity of conclusions in general.

The upgrades that we propose in this chapter are optimization strategies that treats the

direct solver and the adjoint solver as black box. Namely, the upgrades are applied on the input (adjoint initial condition) and output (the gradient) of the adjoint solver module and on the cost function. Therefore, one needs to follow the instructions in Section 2.6 for adjoint code derivation and the make the modifications on the adjoint initial conditions, the gradient and the cost function as explained in Chapter 3, to derive our methods. These upgrades can be applied for other parabolic wave equations the same way. In the case of RFC, SSR is applied the same way as in RBT, whereas the modifications related to DSR should be applied on the forcing term of the adjoint model instead of the adjoint initial conditions because the error is injected there in the adjoint model (see [58]).

Using DSR with SSR in a multiscale hierarchy opens doors to many different inversion strategies to discover, even with our very basic reduction basis. For example, refinement and coarsening strategies can be executed in cycles with and without synchronization of reduction dimensions in DSR and SSR. Also, windowing techniques can be applied in DSR and SSR after identifying which part of data is most relevant to which part of parameter profile. Alternatively, adaptive refinement and coarsening strategies can be used in DSR and SSR. Needless to say, replacement of linear basis with multiscale Wavelet basis can be a good upgrade, for DSR in particular. Apart from minimizing the reduced data after scale separations and reconstruction in multiscale Wavelet basis, the optimization could be performed to minimize the misfit between Wavelet coefficients of some dominant modes that explain the simulated and measured data. If necessary we can resort to use of more information in the inversion by penalization of the cost function, measuring the phase and angle of arrival of radar beams, to solving multiple problems simultaneously for different radars and maybe even equip a single ship with several radars operating at different frequencies. A combination of aforementioned possibilities should be explored to derive a reliable and efficient inversion technique.

We would like to end the conclusions with some remarks on the optimization. The results obtained using BFGS seems to be the best. We added another optimization technique (the Conjugate Gradient Method of Polak-Ribière [142]) to reiterate over the prediction coming from the BFGS and decrease the cost function further, we did not observe improvement on the quality of results. Another point is that there seems to be a balance between the solution quality and number of optimization parameter. In real-world applications, we might need to end the refinement at a certain number of control parameter per meter and not be able to resolve the details of the atmosphere at the resolution of the forward model simulations. It is important to know how far the refinement should go under what ambient conditions.

Most importantly, the results presented in Chapter 3 are preliminary. The comments should not be accepted without critical thinking. In particular, it is questionable whether the successful application of MPT at $R = 10$ km is thanks to the fitness of the MPT or the problem is already so simple when phase is omitted and it only needed any regularization method to be incorporated to the standard adjoint-based problem in that configuration. In addition, comparison with different penalization techniques is necessary as well as the need to discover different reduction basis and strategies. However, from practical point of view, there is clearly some hope for application at 10-30 km range. The potential difficulties are that, (1) we may not have a receiver at each altitude point on the array antenna (studied in [57]), (2) array antenna can be shorter (studied in [4]) and (3) robustness of the algorithm should be tested (studied in [3]). Additional measurement data could improve the technique, for example, information such as angle of arrival of the beams or multi-frequency data but how to use such additional information is also important as we showed in Chapter 2.

Data reduction could be used with parameter reduction but we are at the beginning of

discovering this technique and more exploration is necessary to retrieve presentable results and lay out its advantages and drawbacks. From the failed inversions, we have the impression that if we added some basic Tikhonov regularization to DSR, we could be talking very positive about the DSR. Alternatively, if the inversions stop at a resolution level earlier than the full-resolution (i.e., at $N_L = N_z$), the results are acceptable for describing the general structure of the ambient parameter distribution.

Another point to discuss is that if there is any point in going further in the direction of RBT. Our initial goal was to have a simple toy problem that we can work on easily before working on RFC, for validating our techniques especially. However, if there is light for practical application in RBT, the algorithm is ready to be tested in real world after developing the projection technique for injecting the real-world measurements into the numerical mesh. In this case, it would be a good idea to upgrade the reduction basis or at least incorporate adaptive refinement strategy to the inversion routine.

All these points and more like stationarity checks at the end of inversion, incorporating multistart optimization strategies, obtaining a good initial guess from derivative-free optimization techniques at low parameter dimensions in the beginning and merging the multiscale technique with penalization techniques are left for the future studies.

3.8 Acknowledgments

A preliminary attempt of multiscale strategies was published in U. Karabaş, Y. Diouane, and R. Douvenot, "A multiscale parametrization for refractivity estimation in the troposphere," in *Proceedings of the 15th European Conference on Antennas and Propagation (EuCAP)*, Mar. 2021, pp. 1–5.
DOI: 10.23919/EuCAP51087.2021.9410989

Chapter 4

Conclusion

Contents

In this chapter, we first present a summary of the content chapter by chapter and then elaborate on some important findings.

4.1 Overview

The important points of the content of Chapter 1, Chapter 2 and Chapter 3 are presented below.

4.1.1 Chapter 1

Naval radar systems operate near sea level by emitting radio waves through the atmosphere. The propagation of the radio waves depends on radio refractive index distribution in the airspace around the radar. Some refractive index distributions can cause the propagation path of radar beam to deviate significantly from what is normally expected and they are called anomalous or nonstandard refractive conditions. Those conditions can give rise to anomalies in radar system performance such as the emergence of blind zones in the airspace. It is essential to know the ambient refractivity accurately to predict radar performance so as to have situational awareness about the performance of radar system.

Refractivity distribution in the atmosphere is unpredictable *a priori*. It is also impractical to measure the atmospheric refractivity distribution in the spatial extent of the radar platform in sufficient detail in real time for the entire operation duration. A technique called Refractivity-From-Clutter (RFC) is proposed to invert the refractivity from clutter measurements taken by the radar. The idea is to exploit the echo of the radar emission that comes back to the ship from wavy sea surface. Since this echo is due to the radio waves which have propagated in the

airspace, then this echo must contain the traces of the ambient refractivity distribution and we should be able to retrieve them.

The difficulty of RFC is that the refractivity m (distributed system parameter) and the received signal power P_R (observable clutter data) are related nonlinearly through a partial differential equation. Inversion of refractivity from clutter data constitutes a nonlinear ill-posed problem which is already difficult to solve in theory even if the forward model is known at the level of perfection. The problem is that, firstly, we cannot expect the clutter data to come with the additional information, such as meteorological conditions, sea radar cross section model and the auxiliary techniques that is necessary to model it well in a particular case, and secondly, we do not know what inversion technique is suited the best for this particular scenario. Apart from that, we do not know what the consequences of deviating from the perfection are in those aspects in terms of solution quality. For example, we do not know up to what resolution level the refractivity can be retrieved depending on the suitability of the approximations. Thirdly, the inversion problem is very complex even in ideal conditions if the parameter model is represented with a high-dimensional vector in the numerical model as required for modern systems operating at high frequencies with precision [57], [58].

Apart from the aforementioned points, we make the following two essential observations. (1) It is almost customary to choose the Wide-Angle Parabolic Equation of Thomson and Chapman (WAPE-TC) as the forward model in RFC community because it is the most accurate WAPE on which efficient split-step numerical technique is applicable. However, Narrow-Angle Parabolic Equation (NAPE), which has the same computational cost as WAPE-TC, is used instead when it comes to adjoint-based RFC systems that can retrieve the details of the refractivity efficiently. (2) The problem is so complex that successful high-dimensional applications actually incorporate case-specific *a priori* information in this or that way. Such a priori information might not be available in real world operations in all conditions. In today's knowledge, we have to incorporate *a priori* information into the solution of the inverse problem but what that information specifically is and how it is incorporated matter. For example, how are we going to take into account the climate change or manipulation if the *a priori* information comes from an artificial intelligence system that is fed with the historical data of the geophysical location collected over the decades? The background knowledge can lead to inferior solutions as much as it could guide us towards the truth. We choose to work with WAPE-TC for high-dimensional adjoint-based inversions and try to rely on data and physics as much as possible to explore the possibility of avoiding such background knowledge.

Therefore, we first try to understand what the possibilities are in ideal conditions if the forward model is known perfectly. To approximate to the reality and reduce the possible modeling errors, we choose the WAPE-TC as the forward model as we said before. Deriving an adjoint model for WAPE-TC is not as straightforward as it is for NAPE and other WAPEs that are used in the acoustics community because it has a square root operator with an argument that changes sign. For this reason, it is necessary to make some assumptions and then check if they are valid. For the validation purposes, we modify our problem from RFC to bistatic configuration. Our initial plan is to develop the technique and knowledge for the derivation and development of some multiscale strategies that we saw in the geophysical data inversion community, and then transfer our knowledge to RFC systems.

4.1.2 Chapter 2

In order to perform the basic inversion task efficiently, the inverse problem is formulated as a simulation driven nonlinear least squares optimization problem where the difference between the measured and simulated data on u is minimized over refractivity parameter m. Depending on whether the phase of the complex field u is measurable or not, we formulate two different cost functions to minimize. We derive two different adjoint models for the two cost functions with some assumptions. The derivations are checked by comparing the gradient computed using adjoint model to that obtained using a finite differences scheme. A quasi plane wave is used as the source.

The inversion tests show that it is easy to invert the refractivity from measurements in the first few kilometers in range in general. The use of measurements with phase allows us to compute the parameter accurately near the radar whereas the removal of the phase information allows us to identify only the synoptic structure of the refractivity at longer ranges. Removal of the phase also reduces the complexity of the error functional topography. This allows retrieval of multimodal solutions for different initial guesses up to a certain distance from the radar. We also show that the inversion accuracy could potentially be improved in an inversion strategy where inversion without phase information could be improved by incorporating the phase information at the second step of inversion.

4.1.3 Chapter 3

In Chapter 2, the features of the problem have been exposed and the validation has been performed using a trilinear objective parameter profile and quasi-plane wave source to illuminate the atmosphere. Use of realistic point source makes refractivity inversion more difficult. In addition, realistic refractivity profiles do not resemble the simple trilinear model used in Chapter 2. Furthermore, realistic data are sparse and contain noise and are expected to be phaseless. Not to mention, theoretical and numerical modeling errors are expected in reality. For at least these reasons, we do not expect to benefit from the refractivity gradient retrieval capability of the basic adjoint-based inversion technique in bistatic configuration in practice as simply as it is portrayed in Chapter 2. To build the confidence before testing the algorithm in real world, we want to obtain perfect inversion results in high-dimensional scenarios by inverting synthetic data in ideal conditions.

In Chapter 3, we show the difficulty that comes from the point source and perturbations on the objective refractivity profile. The main difficulty is that inverted parameters contain more oscillation which usually does not permit identification of the synoptic structure of the objective profile. We tackle this problem using Search Space Reduction (SSR) and Data Space Reduction (DSR) techniques in a multiscale strategy. The idea is to have regular perturbations on the parameter model and to convexify the error functional topography with SSR and DSR respectively. This mitigates the difficulty of inversion and helps us explore what we can achieve without penalizing with case-specific *a priori* information in the background.

Some modifications are proposed to the standard adjoint-based formulations obtained in Chapter 2 in order to achieve SSR and DSR in our multiscale strategy. We validate the gradient under these modifications, like it is done before in Chapter 2. Using different strategies of progressive refinement in the parametrization, we show the advantage of multiscale method at 10 km. More progressive refinement strategies improve the solution quality in the studied

scenarios, at the expense of increasing computational cost. We cannot propose an efficient strategy that improves the solution quality and decrease the computational cost in general. There seems to be a computational cost to pay in order to retrieve quality results without using empirical background knowledge.

The main advantages of SSR and DSR are the following in our context. Using SSR in our multiscale strategy effectively regularizes the solution. We assume that, in some (simple) cases, we expect that the solutions obtained during the refinement are good initial guesses for the next more refined subproblems. Finally we obtain a good initial guess for the original full-scale problem, in which the parameter is resolved at the dimension of numerical mesh of the propagation model, and that is almost impractical to obtain from derivative-free methods due to the dimension of the problem. However, for the studied cases the problem becomes so complex at around 30 km that inversions start badly from the very beginning. Predictions at the first multiscale levels do not represent the global structure of the true parameter and inversions do not go well in general. At that point, we incorporate DSR to the multiscale strategy. We assume that global structure of the data is related to the global structure of the parameter mainly. This gives us improved predictions at low dimensions in general and improves the results. For DSR, we do not have the final results to make general conclusions as we are still developing the technique and more testing is necessary to show the advantages and the limitations of the technique.

4.2 Discussion

4.2.1 Chapter 1

We have started our introduction by presenting the relation between the atmospheric radio refractive index and bending of the radar energy and its effect in radar coverage with an example. We have also mentioned that the refractive index changes dynamically in the lower troposphere and it is not possible to know its distribution accurately at the desired precision so as to estimate the radar coverage at desired accuracy. In the second step we explained that the refraction effects are not specific to our problem. In the third step we explained the relation between received signal power at the radar and radio wave propagation in the troposphere. In the fourth step, we presented the physical model (i.e., the forward model, the propagation model, state equation) that can account for refraction effects in radio wave propagation. In the next steps, we explained why measuring the ambient refractivity is so difficult in our context and why it is more convenient to invert it from radio frequency data the way we do in the thesis. We lastly presented some criteria that our inversion technique should be able to meet and our plan to reach the capabilities.

All these steps that we mentioned serves to prepare the reader for the following questions and conclusions reached in the beginning of the thesis that we should be critical of. Firstly, we limit our goal in this thesis and state it clearly. Our goal is to predict ambient refractivity so as to predict the radar coverage in the airspace. When viewed from this aspect, radar coverage is proportional to the received signal strength (P_R) per unit target radar cross section (σ) as function of position in space. The quantity P_R/σ is proportional to the electromagnetic wave field amplitude $|E|$. The latter is proportional to the reduced wave field amplitude $|u|$ which depends on refractivity m. However, the state function that depends on m in the propagation model is $u \in \mathbb{C}$. This means that perhaps we do not necessarily have to find the true refractivity to explain only the amplitude of the state function (with some negligible error) that explains the radar coverage?

The second step is about where to get some inspiration from to solve our problem. Numerous methods and strategies are developed to tackle inverse problems that are also applicable to our problem. Although there is not a general technique that can tackle all inverse problems well, we guess that the method and strategy that suits to the features of our particular problem is probably already developed somewhere in that rich literature of inverse problems. Enlarging scope with more generic concepts like inversion of distributed system parameter in partial differential equations gives us chance to discover relevant and innovative ideas. Also for the refraction is related to waves, we check if successful applications to get inspiration from exist, outside the RFC, in other wave propagation communities.

We find the problem of underwater acoustic sound speed inversion problem in ocean acoustics and acoustic full-waveform inverse problem in geophysics similar to ours. Different forward models which are close to ours are studied in ocean acoustics, and a very high-dimensional inverse problem is solved successfully in geophysics. By taking into consideration also the work done in our community and the requirements of our ideal inversion technique, we decided that the adjoint approach would be the right way to take for building our RFC system to invert refractivity parameter from clutter data. When it came to choose the forward model and the scenario, we have made the following discussions about the previous work.

- The right way of modeling of clutter from refractive effects depends on the scenario. Studying this problem requires expertise on closure of forward model depending on the scenario. There are PhD's dedicated to how to model one parameter in the relation (for example, sea radar cross section). Beside of the standard difficulties of solving this nonlinear ill-posed problem, some deviations of refractivity from the standard conditions are theoretically non-invertible due to the flow of the radar energy in the airspace. Although we are not sure if these were the reason, the pioneers of the application of adjoint method on RFC were motivated to study a bistatic configuration, which we call RBT in this thesis, to develop their techniques in the beginning.

- The inverse problem is already so much complex to the extent that the adjoint-based techniques which are potentially capable of handling millions of parameters efficiently are used for inverting around 25 parameters in the successful real-world applications, and even that is made possible by incorporating case-specific *a priori* information.

- When the inversion fails, it is difficult to understand the reason and propose the correct remedies that can lead to successful high-dimensional applications. For example, we do not understand if there is a theoretical or numerical conclusion about up to what resolution the refractivity can be retrieved per application or if the mathematical propositions break in the numerical model (unexpectedly) at some point strangely and what role the forward model plays in this, in particular.

- The inversion can fail when inverting high-dimensional parameter from synthetically generated data coming from the forward model of the inversion routine. It means that failure is a possibility even if no modeling, measurement error and noise exists. Then, even in ideal conditions, there are some issues related to the invertibility and/or problem complexity.

- We are not able to deduce how the modeling errors coming from uninformed choices would degrade the inversion quality in real world applications.

- Due to the inevitable trade-off between the inversion accuracy and speed of computations, grid dependency element is usually omitted in the studies. Consequences of this is not

studied from the inverse problem point of view in the literature[1] although the problem is an ill-posed problem.

We concluded that (1) we should use at least theoretically the most accurate propagation model that we could afford for modeling the propagation so that we can tighten our control on the inversion accuracy and have more confidence in our results before testing the ideas in real world. (2) In addition, we need to start from a very simple example and increase the difficulty of inversion step by step. (3) We should also first deal with the most basic element of inversion complexity that comes from the parabolic equation when the state function is known perfectly in some part of the domain. This corresponds to working in the scenario just one step ahead of having a total command on the physical modeling at the level of perfection.

At this point, we have to emphasize that the improvement of the adjoint-based inversion technique with WAPE-TC instead of NAPE is hypothetical. The improvement is suggested from forward modeling point of view and we should be critical of that. The argument is that if forward model approximates to the truth better in the forward problem, then it is reasonable to expect some improvement in the inverse problem as well. To the best of our knowledge, there is not a study in the literature which discuss the influence of choice between NAPE and WAPE-TC on the inversion quality in the context of RFC. Still, some theoretical improvement is expected not only for seaborne but also for airborne and spaceborne emitters[2].

We have to be critical of the choice of tomographic setup in this thesis. This change is made for scientific purposes for the moment, as explained throughout the thesis. In military operation environment, it is not easy to find a receiver antenna at a desired distance from the ship unless the ship operate as a group with others. Therefore, RBT should be seen as part of a system where data coming from different sources are analyzed with different inversion techniques, with its extension to RFC for instance. However, the advantage of RBT is that, in short time, we are able to propose a technique that is ready to be tested on the group of ship in real world.

In Chapter 1, we have also discussed that inverting the details of refractivity distribution accurately becomes important as the frequency of the source increases. We have given a motivating example by comparing the propagation at $f = 2$ GHz to $f = 10$ GHz. In fact, our intention has been to study our inverse problem at frequencies as high as 10 GHz and compare our results to that obtained in [57] at 8 GHz in bistatic configuration using regularization methods. However, we have encountered inversion difficulties throughout this thesis in high-dimensional scenarios and those difficulties prevented us from increasing the frequency of the source above 2 GHz in long range applications in practice. On the other hand, we were able to study the inversion of some realistic complex refractivity distributions in altitude.

We also mentioned some techniques that are used in successful applications of adjoint-based methods found in the literature and how to benefit from these techniques. Firstly, we mentioned the importance of validating the gradient computed using the adjoint-based method each time the method is modified. Validation of the gradient increased our confidence in our derivations. Also, we were able to focus on the optimization part when the inversion fails because we did not have doubt about the validity adjoint-based techniques that we developed throughout the thesis.

[1] Our initial tests indicated that the modeling is done in numerical setups where the modeling have mesh-dependency from inverse problem perspective. We mean that the gradient used in the inversion depends on the mesh size when we make the choices similar to those in the literature. Its impact on the inversion results might be noteworthy to study.

[2] It could be interesting to use WAPE-TC in radio occultation problem because in free space the form of WAPE-TC matches with the one-way equation.

Secondly, we mentioned the benefits of using multiscale strategies in mitigating the inversion difficulty. We made our planning according to these points and other conclusions which can be found in Chapter 1.

We also need to be critical of the assumptions made on the medium properties. We assume that the refractivity does not vary with range, there is not atmospheric attenuation, and the phenomena carries azimuthal symmetry features. Normally this is not the case.

4.2.2 Chapter 2

In the following sections, we use the acronym WAPE to refer to WAPE-TC because it is the only WAPE that we consider in the following.

In Chapter 2, our main goal is to derive and validate the adjoint model of WAPE for RBT. We derive the adjoint model for two different least squares problems: (1) when the measurements include the phase and amplitude of the wave field, (2) when only the amplitude is measurable. The derivation has two main steps: (1) We differentiate the cost function, (2) we write the variational form of the Tangent Linear Model (TLM) of WAPE. The difficulty occurs in the second step when writing the variational form because we need to identify the adjoint of the square root propagation operator whose argument changes sign along the spectrum of the argument. When writing the variational form and deriving the adjoint model, we exploit the following three observations: (1) the numerical mesh acts as a filter effectively on the spectrum, (2) the sign change coincides with the separation of the propagating and evanescent modes in the numerical solution, (3) the argument is positive in the case of propagating modes which are interesting from application point of view and in that context we can assume self-adjointness for its square root according to an already existing theorem in functional analysis [114]. The derivations are verified by checking the gradient that is computed with the adjoint-based approach.

Our second goal is to observe how the lack of phase in radar measurements could impact on the inversion quality. For this purpose, we perform a numerical experiment where the synthetically generated data is used as measurement. Removal of phase is an important lack of information which is likely to happen also in RFC. Many more refractivity solutions could become indistinguishable from the truth when inversion is done from phaseless data. We observe in the inversion results that removal of phase makes the inversions challenging from the point of view of retrieving the true refractivity parameter indeed. However, this lack of knowledge brings an advantage to the retrieval of synoptic structure of the true parameter. The inversion results are very accurate when phase is measurable but also when the measurements are taken in the first few km from the radar. On the other hand, the inversions could retrieve the synoptic structure of the true parameter profile (the gradient information) with some oscillation that allows identification of the global profile shape and with a certain offset from the truth up to further distances from the radar when phase information is removed from the measurements. This scenario also has some interesting multimodality features portrayed in Chapter 2, which are explained with the convexification of the error functional topography and partly with the propagation theory. Lastly, we studied an improved inversion strategy where phase information is incorporated to the optimization process at the end of inversion of phaseless data to re-run the optimization and get better results. The inversion quality have increased for some cases with the decrease of oscillations in solution.

Note that the validation and the inversion tests are executed using synthetically generated data, the excitation source is a quasi-plane wave and the objective (true) refractivity parameter

has a simple trilinear structure. Apart from these points, we should also be critical of that the receiver antenna extends from the sea level to the altitude of interest and it has one receiver at each altitude point when interpreting the results.

4.2.3 Chapter 3

We start Chapter 3 by explaining what we mean by case-specific *a priori* information and why we want to avoid using it as much as possible. We recall the standard adjoint-based formulations that are obtained in Chapter 2, introduce search and data space reduction techniques (SSR and DSR) and explain how to upgrade the standard formulations to benefit from SSR and DSR. Using realistic point source and parameter profiles that contain perturbations, we validate the implementation of the proposed methods. We demonstrate the motivation to use SSR and DSR in a multiscale hierarchy to achieve good inversion results when inverting synthetically generated data.

We need to be critical of the language that we use when talking about the use of *a priori* information especially. When solving this inverse problem, we see that in some way we have to use *a priori* information in the inversion process. Traces of the *a priori* information appears in the initial guess, optimization bounds, and the optimization technique, continuity of the refractivity profile or at somewhere else in the process but it is always there in a way. When we say we try to avoid the use of *a priori* information, it is the case-specific *a priori* information that is used to explain a specific instance of data and that depends on empirical or historical knowledge whose validity is restricted to a specific geophysical location at a specific time or other conditions and we try to emphasize it throughout Chapter 3. What the *a priori* information is and how it is used is important because it can also lead to inferior solutions as much as it can help to solve the problem well. Availability and reliability of such information are also two other aspects that matter.

We explore the benefits of multiscale strategies. We first study different refractivity profiles at 10 km range using multiscale parametrization technique (MPT), meaning SSR is used in a multiscale hierarchy. The multiscale basis is constructed from local piecewise linear functions with different control parameter dimensions. The results show that inversion become easy with MPT at 10 km. There are a number of factors to consider when interpreting these results. (1) The problem complexity should be thought as function of true parameter complexity and range of propagation. For example, inversion can remain easy if the receiver antenna is put further from the radar and true refractivity profile becomes less complex. Also, inversion of some very complex refractivity profiles can be found as very difficult even in short range applications. (2) Achievement of unrealistically good inversion results from synthetically generated data might equally indicate that the short-range application in our context is already simple and we just discovered it properly with MPT and perhaps it is not really a big achievement. (3) We achieved these results using a very simple reduction basis, so there is a lot of room for improvement not only to improve the quality of the results but also the efficiency of the inversion with better reduction bases like wavelet bases. (4) Noise robustness tests should be performed[3].

More complex profiles need more progressive refinement if we want to predict the radar coverage more successfully. Inversion at longer ranges can be achieved at around 30 km with MPT

[3]In fact, we performed some basic tests using Additive White Gaussian Noise and saw that the inversion results had some robustness, but what is really interesting at this point is to have a realistic noise model and try to mimic the conditions in real-world applications.

depending on the true profile complexity and the inversions can become very costly from computational point of view. It seems that there is a computational cost to pay with more iterations for not exploiting case-specific *a priori* information if we want good inversion results. MPT reaches its own limits in our studied cases. We maintain the inversion success by upgrading it with "SSR Method 2" described in the Chapter which should work in synchronization with the DSR dimensions in the refinement strategy. The presented successful results are not representative of generic performance and more testing is necessary to explore what can be achieved with this optimization strategy. This method is under development at the time of redaction of this manuscript.

Also note that we use a reduction basis which is primitive when compared to wavelet basis that is commonly used in the geophysical data inversion. We are not at a position to defend our choice over the option of wavelets; we only wanted to see if it is really necessary to use an advanced technique where the scale separations are probably done better than we do in our most basic multiscale technique. In fact, we have had the idea of using adaptive refinement and coarsening strategies that are easy to implement in our technique and it remains a way to explore.

4.3 Future Work

There are multiple directions to follow after this work. These directions can be grouped into five categories according to the theme: assumptions, applications, optimization, multiscaling and regularization.

Assumptions The validity of the model can be extended. The main assumptions that we would like to mention here is as follows: range-dependency of the refractivity, atmospheric attenuation, 3D propagation. It would be interesting to see the performance of the inversion algorithm for retrieving the range-dependent refractivity field. We believe that this could be the next step in RBT to test it in real world. It should be easy to account for the range dependency by dropping the integral in the gradient formulation:

$$\nabla_m J = \Re\left\{jk_0 w_m(r,z)\overline{u_m(r,z)}\right\}. \tag{4.1}$$

Perhaps it would be interesting to consider the atmospheric attenuation by considering complex refractivity this time $m \in \mathbb{C}$ and perturbations $\hat{m} \in \mathbb{C}$ in the tangent linear model and follow the process in Chapter 2, which should yield a gradient vector with also a complex part this time. 3D effects could be taken into account by considering, for instance, the 3D wide-angle parabolic equation in [97, Equation C.31] and an adjoint model can be derived similar to the 2D case by exploiting the self-adjointness of the square root propagation operator $\sqrt{k_0^2 + \partial_y^2 + \partial_z^2}$ in this equation when its argument is positive.

Applications It is important to decide if it is interesting to continue on RBT or to switch to RFC configuration. Since the validation of the assumptions in the adjoint model derivation is done easily in RBT, there is not much interest in continuing in this direction if there is not motivation to create RBT application and test the ideas in real world. If RBT is the direction, then it is necessary to check the resolution level that we can ideally achieve with fewer receivers and shorter array antenna and how to do the data projection from physical domain to the

numerical domain. Robustness tests should be executed as well.

In the case of RFC, the left-hand side of the adjoint parabolic equation remains unchanged, so there is not theoretical work related to the square root propagation operator that should be performed again. However, we still recommend to run some validation tests to check if the new right-hand side is implemented properly in the algorithm. Another interesting point about RFC could be to check the dependency of the inversion results on different clutter models so as to see if the models support accurate high-dimensional inversions. Also, the influence of the mesh could be studied for both RFC and RBT.

Optimization There are many capabilities that could be developed from optimization point of view. Starting from the most basic one, we could impose a convergence criterion on the cost function, norm of the gradient or relative change in parameter model perturbations. The problem that prevented us from imposing such a condition is that the optimization topography is irregular and sometimes the cost function can remain flat before a significant decrease. We have had some cases which could be accomplished if an earlier termination is not given by a convergence criterion when a plateau is met in the convergence history. In a multiscale strategy, the consequences of premature termination like that has been very much significant according to our experience. Today the algorithm ends the optimization when the cost function cannot be decreased in the computed descent direction.

Multiscaling In real world scenarios it can be interesting to upgrade the multiscale basis with a wavelet basis or at least apply adaptive refinement and coarsening strategies if the basis is going to be kept unchanged. Other options are listed in detail in the conclusion section of the Chapter 3. The most important ones, in our view, are to enrich the data with phase measurements, use radars operating at different frequencies and applying the windowing techniques on the data in a multiscale strategy during the inversions.

Regularization A Tikhonov type regularization could be combined with the multiscale methods. In real world applications, we can also exploit the fact that the atmosphere evolves slowly in time. In that case, a generalized Tikhonov type regularization with the inversion result obtained at the previous time step can help us to improve the solution quality and efficiency. In a similar way, when information is known on the refractivity, it could be used for penalizing the cost function.

Appendix A

Remarks on the eigenvalue problem

The eigenvalue problem of operator ∂_z^2 is given below:

$$-\partial_z^2 u = \lambda u,\ z \in [0, Z] \tag{A.1a}$$

$$u(0) = u(Z) = 0 \tag{A.1b}$$

Exact analytical solution

For $k \in \mathbb{N}$ the eigenfunctions are given by:

$$u_k(z) = \sin \frac{k\pi z}{Z}, \tag{A.2}$$

and the eigenvalues are given by:

$$\lambda_k = \left(\frac{k\pi}{Z}\right)^2. \tag{A.3}$$

The eigenvalue sequence tends to $+\infty$.

Remark: If we replace $-\partial_z^2$ by ∂_z^2, the eigenvalues are negative and tend to $-\infty$.

Numerical solution

Finite difference method (equivalent to Finite Element Method with first-order polynomial functions and regular mesh)

$$-\partial_z^2 u \simeq -\frac{u_{k+1} - 2u_k + u_{k-1}}{\Delta z^2} = \lambda u \tag{A.4}$$

leads to the linear system:

$$\frac{1}{\Delta z^2}\begin{pmatrix} 2 & -1 & 0 & 0 & \cdots & 0 \\ -1 & 2 & -1 & 0 & \cdots & 0 \\ 0 & \ddots & \ddots & \ddots & \ddots & \vdots \\ \vdots & \ddots & \ddots & \ddots & \ddots & 0 \\ \vdots & & \ddots & -1 & 2 & -1 \\ 0 & \cdots & \cdots & 0 & -1 & 2 \end{pmatrix}\begin{pmatrix} u_1 \\ u_2 \\ \vdots \\ \vdots \\ \vdots \\ u_N \end{pmatrix} = \lambda \begin{pmatrix} u_1 \\ u_2 \\ \vdots \\ \vdots \\ \vdots \\ u_N \end{pmatrix} \tag{A.5}$$

with $Z = (N+1)\Delta z$ and $u(0) = u(Z) = 0$ the boundary conditions. The eigenvalues of this matrix are "well-known":

$$\lambda_k = \frac{4}{\Delta z^2} \sin^2 \left(\frac{k\pi}{2(N+1)} \right), \ 1 \leq k \leq N. \tag{A.6}$$

The eigenvectors up to a multiplicative constant are:

$$V^{(k)} \ \text{ of componenets } \ V_i^{(k)} = \sin^2 \left(i \frac{k\pi}{(N+1)} \right). \tag{A.7}$$

The greatest eigenvalue is:

$$\lambda_{\max} = \lambda_N = \frac{4}{\Delta z^2} \sin^2 \left(\frac{N\pi}{2(N+1)} \right). \tag{A.8}$$

if $N >> 1$ then $\lambda_{\max} \simeq 4/\Delta z^2$.

Remark: The exact eigenvalue of order N is $(N\pi/Z)^2$ and as $Z = (N+1)\Delta z$, it is $(N\pi/(N+1)\Delta z)^2 \simeq \pi^2/\Delta z^2$, which is the same order of magnitude in Δz.

Conclusion

$k_0^2 + \partial_z^2$ is positive if $\lambda_{\max}(\partial_z^2) + k_0^2 \geq 0$. With the Finite Difference scheme we write:

$$-\frac{4}{\Delta z^2} + \left(\frac{2\pi}{\lambda_0} \right)^2 \geq 0 \tag{A.9}$$

and we obtain:

$$\Delta z \geq \frac{\lambda_0}{\pi}. \tag{A.10}$$

Remark: In addition, the descriptions made in the thesis dissertation of Thomas Bonnafont [97], from whom we inherit the forward model, shows that the maximum eigenvalue associated with the operator ∂_z^2 in the spectral transforms is $4/\Delta z^2$, which leads to the same conclusion as (A.10). We have tested the condition empirically and verified that it is $\Delta z \geq \frac{\lambda_0}{\pi}$ for the split-step wavelet technique that we used throughout this thesis.

Remark: The analysis is done to show the relation between the wavelength λ_0 and the mesh step size Δz that makes the argument of the square root positive. The main point is that Δz and λ_0 are related to each other up to a multiplicative constant C such that $\Delta z \geq C\lambda_0$ where C depends on the solution method. Note that $C = \frac{1}{2}$ for the exact solution and $C = \frac{1}{\pi}$ for the numerical solution that we considered, provided that $u(Z) = 0$.

References

[1] U. Karabaş, Y. Diouane, and R. Douvenot, "On the use of variational adjoint approach on wide-angle approximation of parabolic equation with the method of split-step wavelet," in *Huitième conférence plénière biennale du GDR ONDES*, Oct. 2019.

[2] ——, "On the use of adjoint methods for refractivity estimation in the troposphere," in *14th European Conference on Antennas and Propagation (EuCAP)*, Mar. 2020, pp. 1–5.

[3] ——, "A variational adjoint approach on wide-angle parabolic equation for refractivity inversion," *IEEE Transactions on Antennas and Propagation*, vol. 69, no. 8, pp. 4861–4870, Aug. 2021.

[4] ——, "A multiscale parametrization for refractivity estimation in the troposphere," in *15th European Conference on Antennas and Propagation (EuCAP)*, Mar. 2021, pp. 1–5.

[5] T. S. Pittman, "A climatology-based model for long-term prediction of radar beam refraction," Master's Thesis, U.S. Air Force Institute of Technology, Mar. 1999.

[6] M. I. Skolnik, *Introduction to Radar Systems*, 3rd ed. New York, NY, USA: McGraw-Hill, 2001.

[7] H. V. Hitney and J. H. Richter, "Integrated refraction effects prediction system (IREPS)," *Naval Engineers Journal*, vol. 88, no. 2, pp. 257–262, Apr. 1976.

[8] R. Douvenot, V. Fabbro, P. Gerstoft, C. Bourlier, and J. Saillard, "Real time refractivity from clutter using a best fit approach improved with physical information," *Radio Science*, vol. 45, no. 1, Art. no. RS1007, Feb. 2010.

[9] R. Douvenot, "Propagation des ondes electromagnétiques par modèles split-step : problèmes direct et inverse," Habilitation à diriger des recherches, Université Toulouse 3 Paul Sabatier, Toulouse, France, Nov. 2018.

[10] G. B. Baumgartner, H. V. Hitney, and R. A. Pappert, "Duct propagation modelling for the integrated-refractive-effects prediction system (IREPS)," *IEE Proceedings F (Communications, Radar and Signal Processing)*, vol. 130, no. 7, pp. 630–642, Dec. 1983.

[11] W. L. Patterson, "Advanced refractive effects prediction system (AREPS)," in *IEEE Radar Conference*, Apr. 2007, pp. 891–895.

[12] G. D. Dockery, R. S. Awadallah, D. E. Freund, J. Z. Gehman, and M. H. Newkirk, "An overview of recent advances for the TEMPER radar propagation model," in *IEEE Radar Conference*, Apr. 2007, pp. 896–905.

[13] Y. Hurtaud, J. Claverie, M. Aidonidis, and E. Mandine, "Une préfiguration des futures aides tactiques : Filecode PREDEM," *La Revue de l'électricité et de l'électronique*, no. 2, pp. 31–41, Feb. 2008.

[14] *TERPEM User Guide*, Signal Science, Abingdon, U.K., 2005.

[15] O. Ozgun, G. Apaydin, M. Kuzuoglu, and L. Sevgi, "PETOOL: MATLAB-based one-way and two-way split-step parabolic equation tool for radiowave propagation over variable terrain," *Computer Physics Communications*, vol. 182, no. 12, pp. 2638–2654, Dec. 2011.

[16] D. J. Thomson and N. R. Chapman, "A wide-angle split-step algorithm for the parabolic equation," *The Journal of the Acoustical Society of America*, vol. 74, no. 6, pp. 1848–1854, Dec. 1983.

[17] H. Zhou, R. Douvenot, and A. Chabory, "Modeling the long-range wave propagation by a split-step wavelet method," *Journal of Computational Physics*, vol. 402, Art. no. 109042, Feb. 2020.

[18] M. Levy, *Parabolic Equation Methods for Electromagnetic Wave Propagation*. Edison, NJ, USA: IET, 2000, vol. 45.

[19] C. L. Pekeris, "Accuracy of the earth-flattening approximation in the theory of microwave propagation," *Physical Review*, vol. 70, no. 7-8, pp. 518–522, Oct. 1946.

[20] B. R. Bean, "The radio refractive index of air," *Proceedings of the IRE*, vol. 50, no. 3, pp. 260–273, Mar. 1962.

[21] D. F. Glevy, "An assessment of radio propagation affected by horizontal changes in refractivity," Naval Electronics Laboratory Center, San Diego, CA, USA, Tech. Note 3153, May 1976.

[22] J. Goldhirsh and D. Dockery, "Propagation factor errors due to the assumption of lateral homogeneity," *Radio Science*, vol. 33, no. 2, pp. 239–249, Mar. 1998.

[23] E. K. Smith and S. Weintraub, "The constants in the equation for atmospheric refractive index at radio frequencies," *Proceedings of the IRE*, vol. 41, no. 8, pp. 1035–1037, Aug. 1953.

[24] R. A. Helvey, "Radiosonde errors and spurious surface-based ducts," *IEE Proceedings F (Communications, Radar and Signal Processing)*, vol. 130, no. 7, pp. 643–648, Dec. 1983.

[25] J. R. Rowland and S. M. Babin, "Fine-scale measurements of microwave refractivity profiles with helicopter and low-cost rocket probes," *Johns Hopkins APL Technical Digest*, vol. 8, no. 4, pp. 413–417, 1987.

[26] R. C. Cherrett, "Capturing characteristics of atmospheric refractivity using observations and modeling approaches," Ph.D. Dissertation, Naval Postgraduate School, Monterey, CA, USA, Jun. 2015.

[27] T. A. Smith, T. J. Campbell, R. A. Allard, and S. N. Carroll, "Coupled ocean/atmosphere mesoscale prediction system (COAMPS), version 5.0, revision 2.0 (user's guide)," Naval Research Laboratory, Stennis Space Center, MS, USA, Mem. Rep. NRL/MR/7320--12-9407, May 2012.

[28] J. H. Richter, "High resolution tropospheric radar sounding," *Radio Science*, vol. 4, no. 12, pp. 1261–1268, Dec. 1969.

[29] E. E. Gossard, "Radar research on the atmospheric boundary layer," in *Radar in meteorology*, In: Atlas D. (eds) Radar in Meteorology. American Meteorological Society, Boston, MA, USA, 1990, pp. 477–527.

[30] R. G. Strauch, W. C. Campbell, R. B. Chadwick, and K. P. Moran, "Microwave FM-CW Doppler radar for boundary layer probing," *Geophysical Research Letters*, vol. 3, no. 3, pp. 193–196, Mar. 1976.

[31] R. B. Chadwick and E. E. Gossard, "Radar remote sensing of the clear atmosphere—Review and applications," *Proceedings of the IEEE*, vol. 71, no. 6, pp. 738–753, Jun. 1983.

[32] A. Willitsford and C. R. Philbrick, "Lidar description of the evaporative duct in ocean environments," in *Proceedings of SPIE, Remote Sensing of the Coastal Oceanic Environment*, International Society for Optics and Photonics, vol. 5885, Sep. 2005, pp. 140 –147.

[33] W. G. K. McLean, G. Fu, S. P. Burton, and O. P. Hasekamp, "Retrieval of aerosol microphysical properties from atmospheric lidar sounding: An investigation using synthetic measurements and data from the ACEPOL campaign," *Atmospheric Measurement Techniques*, vol. 14, no. 6, pp. 4755–4771, Jul. 2021.

[34] K. D. Anderson, "Inference of refractivity profiles by satellite-to-ground RF measurements," *Radio Science*, vol. 17, no. 3, pp. 653–663, May–Jun. 1982.

[35] A. R. Lowry, C. Rocken, S. V. Sokolovskiy, and K. D. Anderson, "Vertical profiling of atmospheric refractivity from ground-based GPS," *Radio Science*, vol. 37, no. 3, pp. 1–21, Jun. 2002.

[36] B. Wang, Z.-S. Wu, Z.-W. Zhao, and H.-G. Wang, "A passive technique to monitor evaporation duct height using coastal GNSS-R," *IEEE Geoscience and Remote Sensing Letters*, vol. 8, no. 4, pp. 587–591, Jul. 2011.

[37] H.-G. Wang, Z.-S. Wu, S.-F. Kang, and Z.-W. Zhao, "Monitoring the marine atmospheric refractivity profiles by ground-based GPS occultation," *IEEE Geoscience and Remote Sensing Letters*, vol. 10, no. 4, pp. 962–965, Dec. 2012.

[38] V. Synytskyi, "An experimental study of tropospheric fluctuations variability using the radiosetting of GPS satellites over land," in *2020 IEEE Ukrainian Microwave Week (UkrMW)*, 2020, pp. 364–367.

[39] S. Vasudevan, R. H. Anderson, S. Kraut, P. Gerstoft, L. T. Rogers, and J. L. Krolik, "Recursive Bayesian electromagnetic refractivity estimation from radar sea clutter," *Radio Science*, vol. 42, no. 2, Apr. 2007.

[40] C. Yardim, "Statistical estimation and tracking of refractivity from radar clutter," Ph.D. Dissertation, UC San Diego, San Diego, CA, USA, 2007.

[41] J. L. Krolik and J. Tabrikian, "Tropospheric refractivity estimation using radar clutter from the sea surface," in *Proceedings of the 1997 Battlespace Atmospherics Conference*, SPAWAR Sys. Command Tech. Rep. 2989, San Diego, CA, USA, Mar. 1998, pp. 635–642.

[42] J. L. Krolik, J. Tabrikian, A. Vasudevan, and L. T. Rogers, "Using radar sea clutter to estimate refractivity profiles associated with the capping inversion of the marine atmospheric boundary layer," in *IEEE International Geoscience and Remote Sensing Symposium*, Jun. 1999, pp. 649–651.

[43] L. T. Rogers, C. P. Hattan, and J. K. Stapleton, "Estimating evaporation duct heights from radar sea echo," *Radio Science*, vol. 35, no. 4, pp. 955–966, Jul. 2000.

[44] L. Ai-guo, C. Hao, X. Ze-min, and Z. Mo, "Estimation of refractivity profile from radar sea clutter and key problems," in *CIE International Conference on Radar*, DOI: `10.1109/ICR.2006.343379`, IEEE, 2006, pp. 1–4.

[45] L. Rosenberg, S. Watts, and M. S. Greco, "Modeling the statistics of microwave radar sea clutter," *IEEE Aerospace and Electronic Systems Magazine*, vol. 34, no. 10, pp. 44–75, Oct. 2019.

[46] H. Dougherty and B. Hart, "Recent progress in duct propagation predictions," *IEEE Transactions on Antennas and Propagation*, vol. 27, no. 4, pp. 542–548, Jul. 1979.

[47] P. Gerstoft, L. T. Rogers, J. L. Krolik, and W. S. Hodgkiss, "Inversion for refractivity parameters from radar sea clutter," *Radio science*, vol. 38, no. 3, p. 8053, Jun. 2003.

[48] J. Tabrikian, J. L. Krolik, and S. Vasudevan, "Estimating tropospheric refractivity parameters from radar sea clutter," in *Proceedings of the IEEE Signal Processing Workshop on Higher-Order Statistics*, 1999, pp. 345–348.

[49] P. Gerstoft, L. T. Rogers, W. S. Hodgkiss, and L. J. Wagner, "Refractivity estimation using multiple elevation angles," *IEEE Journal of Oceanic Engineering*, vol. 28, no. 3, pp. 513–525, Jul. 2003.

[50] A. Barrios, "Estimation of surface-based duct parameters from surface clutter using a ray trace approach," *Radio science*, vol. 39, no. 6, Art. no. RS6013, Dec. 2004.

[51] C. Yardim, P. Gerstoft, and W. S. Hodgkiss, "Estimation of radio refractivity from radar clutter using Bayesian Monte Carlo analysis," *IEEE Transactions on Antennas and Propagation*, vol. 54, no. 4, pp. 1318–1327, Apr. 2006.

[52] ——, "Statistical maritime radar duct estimation using hybrid genetic algorithm–Markov chain Monte Carlo method," *Radio Science*, vol. 42, no. 3, Art. no. RS3014, Jun. 2007.

[53] B. Wang, Z.-S. Wu, Z. Zhao, and H.-G. Wang, "Retrieving evaporation duct heights from radar sea clutter using particle swarm optimization (PSO) algorithm," *Progress In Electromagnetics Research M*, vol. 9, pp. 79–91, 2009.

[54] M. I. Skolnik, *Radar Handbook*, 3rd ed. New York, NY, USA: McGraw-Hill Education, 2008.

[55] A. Karimian, C. Yardim, P. Gerstoft, W. S. Hodgkiss, and A. E. Barrios, "Refractivity estimation from sea clutter: An invited review," *Radio Science*, vol. 46, no. 6, pp. 1–16, Dec. 2011.

[56] R. Douvenot, V. Fabbro, P. Gerstoft, C. Bourlier, and J. Saillard, "A duct mapping method using least squares support vector machines," *Radio Science*, vol. 43, no. 6, Art. no. RS6005, Dec. 2008.

[57] X.-F. Zhao, S.-X. Huang, and H.-D. Du, "Theoretical analysis and numerical experiments of variational adjoint approach for refractivity estimation," *Radio Science*, vol. 46, no. 1, Art. no. RS1006, Feb. 2011.

[58] X.-F. Zhao and S.-X. Huang, "Refractivity from clutter by variational adjoint approach," *Progress In Electromagnetics Research B*, vol. 33, pp. 153–174, 2011.

[59] X. Zhao and S. Huang, "Estimation of atmospheric duct structure using radar sea clutter," *Journal of the Atmospheric Sciences*, vol. 69, no. 9, pp. 2808–2818, Sep. 2012.

[60] ——, "Atmospheric duct estimation using radar sea clutter returns by the adjoint method with regularization technique," *Journal of Atmospheric and Oceanic Technology*, vol. 31, no. 6, pp. 1250–1262, Jun. 2014.

[61] X. Zhao, C. Yardim, D. Wang, and B. M. Howe, "Estimating range-dependent evaporation duct height," *Journal of Atmospheric and Oceanic Technology*, vol. 34, no. 5, pp. 1113–1123, May 2017.

[62] X. Zhao, ""Refractivity-from-clutter" based on local empirical refractivity model," *Chinese Physics B*, vol. 27, no. 12, Art. no. 128401, Dec. 2018.

[63] V. Fountoulakis and C. Earls, "Duct heights inferred from radar sea clutter using proper orthogonal bases," *Radio Science*, vol. 51, no. 10, pp. 1614–1626, Oct. 2016.

[64] X. Zhu, J. Li, M. Zhu, Z. Jiang, and Y. Li, "An evaporation duct height prediction method based on deep learning," *IEEE Geoscience and Remote Sensing Letters*, vol. 15, no. 9, pp. 1307–1311, Sep. 2018.

[65] S. E. Penton and E. E. Hackett, "Rough ocean surface effects on evaporative duct atmospheric refractivity inversions using genetic algorithms," *Radio Science*, vol. 53, no. 6, pp. 804–819, Jun. 2018.

[66] C. Tepecik and I. Navruz, "A novel hybrid model for inversion problem of atmospheric refractivity estimation," *AEU-International Journal of Electronics and Communications*, vol. 84, pp. 258–264, Feb. 2018.

[67] M. A. Gilles, C. Earls, and D. Bindel, "A subspace pursuit method to infer refractivity in the marine atmospheric boundary layer," *IEEE Transactions on Geoscience and Remote Sensing*, vol. 57, no. 8, pp. 5606–5617, Aug. 2019.

[68] J. O. Pralits, A. Hanifi, and D. S. Henningson, "Adjoint-based optimization of steady suction for disturbance control in incompressible flows," *Journal of Fluid Mechanics*, vol. 467, pp. 129–161, Sep. 2002.

[69] P.-Y. Passaggia and U. Ehrenstein, "Adjoint based optimization and control of a separated boundary-layer flow," *European Journal of Mechanics - B/Fluids*, vol. 41, pp. 169–177, Sep.–Oct. 2013.

[70] J. B. Freund, "Adjoint-based optimization for understanding and suppressing jet noise," *Journal of Sound and Vibration*, vol. 330, no. 17, pp. 4114–4122, Aug. 2011.

[71] J. D. Jansen, "Adjoint-based optimization of multi-phase flow through porous media – A review," *Computers & Fluids*, vol. 46, no. 1, pp. 40–51, Jul. 2011.

[72] C. M. Pappalardo and D. Guida, "Adjoint-based optimization procedure for active vibration control of nonlinear mechanical systems," *Journal of Dynamic Systems, Measurement, and Control*, vol. 139, no. 8, Aug. 2017.

[73] C. M. Pappalardo and D. Guida, "Control of nonlinear vibrations using the adjoint method," *Meccanica*, vol. 52, no. 11, pp. 2503–2526, Sep. 2017.

[74] K. Dems and Z. Mróz, "Variational approach by means of adjoint systems to structural optimization and sensitivity analysis—II: Structure shape variation," *International Journal of Solids and Structures*, vol. 20, no. 6, pp. 527–552, 1984.

[75] ——, "Variational approach to sensitivity analysis in thermoelasticity," *Journal of Thermal Stresses*, vol. 10, no. 4, pp. 283–306, 1987.

[76] L. Chirco and S. Manservisi, "An adjoint based pressure boundary optimal control approach for fluid-structure interaction problems," *Computers & Fluids*, vol. 182, pp. 118–127, Mar. 2019.

[77] C.-S. Liu, W. Qu, and Y. Zhang, "Numerically solving twofold ill-posed inverse problems of heat equation by the adjoint Trefftz method," *Numerical Heat Transfer, Part B: Fundamentals*, vol. 73, no. 1, pp. 48–61, Jan. 2018.

[78] G. D. Egbert and A. Kelbert, "Computational recipes for electromagnetic inverse problems," *Geophysical Journal International*, vol. 189, no. 1, pp. 251–267, Apr. 2012.

[79] R.-E. Plessix, "A review of the adjoint-state method for computing the gradient of a functional with geophysical applications," *Geophysical Journal International*, vol. 167, no. 2, pp. 495–503, Nov. 2006.

[80] C. Bunks, F. M. Saleck, S. Zaleski, and G. Chavent, "Multiscale seismic waveform inversion," *Geophysics*, vol. 60, no. 5, pp. 1457–1473, Sep. 1995.

[81] J. Virieux and S. Operto, "An overview of full-waveform inversion in exploration geophysics," *Geophysics*, vol. 74, no. 6, pp. WCC127–WCC152, Nov. 2009.

[82] S. Operto, Y. Gholami, V. Prieux, A. Ribodetti, R. Brossier, L. Metivier, and J. Virieux, "A guided tour of multiparameter full-waveform inversion with multicomponent data: From theory to practice," *The Leading Edge*, vol. 32, no. 9, pp. 1040–1054, Sep. 2013.

[83] C Ravaut, S Operto, L Improta, J Virieux, A Herrero, and P Dell'Aversana, "Multiscale imaging of complex structures from multifold wide-aperture seismic data by frequency-domain full-waveform tomography: application to a thrust belt," *Geophysical Journal International*, vol. 159, no. 3, pp. 1032–1056, Dec. 2004.

[84] C. Chavent and J. Liu, "Multiscale parametrization for the estimation of a diffusion coefficient in elliptic and parabolic problems," *IFAC Proceedings Volumes*, vol. 22, no. 4, pp. 193–202, Jun. 1989.

[85] Y. Pan, L. Gao, and T. Bohlen, "High-resolution characterization of near-surface structures by surface-wave inversions: From dispersion curve to full waveform," *Surveys in Geophysics*, vol. 40, no. 2, pp. 167–195, Mar. 2019.

[86] L. Xu, C. Yardim, S. Mukherjee, R. J. Burkholder, Q. Wang, and H. J. S. Fernando, "Frequency diversity in electromagnetic remote sensing of lower atmospheric refractivity," *IEEE Transactions on Antennas and Propagation*, in press, DOI: 10.1109/TAP.2021.3090828,

[87] J. Tabrikian and J. L. Krolik, "Theoretical performance limits on tropospheric refractivity estimation using point-to-point microwave measurements," *IEEE Transactions on antennas and propagation*, vol. 47, no. 11, pp. 1727–1734, Nov. 1999.

[88] J. Compaleo, C. Yardim, and L. Xu, "Refractivity-from-clutter capable, software-defined, coherent-on-receive marine radar," *Radio Science*, vol. 56, no. 3, Art. no. e2020RS007173, Mar. 2021.

[89] Q. Wang, D. P. Alappattu, S. Billingsley, B. Blomquist, R. J. Burkholder, A. J. Christman, E. D. Creegan, T. De Paolo, D. P. Eleuterio, H. J. S. Fernando, *et al.*, "CASPER: Coupled air–sea processes and electromagnetic ducting research," *Bulletin of the American Meteorological Society*, vol. 99, no. 7, pp. 1449–1471, Jul. 2018.

[90] Q. Wang, R. J. Burkholder, C. Yardim, L. Xu, J. Pozderac, A Christman, H. J. S. Fernando, D. P. Alappattu, and Q. Wang, "Range and height measurement of X-band EM propagation in the marine atmospheric boundary layer," *IEEE Transactions on Antennas and Propagation*, vol. 67, no. 4, pp. 2063–2073, Apr. 2019.

[91] M. Wagner, H. Groll, A. Dormiani, V. Sathyanarayanan, C. Mecklenbräuker, and P. Gerstoft, "Phase coherent EM array measurements in a refractive environment," *IEEE Transactions on Antennas and Propagation*, vol. 69, no. 10, pp. 6783–6796, Oct. 2021.

[92] R. N. López and V. S. del Río, "High temporal resolution refractivity retrieval from radar phase measurements," *Remote Sensing*, vol. 10, no. 6, Art. no. 896, Jun. 2018.

[93] B. L. Cheong, R. D. Palmer, C. D. Curtis, T.-Y. Yu, D. S. Zrnic, and D. Forsyth, "Refractivity retrieval using the phased-array radar: First results and potential for multimission operation," *IEEE Transactions on Geoscience and Remote Sensing*, vol. 46, no. 9, pp. 2527–2537, Sep. 2008.

[94] S. Park and F. Fabry, "Simulation and interpretation of the phase data used by the radar refractivity retrieval algorithm," *Journal of Atmospheric and Oceanic Technology*, vol. 27, no. 8, pp. 1286–1301, Aug. 2010.

[95] J. R. Rodon, A. Broquetas, A. M. Guarnieri, and F. Rocca, "Geosynchronous SAR focusing with atmospheric phase screen retrieval and compensation," *IEEE Transactions on Geoscience and Remote Sensing*, vol. 51, no. 8, pp. 4397–4404, Aug. 2013.

[96] R. Douvenot, V. Fabbro, and K. Elis, "Parameter-based rules for the definition of detectable ducts for an RFC system," *IEEE Transactions on Antennas and Propagation*, vol. 62, no. 11, pp. 5696–5705, Nov. 2014.

[97] T. Bonnafont, "Modeling the atmopsheric long-range electromagnetic waves propagation in 3D using the wavelet transform," Ph.D. Dissertation, Université Toulouse 3 Paul Sabatier, Toulouse, France, Nov. 2020.

[98] D. Dockery and J. R. Kuttler, "An improved impedance-boundary algorithm for Fourier split-step solutions of the parabolic wave equation," *IEEE Transactions on Antennas and Propagation*, vol. 44, no. 12, pp. 1592–1599, Dec. 1996.

[99] H. V. Hitney, J. H. Richter, R. A. Pappert, K. D. Anderson, and G. B. Baumgartner, "Tropospheric radio propagation assessment," *Proceedings of the IEEE*, vol. 73, no. 2, pp. 265–283, Feb. 1985.

[100] L. T. Rogers, "Effects of the variability of atmospheric refractivity on propagation estimates," *IEEE Transactions on Antennas and Propagation*, vol. 44, no. 4, pp. 460–465, Apr. 1996.

[101] R. Douvenot, V. Fabbro, C. Bourlier, J. Saillard, H.-H. Fuchs, and H. Essen, "Refractivity from sea clutter applied on VAMPIRA and Wallops' 98 data," in *2008 International Conference on Radar*, Sep. 2008, pp. 482–487.

[102] C. Yardim, P. Gerstoft, and W. S. Hodgkiss, "Tracking refractivity from clutter using Kalman and particle filters," *IEEE Transactions on Antennas and Propagation*, vol. 56, no. 4, pp. 1058–1070, Apr. 2008.

[103] H. Barucq, G. Chavent, and F. Faucher, "A priori estimates of attraction basins for nonlinear least squares, with application to Helmholtz seismic inverse problem," *Inverse Problems*, vol. 35, no. 11, Art. no. 115004, Nov. 2019.

[104] M. Kern, *Numerical Methods for Inverse Problems*. Hoboken, NJ, USA: Wiley, 2016.

[105] M. Meyer and J.-P. Hermand, "Optimal nonlocal boundary control of the wide-angle parabolic equation for inversion of a waveguide acoustic field," *The Journal of the Acoustical Society of America*, vol. 117, no. 5, pp. 2937–2948, May 2005.

[106] F. B. Jensen, W. A. Kuperman, M. B. Porter, and H. Schmidt, *Computational Ocean Acoustics*. New York, NY, USA: Springer-Verlag, 2011.

[107] F. D. Tappert, "The parabolic approximation method," in *Wave Propagation and Underwater Acoustics*, Berlin, Germany: Springer, 1977, pp. 224–287.

[108] J. R. Kuttler, "Differences between the narrow-angle and wide-angle propagators in the split-step Fourier solution of the parabolic wave equation," *IEEE Transactions on Antennas and Propagation*, vol. 47, no. 7, pp. 1131–1140, Jul. 1999.

[109] M. D. Feit and J. A. Fleck, "Light propagation in graded-index optical fibers," *Applied Optics*, vol. 17, no. 24, pp. 3990–3998, Dec. 1978.

[110] M. Asch, M. Bocquet, and M. Nodet, *Data assimilation: methods, algorithms, and applications*. Philadelphia, PA, USA: SIAM, 2016.

[111] J. Monnier, *Variational Data Assimilation: From optimal control to large scale data assimilation*. Open Online Course, INSA Toulouse, 2021,
URL: `https://www.math.univ-toulouse.fr/~jmonnie/Enseignement/VDA.html`.

[112] G. Chavent, *Nonlinear Least Squares for Inverse Problems: Theoretical Foundations and Step-by-Step Guide for Applications*. Dordrecht, The Netherlands: Springer, 2010.

[113] H. Brezis, *Functional Analysis, Sobolev Spaces and Partial Differential Equations*. New York, NY, USA: Springer, 2010.

[114] A. Wouk, "A note on square roots of positive operators," *SIAM Review*, vol. 8, no. 1, pp. 100–102, Jan. 1966.

[115] D. Lee, G. Botseas, and J. S. Papadakis, "Finite-difference solution to the parabolic wave equation," *The Journal of the Acoustical Society of America*, vol. 70, no. 3, pp. 795–800, 1981.

[116] J. R. Kuttler and G. D. Dockery, "Theoretical description of the parabolic approximation/Fourier split-step method of representing electromagnetic propagation in the troposphere," *Radio science*, vol. 26, no. 2, pp. 381–393, Mar.–Apr. 1991.

[117] S. Mukherjee and C. Yardim, "Accurate computation of scintillation in tropospheric turbulence with parabolic wave equation," *IEEE Transactions on Antennas and Propagation*, vol. 69, no. 8, pp. 4748–4757, Aug. 2021.

[118] H. Zhou, "Modeling the atmospheric propagation of electromagnetic waves in 2D and 3D using Fourier and wavelet transforms," Ph.D. Dissertation, Université Toulouse 3 Paul Sabatier, Toulouse, France, Apr. 2018.

[119] J. Nocedal and S. Wright, *Numerical Optimization*. New York, NY, USA: Springer-Verlag, 2006.

[120] P. Wolfe, "Convergence conditions for ascent methods," *SIAM Review*, vol. 11, no. 2, pp. 226–235, Apr. 1969.

[121] ——, "Convergence conditions for ascent methods. II: Some corrections," *SIAM Review*, vol. 13, no. 2, pp. 185–188, Apr. 1971.

[122] J. Kaipio and E. Somersalo, *Statistical and Computational Inverse Problems*. New York, NY, USA: Springer, 2005.

[123] J. L. Mueller and S. Siltanen, *Linear and Nonlinear Inverse Problems with Practical Applications*. Philadelphia, PA, USA: SIAM, 2012.

[124] Y. O. Yuan, F. J. Simons, and E. Bozdağ, "Multiscale adjoint waveform tomography for surface and body waves," *Geophysics*, vol. 80, no. 5, pp. R281–R302, Sep. 2015.

[125] D. H. Wolpert and W. G. Macready, "No free lunch theorems for optimization," *IEEE Transactions on Evolutionary Computation*, vol. 1, no. 1, pp. 67–82, Apr. 1997.

[126] J. Liu, "A multiresolution method for distributed parameter estimation," *SIAM Journal on Scientific Computing*, vol. 14, no. 2, pp. 389–405, Mar. 1993.

[127] X. Zhao, "Range-dependent refractivity remote sensing from radar clutter," in *IEEE International Geoscience and Remote Sensing Symposium (IGARSS)*, Jul. 2018, pp. 9351–9354.

[128] Y. Diouane, S. Gratton, X. Vasseur, L. N. Vicente, and H. Calandra, "A parallel evolution strategy for an earth imaging problem in geophysics," *Optimization and Engineering*, vol. 17, no. 1, pp. 3–26, Mar. 2016.

[129] D. Oldenburg, P. McGillivray, and R. Ellis, "Generalized subspace methods for large-scale inverse problems," *Geophysical Journal International*, vol. 114, no. 1, pp. 12–20, 1993.

[130] B. L. N. Kennett, M. S. Sambridge, and P. R. Williamson, "Subspace methods for large inverse problems with multiple parameter classes," *Geophysical Journal International*, vol. 94, no. 2, pp. 237–247, Aug. 1988.

[131] J. Skilling and R. K. Bryan, "Maximum entropy image reconstruction: general algorithm," *Monthly Notices of the Royal Astronomical Society*, vol. 211, pp. 111–124, 1984.

[132] S. Kraut, R. H. Anderson, and J. L. Krolik, "A generalized Karhunen-Loeve basis for efficient estimation of tropospheric refractivity using radar clutter," *IEEE Transactions on Signal Processing*, vol. 52, no. 1, pp. 48–60, Jan. 2004.

[133] B. R. Bean and G. D. Thayer, "Models of the atmospheric radio refractive index," *Proceedings of the IRE*, vol. 47, no. 5, pp. 740–755, May 1959.

[134] B. R. Bean, B. A. Cahoon, C. A. Samson, and G. D. Thayer, *A World Atlas of Atmospheric Radio Refractivity*. ESSA Monograph 1, U.S. Government Printing Office, Washington, DC, USA, 1966.

[135] K. Tao and Y. Baba, "On the distribution of refractive index in the lower atmosphere in Japan (Study of radio dynamic climatology)," *Journal of the National Institute of Information and Communications Technology*, vol. 1, no. 5, pp. 17–28, 1954.

[136] S. M. Kulshrestha, "Radio climatology of India," *Indian Journal of Radio and Space Physics*, vol. 16, pp. 5–10, Feb. 1987.

[137] E. V. Batueva, D. D. Darizhapov, B. I. Samdanov, and W.-M. Boerner, "Cartography and monitoring of the tropospheric state," in *Proceedings of SPIE, Fifth International Symposium on Atmospheric and Ocean Optics*, International Society for Optics and Photonics, vol. 3583, Jan. 1999, pp. 565–571.

[138] F. Mesnard and H. Sauvageot, "Climatology of anomalous propagation radar echoes in a coastal area," *Journal of Applied Meteorology and Climatology*, vol. 49, no. 11, pp. 2285–2300, Nov. 2010.

[139] T. Akiyama, "Studies on the radio refractive index in the tropospheric atmosphere," *Review of Electrical Communication Laboratory*, vol. 25, no. 1–2, pp. 79–95, Jul.–Aug. 1977.

[140] W. L. Patterson, "Historical electromagnetic propagation condition database description," Naval Ocean Systems Center, San Diego, CA, USA, Tech. Doc. 1149, Sep. 1987.

[141] W. L. Patterson, "Advanced refractive effects prediction system (AREPS), version 1.0 user's manual," Space and Naval Warfare Systems Center, San Diego, CA, USA, Tech. Doc. 3028, Apr. 1998.

[142] E. Polak and G. Ribiere, "Note sur la convergence de méthodes de directions conjuguées," *Revue Française d'Informatique et de RechercheOpérationnelle*, vol. 16, no. R1, pp. 35–43, 1969.